THE UNIVERSITY OF CHICAGO

DEVELOPMENT AND APPLICATION OF ADVANCED CONE-BEAM CT ACQUISITION STRATEGIES FOR IMAGE-GUIDED THERAPIES

A DISSERTATION SUBMITTED TO
THE FACULTY OF THE DIVISION OF THE BIOLOGICAL SCIENCES
AND THE PRITZKER SCHOOL OF MEDICINE
IN CANDIDACY FOR THE DEGREE OF
DOCTOR OF PHILOSOPHY

COMMITTEE ON MEDICAL PHYSICS

BY
ERIK PEARSON

CHICAGO, ILLINOIS
JUNE 2013

ProQuest LLC.
789 East Eisenhower Parkway
P.O. Box 1346
Ann Arbor, MI 48106 - 1346

for my family and friends

whose love and support carried me through

TABLE OF CONTENTS

LIST OF FIGURES

LIST OF TABLES

LIST OF ALGORITHMS

ACKNOWLEDGMENTS

There have been so many that have contributed to where I am today, teachers and professors that offered instruction and guidance, friends and family that gave support and encouragement. Unfortunately it is just not possible to recognize them all here but I would like to thank a few.

First and foremost I would like to thank Chuck Pelizzari for being an incredible advisor and mentor. He provided the freedom for me to pursue many different ideas, guidance when I was in need of it and help when I got stuck. I was extremely fortunate to have Xiaochuan Pan as an advisor as well. I learned a great deal from his terrific depth of knowledge in image reconstruction and his enthusiasm for the research has been an inspiration.

I am grateful to my committee members, Hania Al-Hallaq, Chet Reft and Jeff Siewerdsen for their time, support and insightful feedback on my work. And I would like to thank all the faculty, staff and students of the GPMP for creating a great environment for learning and collaborative research.

I would like to thank my undergraduate research advisor, Karl Unruh, and Tom Ekiert who fostered my passion for experimental research and prepared me for my time as a graduate student.

Emil Sidky has been an invaluable resource, with an astounding knowledge of all things reconstruction and the skill and patience to share that knowledge. Seung Cho generously shared his experience and helped get me off to a running start.

I would like to profusely thank Karl Farrey and the rest of the Radiation Oncology clinical staff for their support on the clinical systems and for allowing me to attach my home built hardware and run them after hours. This work would not have been possible with out their assistance and trust.

Fellow students and friends, especially Andrew Jamieson, Zac Labby, Liz Hipp, Phil Vargas, Bill Sensakovic and Xiao Han, have provided much needed distraction, commiseration, encouragement and inspiration. I am excited to see the amazing things I know they will all go on to do.

Most of all, I am indebted to my parents for their never ending love, support and encouragement. They have made it all possible.

ABSTRACT

In addition to its traditional role in diagnostics, CT has recently been increasingly utilized as a guidance tool in therapeutic procedures. This has been driven, in a large part, by advances in flat-panel x-ray detector technologies that have enabled the rapid development of flat-panel cone-beam CT (CBCT). Guidance systems typically consist of a flat panel detector mounted opposite a kilovoltage x-ray tube often on a C-arm in interventional radiology or image-guided surgery or mounted directly to linear accelerator for image-guided radiation therapy (IGRT). These systems have enabled new therapies and made existing therapies more accurate and safer for the patient. However, CT imaging involves additional x-ray exposure to the patient and we must consider the "As low as reasonably achievable" (ALARA) principle of the USNRC and the AAPM Task Group 75 report that states it is no longer safe to consider imaging dose negligible and "that strategies for reducing the imaging dose and volume of exposed anatomy be pursued wherever possible, even when they require developing new image acquisition and reconstruction techniques"

In that regard we have developed four targeted image acquisition strategies, enabled by a custom dynamic collimation device, that contain sufficient information to have clinical utility with substantially lower dose away from the target region than conventional methods. The design, development and verification of the dynamic collimator are described followed by the first imaging strategy, dynamic collimation of fluoroscopy for tracking implanted lung fiducials. The second imaging application, conformal ROI imaging in CBCT, reconstructs a region of interest (ROI) from restricted illumination data with the chord based BPF algorithm. This approach accurately recovers the ROI, but only the ROI, with highly targeted imaging dose. Additionally this approach is limited to certain peripheral ROIs.

To overcome these limitations we developed the intensity weighted ROI (IWROI) imaging method that uses filters to spatially vary the intensity of the beam instead of opaque blades to collimate the beam. In this way we acquire complete data of the patient that allows for reconstruction of the whole volume with standard reconstruction algorithms and is not

limited to peripheral regions. However, the parts of the projection data measured with the low intensity (filtered) beam have higher noise which propagates back in to the reconstructed image during reconstruct resulting in a high quality image within the ROI and a lower quality, noisy image of the rest of the patient. The lower quality region can still be useful in image guidance, e.g. for alignment to high contrast structures such as bone or the skin surface. This technique has been developed with both statically mounted filters on the x-ray source and with dynamic filtration with the collimator.

CHAPTER 1

INTRODUCTION

> If the hand be held before the fluorescent screen, the shadow shows the bones darkly, with only faint outlines of the surrounding tissues.
>
> (Wilhelm Conrad Röntgen, 1895[1])

The above account describes one of the first radiographs ever taken, Figure 1.1a, by Wilhelm Röntgen of his wife's hand in 1895. The medical implications of the radiograph were almost immediately evident with the first reported clinical x-rays taken in January of 1896 by John Hall-Edwards in Birmingham and later that same month by A E Wright of Yale[2]. Today radiography is a standard part of medical practice with an estimated 182.9 million x ray procedures performed in the US in 2010, which has increased an average of 5.5% per year over the preceding five years[3]. However, despite the prevalence and great utility in certain applications, radiography also has its limitations. Most notably, the entire thickness of the site being imaged is projected onto a plane and as such overlapping structures can create images that are difficult to interpret and may obscure small lesions.

This problem of overlapping structures has been overcome, in a large part, by the development of x ray computed tomography (CT). CT uses many radiographs taken from different angles distributed around the object of interest from which the full 3D structure is mathematically reconstructed. The developing theory of tomographic reconstruction began early in the 20th century but its practical impact in medicine is credited Allan Macleod Cormack who published a theoretical basis[5,6] of computed tomography in 1963 and 1964 and also to Sir Godfrey Hounsfield[7] who independently developed the first systems at EMI Central Research Laboratories. The first patient scan was performed in 1971 at Atkinson Morley Hospital in the UK. A representation of that original image is shown in Figure 1.1b. Since then image quality has improved dramatically and CT imaging has become a mainstay of modern medicine with an estimated 81.9 million CT procedures performed in the US in

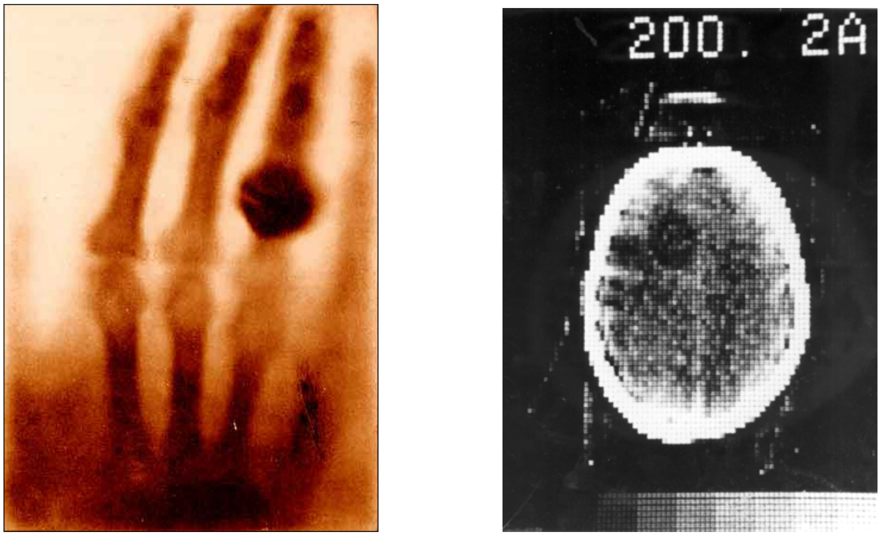

(a) (b)

Figure 1.1: (a) First x ray radiograph taken by Wilhelm Röntgen in 1895 of his wife's hand. Public domain image courtesy of The National Institutes of Health, National Library of Medicine. (b) Early patient CT image taken at Atkinson Morley Hospital, Wimbledon, London, UK. (Image courtesy of the British Journal of Radiology[4])

2010, representing an average annual growth rate of 6% over the preceding 3 years[8].

Recently, CT has been increasingly utilized as guidance system in therapeutic procedures, rather than the traditional diagnostic role. This has been driven, in a large part, by the developments in flat-panel x-ray detectors which has enabled the cone-beam CT (CBCT) systems used in these procedures. These systems consist of flat panel detector mounted opposite a kilovoltage x-ray tube often on a C-arm in interventional radiology or image-guided surgery or mounted directly to linear accelerator for image-guided radiation therapy (IGRT). These guidance oriented CBCT systems provide a unique opportunity in that the patient anatomy is already known and the critical part of the image is often restricted to a predetermined region. Using this fact we developed several techniques that can provide sufficient utility for the guidance task with substantially less radiation exposure to the patient.

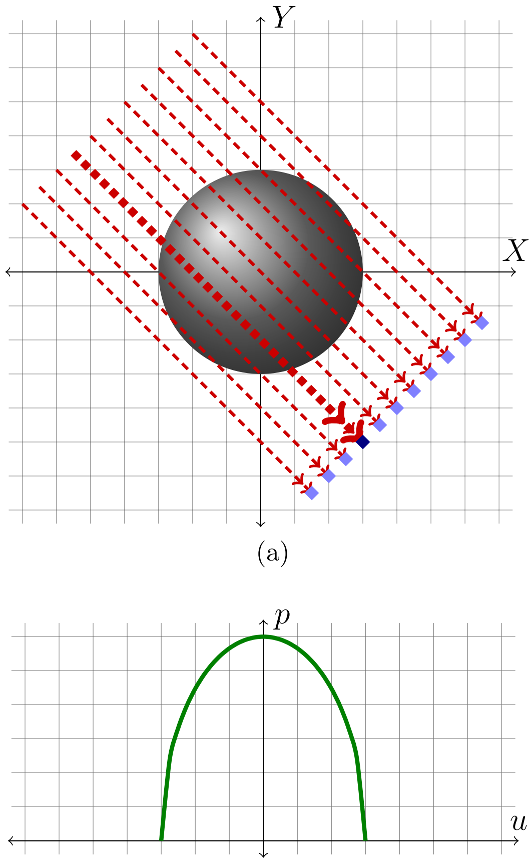

(a)

(b)

Figure 1.2: Parallel projection geometry

1.1 CT Principles

1.1.1 Parallel Beam CT

The first CT scanners used a narrowly collimated, pencil beam x ray source opposite a small area detector which rastered linearly over the object and then the whole system is rotated about the object being scanned. This scanning geometry is shown in 1.2a. Along each pencil beam some of the photons will interact in the object being scanned, either absorbed or scattered out of the path. The probability of a photon interacting in a unit thickness of material is known as the linear attenuation coefficient (μ) and is a local property of the material. Thus in each infinitesimal thickness (dl) along the path for N incident photons the change in the number is

$$dN = -\mu N dl \tag{1.1}$$

Integrating along the pencil beam we find that the number of photons reaching the detector is proportional to the number of incident photons N_0 as

$$N = N_0 e^{-\int \mu(\vec{r}) dl} \tag{1.2}$$

The task of CT is to recover the 3D distribution of the linear attenuation coefficients ($\mu(\vec{r})$) from multiple measurements. This process is known as reconstruction. Typically we take the projection data (p) for a given view angle (θ) to be the log ratio of an unattenuated to an attenuated measurement (using I for intensity rather than the N above) with u denoting the detector coordinate system:

$$p(u;\theta) = \ln\left(\frac{I_0}{I}\right) = \int \mu(\vec{r}) dl \tag{1.3}$$

For the spherical object case the projection data is plotted in 1.2b. In the case of straight, parallel lines this is the Radon transform which can be inverted by filtered back projection (FBP). The image ($f(x, y)$), which in CT is typically an estimate of $\mu(\vec{r})$, can be recovered from these projection data by filtering the data in the Fourier spatial frequency domain by a ramp function ($|\omega|$) and then backprojection in to the image. Backprojection casts the values from the projection data back into the image volume along the ray connecting the source point to the detector element.

$$f(x, y) = \int\int \mathcal{F}\left(p(u;\theta)\right) |\omega| e^{j2\pi\omega u} d\omega d\theta \tag{1.4}$$

where $\mathcal{F}$ indicates the fourier transform.

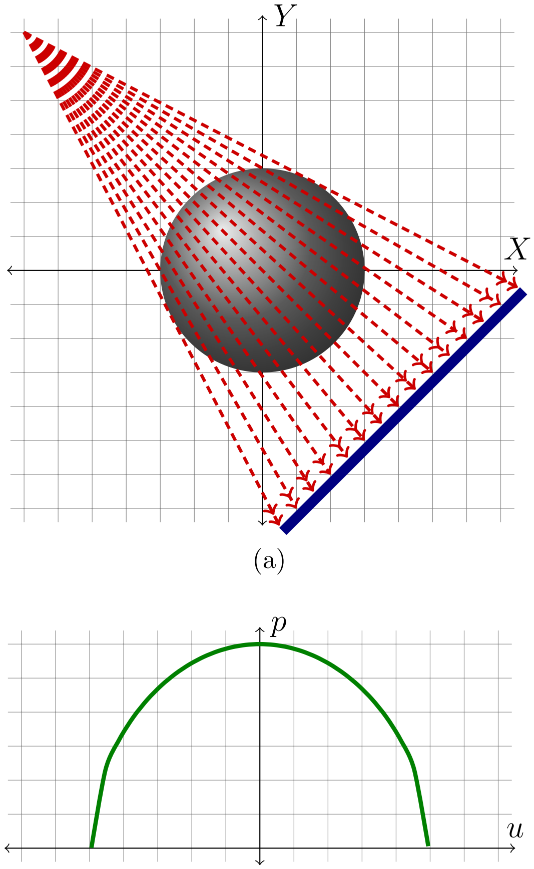

(a)

(b)

Figure 1.3: Fan beam projection geometry

1.1.2 Fan Beam CT

First generation CT scanners utilized the parallel beam geometry, with a narrowly collimated beam rastered across the object at each view angle. The mechanical complexity required to achieve this mathematically tractable geometry was high; thus, motivating the development of reconstruction methods capable of dealing with a more practical fan beam geometry. Here a point x ray source could simply rotate about the object, with either a translating point detector, or a segmented line or arc detector.Figure 1.3 shows a fan beam geometry with a linear detector.

There are generally two approaches to the fan beam reconstruction problem, rebinning to a parallel beam geometry or direct inversion. With the diverging rays from many different views, one can imagine that in principle they can be regrouped into sets of parallel rays that can then be reconstructed with the method above. However, in practice, the discrete sampling require interpolation to convert to a parallel beam set that can result in a loss of spatial resolution. The alternative, and preferred approach is a direct inversion of the fan beam which can be worked out from the geometry. Detailed derivations for both curved and flat detectors can be found in the textbook by Kak and Slaney[9].

1.1.3 Helical CT

The parallel and fan beam reconstruction methods discussed above utilize a 1D detector, either arc or line and reconstruct a single slice through the patient. In order to cover a volume of interest the patient can be translated and the volume can be built slice by slice in a step and shoot fashion. However, with modern diagnostic CT systems which can rotate continuously at high speeds the step and shoot approach is slow and inefficient. Instead the patient is fed through the rotation gantry at a constant rate. From the patient's perspective the x ray source moves in a spiral or helix around them, hence the name. Helical CT data can also be reconstructed with the FBP methods above and this is considered the current gold standard in volumetric CT imaging.

1.1.4 Flat-Panel Cone-Beam CT

With recent, rapid advances in amorphous silicon thin-film-transistor (TFT) technology the size and availability of flat-panel x ray detectors has been increasing while the cost has been dropping. These detectors use TFTs made with a similar process as LCD monitors and TVs however the pixels contain photodiodes which make them sensitive to light. They are then coupled to scintillating screens, often cesium-iodide to convert the impinging x-rays into light resulting in sensitive, large area detectors with good spatial resolution. These detectors, paired with a standard kV x ray tube, were mounted to radiotherapy linear accerelators and C-arm systems and have become an important part of medical imaging[10–16].

Reconstruction

The large area detector and point source create a cone (or pyramid) of illumination which allows a volume of the patient to be imaged in one circular rotation about the patient. Cone-beam CT (CBCT) does not provide sufficient data for mathematically exact recovery. However the FBP based approximation of Feldkamp, Davis and Kress[17], which has come to be referred to simply as FDK, has proven itself to be practically useful and is the current standard in CBCT reconstruction. As this algorithm plays an important role in this work a description of the major steps is provided. The following description generally follows the naming conventions and organization of Siewerdsen's 2011 AAPM educational course[18].

Data preprocessing is applied to both the I and I_0 measurements to correct for detector response, bad pixels and other known measurement errors where I contains the object being scanned and I_0 is an air field image.

Log normalization recovers the integral attenuation from the I and I_0 measurements. In the cone-beam case the images are now two dimensional and we use the coordinates u and v where u is the direction on the detector perpendicular to the axis of rotation and v is parallel. The data are acquired for a set of view angles θ.

$$p_1(u, v; \theta) = \ln \left(\frac{I_0}{I(u, v; \theta)} \right) \tag{1.5}$$

Cosine (Feldkamp) Weighting accounts for the ray divergence in the cone-beam geometry. The source to detector distance is written as SDD.

$$p_2(u, v; \theta) = p_1(u, v; \theta) \left(\frac{SDD}{\sqrt{SDD^2 + u^2 + v^2)}} \right) \tag{1.6}$$

Data Redundancy Weighting also called Parker weighting[19] is required when the reconstruction is performed for short scan data. That is only $\pi + \phi_{fan}$ data is acquired, instead of the full 2π where ϕ_{fan} is the fan angle of the beam.

$$p_3(u,v;\theta) = p_2(u,v;\theta)w_3(u;\theta) \tag{1.7}$$

The weighting factor is calculated as:

$$w_3(u;\theta) = \begin{cases} \sin^2\left(\frac{\pi\theta}{2\phi_{fan}-4\phi(u)}\right), & \text{where} \quad 0 \le \theta \le \phi_{fan} - 2\phi(u) \\ 1, & \text{where} \quad \phi_{fan} - 2\phi(u) \le \theta \le \pi - 2\phi(u) \\ \sin^2\left(\frac{\pi(\pi+\phi_{fan}-\theta)}{2\phi_{fan}+4\phi(u)}\right), & \text{where} \quad \pi - 2\phi(u) \le \theta \le \pi + \phi_{fan} \end{cases} \tag{1.8}$$

where

$$\phi(u) = \tan^{-1}\left(\frac{u-u_0}{SDD}\right) \tag{1.9}$$

Ramp Filtering is once again applied in the spatial frequency domain, which can also be expressed as a convolution in the spatial domain.

$$\begin{aligned} p_4(u,v;\theta) &= \mathcal{F}^{-1}\left[\mathcal{F}[p_3(u,v;\theta)]|\omega|)\right] \\ &= p_3(u,v;\theta) * \left(-\frac{1}{2\pi^2u^2}\right) \end{aligned} \tag{1.10}$$

Apodization Window Filtering provides noise control. The ramp filter amplifies high frequencies however the frequency content of the data is limited by the measurement hardware and typically the highest frequencies contain only noise. An apodizing filter $F_{win}(\omega,\nu)$ is used to suppress the high frequency amplification. There are many functions used for this purpose, such as the Butterworth, Hann and Hamming windows. This can also be applied in the Fourier or spatial domains.

$$\begin{aligned} p_5(u,v;\theta) &= \mathcal{F}^{-1}\left[\mathcal{F}[p_4(u,v;\theta)]F_{win}(\omega,\nu)\right] \\ &= p_4(u,v;\theta) * f_{win}(u,v) \end{aligned} \tag{1.11}$$

Backprojection is the final step in the reconstruction chain. The corrected, weighted and filtered values of the projection data are cast back along the rays toward the source point into the image volume.

The process is repeated for each view angle θ to recover the image volume.

1.1.5 Practical Challenges

There are many challenges that arise when translating the reconstruction theories from above to practical implementations on physical systems. They range from more theoretical considerations like the imaging model's simplifications of the underlying physical processes and sampling considerations for the discretization of the continuous model to hardware considerations like system geometry calibration. These issues are generally beyond the scope of this work however we introduce two that are of particular importance.

Polychromatism

The x ray field emitted from a standard imaging tube contains photons from a spectrum of different energies. A plot of the spectra relevant to this work can be found in Figure 4.3. If we include the energy dependence of the attenuation the imaging model can be more accurately written as

$$I = I_0 \int S(E) e^{-\int \mu(\vec{r},E) dl} dE \tag{1.12}$$

where $S(E)$ is the normalized spectrum and μ is now a function of energy as well as position. This non-linearity can cause artifacts in the reconstructed image, known as beam hardening artifacts, that can present as cupping or dark shading between high density regions. There are established approaches to reduce these artifacts[20–22]. However the polychromatic nature of the beam is particularly relevant to the technique proposed in chapter 4 because we cause $S(E)$ to become a strong function of position which requires new correction methods.

Scatter

The imaging model above assumes that photons that undergo any interaction, scatter or absorption, are not detected. This is necessary since the scattering process is stochastic and is also a reasonable assumption for the fan beam geometry. With a fan beam only a small volume of the patient is illuminated which is relatively far from a narrow detector, thus the probability that a photon that scatters through any angle is detected is quite low. However in CBCT a large volume is illuminated and the large area detector greatly increases the odds of scattered photons being detected. In fact for a clinical CBCT of the pelvis the scatter to primary ratio may be $> 100\,\%$[23], meaning more of the detected photons were scattered than not. In comparison, the SPR of a diagnostic CT scanner with a fan beam geometry is typically $< 10\,\%$. The scatter fluence can degrade the image's quantitative accuracy and contrast and cause shading artifacts, which often appear as dark streak emanating from high contrast structures[24]. The methods presented here can reduce scatter and potentially mitigate these effects.

1.2 CBCT for Image Guidance

1.2.1 CBCT in Radiation Therapy

External beam radiation therapy is commonly prescribed for many types of cancer. Generally, the procedure is as follows. Prior to treatment the patient is brought in for simulation in which, the patient is placed in the treatment position and fitted for any necessary immobilization devices and small alignment marks or tattoos may be made on the skin surface for visual alignment. While in the treatment position a diagnostic quality CT scan (often with a large-bore helical scanner) is taken. These images are used for treatment planning, dose calculation and as reference for patient setup. The radiation is often delivered every weekday for several weeks. This fractionated technique has been used since the early days of radiotherapy[25] and has been found to be beneficial due to the different radiobiological properties of cancerous and normal tissue.

While a fractionated course of radiation therapy has substantial beneficial impact on differential kill and sparing, respectively, of tumor and healthy tissue it also presents the challenge of correctly targeting the tumor volume every day. Traditionally this was done simply by aligning the beam to the surface marks made on the patient during the planning phase and possibly MV portal films, with additional diagnostic CT scans only acquired if indicated by observed changes in the patient, such as substantial weight change. This process presupposes that the anatomy does not change over the course of treatment, clearly an imperfect assumption. Now, the treatment vault in a cutting edge radiation oncology clinic is teeming with devices to help properly position the patient. Many of these still rely on external surrogates for tumor position, such as infra-red stereoscopic cameras with reflectors mounted on the patient and/or immobilization devices and speckle projectors with arrays of optical cameras for 3D skin surface reconstruction[26]. However, these suffer the same limitation that the surface does not necessarily reflect the internal anatomy.

For alignment with internal anatomical structures ultrasound, MRI, RF fiducials, MV x-rays from the treatment accelerator and kV x ray sources are all used. An ultrasound transducer registered to the room coordinate system has been used[27] and can provide good soft tissue imaging. However, it needs to be manually operated by a skilled technician and only works for some anatomical sites. Using the MV x-rays from the treatment head provides a nice "beams-eye view" but has poor soft tissue contrast so is typically only effective for alignment of the high contrast skeletal structures. Recent developments have mounted kV x ray tubes and flat-panel digital detectors to the gantry[14,16,28–30] and many newer linear accelerators now come equipped with kV imaging hardware, as shown in Figure 1.4. This provides a good combination of easy volumetric imaging and adequate soft tissue contrast for direct localization of the target volume and organs at risk. These kV imaging systems can be used to acquire single or multiple radiographs, or to perform a CBCT scan with the patient in the treatment position. The data sets obtained from kV CBCT positioning

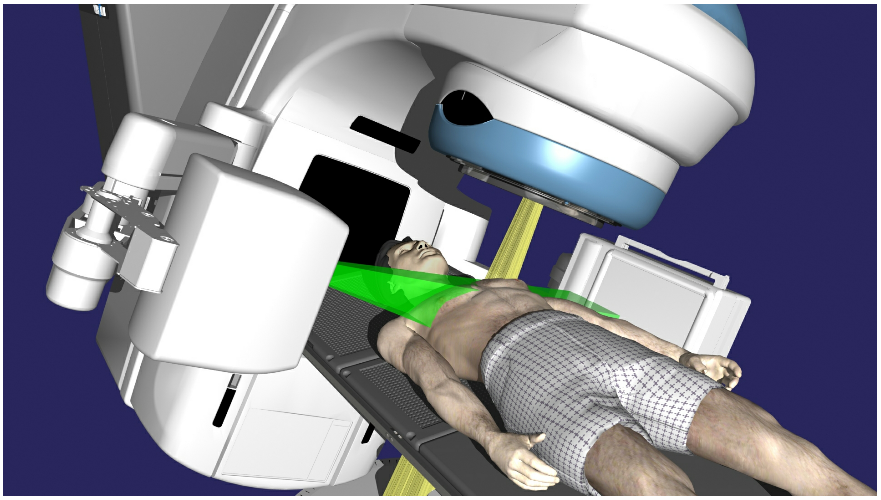

Figure 1.4: An illustration of the Trilogy linear accelerator by Varian Medical Systems Inc with an on-board imaging device (OBI). The yellow cone represents the treatment beam. The green cone is the imaging beam, emerging from a kV source on the left side of the image and striking a digital detector partly obscured by the patient. (Image courtesy of Varian Medical Systems, Inc. All rights reserved.)

scans have the added advantage of being able to be used for dose calculation[31] which may in the future enable dose reconstruction in adaptive radiation therapy or on-line replanning for more accurate treatment delivery[32].

While the kV CBCT is proving to be useful for target localization in image guided radiation therapy (IGRT)[33–35] it also uses ionizing radiation and so we must consider the imaging dose to the patient[36]. The dose to individual organs has been measured for standard imaging protocols and range from negligible to around 10 cGy per scan depending on site and procedure[37,38]. This may be small compared to the dose delivered for therapy but it is untargeted and deposited in healthy tissue and therefore needs to be minimized.

1.2.2 Motivation for Region of Interest Imaging

Dose to the patient from CBCT imaging can be reduced by altering the x ray fluence, beam energy or the number of views acquired. Most dose reduction strategies currently use a reduced fluence approach. Often this is done by reducing the tube current which can be done on a view-by-view basis to account for differences in patient thickness from different angles[39,40]. It can also be done uniformly across all views, further reducing dose but resulting in noisier projection data. There has been work on statistically driven iterative techniques for smoothing the data[41–43] or for reconstructing it directly[44–46]. Another approach to limiting the patient exposure in which there has recently been great progress is to reduce the number of angular samples, few-view reconstruction[47–49].

The aforementioned dose reduction methods are global in nature, that is, they are applied generally during acquisition without consideration of the specific imaging requirements. An alternate approach is to image only the region of interest (ROI) by restricting the x ray field to only cover this region. This is often possible in guidance applications because, unlike diagnostics, the object of interest and its location has been previously determined and the imaging is being performed to confirm the location or locate a surgical instrument relative to it. With traditional analytical techniques, such as FDK, such restricted illumination results in truncation artifacts[24,50] in the reconstructed image.

1.2.3 Existing ROI imaging techniques

Most of the previous work on ROI imaging falls into one of two categories. The first is local (or lambda) tomography[51–53]. This is an analytic reconstruction approach to the interior problem[50], however this does not recover the typical image function f representing the spatial distribution of the coefficient of attentuation but instead it recovers $Lf = \Lambda f + \mu \Lambda^{-1} f \quad : \Lambda = \sqrt{-\Delta}$ where Δ denotes the Laplacian operator. The image Lf has some interesting features, such as edge enhancement, but it does not contain the attenuation information crucial to current IGRT advances such as dose verification and adaptive replanning.

The other general category is advanced algorithms that can reconstruct from reduced data. There are several[54–57] from which we will use the chord based methods[58–61] which can give accurate results and are devoid of truncation artifacts, for certain types of ROIs. However, in the case of the interior ROI there is no practically useful analytic solution to the reconstruction problem.

1.3 Scope of Work

In order to reduce the risks associated with radiation exposure for the patient yet provide CBCT images which enable safer and more accurate therapeutic procedures we have developed four targeted imaging acquistion strategies. Three of these strategies require dynamic control over the x ray field during acquisition, in ways that are not possible with current hardware. We begin with describing the development of a novel collimation device that can be mounted on clinical imaging hardware in chapter 2. The first imaging application, presented in chapter 2, is dynamic collimation for fluoroscopic tracking of implanted lung fiducials during therapy.

Region of interest imaging enabled by the advanced chord based algorithms is developed in chapter 3. The first half of the chapter is a simulation study exploring a clinical use case for this kind of ROI imaging for postmastectomy radiation therapy patients. This study includes the development of an automated patient-linac collision detection system to determine safe patient positioning for offset ROI imaging. The second half of the chapter focuses on real-data experimental studies on phantoms.

The concept of intensity weighted ROI imaging is introduced in chapter 4. The idea of this approach is to target the image quality and consequently the imaging dose to the region of interest but retain the ability to reconstruct the whole object, but at lower image quality. This is accomplished by spatially varying the intensity of the imaging beam with weighting filters. In this chapter they are statically fixed to the x ray source creating a cylindrical ROI. The details of the necessary steps for reconstruction as well as a detailed dose sparing study using Monte Carlo methods are presented.

Several other investigators have also reported on intensity weighting CT concepts[62–67]. So far this work has been restricted to theoretical analysis. The work of Graham and Bartolac of the University of Toronto has involve techniques for selecting optimal fluence weighting patterns and will be further discussed in the path forward section of chapter 6

Finally, in chapter 5 we extend the methods of chapter 4 with the capabilities of the dynamic collimator, equipped with weighting filters rather than opaque blades, for intensity-weighted ROI imaging for arbitrary regions. Results are shown for periphereal as well as interior ROIs and dose sparing results are performed with Monte Carlo simulations.

CHAPTER 2

DYNAMIC COLLIMATION

2.1 Introduction

The imaging techniques presented in this work require dynamically restricting or spatially modulating the intensity of the imaging beam upstream of the patient during the CT acquisition. The kV source on Varian linear accelerators is equipped with lead collimator blades which can define a rectangular aperture of arbitrary size and position anywhere within the detector area. However, the blades cannot be moved while the kV beam is on, so do not themselves provide a mechanism to achieve dynamic collimation nor can the blade material be altered to allow for different levels of filtration. Accordingly, we have designed an accessory dynamic kV collimator that can be attached to the source housing downstream of the blades, in the usual position of the bowtie filter.

2.2 Collimator Design

The collimator is self contained and attaches to the bowtie mounting bracket making it easily removable so as not to interfere with normal clinical operations. Feedback from the linac concerning gantry position (or in fact any of the machine's motions) is also not readily available, so the dynamic collimator has been designed to operate with no direct input from and no feedback to the linac. In the cone-beam CT case with dynamic ROI illumination, the kV aperture size and shape with varying gantry angle are precomputed and uploaded to the collimator prior to the procedure. The gantry angle is independently measured by an inclinometer mounted on the gantry face. In the fiducial tracking application, as described below, the collimator is driven by an image analysis program which processes the raw fluoroscopic projections to assess the current position of the fiducials and the aperture, apply a suitable margin and transmit a new aperture definition to the collimator.

2.2.1 Hardware

The collimator hardware has undergone several design and fabrication iterations to address specific problems that arose. The original specification was to have two opposed pairs of orthogonally mounted blades with range of motion covering the full detector allowing the field shape to be an arbitrary rectangle. The blades also needed to be interchangeable to allow various materials to be used. In the latest prototype some simplifications were made. After some experimentation we determined that the blade materials most interesting to the studies performed here were 3 mm of copper filtration or completely attenuating, radiopaque blade; thus the blade was made permanently of copper and with a removable lead cover making the system more robust. Additionally, we noted that for the CT applications almost all of the required blade motion was normal to the axis of rotation (trans-axial direction) with very little motion along the rotation axis. Conversely, for fluoroscopic tracking applications the majority of the motion is in the axial direction with little trans-axial motion. For simplicity and in the interest of time the final version of the hardware was simplified to 2 blades but the system was designed to be mounted in either orientation as required by the application.

The blades were 1/8 in (3.175 mm) thick copper mounted on 4 slide cars each for the DryLin N series low profile, low friction linear guide rails from Igus Inc, Providence, RI. The guide rails were mounted to an acrylic base which was fly-cut to a tight surface flatness tolerance to prevent any binding in the blade motion. The base was mounted, with 9.5 cm aluminum stand offs to an aluminum mounting plate which was machined to fit in place of the standard bowtie filter. The blades were driven by L16 linear actuators (Firgelli Technologies, Victoria, British Columbia) which have an unloaded peak speed of 20 mm/s and a nominal positional accuracy of 0.4 mm. With the collimator plane 251.6 mm from the focal spot, Figure 2.1, the magnification factor was 3.975 and gives nominal isocenter plane speed of 79.49 mm/s and accuracy of 1.59 mm. The blades were attached to the linear actuators with stainless steel rod running the width of the collimator blade and through the clevis end of the actuator. For the application requiring radiopaque blades removable covers consisting

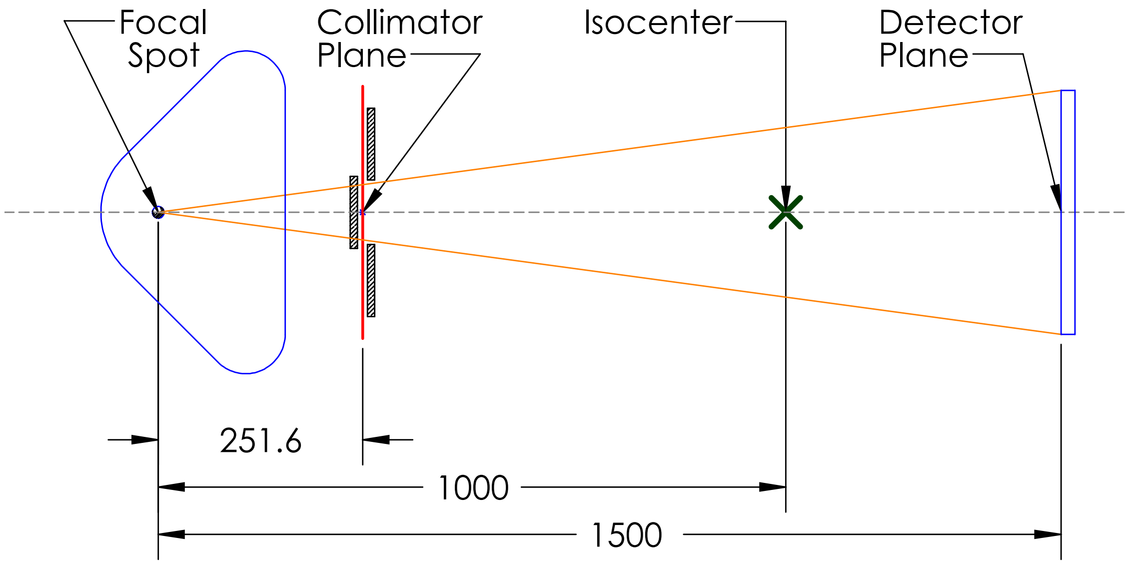

Figure 2.1: The layout and distances (in mm) of the relevant imaging system components

of 1/8 in* lead backed by 1/32 in steel were made. Details of the design and fabrication are given in Appendix A. A photo realistic rendering of the design model is shown in Figure 2.2 and in Figure 2.9 with the optional lead covers and rotated to the axially aligned (fiducial tracking) orientation.

2.2.2 Electronics

The on-board control of the collimator blades is handled by an Overo series computer-on-module(COM) (Gumstix Inc, Portola Valley, CA) with with a TI OMAP 3503 600 MHz ARM Cortex A8 processor, 512 MB RAM and a 4 GB SD card for storage. The gantry angle is monitored by an inclinometer (US Digital, Vancouver, Washington). The inclinometer is monitored by an Arduino Duemilanove microcontroller board with the inclinometer signal lines attached to the interrupt pins of its ATmega168 ensuring that no pulses are missed. The gantry angle is communicated back to the Overo via serial-over-USB. The linear actuators are

---

$*$. Imperial units are used in place of the standard SI units when they represent the specification of stock material sizes or standard fasteners

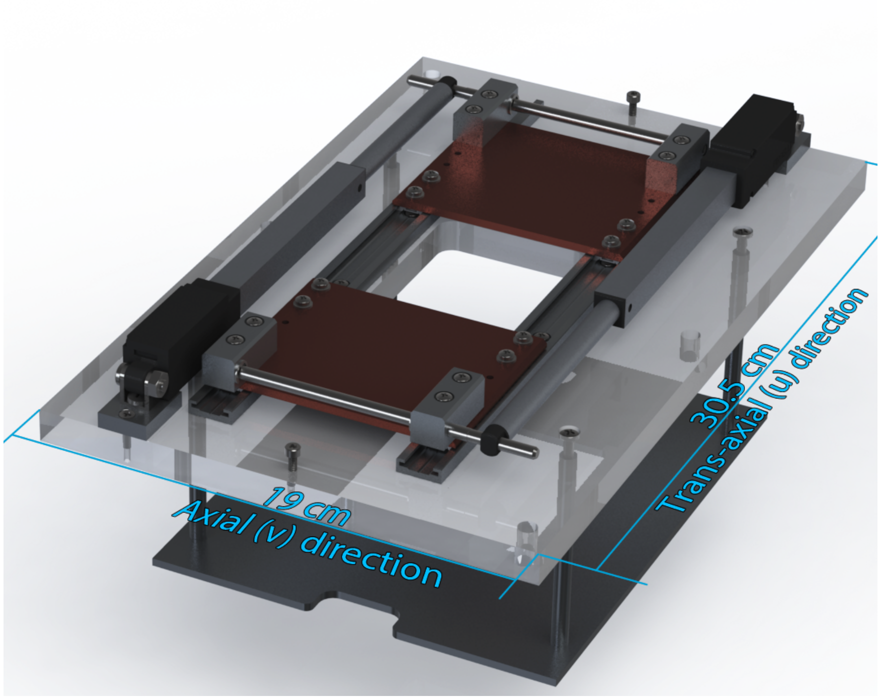

Figure 2.2: Rendering of collimator

controlled by independent dedicated motor controllers (Pololu Corporation, Las Vegas, NV) which provide closed loop feedback control. A diagram of the major electronic components is shown in Figure 2.3.

On startup the Overo automatically launches a python script that is outlined below, Pseudocode 2.1. This script creates 4 threads for handling separate functions independently at different time intervals. The first thread managed the attached LCD display giving status messages about the network connectivity, the gantry angle and the current set points for the blades. The second thread is used to resolve a system issue where the on chip WiFi adapter could be slow to power-up causing it to not come online properly and to occasionally fail to get a DHCP lease from the router. This thread just checks that the system has gotten the expected IP address for the router and if not, restarts the wireless network interface. The third thread handles the communication with the Arduino which monitors the gantry angle via the inclinometer. The code signals the Arduino asking for the current position, then gets the response and scales the encoder reading to the physical angle. The fourth thread handles all of the motor control. It loads the trajectory from file, which is a lookup table of the two blade positions, expressed as pixel position on the detector, versus gantry angle. It also loads a calibration table which is used to convert the position in pixels to the motor target signal, which is the 12 bit digitization (0-4095) of the analog linear potentiometer in the actuator. Thus for each angle position there are two table lookups per blade, each performed with linear interpolation.

The actual communication with the motor controllers is performed in separate programs, written in C# that depend on vendor supplied .net libraries and that run in the open source mono platform on linux. The motor control code is opened as a subprocesses in the python startup code with pipes to standard input which are used to provide the motor target positions. The Arduino runs a simple piece of code that counts the encoder pulses and listens for the serial command to send back the current count. The encoder signal lines are attached to the interrupt pins to avoid any missed pulses during communication and there is a physical push button attached to zero the pulse count.

Algorithm 2.1: Startup code on collimator in dynamic CT mode

```
Angle=0                                   ▷ give globals safe values
x1position=4000
x2position=4000

function Main
    spawn thread: managelcd( )
    spawn thread: checkip( )
    spawn thread: arduinomonitor( )
    spawn thread: motorcontrol( )
end function

function managelcd
    Serial→open(Port to LCD Module)
    repeat
        write network status, angle and blade positions to LCD
        Sleep(0.5 seconds)
    until SIGINT
    Serial→close( )
end function
```

Algorithm 2.1 Continued

```
function checkip
    repeat
        if have active IP address then
            pass
        else
            restart WLAN0 interface
        end if
        Sleep(10 seconds)
    until SIGINT
end function

function arduinomonitor
    Global[a] Angle
    Serial→open(Port for Arduino)
    Serial→write(“a”)                                ▷ signal arduino to start
    Sleep(1 second)                                  ▷ give arduino time
    repeat
        if data in serial buffer then
            AngleString = Serial→readline( )
            Angle = 90.0/2048 * int(AngleString)
        end if
        Serial→write(“a”)                            ▷ Signal to send angle
        Sleep(0.1 seconds)
    until SIGINT
    Serial→close( )
end function

function motorcontrol
    Global x1position, x2position
    x1pipe = open subprocess to C# Jrk Control
    x2pipe = open subprocess to C# Jrk Control
    x1pipe→write(x1position)                         ▷ Open blades at startup
    x2pipe→write(x2position)
    caltable = load calibration from file
    trajectory = load blade positions vs angle from file
    repeat
        x1pixeltarget = trajectory→getX1(Angle)      ▷ Linear Interpolation
        x2pixeltarget = trajectory→getX2(Angle)
        x1target = caltable→X1convert(x1pixeltarget)
        x2target = caltable→X2convert(x2pixeltarget)
        x1pipe→write(x1position)
        x2pipe→write(x2position)
    until SIGINT
end function
```

---

[a] The Global statement is used here to indicate that the function writes to the globally accessible variable. Note that no two threads both write to the same global variable

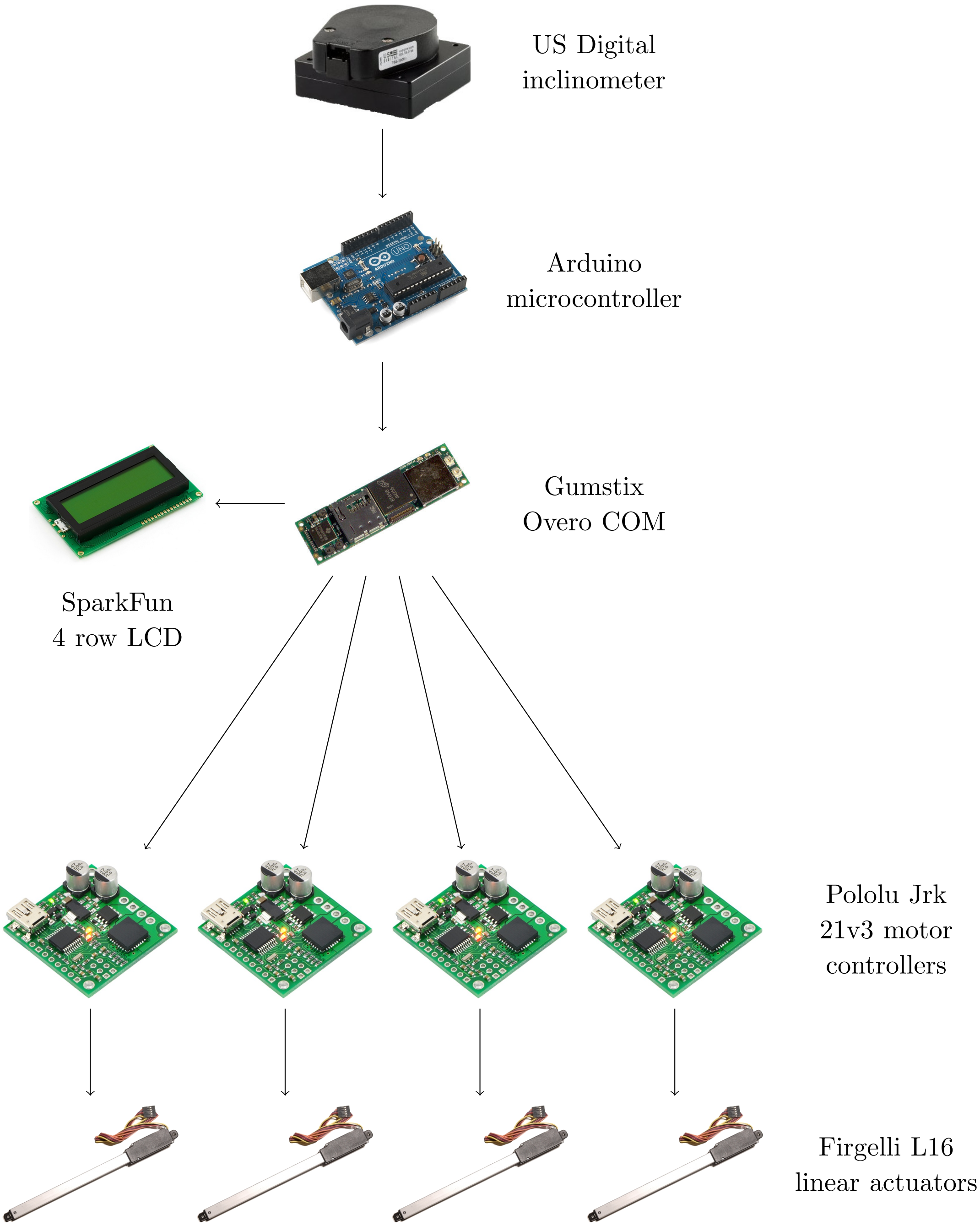

Figure 2.3: Outline of the major components in the electronic control of the collimator.

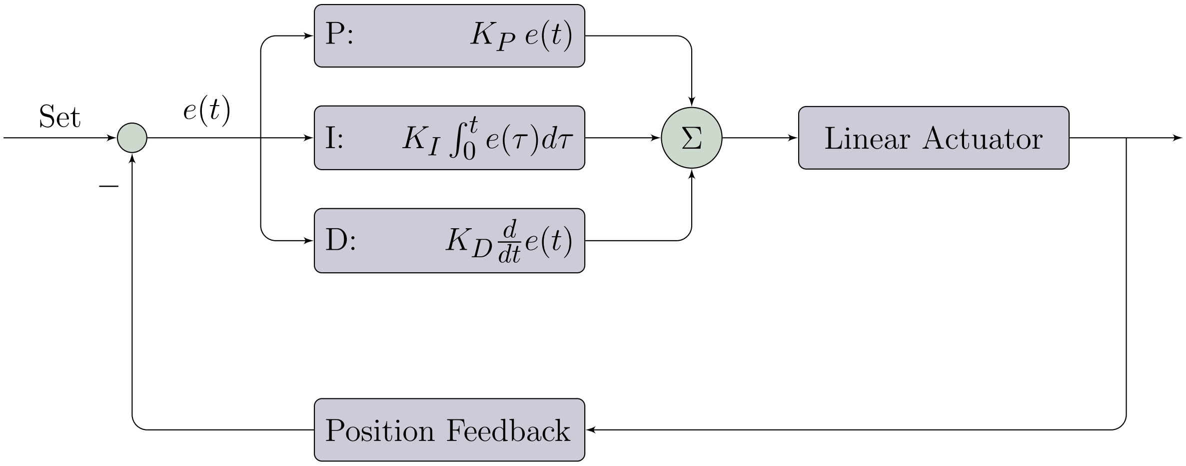

Figure 2.4: Standard PID feedback control loop

2.2.3 Tuning

The motor control uses a three term feedback control method commonly referred to as PID control. A model of the standard PID controller is shown in Figure 2.4 and is so called for the three terms which are, respectively, proportional (P) to the current error, the integral (I) of the error and the derivative (D) of the error. Implementation of the controller requires setting the value of 3 parameters, one for each of the P, I and D terms, indicated as K_P, K_I and K_D in Figure 2.4. The process of setting these parameters is known as tuning[68].

In order to perform the tuning we used a separate external position measurement from transmissive linear strip (LIN-200-6-N) and encoder modules (EM1-0-200-N) from US Digital. The encoder modules were mounted to an aluminum cap machined to fit on to the blade and held in place with a set screw. The transmissive strip was clamped between a piece of aluminum and acrylic. The height and pitch of the strip need to be finely controlled so it was supported on custom made 5/16–40 threaded brass rod standoffs and held in place with knurled thumb screws. The tuning process was undertaken before any imaging was performed so an aluminum shaft was mounted to the underside of the collimator base plate in the center before the aperture was cut in the plastic, allowing the whole system to be mounted in the chuck of a rotary table so the gravitational effects could be explored under

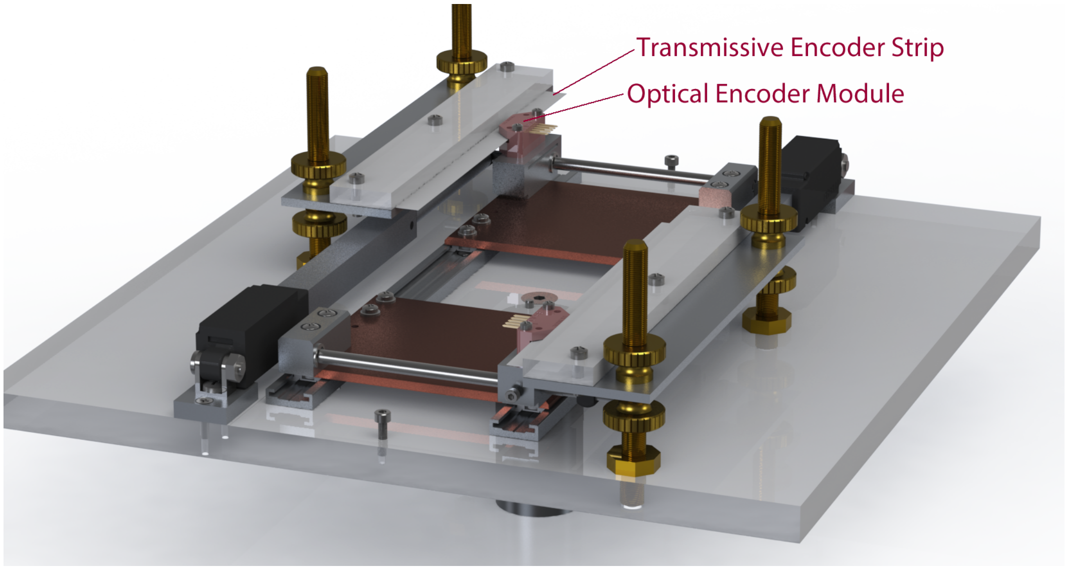

Figure 2.5: Rendering of collimator with linear encoder feedback rig

static conditions. Otherwise the motor loads were the same as those experienced during imaging.

The motors were driven by the Pololu controllers in an open loop mode. The encoders were read out by a computer running Labview with a NI-7340 motion control card and nuDrive amplifier (National Instruments) which also monitored the drive signal on an analog input. The motors were driven through several arbitrary wave forms (controlled manually) and their position recorded. A data set containing the motor input, the position and the time were fit to a transfer function model with 2 zeros and 4 poles. The best fit model was

$$P(s) = \frac{0.01306 + 0.2196s^{-1} - 0.2318s^{-2}}{1 - 1.927s^{-1} + 0.6694s^{-2} + 0.4457s^{-3} - 0.1882s^{-4}} \tag{2.1}$$

This model was then tested against a dataset from an independent run showing that the model predicted position agrees well with the measured position as shown in Figure 2.6.

The analytic system model was used to choose the 3 PID parameters to provide the fastest dynamic response while remaining stable. This process yielded: $K_P = 10$, $K_I = 0.125$ and $K_D = 0$. For comparison the parameter chosen by hand tuning for the best system response were $K_P = 30$, $K_I = 0.125$ and $K_D = 0$. We see that the two methods agreed exactly

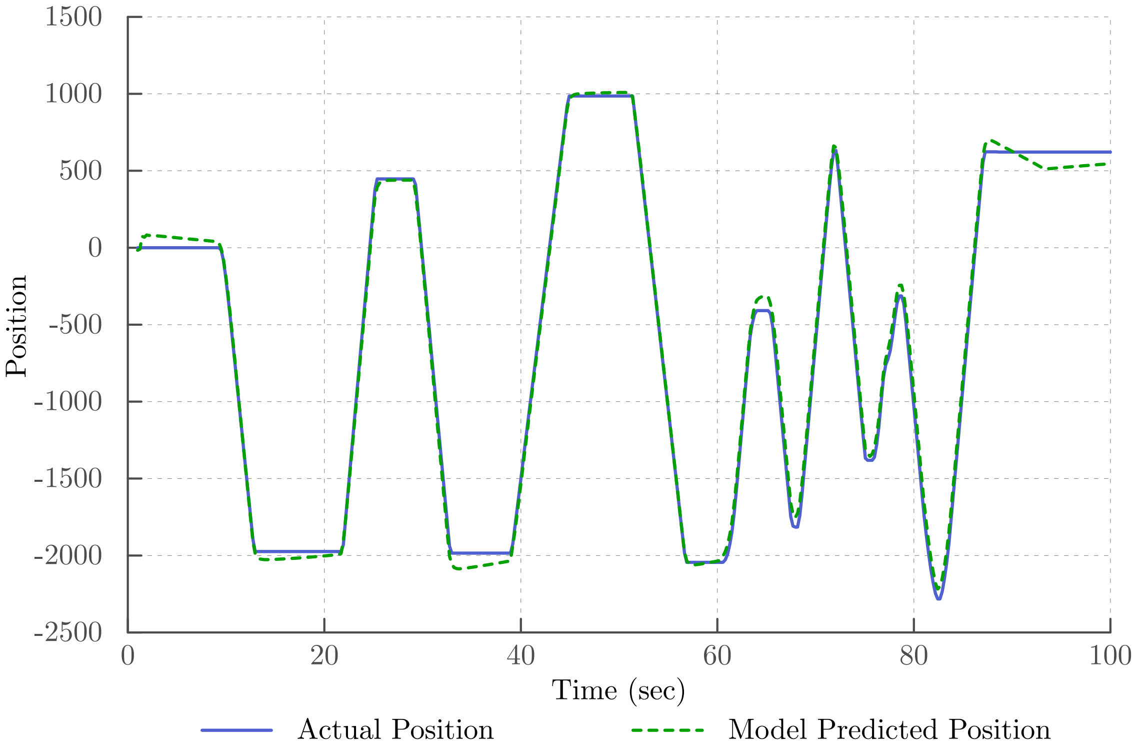

Figure 2.6: System Modeling

for the integral and derivative term (both resulting in no derivative term) but varying in the proportional term. We expect that this disagreement is a result of the limited effective sampling frequency in the model based approach. The motor driving signal is pulse width modulated which is a square wave where the the duty cycle, or fraction of the cycle where the signal is held high, determines the effective analog voltage the motor sees. In this experiment the driving signal was sampled rapidly but then digitally filtered to get the analog equivalent but at a lower effective sample rate. This lower sample rate may have affected the ability of the model to capture high frequency response properly causing it to underestimate the proportional term. If this process were repeated we would recommend analog filtering on the PWM signal prior to digital sampling. Gravitational effects from collimator orientation were found to be negligible in the choice of PID parameters. Both sets of values listed above were tested on the bench top and the higher K_P value was chosen for the remainder of the work.

2.2.4 Calibration

In order to calibrate the physical coordinates of the motor feedback to the imaging system coordinates the collimator was mounted to the kV source and then each blade was separately stepped through various positions. At each step a radiograph was acquired. The set of radiographs was then automatically processed as follows to determine blade edge position. Each radiograph was read from file and decompressed. The histogram was generated, which was bimodal with one peak corresponding to the values under the collimator blade and the other peak to values in the open field. The edge threshold value was chosen as the midpoint between the two peak values in the histogram. The center row of the detector was then fit to a piecewise continuous spline with control points spaced 32 pixels apart. The blade edge position was then determined by finding where the spline crosses the edge threshold. This process is shown in Figure 2.7. A calibration table was then made from the commanded motor position and the identified blade edge position in the image as shown in Figure 2.8. This procedure was automated in Matlab; it communicated with the collimator directly, prompted the user when to acquire a radiograph and automatically processed the images when all acquisitions were completed.

2.3 Lung Fiducial Tracking Application

2.3.1 Introduction

Intra-fraction organ motion can greatly hamper the advantage of highly conformal dose techniques such as intensity modulated radiation therapy (IMRT)[34,69]. To minimize the adverse dosimetric effect caused by tumor motion, many current[70–74] and next-generation[75] image-guided radiation therapy (IGRT) techniques utilize tumor position knowledge throughout the beam delivery process. For certain target sites that undergo strong respiratory based motion, indirect tumor location methods, such as external skin marker tracking[71,76] or breath monitoring techniques[77], can provide real-time 3D target tracking. However, the correla-

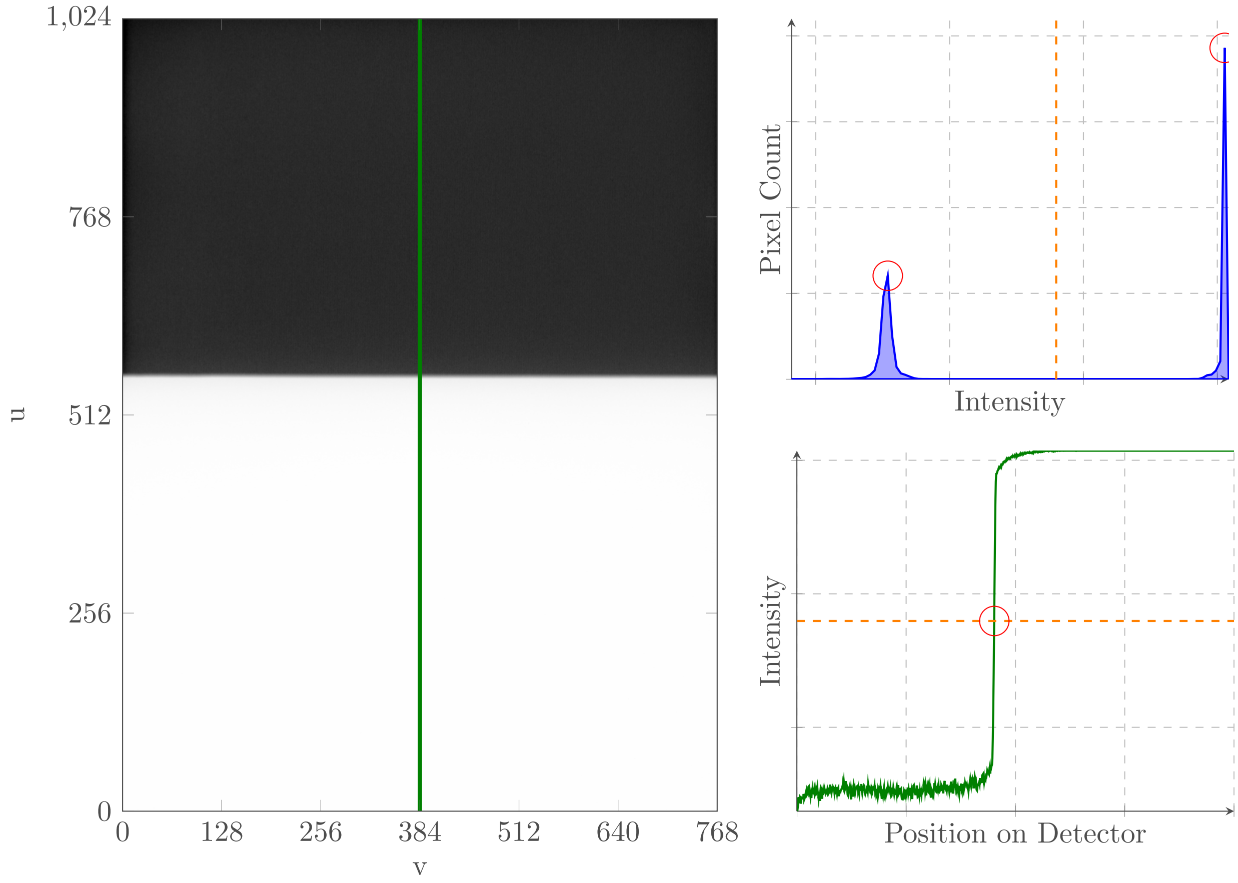

Figure 2.7: The left panel shows a sample radiograph with one blade extended roughly halfway. The upper right panel shows the histogram of the image with the two peak values automatically identified. The edge threshold (orange line) is set as the midpoint of these two peaks and the blade position is determined to be where the middle row crosses this value, lower right panel.

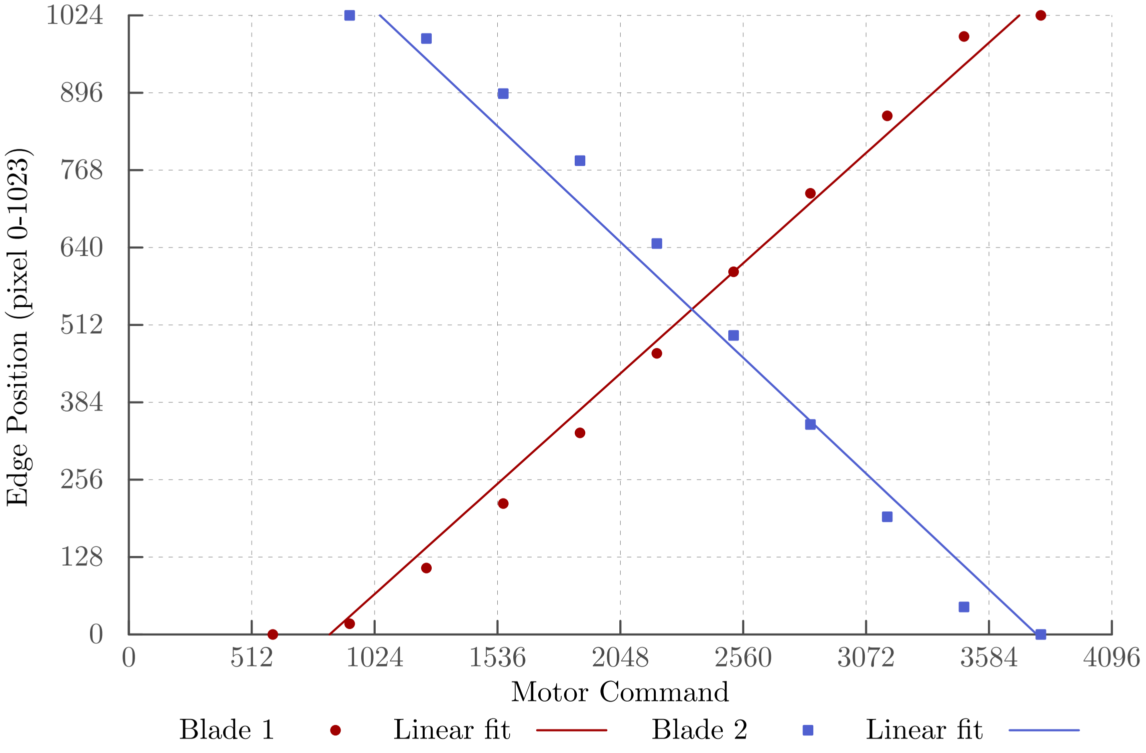

Figure 2.8: Plot of calibration table data after automatic calibration. Linear fit shown for reference only, collimator uses interpolation on actual data points.

tion between external body parameters and internal organ motion is complex and may have large associated uncertainties[78,79]. For organs, such as the prostate, that show weak, or nonexistent external-to-internal correlation, indirect tracking is not an option and direct tumor tracking methods are preferred. Direct methods include stereoscopic kV imaging[80–82], combined MV-kV imaging[83,84], ultrasound guidance, or electromagnetic transponders[85].

The high radiation dose cost to patients when employing continuous fluoroscopic imaging is a serious concern for real-time kV image based internal motion tracking[36,86]. However this dose may be reduced substantially just by restricting the image area. Generally, for kV intrafractional tracking purposes, sufficient kV image information should simply be the projected images of the metallic fiducial markers or a small area encompassing the target. A single Au cylindrical marker is typically (3 mm in length and 0.8 mm in diameter. An imaging field of just a few centimeters by a few centimeters would be sufficient to visualize even a cluster of implanted fiducials this corresponds to just a few percent of the total kV image

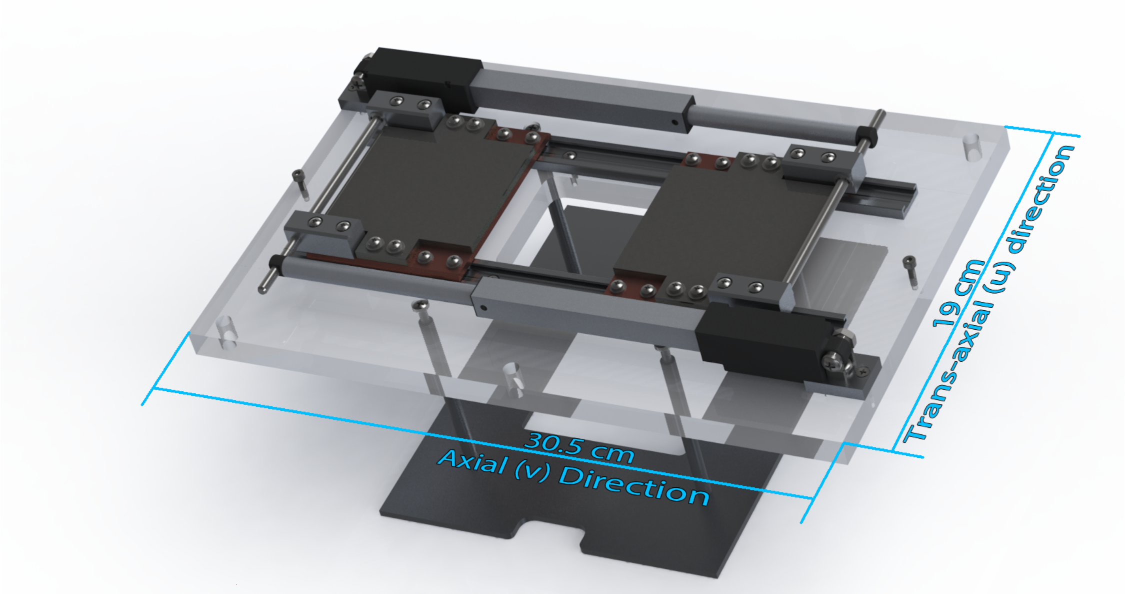

Figure 2.9: Rendering of collimator in tracking application configuration

area (40 cm × 30 cm detector). As such, most of the radiation from a full frame exposure is unnecessary. To lower diagnostic kV dose in this setting as well as in cone-beam CT, we have applied our dynamic collimator for selective region-of-interest (ROI) imaging of the patient.

2.3.2 System Overview

For this application the kV collimator had to be modified from the configuration described above. The collimator was rotated 90° to align the blade motion with axis of gantry rotation and the lead covers were installed on the blades to make them radiopaque. This configuration is shown in Figure 2.9. The electronic control was also altered for this application as shown in Figure 2.10. The gantry angle, as measured by the inclinometer, was no longer required. Instead the blade positions were fed directly to collimator over a wireless connection from the imaging control computer running our tracking software.

The image capture and analysis process used for the tracking software suffers from lack of direct interaction with the linac's imaging system, resulting in significant latency due to frame capture and processing. It is obviously very important to minimize the image capture and processing latency in order to achieve good performance in the actual fiducial tracking application. The condition we require of the collimator is that it does not contribute significantly to the overall latency, and that it accurately follows the commanded trajectory. Thus, we have chosen to assess the performance of the collimator subsystem in a way that does not depend on other latencies. The collimator's function is to move its blades quickly and reliably to a commanded position. Whether or not the computation of that position is subject to latency, the collimator's performance can usefully be characterized simply in terms of its ability to follow a commanded position, that is, its speed and accuracy in moving the kV beam to the commanded position. We have designed a testing setup wherein a precomputed aperture trajectory is fed directly to the collimator without image processing latency, and the difference between the commanded and achieved apertures is measured. Whether or not the resulting radiographs can be captured, analyzed and converted to an aperture trajectory interactively in a timely manner becomes irrelevant to the collimator characterization. With the collimator performance thus characterized, the effect of variable software lag on overall system performance can also be simulated.

2.3.3 Software Tracking

Algorithm overview

The fiducial position is extracted using a template matching approach as described in[87,88]. At the start of the imaging session the fiducial is manually identified in the projection image. The 15 × 15 pixel region surrounding this seed point is used as the template. In each successive frame the template is matched against the 41 × 41 pixel neighborhood of the last known location. The correlation score for each point in this neighborhood is calculated as

$$R_{u,v}^2 = \frac{\sum\limits_{i,j \in template} \left(f_{u+i,v+j} - \overline{f_{u,v}}\right)\left(p_{i,j} - \overline{p}\right)}{\sqrt{\sum\limits_{i,j \in template} \left(f_{u+i,v+j} - \overline{f_{u,v}}\right)^2}\sqrt{\sum\limits_{i,j \in template} \left(p_{i,j} - \overline{p}\right)^2}} \tag{2.2}$$

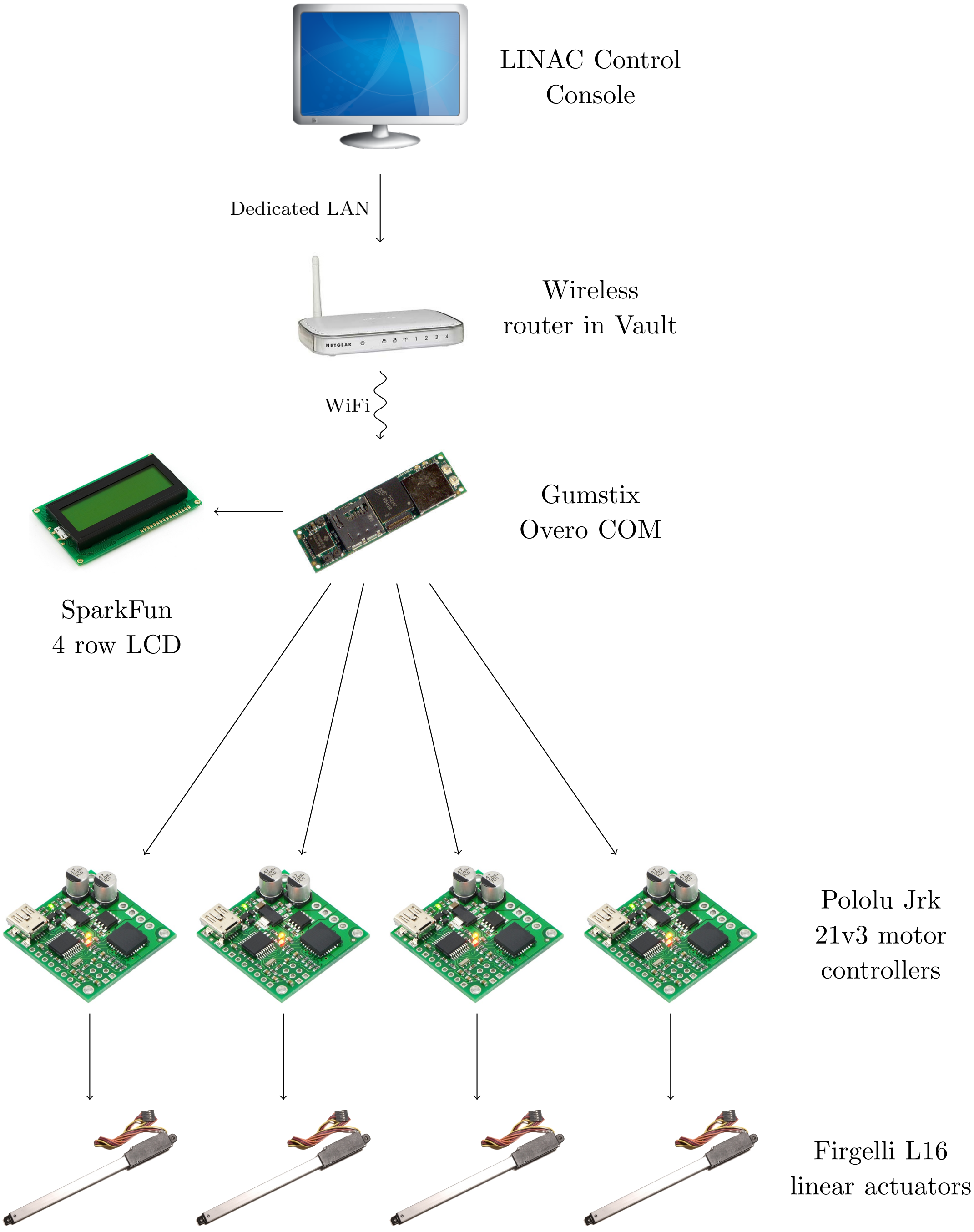

Figure 2.10: Major components in control of collimator for tracking configuration

where $f_{u,v}$ is the image and $p_{i,j}$ is the template and the overbar denotes the average over the neighborhood calculated as

$$\overline{f_{u,v}} = \frac{1}{n} \sum_{i,j \in template} f_{x+i,y+j} \tag{2.3}$$

$$\overline{p} = \frac{1}{n} \sum_{i,j \in template} p_{i,j} \tag{2.4}$$

The location with the maximum correlation score is set as the current location if the score is above a preset threshold, otherwise the search region is expanded. Once found the current location is transmitted to the collimator and the process continues with the next frame when it becomes available.

Determination of software lag

The prototype tracking system is setup to run with minimal interference with the clinical setup. The only changes made to the standard imaging workflow are to enable the saving of the fluoroscopic data to hard drive and adjusting the acquisition frame rate. As such our tracking code does not have access to the image data until the clinical system is finished writing it to disk. The clinical system is a black box, in which we do not know the exact process, but we speculate that the major, time consuming steps are shown in Figure 2.11. The tracking algorithm process, outlined in green, is required to read the data in from disk and decompress it before any processing can begin. This process is suboptimal but limited mainly by the level of integration with the clinical hardware. In order to determine the resultant lag we set up a fiducial on a 3-axis motion platform driven in real-time by a PC running LabView in the field of view. This PC was set to drive the fiducial in a sinusoidal motion and record the true position of the fiducial and the output of the tracking algorithm. At the default frame rate of 10 Hz we observed that the lag in processing the projections caused a bottleneck and the position returned by the tracking algorithm was entirely out of

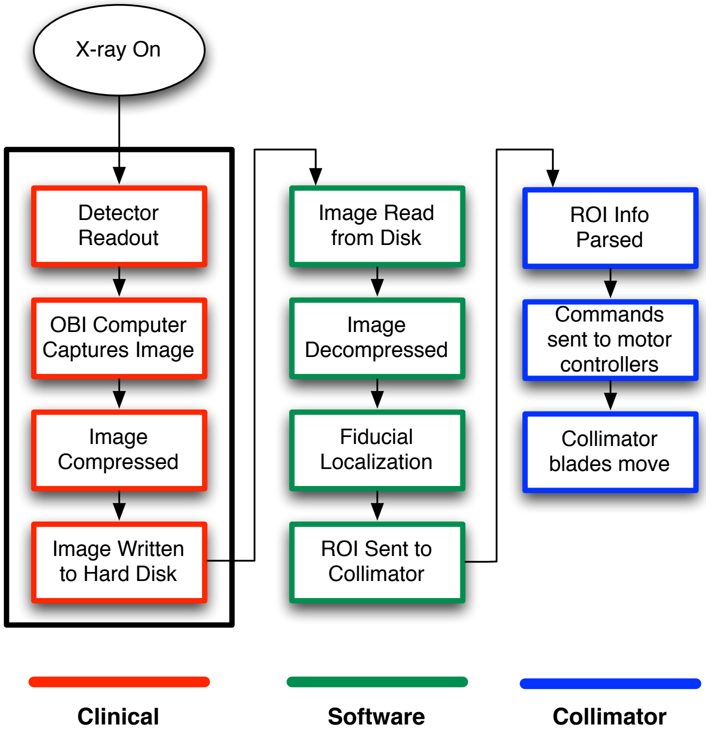

Figure 2.11: An overview of the major steps in the fiducial tracking process. The steps outlined in red happen on the clinical workstation, the black box indicates that we don't know the details of this process but infer the listed steps. The green boxes indicate the steps taken by our tracking software that runs on the clinical system, and finally the blue boxes indiacte the steps taken by the collimator.

sync with the actual position as shown in Figure 2.12. With the frame rate slowed to 5.5 Hz we see that the phase shift in the output of the tracking algorithm, shown in Figure 2.13 corresponds to a 508 ms delay. This half second lag is a problem for accurate real time tracking, for the remaining studies the collimator was driven from the realtime position available in LabView and not the position determined by the image tracking software.

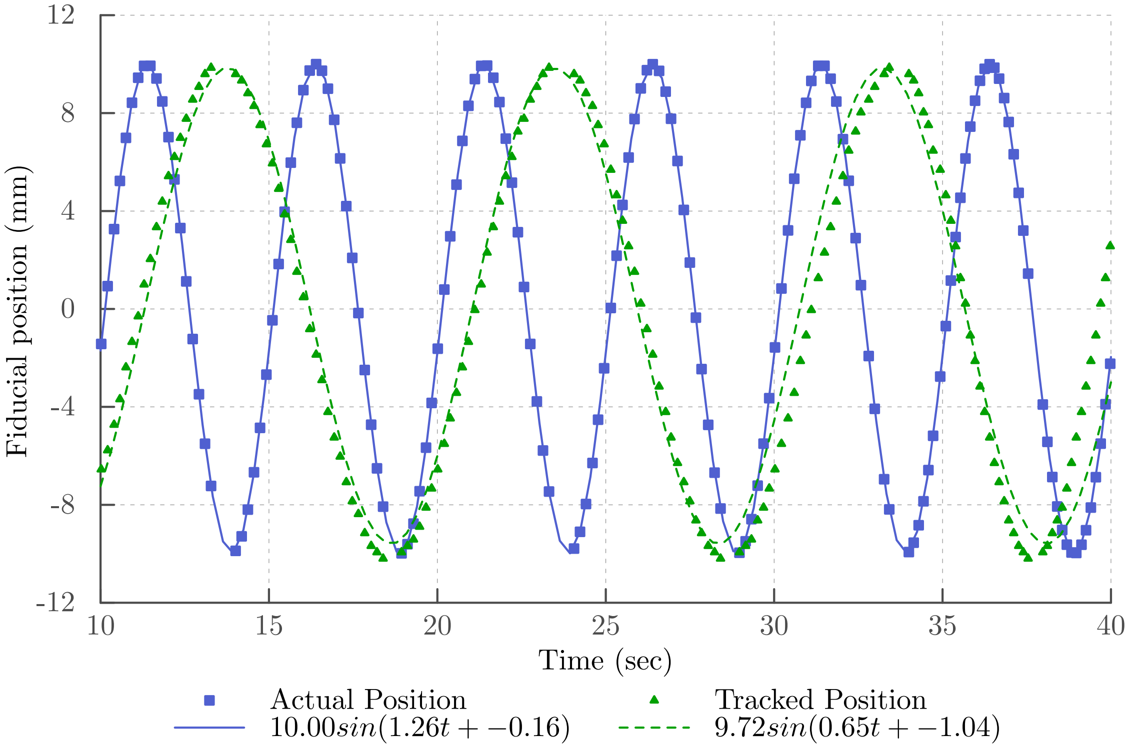

Figure 2.12: 10Hz frame rate tracking lag

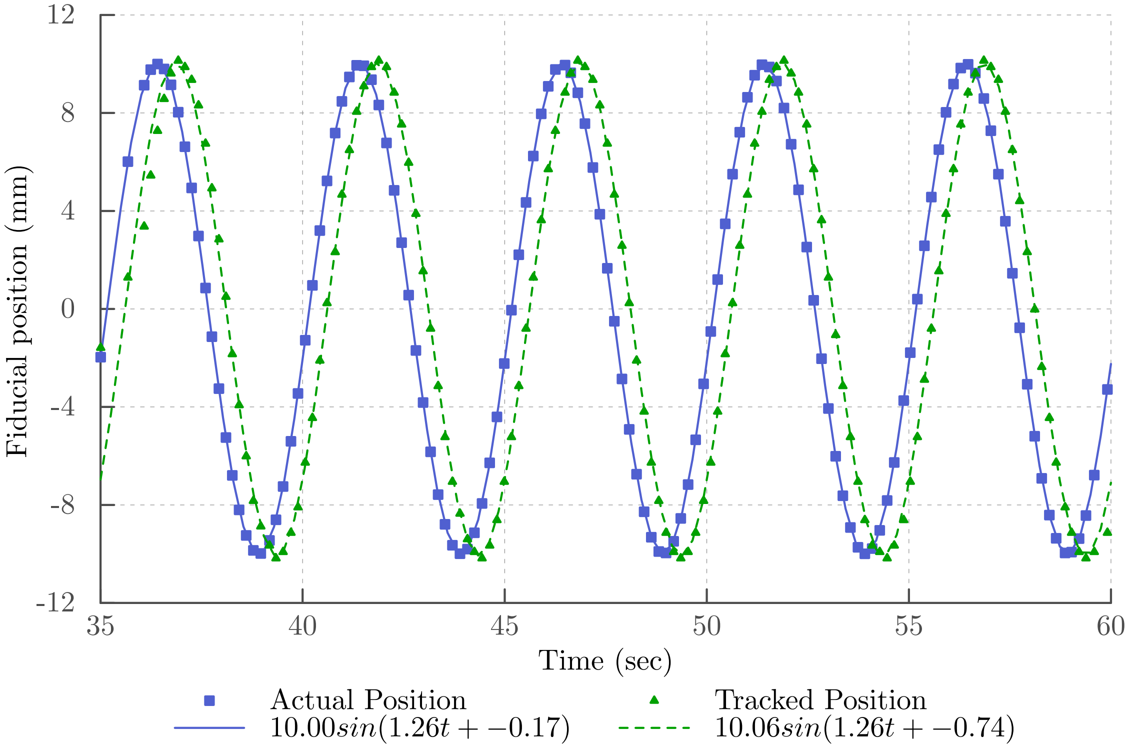

Figure 2.13: 5.5 Hz frame rate tracking lag

2.3.4 Experimental Study

Methodology

In order to characterize the performance of the collimator for the fiducial tracking application realistic motion profiles for lung fiducials in a free breathing patient are required. Unfortunately this data was not readily available, however there have been numerous methods for relating lung motion to a more readily available surrogate[73,89–92]. We used the model developed at Washington University, St. Louis by Daniel Low, PhD and colleagues[93,94]. The authors used simultaneous four dimensional CT and quantitative spirometry to develop a motion model parameterized by tidal volume (v) and flow rate(f).

$$\vec{X}(v, f : \vec{X_0}) = \vec{X_0} + \vec{\alpha}(\vec{X_0})v + \vec{\beta}(\vec{X_0})f \tag{2.5}$$

The $\vec{\alpha}$ and $\vec{\beta}$ terms are local parameters determined from the 4DCT dataset which represent the local lung expansion related to tidal volume and the hysteresis motion related to the flow rate respectively. These parameters vary throughout the lung for example the magnitudes are much greater near the diaphragm than in the apex of the lung.

Dr. Low generously provided us with the spirometry data of 30 patients with up to 14 minutes of free breathing for each which was acquired under and IRB protocol at the University of Washington, St. Louis . Similarly to the original method[94] we first smoothed the spirometry signal. The tidal volume data was smoothed with a 40 point box filter and the flow data was estimated as the analytic derivative of a 220 point polynomial fit of the data. The raw data and the results after smoothing for part of one patient's trace are shown in Figure 2.14. For all available patients we generated trajectories with parameters simulating small, apex like motion, medium, mid-lobe motion and large diaphragamatic motion. The averages and extrema are summarized in table 2.1 along the principal components and the vector sum. From section 2.2.1, the collimator is capable of an isocenter plane speed of 79.49 mm/s which is easily capable of all of the average speeds but the peak speeds exceed

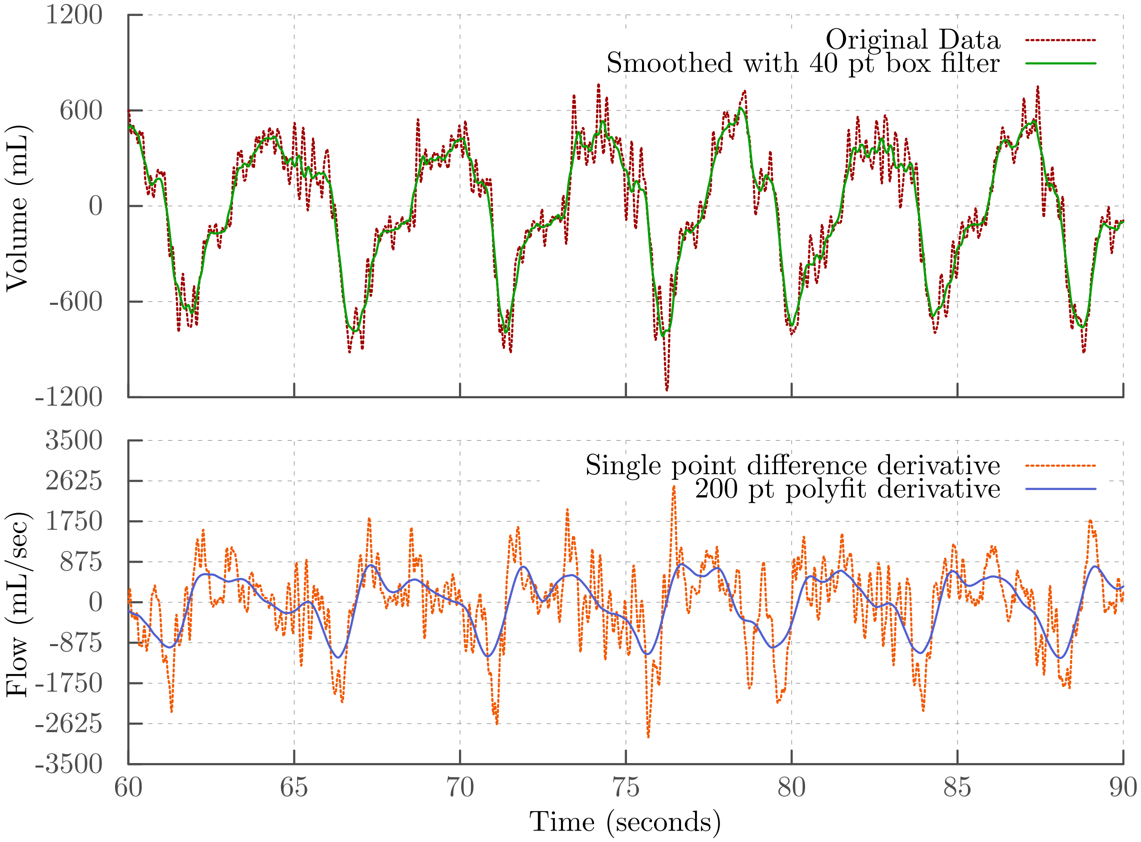

Figure 2.14: Sample of spirometery data for patient A

this for some cases. The aperture size for the collimator thus needs to be chosen carefully with respect to the fiducial motions to minimize the chance of losing the fiducial. As a fallback the collimator could be quickly opened if the tracking software is unable to locate the fiducial.

To test the collimator with an average trajectory we used the reported mean values[94] for the left lung of $|\vec{\alpha}| = 23.2$ mm/L and $|\vec{\beta}| = 3.7$ mm s/L. A 60 second trace of one patient with the above parameters and the major component of the motion aligned to the superior-inferior direction in order to maximally challenge the collimator is shown in Figure 2.15.

		Small α & β (Apex)			Average α & β (Mid Lung)			Large α & β (Diaphragm)		
		Mean	StdDev	Max	Mean	StdDev	Max	Mean	StdDev	Max
Speed (mm/s)										
Major Axis	Mean	6.6	2.4	13.1	12.0	4.4	23.8	17.6	6.5	34.9
	Max	46.8	23.7	109.3	85.2	43.1	198.9	124.8	63.2	291.5
Minor Axis	Mean	0.9	0.3	1.7	1.6	0.6	3.2	3.5	1.3	7.0
	Max	6.2	3.2	14.6	11.6	5.8	27.0	25.0	12.6	58.3
Combined	Mean	6.7	2.4	13.2	12.1	4.4	24.0	17.9	6.6	35.6
	Max	47.2	23.9	110.3	86.0	43.5	200.8	127.3	64.4	297.3
Amplitude (mm)										
	Min	7.0	2.7	13.5	12.7	5.0	24.5	18.7	7.3	35.9
	Mean	12.8	3.4	19.8	23.4	6.2	36.1	34.3	9.1	52.8
	Max	19.8	6.5	36.7	36.0	11.8	66.8	52.8	17.3	97.9
Period (s)										
	Min	2.3	0.4	3.5	2.3	0.4	3.5	2.3	0.4	3.5
	Mean	4.4	1.4	8.2	4.4	1.4	8.2	4.4	1.4	8.2
	Max	8.3	4.8	28.0	8.3	4.8	28.0	8.3	4.8	28.0

Table 2.1: Summary of dynamic characteristics of the trajectories generated for 30 patients with α and β chosen simulate small, apex like motion, medium mid-lobe motion and large diaphragmatic motion.

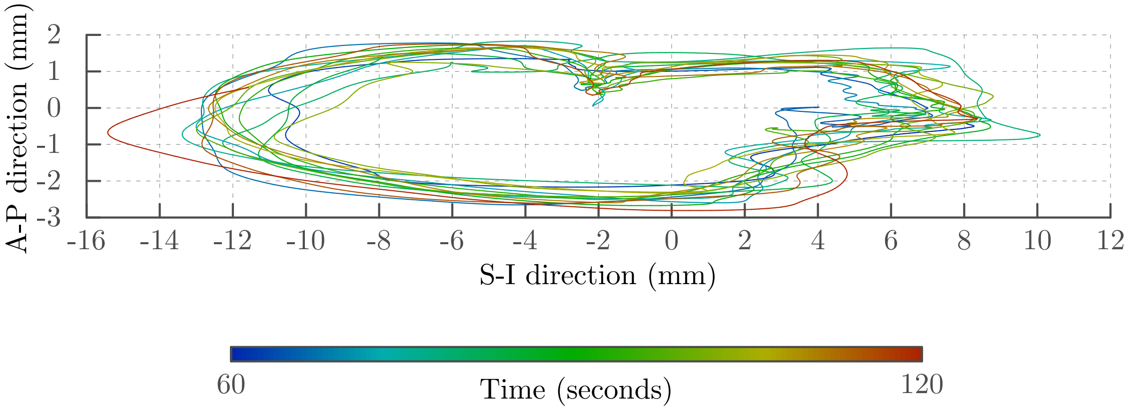

Figure 2.15: Sample trajectory generated from patient spirometery data

Figure 2.16: Photograph of the fiducial tracking experimental setup. The 3-axis motion stage is on retracted couch top and the collimator is mounted on the kV source.

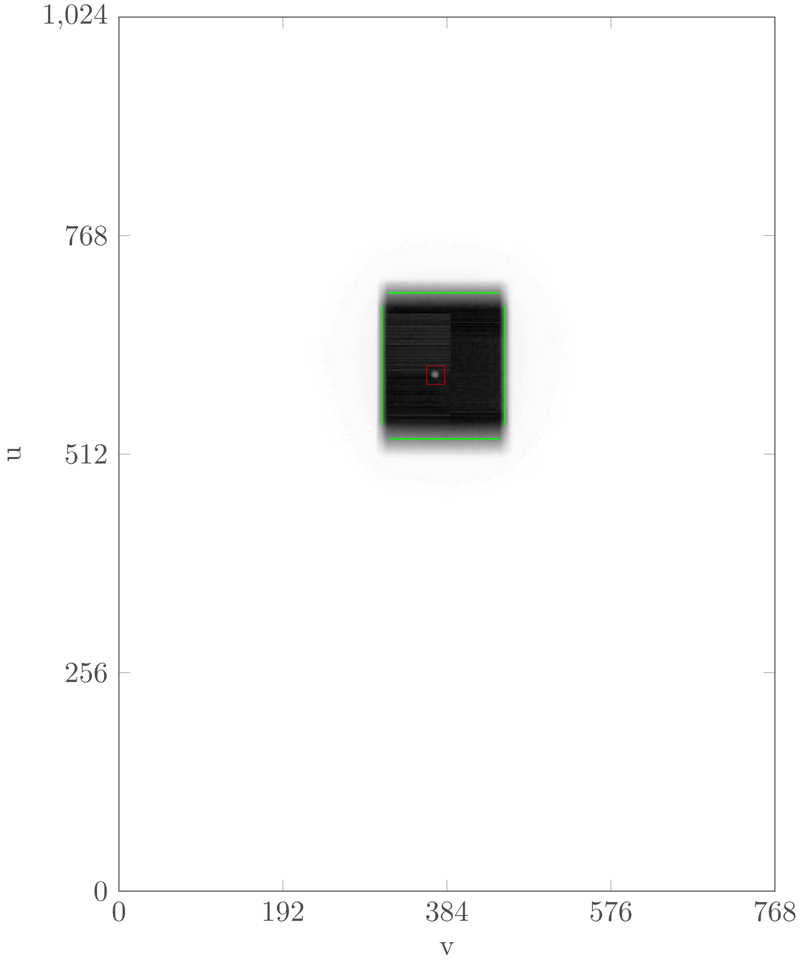

Figure 2.17: Single frame of fluoroscopic acquisition. Blade edges automatically identified shown with green lines, region with highest template match score shown with red box.

Results

A single fiducial was placed on a low density foam board and attached to the 3-axis motion stage, shown in Figure 2.16. The stage was driven through a motion profile generated with the method described above. The collimator was fed the stage position directly from the controlling computer in lieu of a fiducial position detected by imaging processing due to the lag. The system was left running for over 4 minutes with bursts of fluoroscopic data acquired throughout. The data was processed retrospectively to determine how well the collimator was able to maintain its tracking of the fiducial.

The fluoroscopic images were processed in Matlab with the fiducial identified using template matching as described above. The collimator blade edges were identified with a linear Hough transform on a threshholded gradient magnitude image. A sample image with the detected blade edges and fiducial match indicated can be seen in Figure 2.17.

The fiducial position and the blade edges were extracted in each frame of the fluoroscopic study, this is plotted in Figure 2.18 for three burst of fluoro over 4 minutes. From this plot it appears the system is performing reasonably well with all motions in sync, though it is unexpectedly biased towards the jaw shown with the green line. When we extract the fiducial's observed position in the images and plot it with the original planned trajectory we see that there is a discrepancy Figure 2.19 that is corrected with a scaling factor. This error is likely a miscalibration in the motion system used to control the fiducial. However, as the collimator was driven directly from the planned signal and not from the image processing to avoid the lag as discussed above, its motion was unaffected by this error and we can analyze its performance with respect to the signal it was driven from. In this case if we look at the distance from the center of the aperture to the commanded fiducial position Figure 2.20 it never exceeded 1.7 mm from the aperture center and the root mean square distance was 0.8 mm.

The dose sparing for the patient is closely related to the aperture size. For the experimental aperture, which is relatively large for the motion amplitude, the integrated detector signal over the course of the study, as a ratio to the uncollimated signal is shown in Figure 2.21. Only a relatively small portion of the original field of view gets any exposure at all. Expressed as the dose-area-product (DAP) the dose from the aperture shown is 3.3 % of a full frame exposure.

2.4 Summary

A computer-controlled dynamic x-ray collimator was designed and fabricated to allow conformal illumination during radiographic, fluoroscopic or cone-beam CT imaging. The collimator can be mounted on the x-ray source of a linac-integrated imaging system, with no require-

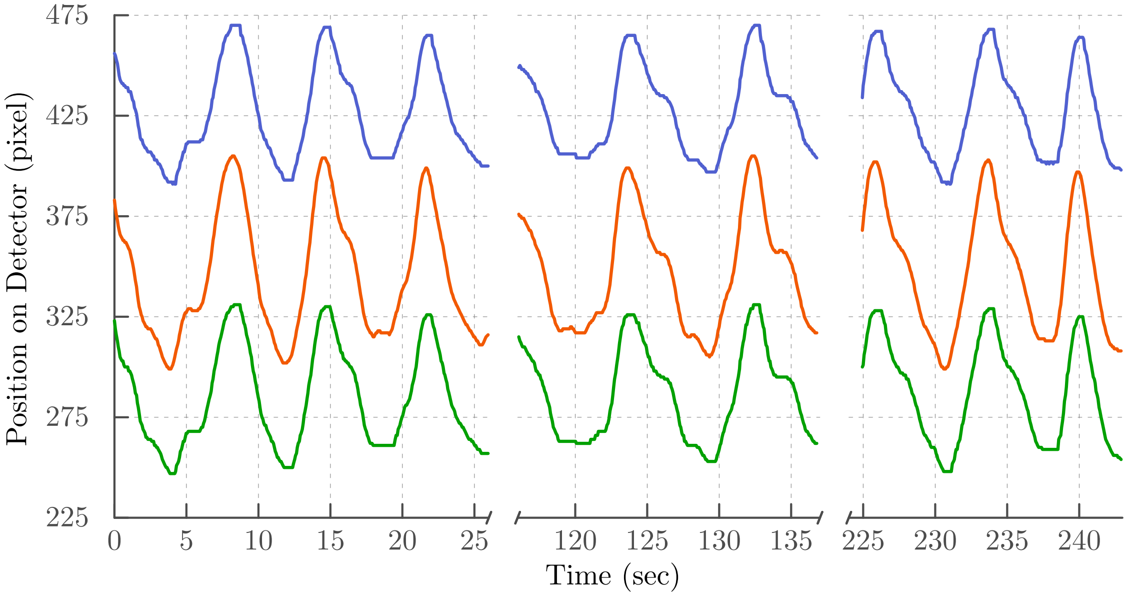

Figure 2.18: The fiducial position (orange) over the course of the study with the blade edge positions as identified in the fluoroscopic images (blue and green)

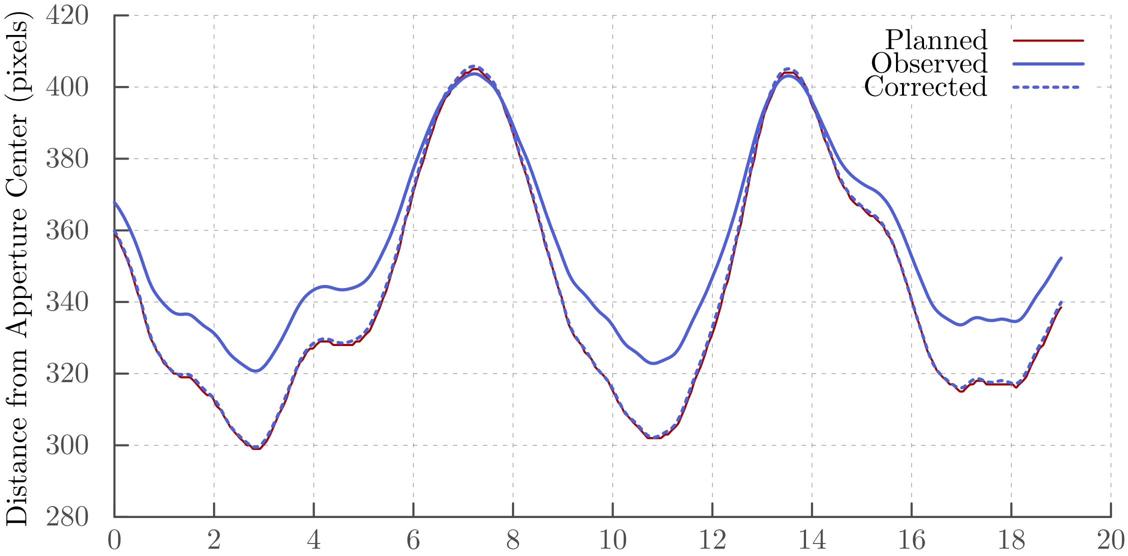

Figure 2.19: The observed trajectory (solid blue line) differed from the planned trajectory (solid red line) by a scaling about the origin of motion. The corrected position shown in blue dashed line.

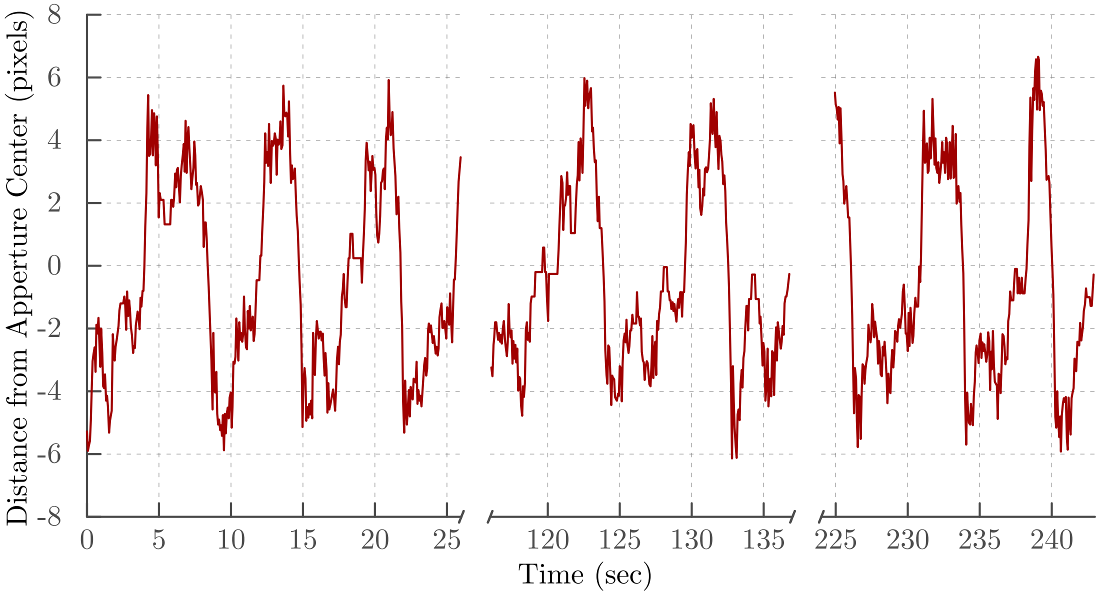

Figure 2.20: The distance from aperture center to commanded position.

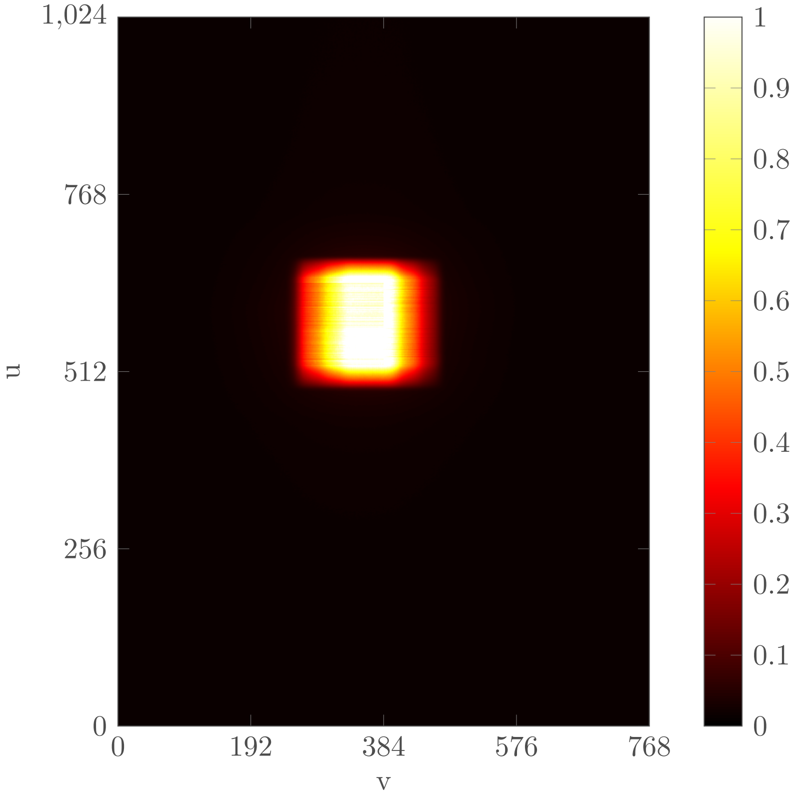

Figure 2.21: Ratio of detector signal integrated over 3 fluoro acquisitions to open field

ment for communication with the linac motion control systems. Collimation supports both intensity-weighted and true conformal imaging through the use of partially transmitting copper blades to which opaque lead covers can be added. The performance characteristics of the collimator (blade speed, range of travel, repeatability, latency) were designed to be adequate for conformal CBCT imaging of a desired 3D volume, and were also demonstrated in this chapter to be adequate for tracking fiducials implanted in moving lung tumors. With the demonstrated accuracy of the tracking capabilities only modest margins would need to be added to fiducial cluster to keep it in view allowing for tight collimation and substantial dose reduction.

CHAPTER 3

CONFORMAL REGION OF INTEREST IMAGING

3.1 Introduction

The first half of this past decade saw considerable achievements in the development of analytic inversion techniques used for CT reconstruction[95–98]. Many of these algorithms have been shown to have interesting properties such as theoretical exactness for some geometries, the ability to reconstruct from non-standard trajectories and robustness against some forms of truncation. The work in this chapter will focus on the chord based techniques developed by Pan and colleagues[61] for conformal ROI imaging, by which we mean restricting the x ray field to strictly illuminating the ROI with radiopaque collimation.

3.2 ROI imaging with advanced reconstruction methods

The chord based methods were originally developed for helical cone-beam CT and are exact for this trajectory. In therapeutic settings the hardware is often constrained to a circular motion. A circular trajectory is identical to a helical trajectory with a pitch of zero; therefore the central plane can be reconstructed exactly with the original technique. For full volume

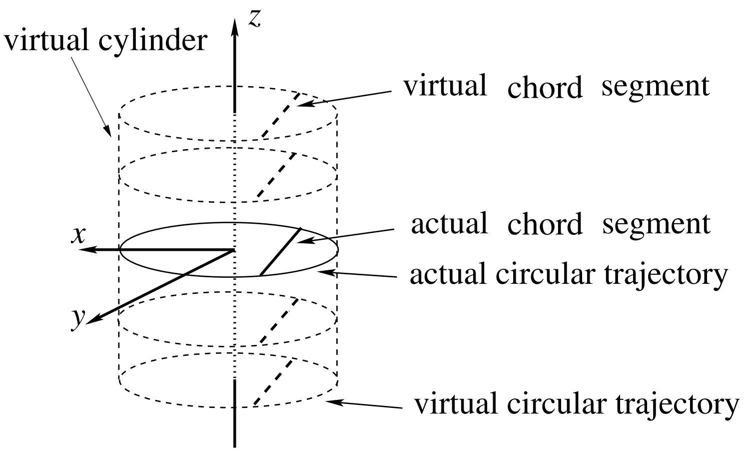

Figure 3.1: Virtual chord segments are used in slices away from the central plane for approximate reconstruction of these slices.

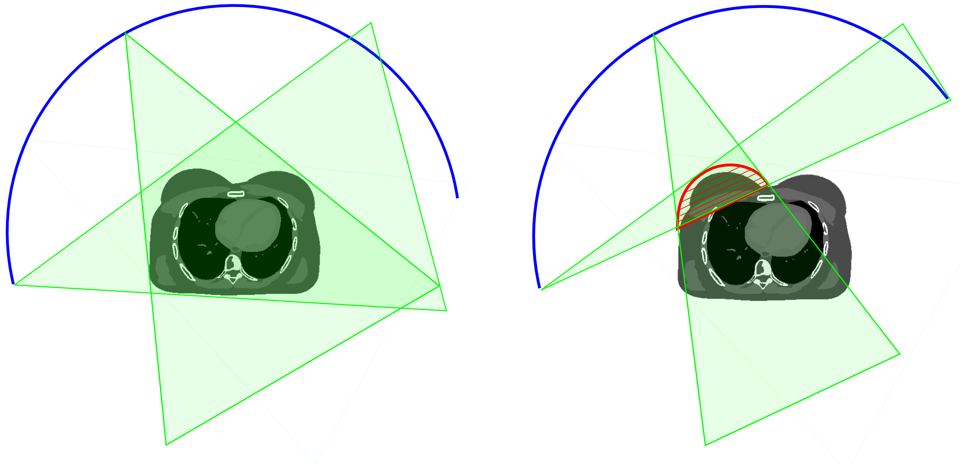

(a) FDK (b) BPF

Figure 3.2: The required illumination for two sample projections for breast imaging are shown for FDK and BPF in (a) and (b) respectively. The required scan range is indicated by the blue arc and the ROI by the red region.

coverage an approximate extension to the technique was introduced using the concept of virtual chords[99]. The idea of virtual chords is shown in Figure 3.1. A set of chords, virtual and actual, can be chosen to fill the desired reconstruction volume.

Utilizing the chord based back-projection-filtration (BPF) technique we have freedom to arrange the set of reconstruction chords to best fill the desired region. A pair of data sufficiency conditions has also been identified[58,100] which prove that the image can be accurately reconstructed along the chord with reduced data. Specifically, the first condition is that the angular reconstruction interval must span the arc formed by the intersection of the chord with the source trajectory. The second condition is that the illumination must be sufficient to cover the chord support segment, or the intersection of the chord and the reconstructed object, at each projection view. Practically this means that we can acquire sufficient data for accurate reconstruction from a smaller angular range with a smaller illumination field at each view than necessary for standard reconstruction techniques and this equates to reduced imaging dose. In Figure 3.2 we see an example for breast imaging. The region of interest is indicated in red with the orientation of the reconstruction chords indicated by the parallel red lines through the ROI. A standard reconstruction would require the entire body to be

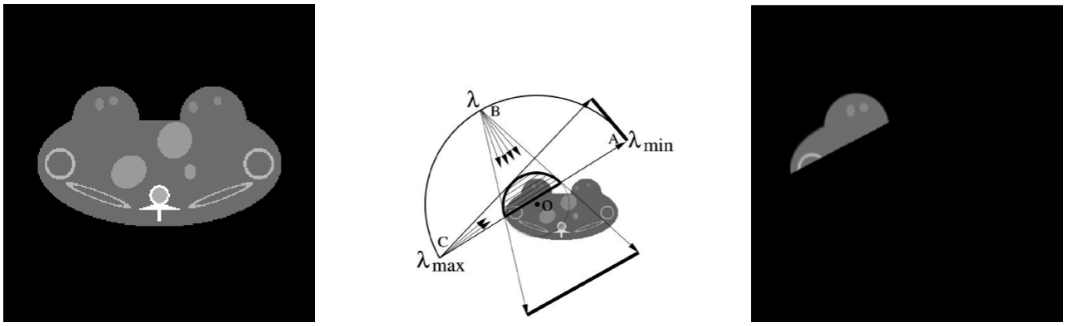

(a) (b) (c)

Figure 3.3: Simulation results for a chord based reconstruction of a breast ROI. The original digital phantom is shown in (a), the reconstruction geometry in (b) and the reconstruction result in (c). (Image courtesy of Medical Physics[101])

fully illuminated through at least 180° plus the fan angle of the beam, as depicted in Figure 3.2a. However, for BPF reconstruction the necessary source trajectory is indicated in blue, for this ROI this is only slightly less than 180° but, more significantly, the illumination only needs to cover the ROI not the whole body as shown in Figure 3.2b. Results from a preliminary study with simulated data are shown in Figure 3.3.

3.3 PMRT Simulation Case Study

3.3.1 Introduction

Postmastectomy radiation therapy (PMRT) is often prescribed for patients with advanced breast cancer and has been shown to reduce local-regional recurrence and improve survival[102,103]. The radiotherapy target is the chest wall, axillary lymph nodes, and the supraclavicular fossa. Patients are normally positioned for therapy with arms extended above the head in order to minimize both dose to the uninvolved arm tissue, and perturbations to the delivered dose distribution. The shoulder is the most mobile joint in the human body and difficult to position with a high level of reproducibility, thus the target area can be substantially affected by shoulder and arm position. Accordingly, this treatment is a good candidate for the regular use of imaging for patient position verification.

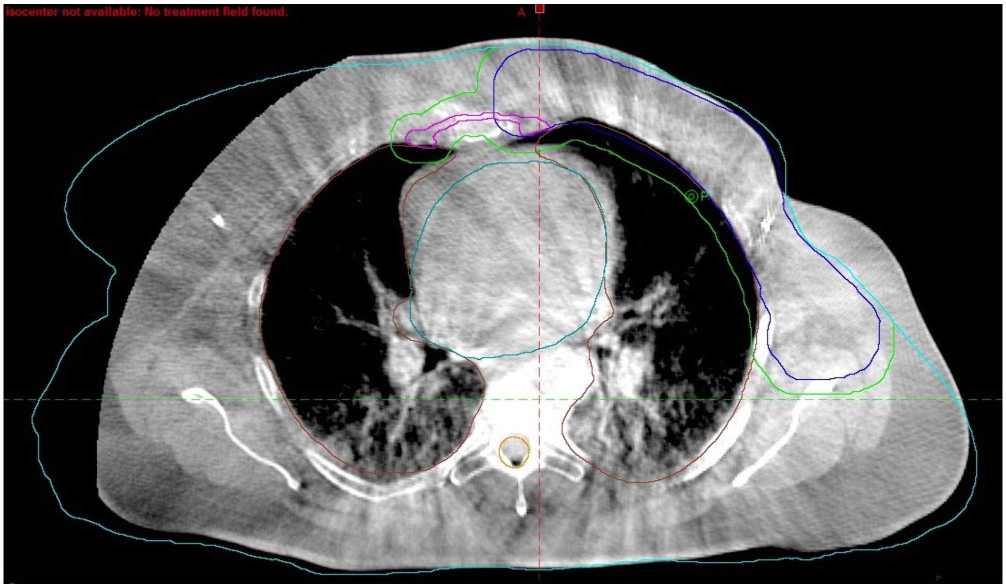

Figure 3.4: An example clinical reconstuction of a PMRT patient CBCT used for setup. The contours from the treatment planning process have been overlain.The outer cyan contour represents the expected skin surface, notice the large section missing on the left.

There are however a number of problems which result in both practical difficulties and suboptimal image quality in the application of CBCT to image guidance for PMRT. Standard CBCT imaging approaches utilize the FDK algorithm which requires projection of the entire patient cross-section from at least 180° plus the beam fan angle. Since the size of CBCT detectors is limited, e.g. 40 cm, imaging a PMRT patient with arms up utilizes a half-fan geometry where the detector is offset by nearly half its width and the gantry rotated through a full 360 degrees. Even so, some projections may be truncated, leading to suboptimal image quality as seen in Figure 3.4.

The breast is a particularly radiosensitive organ and therefore efforts need to be taken to spare the contralateral breast from exposure to imaging radiation. Thus, strategies to minimize imaging dose to non-target regions take on increased importance in breast and chest wall IGRT. We have applied recent developments in region-of-interest CBCT to this problem, since they offer the opportunity to reduce both the illuminated area and the angular scan range required for accurate reconstruction, while also offering improved image quality in the reconstructed region of interest. Previously, chord based BPF algorithms have been shown able to reconstruct exactly certain ROIs from limited data[60,104]. The PMRT geometry is typically well suited to using a chord based reconstruction approach to reduce the field of view, angular scan range and truncation artifacts that degrade the traditional FDK reconstruction. This should produce images of superior quality and reduce the dose to the contralateral side. As discussed below however, PMRT imaging has significant potential for collisions with the imaging detector and/or linac head. Here we introduce a software based collision prediction method which can be used to optimize placement of the imaging isocenter and calculate the required rotation arc and illumination from each view and perform the ROI reconstruction from projection data simulalated from the patient's planning CT.

3.3.2 Materials and methods

Collision Prediction

Due to the large lateral distance across the elbows of a supine PMRT patient with arms raised above her head, and the desire to image with the patient offset to one side, as will be the case during treatment, there is a high potential for collision. To plan the imaging acquisition to avoid collisions, we have developed a software prediction method which uses the Visualization Toolkit (VTK, Kitware Inc.) and the open source vtkbioeng library from Goodwin Lawlor (http://www.bioengineering-research.com/).

The collision detection process begins with extraction of the skin surface from the treatment planning CT by thresholding and a marching cubes contouring filter. This yields a detailed patient surface representation shown in Figure 3.5a, however the planning scan seldom extends far enough superiorly to include the patient's elbows. Therefore we also utilize a 3D surface model from the VisionRT system of multiple stereoscopic optical cameras which is then registered to the CT scan contour, Figure 3.5c. Finally, a model of the treatment tabletop is inserted into the scene.

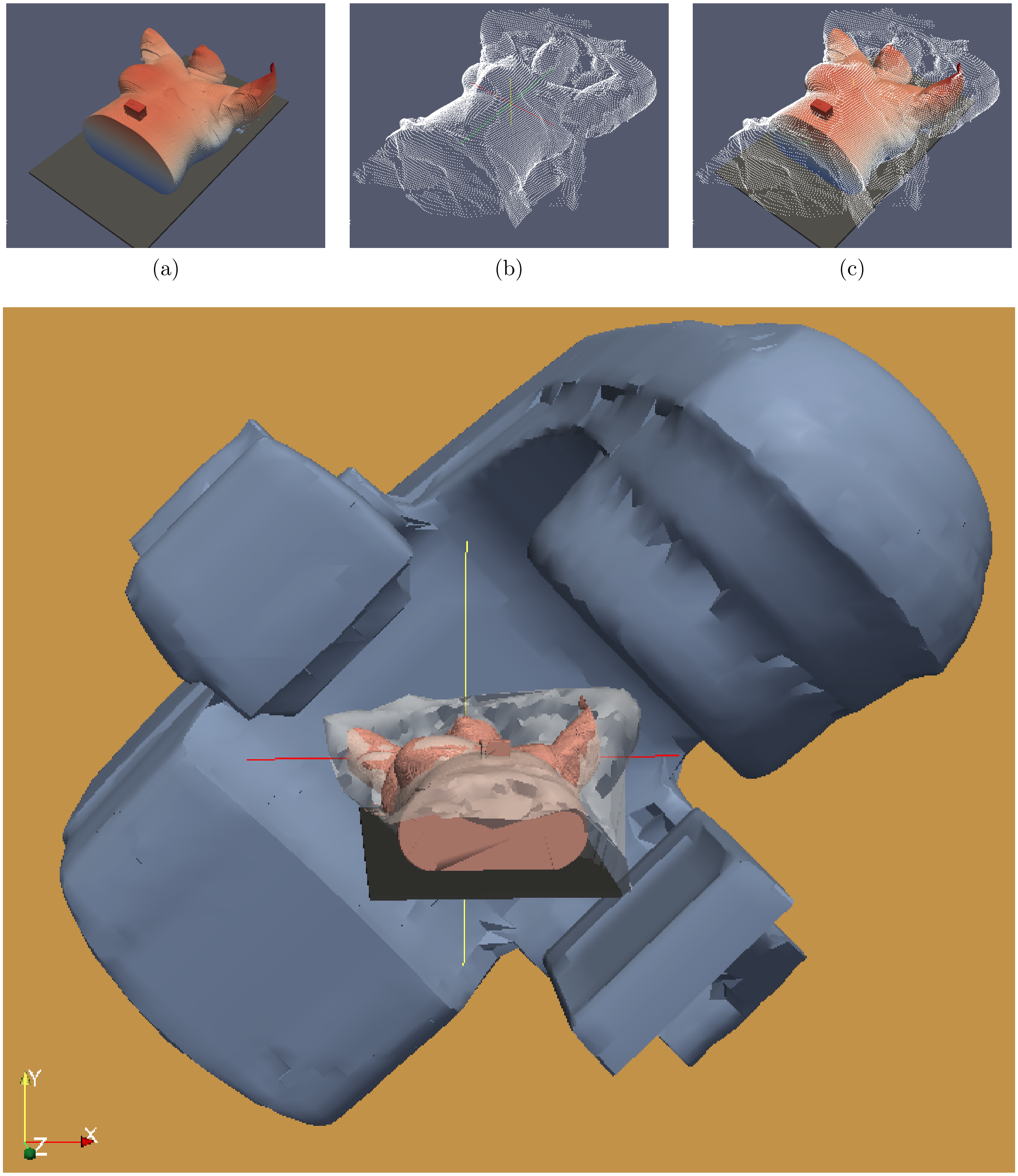

(a) (b) (c)

(d)

Figure 3.5: A rendering of the collision prediction model. The patient's extracted CT contour (a) and the VisionRT generated 3D surface (b) are co-registered (c) and then combined with the model of the linac (d). Note the small distance between the patient's elbow and the linac head.

A 3D model of the Trilogy linear accelerator (Varian Medical Systems) has been generated to accurately represent the outer linac surfaces which may collide with the patient or couch. The linac isocenter can be aligned with the patient to simulate any proposed imaging isocenter, an example setup is shown in Figure 3.5d. The accelerator can then be rotated through the desired angular range testing for collisions. The collision detection algorithm (from the vtkbioeng library) is based on the native VTK oriented bounding box tree for efficiency. This approach determines the tightest fitting bounding box by orienting it along the eigenvectors of the covariance matrix. Split planes are then recursively chosen that roughly divide the complexity of the geometry in half. Using this approach much of the geometry complexity can be quickly excluded allowing the algorithm to process approximately one rotation angle per second on a single core of a standard desktop computer.

Acquisition Planning

From the treatment planning data, e.g. target volume, organs at risk and dose distribution, we can identify the minimum ROI required for the scan to be clinically useful for patient setup as well as regions where illumination is to be avoided. Currently we use this information to manually determine the ROI and reconstruction chord arrangement, which determines the required angular scan range. The proposed rotation center and arc are used to predict collisions as described above, and the results used iteratively to adjust the imaging geometry until a collision free geometry is found. Approaches for streamlining and automating this process are under investigation.

In practice, one would also use dynamic collimation of the imaging beam to increase dose sparing to the contralateral side. This requires a plan for the upper and lower collimator blade motions with view angle. To generate this we mask the planning CT scan to the ROI of interest and forward project using the geometry determined in the previous steps. This gives the required data support on the detector plane. The first and last non-zero values in each row of this sinogram define the edges of the required field of view, and a margin may

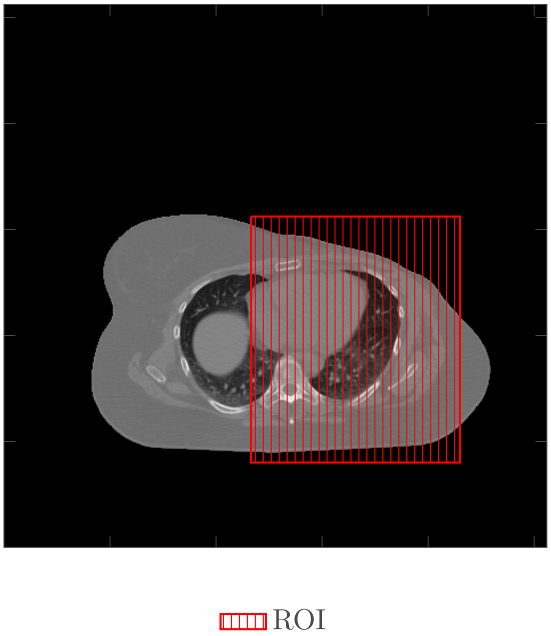

Figure 3.6: The ROI chosen for this study shown over the planning CT scan. The hatch marks indicate that the reconstruction was performed with parallel, AP aligned chords.

be added for setup uncertainty. They can be smoothed if needed to ensure deliverability. Additionally, in the case that the required detector support exceeds the physical detector dimension, we anticipate this can be overcome by traversing the imaging arc twice (i.e. in this case, two 190 degree arcs, requiring approximately the same imaging time as the currently utilized 360 degree half-fan scan) with the detector offset in opposite directions, in essence generating a single, larger “virtual detector”.

Image Reconstruction

Simulation data were generated by artificially masking the forward projections of the patient planning scan with the scan geometries determined above. The reconstruction is done with the chord-based BPF algorithm[60]. We use a parallel chord arrangement with the orientation established in the acquisition planning steps above. Reported here are simulation results with projection data generated from the forward projection of an actual patient treatment planning scan, which have been artificially truncated to simulate the data resulting from the

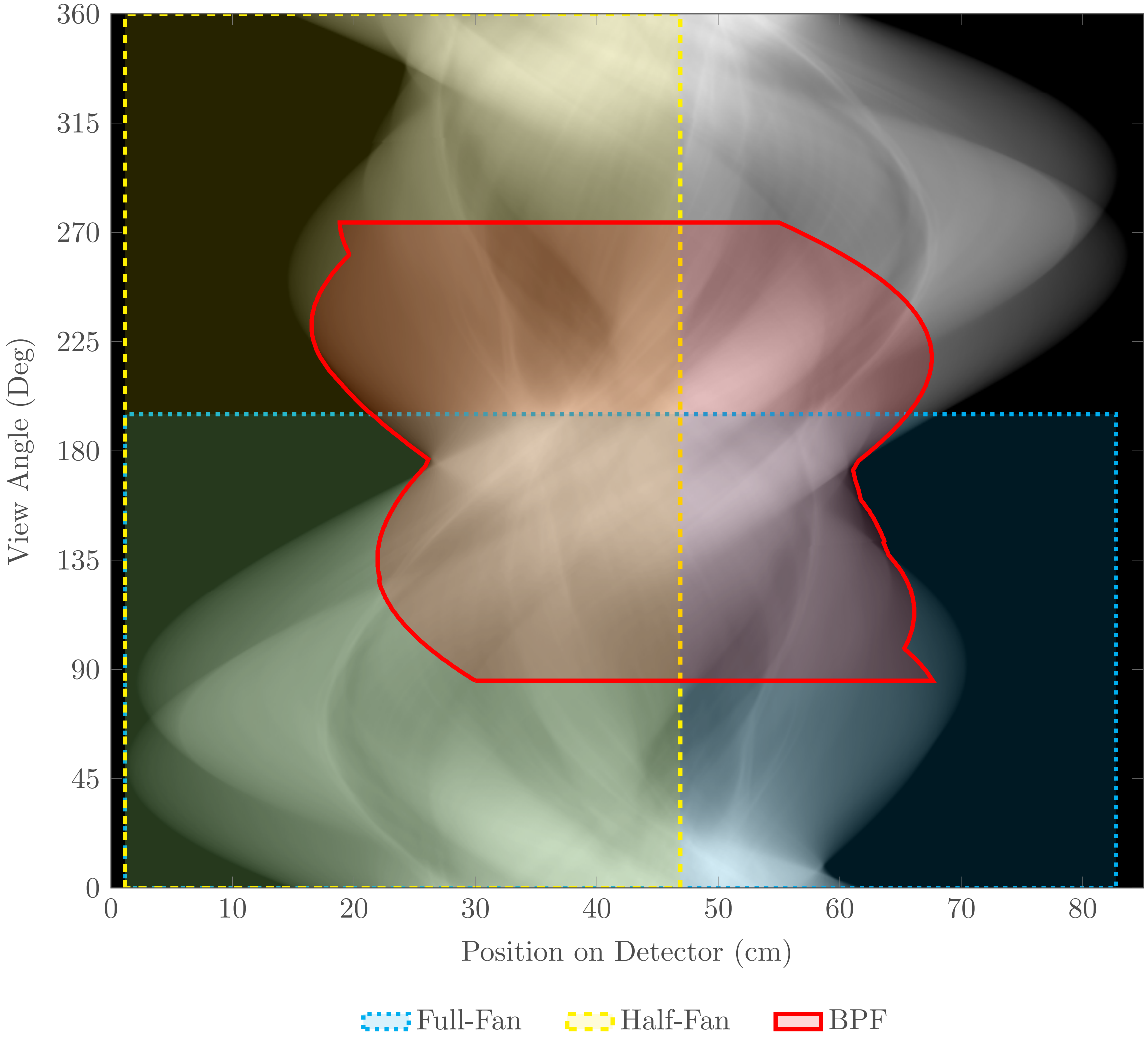

Figure 3.7: The full sinogram data for the planning CT slice used in the simulation study. Cyan dashed contour: data range required for a "full fan, half scan" (symmetric detector) geometry to avoid truncation. Yellow dash-dot contour: data required for a "half fan, full scan" to avoid truncation. Red solid line: data required for dynamic illumination BPF reconstruction.

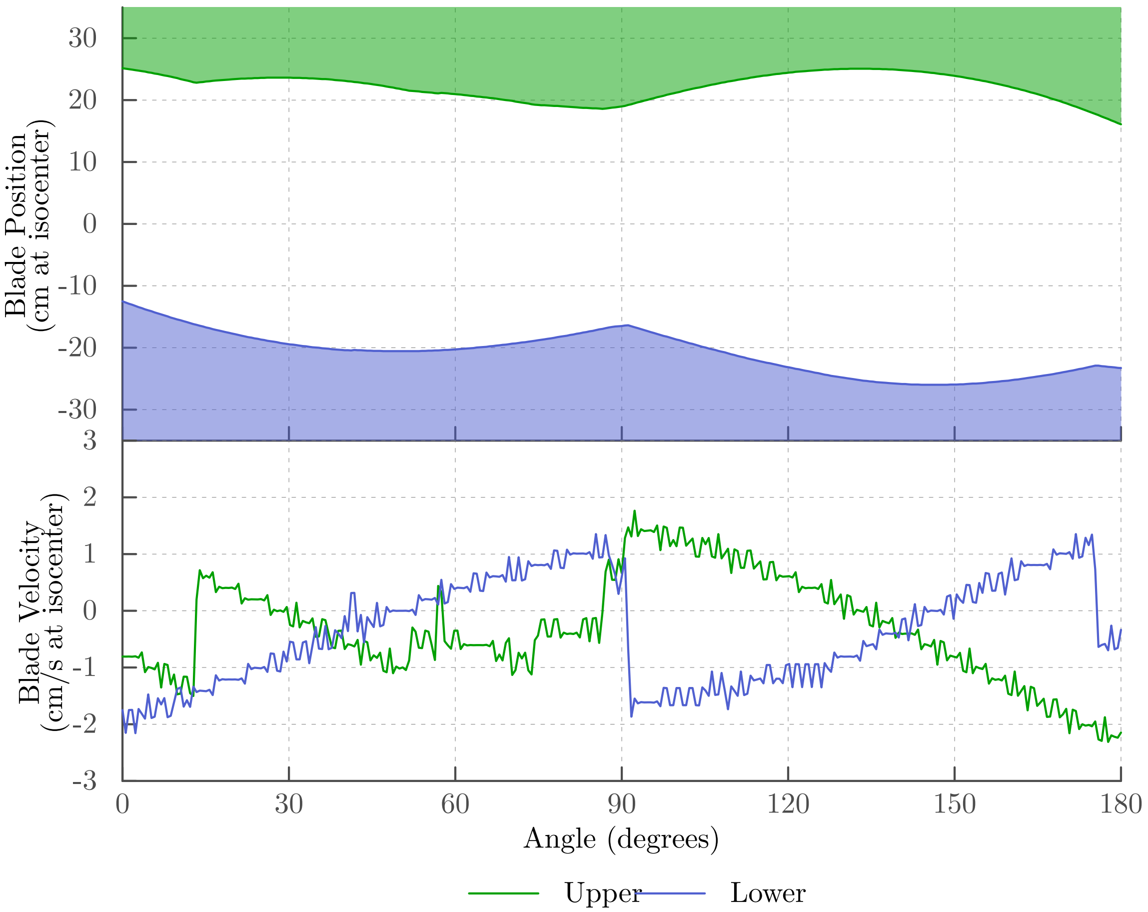

Figure 3.8: The collimator blade sequencing shown vs gantry angle for the case study shown here. The top plot shows the absolute jaw position, as projected at the isocenter with the filled regions indicating the blade coverage. The lower plot shows the corresponding blade velocity. For this case the required blade velocities are well within the hardware capabilities of 8 cm/s

	Arc Length (deg)	Detector Size (cm)	Collision
Full Fan FDK	195	**82**	No
Half Fan FDK	360	47	**Yes**
BPF	190	47	No

Table 3.1: Detector Requirements and Collision Prediction for BPF and FDK Imaging Strategies

proposed dynamic illumination strategy.

3.3.3 Results

The results from a single patient setup with simulated reconstruction results are presented as a proof of concept. For this patient it was decided that a roughly hemi-thoracic ROI would be ideal for providing sufficient information for patient setup and sparing the contralateral breast. AP aligned parallel chords were chosen for the reconstruction geometry as shown in Figure 3.6. We found that by shifting approximately 7 cm both anteriorly and to the patient's left, we were able to image over approximately a 190° arc. The collision prediction model is shown in Figure 3.5. In Figure 3.7 the full data sinogram is shown with the data ranges required for a traditional full-fan/half-scan, a half-fan/full-scan and the proposed conformal ROI technique. A summary of results is given in table 3.1. Note that, with this patient setup, a typical half-fan/full-scan geometry would cause a patient collision. With a symmetric detector full-fan/half-scan geometry the collision could be avoided but would require an 82 cm wide detector, more then double what is on the current system.

The collimator blade sequence and velocity for this scan setup are shown in Figure 3.8. Note that the blade speeds are well within the capabilities of the collimator hardware. If required to ensure deliverability a trajectory could be smoothed out, slightly enlarging the collimated field size in places, to allow accurate delivery from the hardware without compromising the image reconstruction.

The BPF reconstruction results from the simulated projection data are shown in Fig-

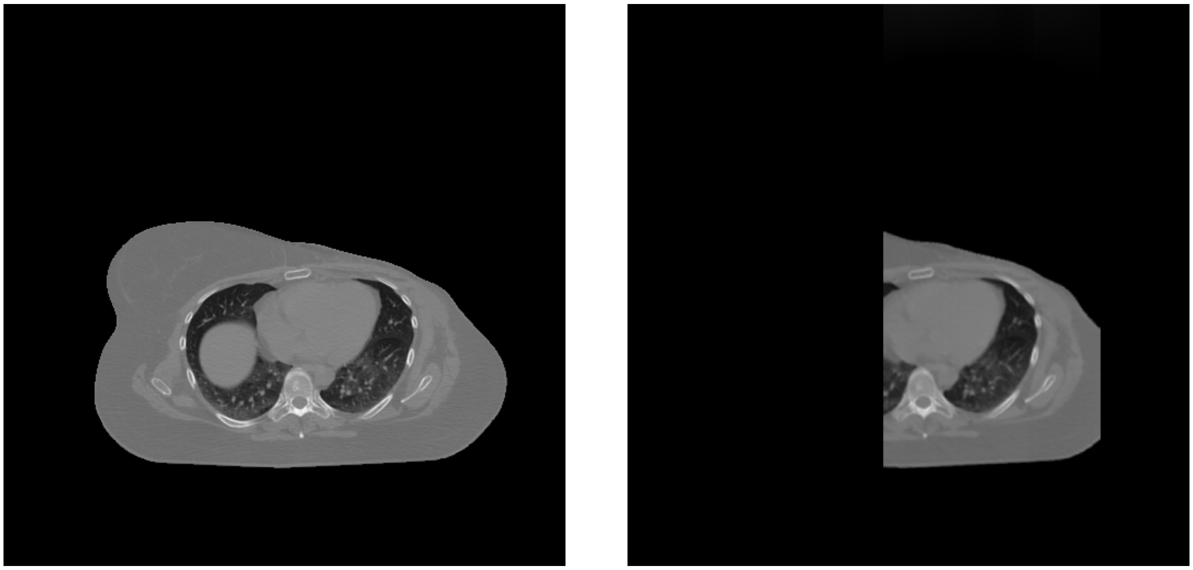

Figure 3.9: (a) Slice from the original patient treatment planning CT scan. The full scan data were forward projected, and masked to simulate the truncation due to the dynamic illumination strategy. (b) Image reconstructed from the masked projections using BPF algorithm.

ure 3.9. Note the lack of truncation artifacts despite the large degree of transverse truncation. This simulation approach does not, however, properly account for other image degrading factors such as scatter which can be a significant factor in cone-beam CT (and should be reduced in the ROI images due to the smaller imaging beam size at many angles). As such these results are not meant to indicate the image quality achievable with this method.

3.4 Real Data Study

3.4.1 Introduction

With the collimator developed in chapter 2 we are now able to perform the type of dynamic x ray field shaping required for conformal ROI imaging with the clinical imaging system. The following section describes the experimental setup, reconstruction process and results for chord-based conformal imaging of peripheral ROIs with two separate phantoms.

(a) (b)

Figure 3.10: The head section of the RANDO Man phantom (a) and the Chicken phantom (b) setup for planning scan on the Philips Brilliance Big Bore sim CT

3.4.2 Methods and Materials

Phantoms

Two phantoms were used for these real data studies. The first is the head section of the RANDO Man phantom (The Phantom Laboratory, Salem, NY) which is a standard anthropomorphic phantom used for dosimetry in radiation therapy. It consists of real human skeleton cast in a soft tissue equivalent urethane plastic. The natural skeleton provides good, high contrast, detailed structure however the phantom lacks any low contrast structures relevant for soft tissue discrimination in a clinical setting. The second phantom was designed to provide soft tissue information. It was a common supermarket roasting chicken, with the giblet bag and a standard bread cube stuffing in the thoracic cavity.

Acquisition Planning

Both phantoms were first setup on the Philips Brilliance Big Bore 16-slice helical CT scanner in the radiation oncology department, shown in Figure 3.10. The images were then imported into the Pinnacle^3 treatment planning system (Philips Electronics, Amersterdam, Netherlands), on which ROI contours were drawn. The process of acquiring a planning scan and marking relevant regions of the anatomy in the treatment planning system are a standard part of the patient treatment process. We then extracted the ROI contours from Pinnacle^3 and projected them onto the detector plane to determine the blade trajectories for the dynamic collimator. Due to limitations of the clinical hardware a full 360° of data was planned and acquired, the subsection needed for the BPF reconstruction was selected from that set.

The ROIs were chosen as peripheral regions so as to be reconstructable with BPF and so as to be deliverable with the collimator hardware. The ROIs are shown in Figure 3.12 over the reference scan taken with the OBI with the phantom in the position for the conformal experiments and not the planning scan upon which they were drawn. The region of the ear in the RANDO plan and the small section of thigh on the left edge of the chicken plan were not intended to extend outside the ROI. This indicates that insufficient margins were used to account for our setup uncertainties. The blade trajectory for the RANDO ROI is shown in Figure 3.11.

Collimator Setup

The collimator was setup up in the CT imaging configuration, that is with the blade motion perpindicular to the axis of rotation. The lead covers were added to the blades which provide an additional 3 mm of lead and 0.8 mm steel to the existing 3 mm of copper. This combination is effectively radiopaque for the beam energy with only $7.81 \times 10^{-4}\,\%$ of the highest energy (125 kVp) photons making it through. The collimator was mounted on the kV source in place of the bowtie filter and the electronics board was attached to the face of the linac with adhesive dual lock strips. The motor power cables were run along the robotic arm supporting the kV source and zip-tied in place. Power for the system, 12 VDC for the motors and 5 VDC was provided by a benchtop power supply located off gantry and connected to the control board with a multiconductor cable long enough to wrap around the outer surface of the gantry as it rotated. A counter-weighted block and tackle system was used as a cable

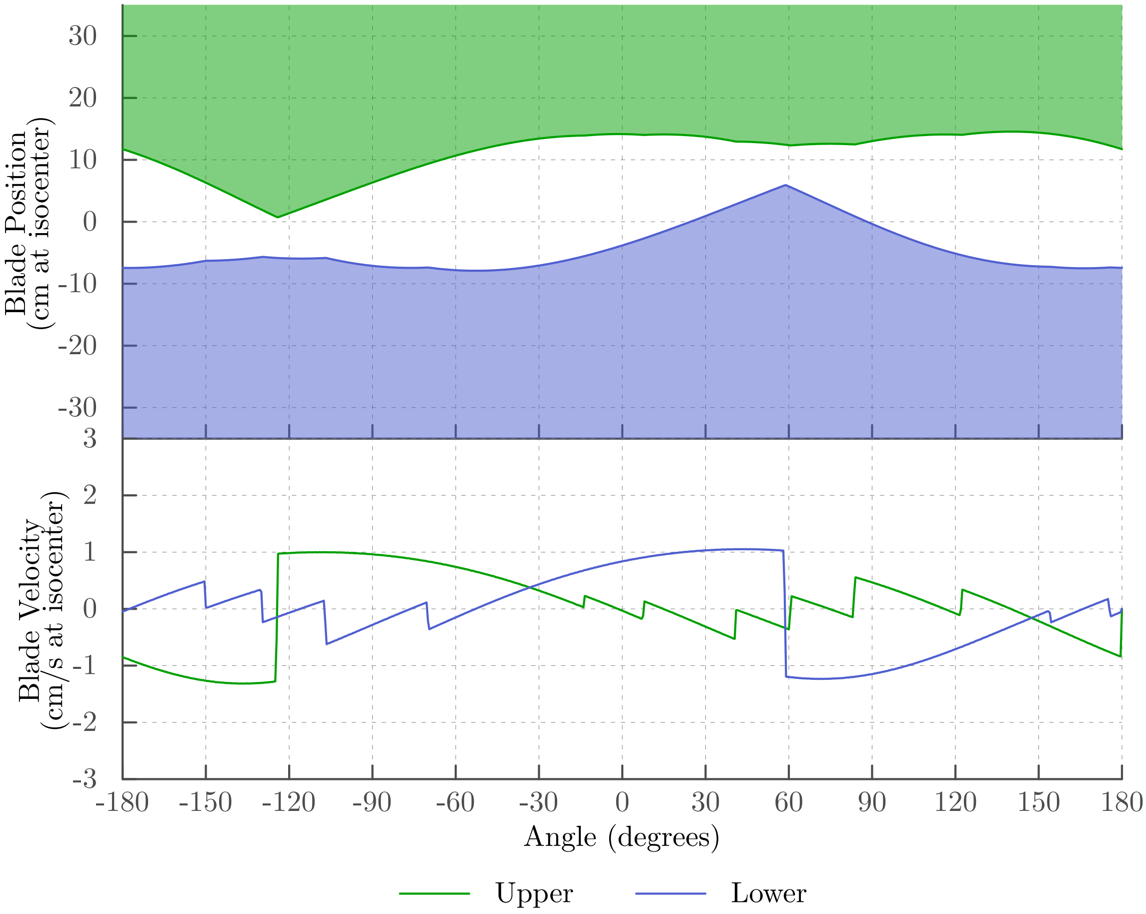

Figure 3.11: The collimator blade sequencing shown vs gantry angle for the RANDO cheek ROI. The top plot shows the absolute jaw position, as projected at the isocenter and the lower plot shows the corresponding blade velocity. For this case the required blade velocities are well within the hardware capabilities of 8 cm/s

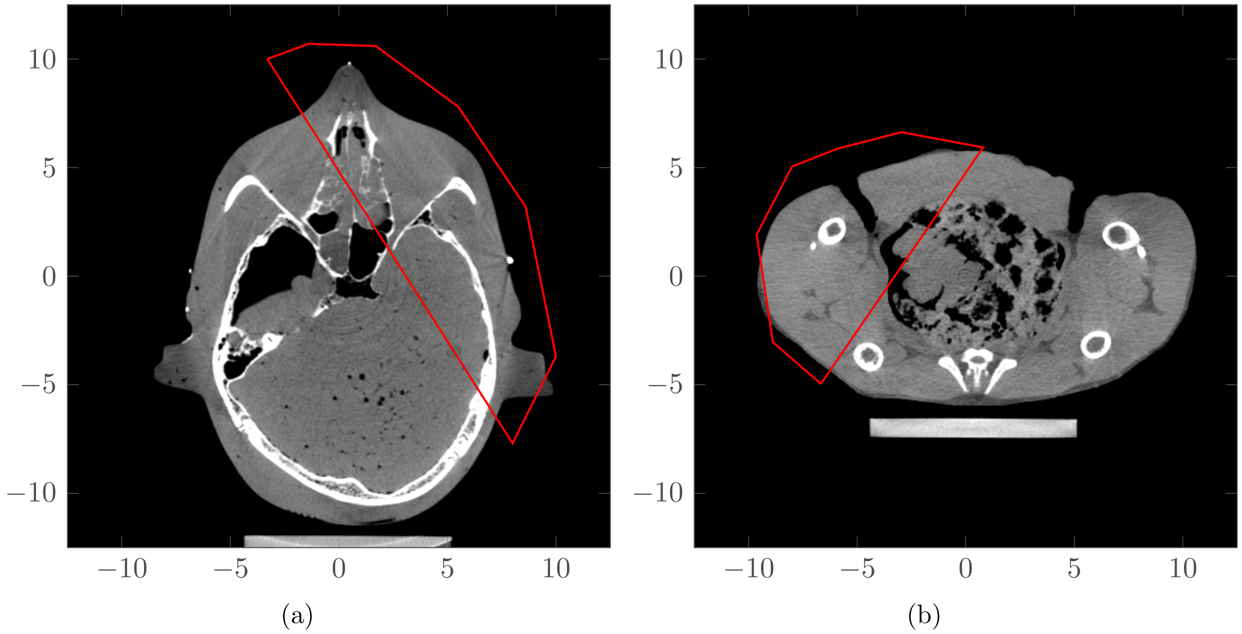

Figure 3.12: Cheek ROI plotted over reference reconstruction of Rando (a) and anterior periphreal ROI plotted over the reference reconstruction of the chicken phantom (b). Axes are in centimeter scale. There is evidence of setup error between the planning scan and the OBI acquisition where the ear and part of the thigh extend outside the region.

retractor. The collimator inclinometer was zeroed with the gantry at the 0° position and the blades were calibrated with the method described in section 2.2.4.

Image Reconstruction

The BPF reconstructions in the previous section were performed with parallel chords, aligned with the image grid and uniquely filling the reconstruction volume. This simplifies the problem but is severely limiting in the flexibility of the ROI specification. Prior to the real data studies the code was updated to allow arbitrary chord specification. There are two primary differences in moving from the previous chord arrangement to more general setups.

The first is the additional interpolation required. In the chord based reconstructions the image is formed along the chord, and in the previous arrangement the chords were aligned with the imaging grid making the mapping of the data from the chord back to the standard

Cartesian array used for image storage and display quite straightforward. With chords aligned at an an arbitrary angle to the image grid there is additional interpolation that must occur to map the data on the chord back to the image array. This can, in principle, cause numerical artifacts in the reconstruction, however in practice with well matched sampling of the chords and image array this is seldom a problem. Generally, the appreciable effect is in the additional computational burden.

The other difference is that the chord to voxel mapping is no longer unique. With the parallel chords aligned with the imaging grid they were setup so that each voxel is intersected by exactly one chord thus uniquely determining the image intensity values. With the more arbitrary chord arrangement there may be many chords that intersect a single voxel and should be averaged. This is accomplished by first filling all the chords with ones and mapping them back to the image array to determine a filling factor. After the reconstruction of the projection data it is weighted by this filling factor.

There are four chord arrangements that we consider in this section, two each for the full FOV and the ROI reconstruction. For the reference images we use a BPF reconstruction of the full FOV from the fully illuminated data set using both a parallel chord set as previously described as well as a diverging, fan-beam like arrangement where chords are drawn from a single source point along diverging rays to cover the FOV and is repeated at many source points along the source trajectory circle. While theoretically the same, for the continuous model with noise free data, there are practical differences. The parallel chord set can be reconstructed from a more limited scan arc, about 209° for a 25 cm FOV, but the fan-beam arrangement uses more of the full scan data, potentially providing better noise performance.

For the ROI reconstruction the chord arrangements may depend on the shape of the ROI, however all reconstructable ROIs will consist of one long straight edge that bisects the object and an arbitrary convex edge outside the object to be reconstructed. The shortest imaging arc will come from a unique set of chords parallel to the straight edge passing through the object. Alternatively, a chord set that makes more complete usage of the scan data would

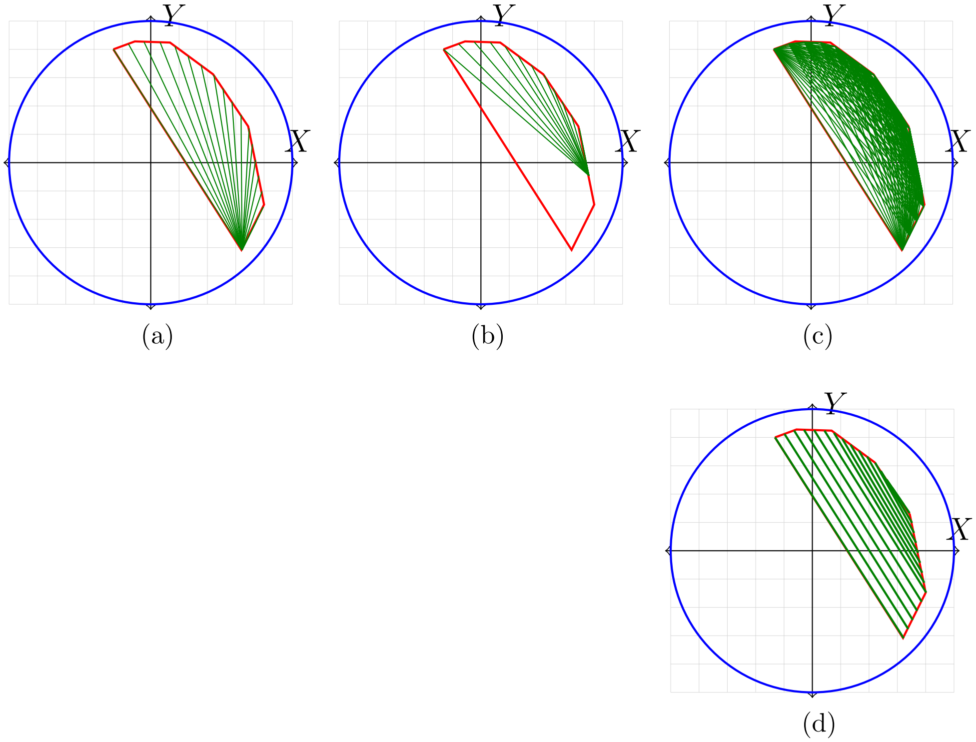

Figure 3.13: The 25 cm FOV is shown in blue and the RANDO cheek ROI shown in red. The top row shows how the overlapping chord set is generated. The first point on the outer edge is connected to all other points along the edge (a) then each subsequent point is connected to all remaining, e.g. (b), creating a complete chord set (c). The non-overlapping chord set is shown in (d)

be to fill the volume with divergent chords originating from points along the outer edges, as show in Figure 3.13.

3.4.3 Results

Image Reconstruction

Table 3.2 shows the minimum scan ranges required for the reconstructions. For the ROIs considered here we find the the BPF reconstruction can be performed with the shortest imaging arc, saving 15° over a short-scan FDK reconstruction. However there are practical considerations for limited arc acquisitions with a LINAC imaging source. The short-scan

	BPF	FDK Short Scan	FDK Full Scan
Full FOV	209°	192°	360°
RANDO ROI	177°	192°	360°
Chicken ROI	177°	192°	360°

Table 3.2: Minimum required arcs for BPF and FDK

FDK can use any $180° + FanAngle$ range, however the BPF reconstruction specifically requires the arc subtended by the long edge of the ROI. The gantry of the accelerator cannot turn in one direction indefinitely, it has about 370° of rotation before it has to turn back the other way. In the case of the RANDO ROI this will not cover the required arc continuously.

Three different ROI reconstruction results are shown for both phantoms. All are shown beside a "Reference" image which is a BPF reconstruction from the fully illuminated dataset with the fan-beam style chord arrangement. The first ROI reconstruction, Figure 3.14 is performed using a masked portion of the fully illuminated data set to show the potential of the technique without the complications of the experimental acquisition with the dynamic collimator. With the exception of the bright edge caused by the truncations caused by the setup error and insufficeint margins the ROI is recovered exactly.

The remaining two reconstructions are for the two ROI chord arrangements introduced above. The divergent, overlapping chord set result is shown in Figure 3.15 and the non-overlapping chord set in Figure 3.16. It should be noted that at the time of acquisition a fully illuminated reference scan was not acquired at the same axial position as the ROI shown here so the reference reconstruction is 2.9 cm offcenter and does not match the axial position of the conformal reconstruction exactly.

Generally the ROIs from the conformal data sets are well recovered; however there are two artifacts evident in the images. The first is an intensity drop out in the image, seen as a dark streak along the edge in RANDO and the upper right corner of the chicken image.

The other is the bright section on the outer edge. Both are a result of the collimator edges. Attempts to correct the bright regions included masking the sinogram prior to reconstruction, shrinking the ROI that was reconstructed, and masking the image post reconstruction. All gave reasonable results but all shared the problem that they further shrunk the recovered ROI, encroaching further on the phantom. The most important step to better reconstructions would be to apply a proper margin to the image ROI for delivery uncertainty, which would also remedy the intensity drop artifact.

3.5 Summary

Conformal ROI imaging was shown to accurately reconstruct peripheral ROIs from restricted illumination cone-beam CT scans using the chord based BPF algorithm. The x ray field was collimated to the bounds of the ROI using the dynamic collimator with radiopaque blades which can reduce the radiation exposure to the tissues outside the ROI. This technique is limited to peripheral regions which can be completely filled with untruncated chords which requires careful planning of the ROI and the CT acquisition. Additionally this approach provides no image information about the parts of the patient outside the ROI.

Additionally, a method for predicting potential collisions between the patient and the linac was developed. A patient model was generated from the planning CT and combined with surfaces generated from stereoscopic optical imaging for parts of the patient that weren't scanned during simulation. The patient model was virtually setup with an engineering model of the accelerator's outer surfaces and potential collision were determined. While this was developed specifically to determine the potential of setting up post mastectomy patients off center for ROI imaging with a limited arc it has broader application in radiation therapy for applications such as non-coplanar fields in IMRT, arc setup in VMAT, and for non-standard imaging trajectories[105].

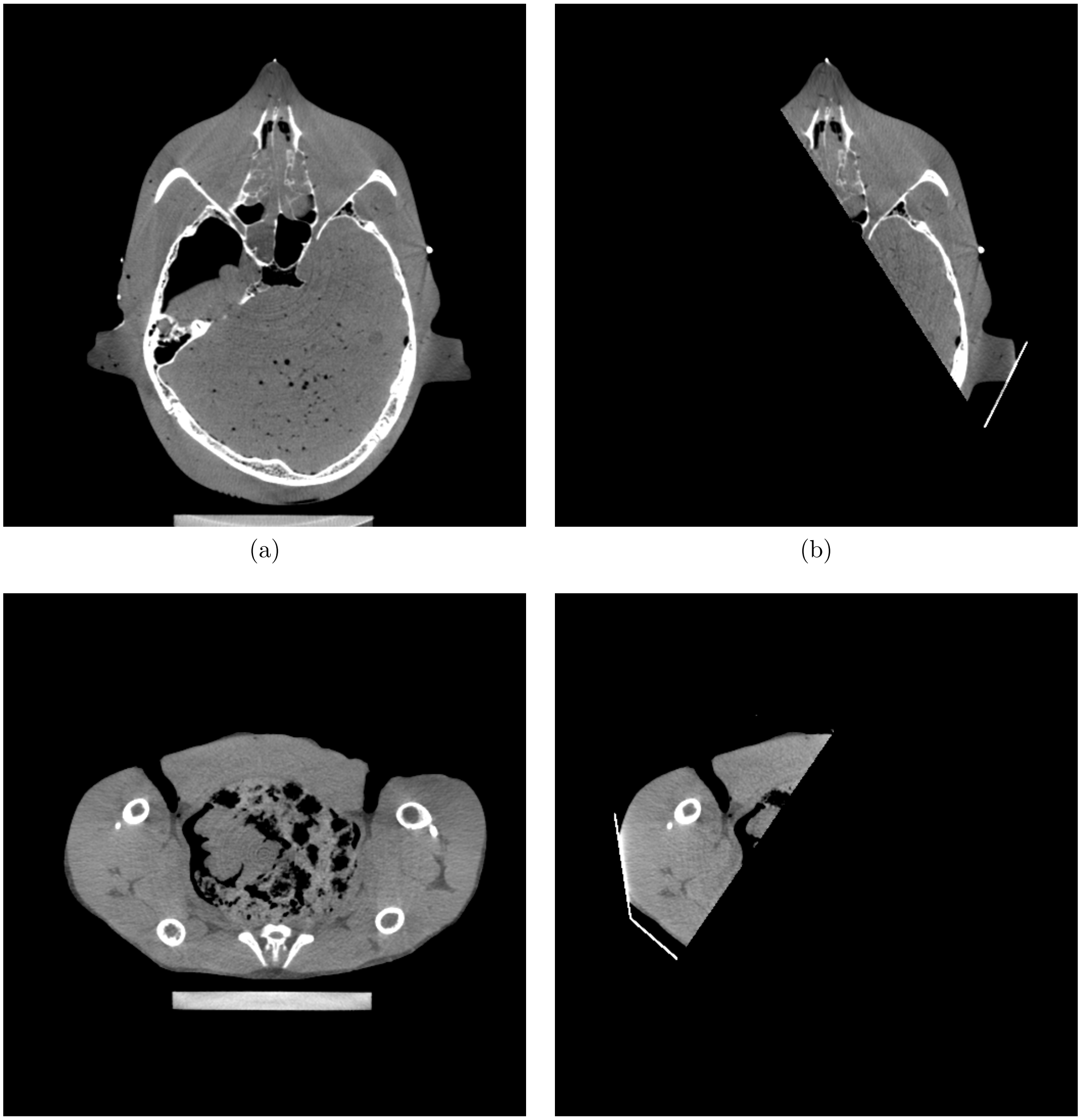

(a) (b)

(c) (d)

Figure 3.14: BPF reconstructions of the RANDO (top) and chicken (bottom) phantoms. Left column is the “reference” reconstruction from full illumination with fan chords. Right is the ROI reconstruction from the fully illuminated and truncated dataset with the overlapping chord arrangement. Display windows are [0.1,0.3] for RANDO and [0.15,0.25] for the chicken. Note that the chicken recon is 2.4 cm off the central slice.

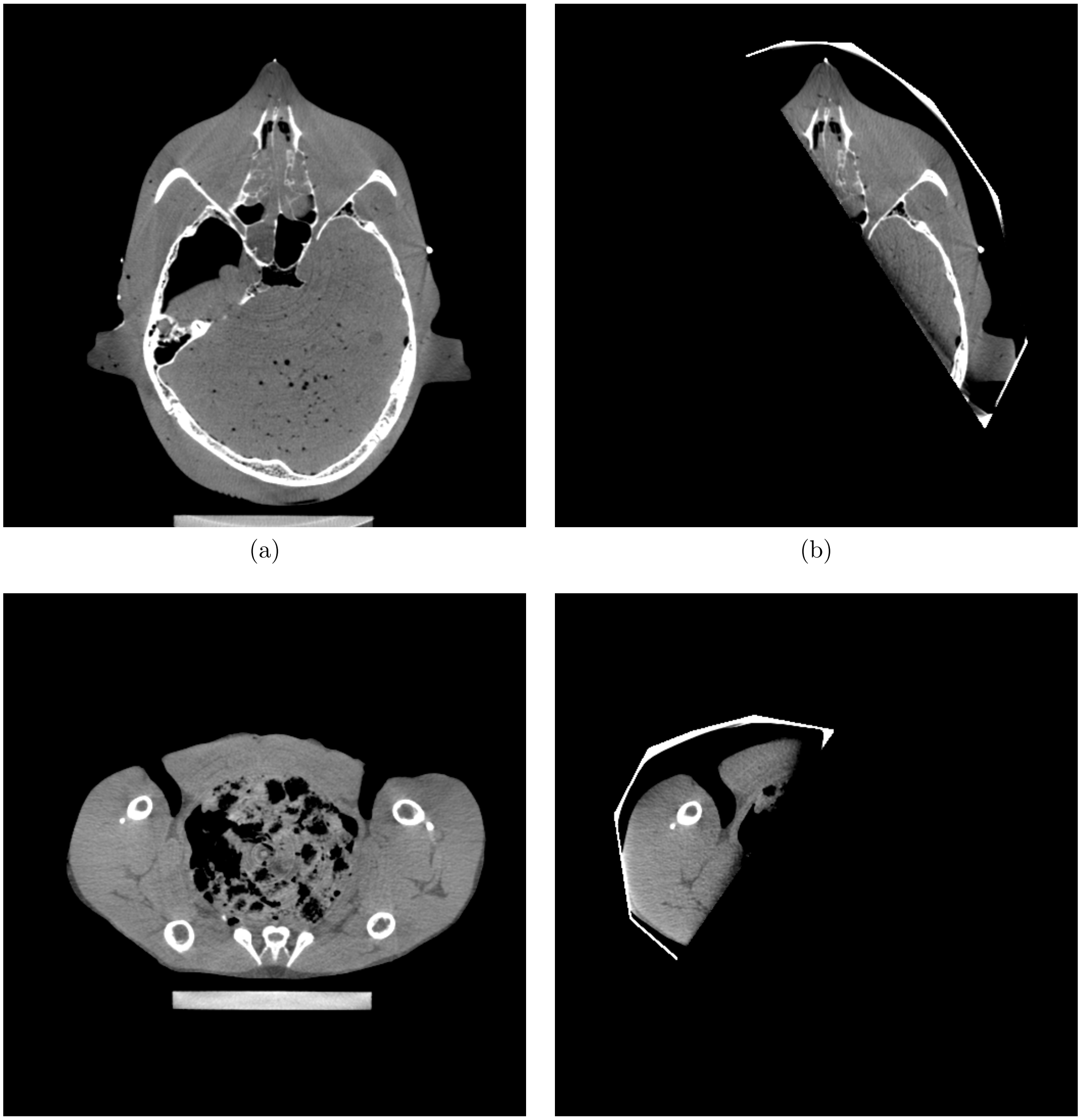

(a) (b) (c) (d)

Figure 3.15: BPF reconstructions of the RANDO (top) and chicken (bottom) phantoms. Left column is the “reference” reconstruction from full illumination with fan chords. Right is the ROI reconstruction from the conformally dataset with the overlapping chord arrangement. Display windows are [0.1,0.3] for RANDO and [0.15,0.25] for the chicken. Note that the chicken reference recon is 2.9 cm off the central slice and does not match conformal position scan exactly.

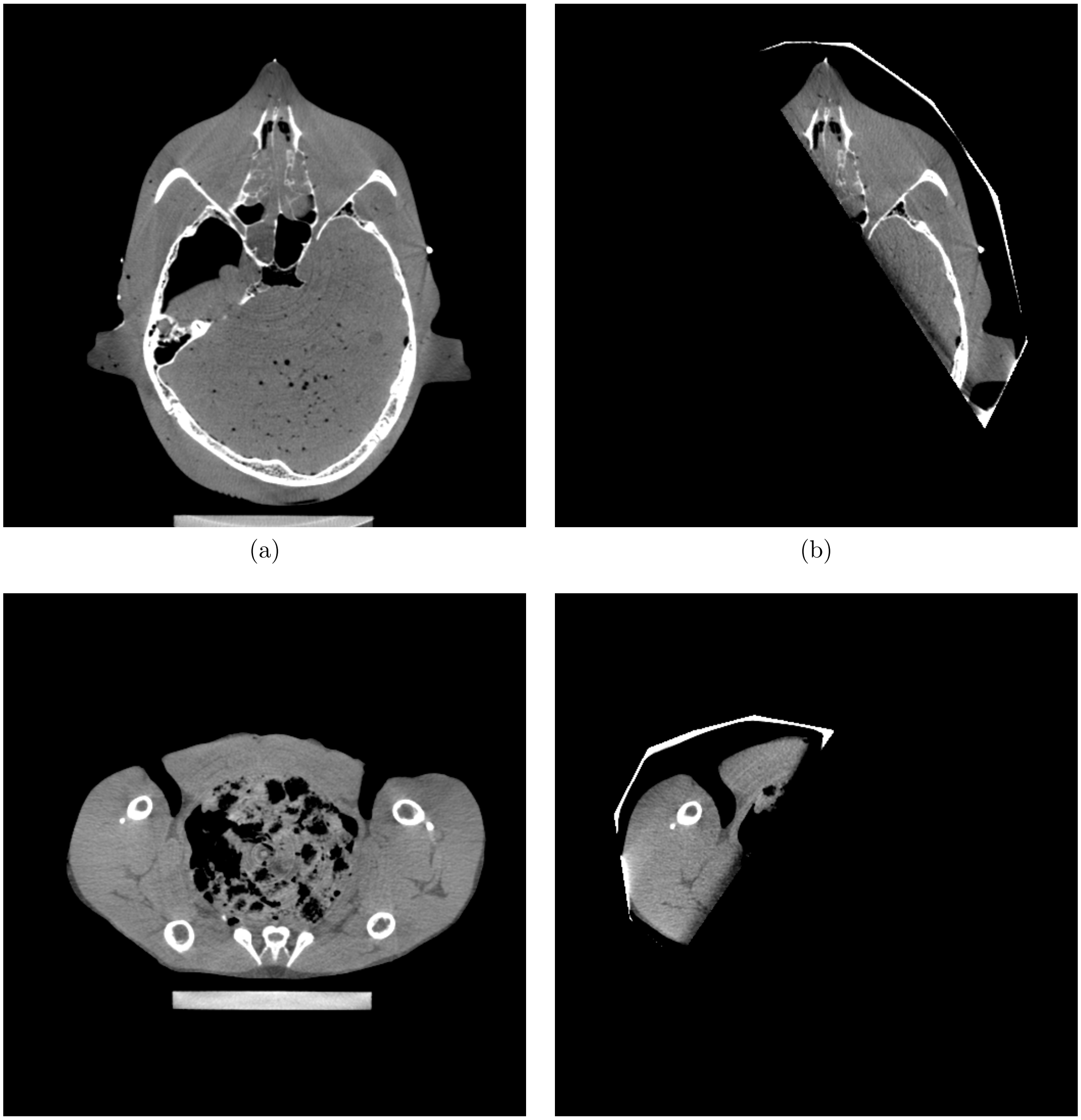

(a) (b)

(c) (d)

Figure 3.16: BPF reconstructions of the RANDO (top) and chicken (bottom) phantoms. Left column is the “reference” reconstruction from full illumination with fan chords. Right is the ROI reconstruction from the conformally dataset with the non-overlapping chord arrangement. Display windows are [0.1,0.3] for RANDO and [0.15,0.25] for the chicken. Note that the chicken reference recon is 2.9 cm off the central slice and does not match conformal scan position exactly

CHAPTER 4

STATIC INTENSITY WEIGHTED REGION OF INTEREST IMAGING

4.1 Introduction

Several of the recent CBCT reconstruction algorithms are able to perform ROI reconstructions for some geometries[60,96–98]. However, as we saw in the previous chapter practical implementation of these methods can be unforgiving to changes in the patient or the patient's setup. Additionally, there is still no practically useful analytic solution for a fully encapsulated, or interior, ROI[50]. Such regions arise often in radiation therapy where the tumor is located deep within the thoracic or abdominal cavity. The intensity weighted region of interest (IWROI) technique is a method we have developed with several key advantages. It can provide dose reduction comparable to traditional ROI imaging while providing sufficient data for reconstruction. Additionally, the full anatomy can be reconstructed, albeit with lower image quality in areas outside the ROI, which can aid in image registration to the skeletal structures.

4.1.1 Theory

The CT model generally begins from the assumption that the transmitted x ray flux is simply the impinging flux attenuated by the intervening materials.

$$I = I_0 e^{-\int \mu(x)dx} \tag{4.1}$$

where the integral is carried over the path along the ray from the source to the detector element. Thus the imaging model is often written as

$$p = \ln\left(\frac{I_0}{I}\right) = \int \mu(x)dx \tag{4.2}$$

where p is the projection data, measured as the natural log of the ratio of the unattenuated intensity to the attenuated intensity. The reconstruction problem is to recover the spatial distribution of the attenuation coefficient $\mu(x)$.

The basic idea of IWROI imaging is to spatially vary the impinging x ray field, through the introduction of filters, in such a manner as to simultaneously provide sufficient data for reconstruction while reducing the dose. From the model presented above we can see that if for some rays we were to reduce the intensity of the x ray field that would introduce a proportional scalar in front of both I_0 and I which would drop out in the projection data and the result would be unaffected.

Rather, the effect on the resulting image from changing the fluence is seen in the noise properties. The emission, attenuation and detection of the x-rays are stochastic processes and we find that increasing the number of photons reduces the variance in the measurement. This is commonly observed as a global effect in CT when the the tube current is too low or a particularly large patient is scanned and the whole image appears noisy. However, in IWROI imaging we spatially vary the source fluence which correspondingly varies the noise level across a single projection, so we must consider how the noise propagates from the projection space into the reconstructed image.

In this work we use both the chord based BPF algorithm as well as FDK. The noise properties of the BPF algorithm have been previously investigated and it was found that the noise propagation is local, in a practical sense[106,107]. This is qualitatively demonstrated and explained in Figure 4.1 and has been verified through numerical simulation[108,109]. The propagation of noise from the projection space into the the image space has been mathematically evaluated for filtered back projection[9] and while it is not local in a rigorous sense[110] we find it to be well enough confined in a practical sense for IWROI imaging.

The remainder of the chapter will be divided into two sections. The first, titled “Preliminary Studies”, will summarize the early work done focusing on filter material selection and preliminary data correction strategies which used the BPF reconstruction algorithm.

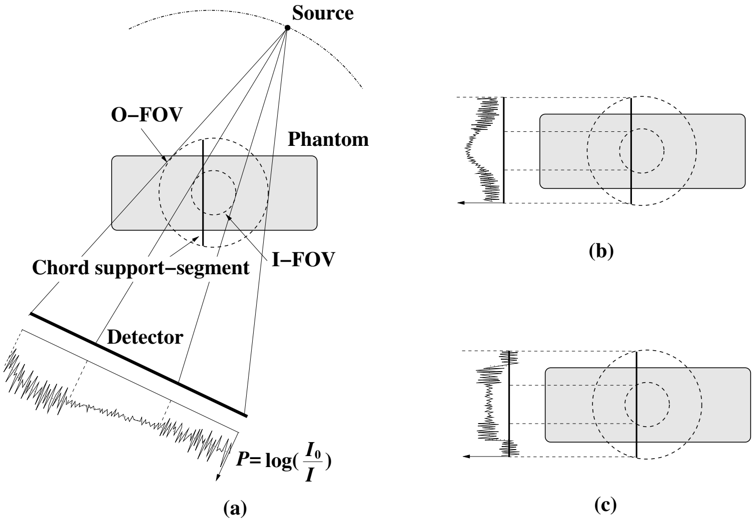

Figure 4.1: In (a) we see that due to the filtration the projection data P has distinct areas of high and low noise levels. After backprojecting on the chord (b) and filtering along the chord (c) we see the the noise levels remain pretty well locally confined.

This work has been previously presented[108,111–114] and published[109,115]. In the final section the focus shifts to practical implementation, using the more common FDK reconstruction algorithm, more advanced data correction techniques and Monte Carlo dose modeling with the anthropomorphic RANDO phantom.

4.2 Preliminary Studies

4.2.1 Implementation

All of the studies were carried out with the OBI on a Varian linear accelerator, as depicted in Figure 1.4. The filter materials and thicknesses were chosen to provide a good distribution of attenuated fluence levels and were made from either aluminum or copper. The selection consisted of 0.32 cm and 0.64 cm of copper and 1.60 cm and 4.80 cm of aluminum. For convenience they will be referred to as Cu1, Cu2, Al1 and Al3, respectively. These filters were statically fixed to the kV source, in place of the bowtie filter, resulting in cylindrical filtered and unfiltered regions. A photograph of the filters in place can be seen along with an illustration of the filtered beam geometry and an example resultant image in Figure 4.2

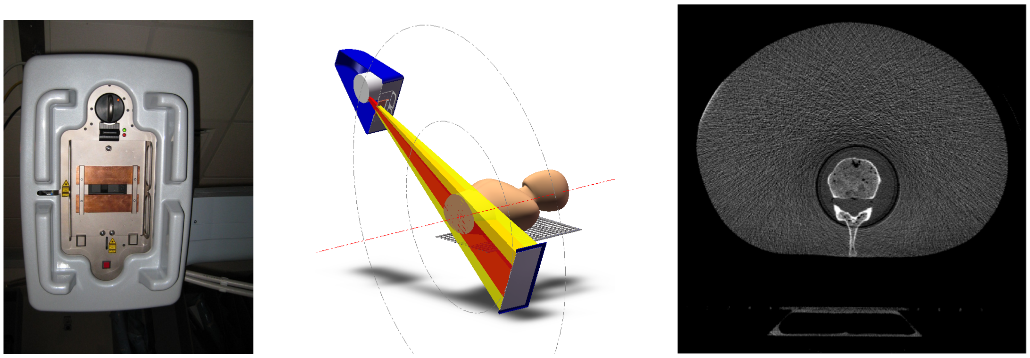
(a) (b) (c)

Figure 4.2: In (a) the Cu1 static filters are shown mounted in place of the traditional bowtie filter. The resulting illumination is shown schematically in (b) with the x ray tube shown in the upper left, the flat-panel detector in the lower right and red indicating the full intensity beam and yellow the filtered beam. A sample reconstruction where the ROI was chosen as the spine is shown in (c).

4.2.2 Data correction

In x ray CT imaging the model used for reconstruction does not exactly match the physical process; rather it is simplified to make the reconstruction a tractable problem. The common model assumes that the x-rays travel only along straight rays from the source to detector, i.e. no scattering and that the impinging beam is mono-energetic. These discrepancies between the model and the real physics result in image degrading artifacts. The substantial changes in intensity and energy spectrum caused by the filters in IWROI increases the effect of some of these artifacts. Here we introduce two empirical approaches for mitigating those artifacts.

Corrections

Scatter is one of the primary degrading factors in cone-beam CT imaging[23,116,117]. In fact the use of intensity weighting filters reduces the amount of scatter, however it is still sufficiently large that it needs to be corrected for. We have adapted a direct method for scatter estimation proposed by Siewerdsen et al.[118] For this approach the x ray tube's field defining lead collimator is closed slightly in the axial direction so part of the projection data is in the shadow of the collimator. Any signal measured in this region is assumed to

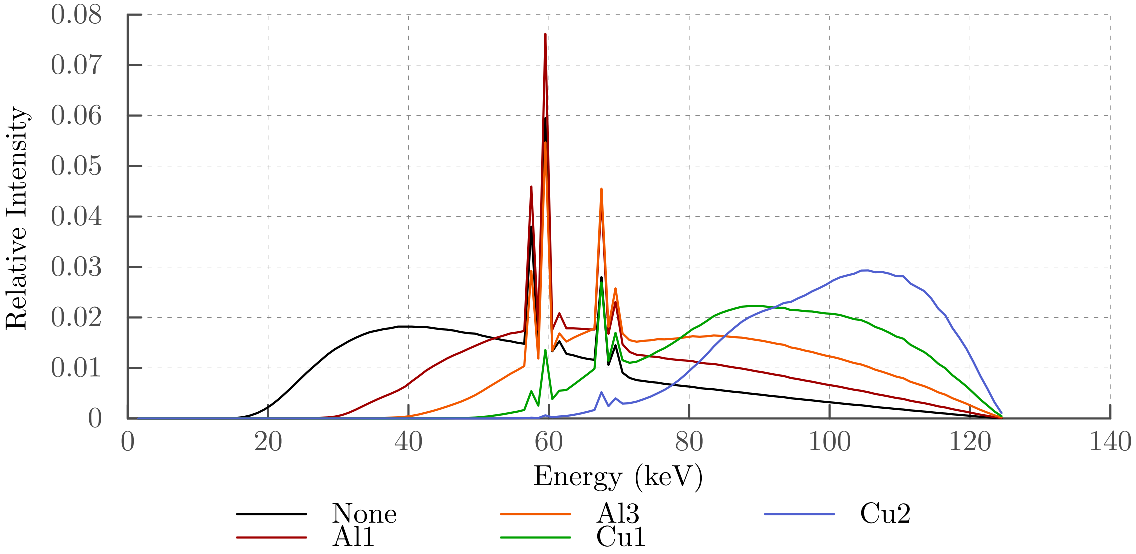

Figure 4.3: The beam spectra normalized by integral area for the various levels of filtration demonstrating the beam hardening caused by the filters

be attributable to scatter. A second order polynomial is fit to each (axial) column in the projection data and then smoothed across the rows. The resulting smooth 2D surface is an estimate of the scatter fluence and is subtracted from the projection data.

Heterogeneous beam quality is caused by the preferential absorption of low energy photons in the filter materials, increasing the average energy of the beam in these regions, as shown in Figure 4.3. The harder, filtered beam will experience lower attenuation for the same tissues, thus the outer region appears darker in the images. Also the transition is sharp in the projection data adding to the strong ring artifact exhibited between the regions. We apply a first-order approximate correction strategy. Representing the different spectra as a single average energy, we can calculate a single correction factor. This correction is simply the ratio of the filtered and unfiltered water attenuation coefficients, which can be measured experimentally by taking projections through a uniform thickness of solid water.

$$P_{filtered}^{corr} = P_{filtered} \times \frac{\int \mu_{unfiltered} dl}{\int \mu_{filtered} dl} \tag{4.3}$$

Due to the energy dependence of the attenuation in the energy range of interest this correction is a good approximation for air, water, muscle or most soft tissue but slightly underestimates the correction for bone.

Results

To test the correction strategy data were taken for both a simple stack of solid water and a pelvic phantom which consisted of the L1 lumbar vertebra inferiorly through mid femur embedded in a uniform Lucite body shaped to resemble a human contour. The results from Cu1 level of filtration are shown in Figure 4.5. The top row is the stack of solid water and the bottom row the pelvic phantom. Both sets have transverse truncation at the left and right extents of the image and were therefore reconstructed with the chord based BPF algorithm with parallel chords aligned with the imaging grid. The left column is uncorrected, the middle column has only the scatter correction applied and the right column has both corrections applied. We can see here that the correction schemes even out the intensity between the inner and outer regions, flatten the cupping artifact in the center of the image and reduce the bright artifact in the transition.

The artifacts in the transition region are due, in part, to misalignment of the blade edges in the I and I_0 data sets in the log-normalization step of the reconstruction. To demonstrate the source of the effect a region of the middle row of an I_0 projection containing a Cu1 filter was extracted. It was then shifted 2 pixels in either direction and the log-normal was calculated with the original data, results shown in Figure 4.4. We see that the misalignment can cause rather substantial errors in the sinogram, either positive or negative.

4.2.3 Image analysis

To evaluate the image quality differences we have looked at noise in the images as well as the contrast to noise ratio (CNR) for both high and low contrast objects. For the noise study a simple stack of solid water was used. In the reconstructed image small square regions were

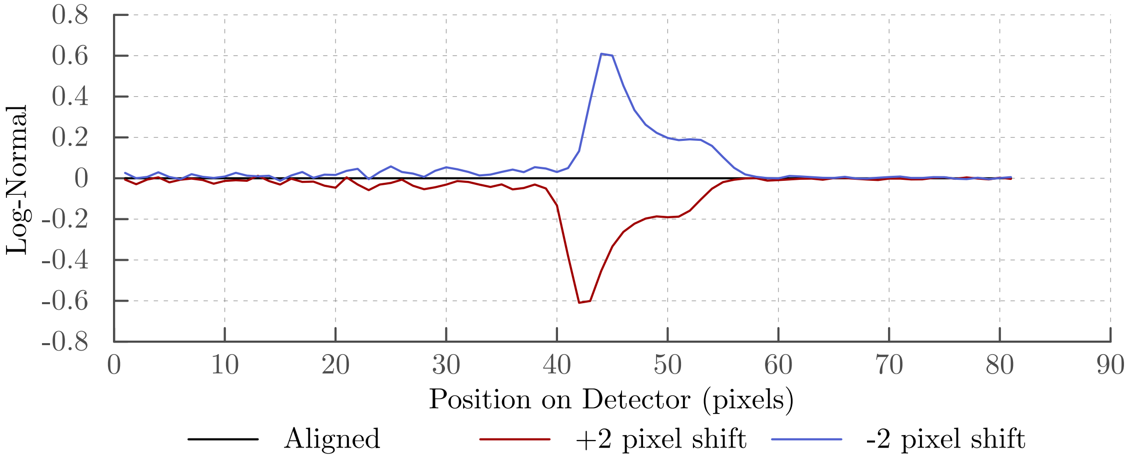

Figure 4.4: The sinogram errors resulting from misalignment of the blade edges in I and I_0 is demonstrated with a section of real projection data containing a copper blade edge and deliberately shifting it 2 pixels in either direction.

	Inner Region	Outer Region
Al1	4.9	6.1
Al3	5.3	9.8
Cu1	5.1	8.3
Cu2	5.0	14.5

Table 4.1: The noise level, measured as the spatial variance of a square region, for various types of filtration.

selected in regions less affected by ring artifacts and avoiding air gaps between the slabs as shown in Figure 4.6. For this study we consider the image noise to be the coefficient of variation over the square regions. The measured noise levels in the inner and outer ROIs are tabulated in table 4.1

For the CNR study the phantom was again assembled from slabs of solid water, however a slab of Lucite was included as a low contrast element and bars of Teflon with air gaps between were included as high contrast elements. Again small square regions were selected in both the Lucite and Teflon materials as well as regions in the solid water to be used as

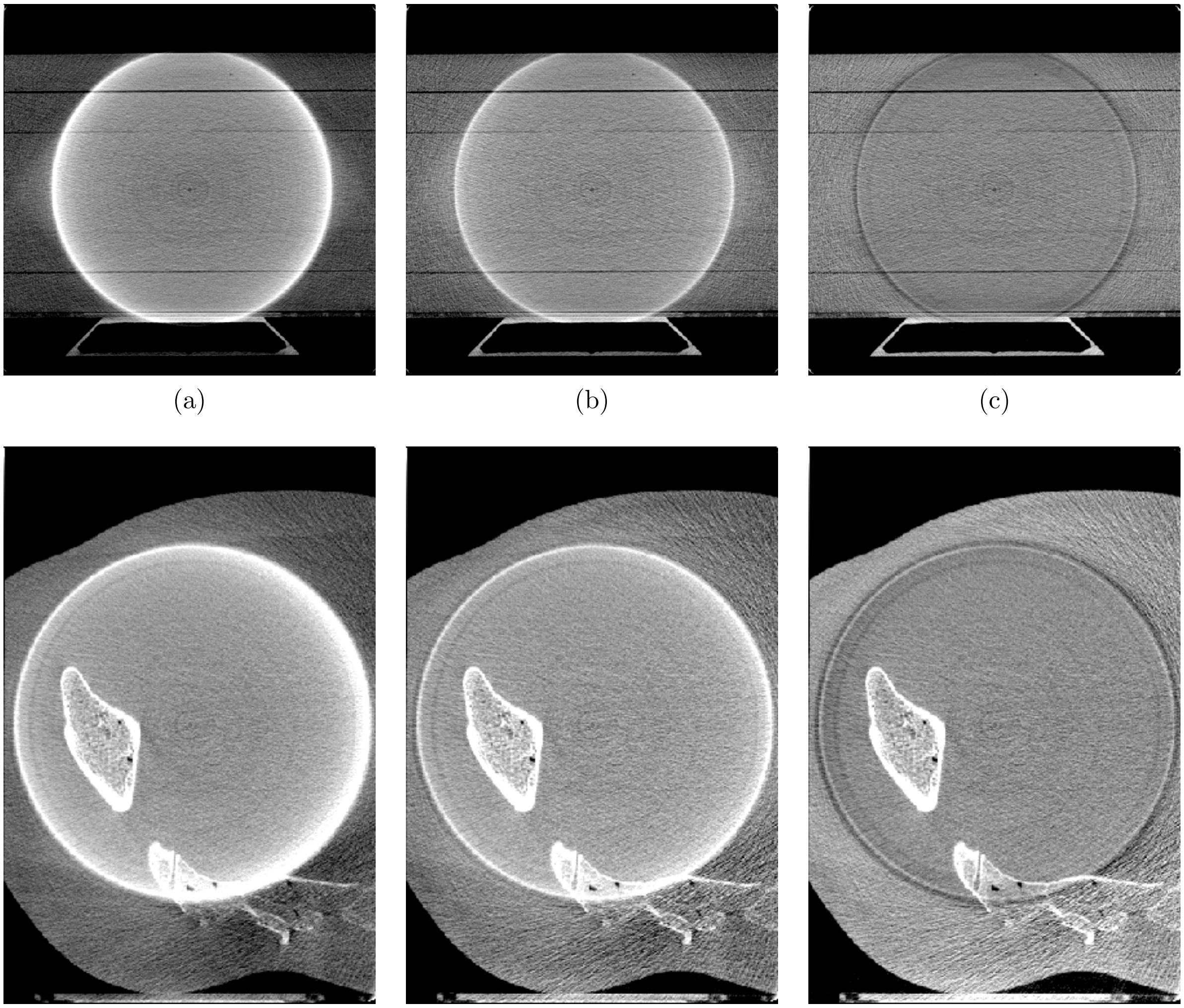

(a) (b) (c)

(d) (e) (f)

Figure 4.5: The results of the data correction techniques. The top row data is from a simple solid water slab phantom and the lower row from the pelvic phantom. Both sets were reconstructed using BPF. The leftmost column is reconstructed from the uncorrected data, the middle column has had only the scatter correction applied and the right column has had both the scatter and beam hardening corrections applied.

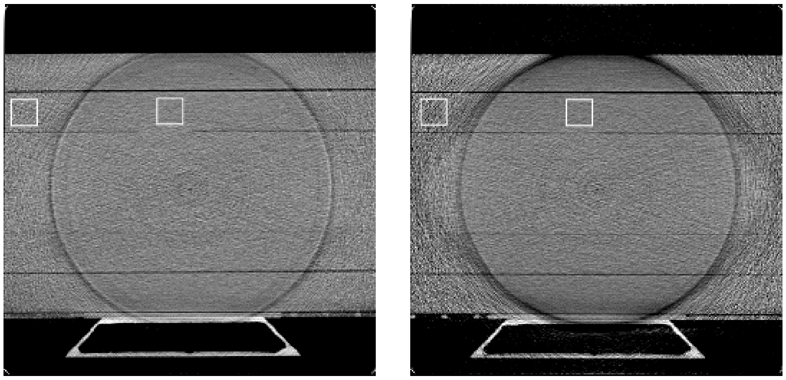

(a) Cu1 (b) Cu2

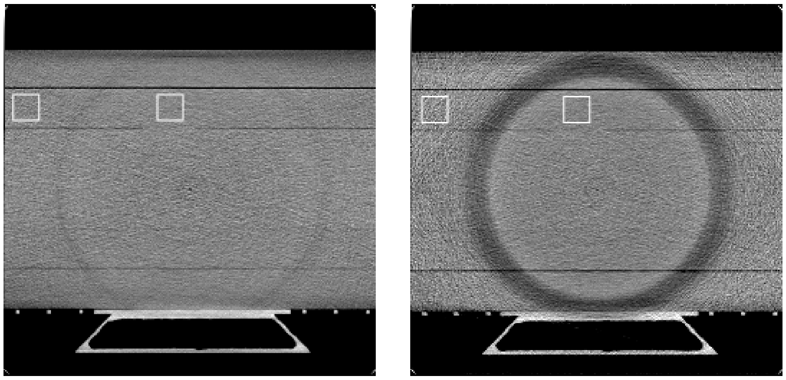

(c) Al1 (d) Al3

Figure 4.6: The noise level measurement for Cu1, Cu2, Al1, and Al3 filtered data sets with the measurement regions indicated.

background as can be seen in Figure 4.7. The CNR was defined as

$$CNR = \frac{\mu_A - \mu_B}{0.5(\sigma_A + \sigma_B)} \tag{4.4}$$

where μ is used to represent the mean and σ the standard deviation. The subscripts A and B denote a contrast element region and a solid water background region respectively. The results are listed in table 4.2

The results of these analyses indicate that the noise level in the inner region is relatively unaffected by the level of filtration while the noise in the outer region increases with greater filtration. Additionally the contrast is relatively well preserved in the filtered region. The calculated CNR generally support this trend. There are a couple of data points that don't

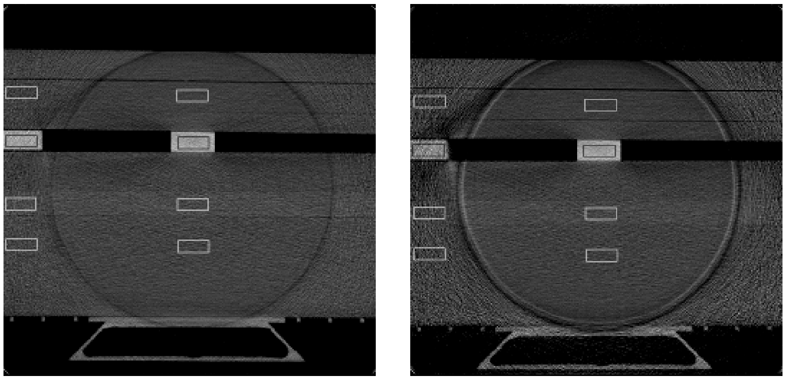

(a) Cu1 (b) Cu2

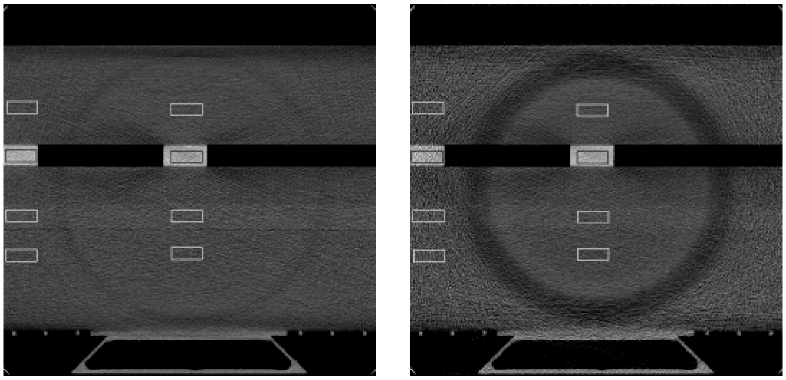

(c) Al1 (d) Al3

Figure 4.7: The contrast to noise ratio measurement for Cu1, Cu2, Al1, and Al3 filtered data sets with the measurement regions indicated.

	Teflon		Lucite	
	Inner	Outer	Inner	Outer
Al1	11.1	8.10	0.701	0.651
Al3	11.8	3.57	0.785	0.197
Cu1	8.53	10.1	0.624	0.775
Cu2	9.46	4.84	0.579	0.214

Table 4.2: CNR measured for high contrast medium (Teflon) and for low contrast medium (Lucite) with respect to solid water in inner and outer ROIs. Contrast and noise are in units of cm^{-1}.

follow this trend, such as the contrast levels for the Al1 filtration, which we believe to have been contaminated by the streak artifacts originating from the dense teflon bars.

4.2.4 Dose Reduction

In order to evaluate the potential dose sparing properties of the technique we first measured the reduction in exposure behind the filters. A parallel plate ionization chamber was used in conjunction with a Keithley dosimeter to measure the exposure in milliroentgen after the various levels of filtration for a fixed kVp, current and time. The results are shown in table 4.3 where we find that for all but the Al1 filter the exposure is reduced by more than 95 %.

	Exposure (mR)	Reduction
No Filter	77.60	—
Al1	14.10	81.8%
Al3	1.74	97.8%
Cu1	2.81	96.4%
Cu2	0.62	99.2%

Table 4.3: Exposure reduction behind the filters studied.

Such a large reduction in the exposure in the filtered regions of the beam is promising for substantial dose sparing for the patient. For a more clinically meaningful indication of dose sparing we used the standard anthropomorphic RANDO man phantom with Gafchromic EBT film placed between two of the slabs at the level of the prostate. The EBT film was calibrated with the 6 MV treatment beam with standard MLC field definitions[119]. We then took cone-beam scans without any filtration, with Cu1 level of filtration and with the radiopaque lead blades to represent the maximum dose reduction from ROI imaging. Three consecutive scans were delivered to the film for each configuration and the analysis was performed on the red channel of the digitized film.

The scan with lead blades is referred to here as a conformal ROI scan. Using film dosimetry gives a full 2D distribution at the chosen slice. The results are presented in

Figure 4.8. The absolute dose distribution from an open field scan is shown in Figure 4.8a. For the the IWROI and conformal ROI scans the dose relative to the open field scan is shown in Figure 4.8b and Figure 4.8c respectively. The ROI is indicated with the white circle. Qualitatively we see the dose distributions are similar with the conformal scan slightly cooler in the periphery. A histogram of the two is included in Figure 4.8d. We see from the 2D distributions that the region of highest dose is in the ROI, as expected. This corresponds to the peak around 70 % in the histogram indicating that even in the unfiltered region there is significant dose sparing due to reduced scatter. We also see the dose to the outer region is greatly reduced with the main peak at about 37 % of the open field scan.

4.2.5 Discussion

In table 4.3 we see that with the exception of Al1 all of the filters provide more than 95 % reduction in the exposure behind the blades, at which point the dose to the patient will be dominated by the unfiltered part of the beam. This was confirmed in Figure 4.8 where the dose difference between Cu1 and radiopaque lead blades was minimal. The Al3 filter, at 4.8 cm, would be difficult to work with for the dynamic collimator and leads to large regions of the image affected by the geometric penumbra. The dose difference between Cu1 and Cu2 will be minimal, while the image quality outside the ROI is much better for Cu1 and it is also less likely to cause streaking artifacts due to photon starvation. Thus, the Cu1 level of filtration was chosen for the remainder of the studies.

4.3 Final Study

4.3.1 Introduction

The final study in this chapter is a more clinically focused continuation of the previous study. As such, the reconstruction algorithm was restricted to FDK, which is the current clinical standard, and a detailed patient and ROI specific dosimetric analysis was carried out. First

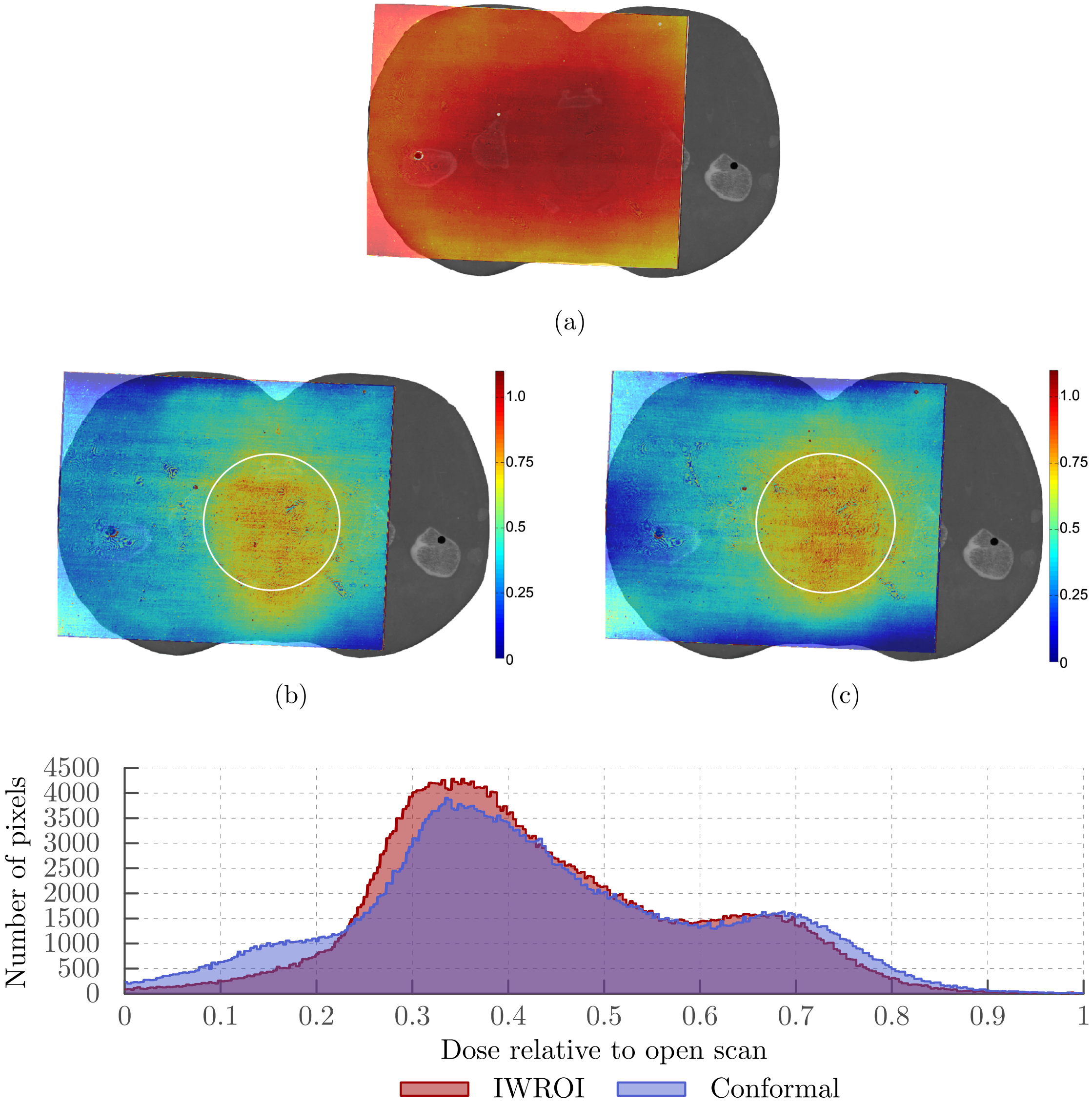

(a)

(b)

(c)

(d)

Figure 4.8: Dose distribution as measured by Gafchromic film is shown overlayed on a photograph representation of the RANDO slice in which it was measured. In (a) the dose distribution from an open field scan is shown. The relative dose from a Cu1 filtered scan and conformal ROI scan are shown in (b) and (c) respectively. The target ROI, corresponding to the prostate region, for both ROI imaging techniques is indicated with the white circle. The histogram of the relative dose distributions of (b) and (c) are shown in (d). The colorbar scale for (a) has been intentionally omitted because there is a weak energy dependence in the response of the film used which may cause some bias in the absolute measurement but does not affect the ratio measurements shown in the other three panels.

	Single Frame	Averaged	Registered and Averaged
Filtered	0.0138	0.0074	0.0048
Unfiltered	0.0075	0.0071	0.0043

Table 4.4: Coefficient of variation for 100 × 100 pixel ROIs in filtered and unfiltered regions of a single projection

we introduce the advances in the data correction process over the preceeding section followed by the reconstruction results for an ROI in the brain region of the RANDO head phantom. Finally, we describe a Monte Carlo model simulation for determining the patient and ROI specific imaging dose distribution. Some of these results were presented at RSNA annual meeting[120].

4.3.2 Updated Data Corrections

We have improved the data correction process to better control noise in the outer ROI and reduce the artifact in the interface region. As indicated in the CT model (4.2) the projection data used for reconstruction is the natural log of the ratio of I_0 to I. This step of the processing is often referred to as the log-normalization step. There are several different methods for obtaining I_0 for this log-normalization step, it can be model based or measurement based. When using measurements often a single frame is taken and applied to each viewl; however we acquire an entire air scan for the I_0 data and match the projections in I and I_0 by view angle. This helps to minimize the misalignment of the two data sets due to gravitational effects. Gravitational sag is known to produce"crescent" artifacts in current clinical systems that use a single view I_0[121] even with the smoother profile of the bowtie filter.

The noise in the projection data is related to the noise in both the I and I_0 measurements. Normally the noise contribution from I_0 is relatively small since the signal is large. However, for the IWROI technique the signal behind the filters is substantially lower so the noise in I_0 is no longer negligible. To control the noise in I_0 all of the projections were registered and

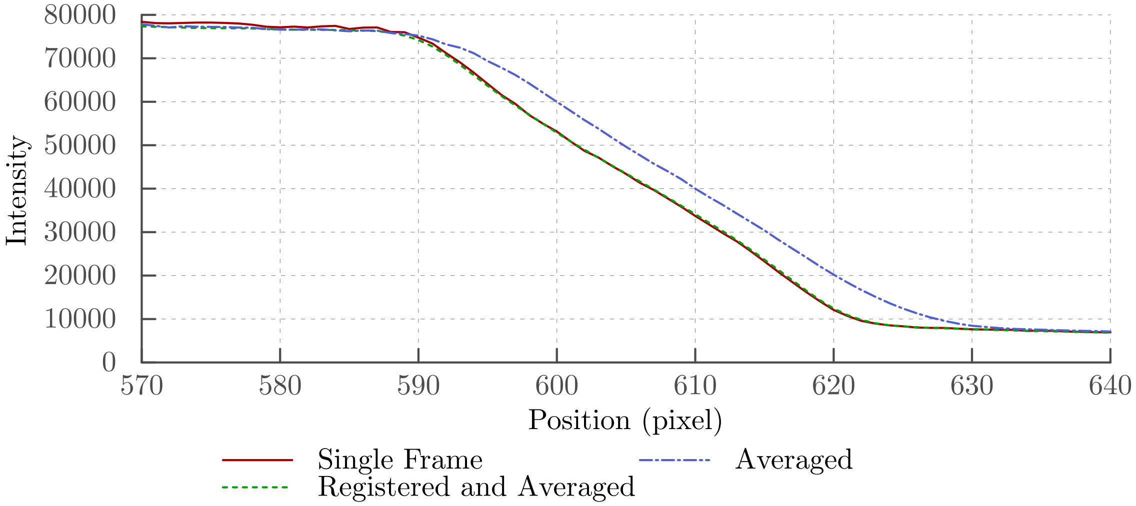

Figure 4.9: Profile across copper blade edge for a single projection frame, with averaging over the whole stack and averaging with registration performed for each projection.

averaged. The reduction of noise is shown in table 4.4 as the coefficient of variation (ratio of standard deviation to the mean) for 100 × 100 pixel regions in the filtered and unfiltered parts of the data. As shown in Figure 4.9 the registration step prevents the broadening of the edge profile due to angular variation of the edge position in the projection image over the course of a scan . The transformation for each view is recorded after the registration, then in the log-normalization step the single, average I_0 frame is transformed back for the appropriate view angle to correct the alignment for gravitational effects.

While using an I_0 measurement that is properly aligned for the view angle takes care of the largest component of the misalignment in the log-normalization there are residual scan-to-scan variations that contribute to the transition region artifacts described in section 4.2.2. To reduce these effects the I_0 frame is registered, with a rigid 1-D translation along the U direction, to the data at each projection angle using a custom cost function.

Algorithm 4.1: Cost Function for Log-Normalization Alignment

```
function EvalShift(testShift)
    $I0_{shifted}$ = SHIFT(I0,testShift)
    sino = LOG($I0_{shifted}$/I)×BeamQuality($I0_{shifted}$)
    sinoRow = $\sum_j sino$                    ▷ sum along V direction (‖ to blade edge)
    return $\sum_{i\in\text{edge region}}|\text{diff}(sinoRow)|$
end function
```

This function performs the log-normalization with the shift to be tested and applies the beam quality correction described in section 4.2.2. The data is then summed along the V direction, which is parallel to the blade edges. Summing in this way enhances the blade edges and reduces anatomical structure. The derivative is taken along this vector, using finite differences, and the absolute value is taken. The cost is then the summed absolute derivative over a region containing the blade edges. This results in a smooth cost function with a well defined minimum, even for a complex structure like the RANDO head phantom, as shown in Figure 4.10. Finding the shift that minimizes this cost results in well aligned I and I_0 data.

In cases where there were remaining ring artifacts in the transition region they could be further reduced by applying an optional local filter to the projection data. When applied, this filter smooths the 15 to 20 pixel region surrounding the blade edge with a 30 pixel wide averaging filter. This can replace strong, bright or dark artifacts in the transition region, identified in section 4.2.2, with a broader, smoother transition.

The scatter correction described in 4.2.2 was not used for the data in this section. At the time of data acquisition the built in, lead blade collimator on the OBI source was not closed enough to provide the data necessary for the scatter fluence estimation described there.

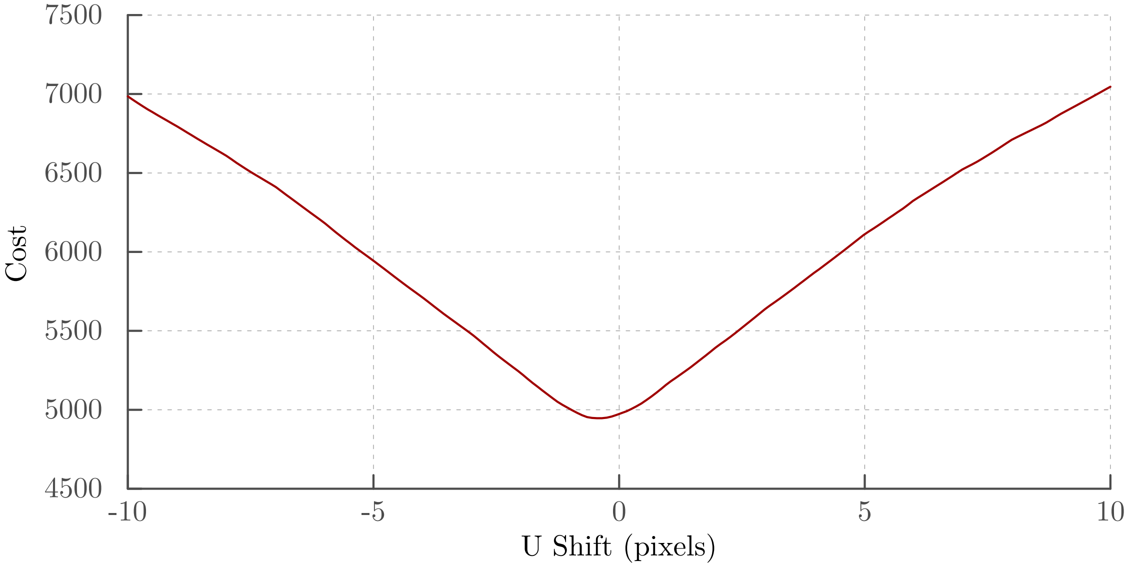

Figure 4.10: Plot of the cost function for a sample view of the RANDO phantom. Optimum shift was found to be −0.367 pixels.

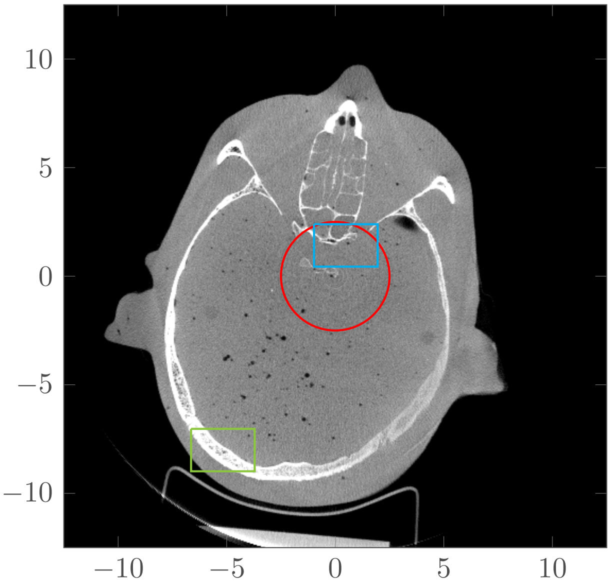

Figure 4.11: The unfiltered FDK reconstruction of the RANDO head phantom with the 5 cm cylindrical ROI shown in red and the regions enlarged in Figure 4.12 and Figure 4.13 shown in cyan and green. Axis scale in centimeters.

4.3.3 Image Reconstruction Results

With statically fixed filters the ROI is constrained to be a cylinder centered on the axis of rotation. For the head phantom the ROI was set to 5 cm in diameter. The location of this ROI is shown as the red circle in Figure 4.11. The FDK reconstruction was performed with 0.488 mm isotropic voxels. The results are shown from two different filtering kernels, the truncated ramp (Ram-Lak) filter with the cut-off set to the Nyquist frequency and a smoother kernel with the cut-off set to 60 % of the Nyquist frequency with a Hann window apodization. These results are shown in Figure 4.12 and Figure 4.13, respectively. Also shown in these figures are enlargements of regions inside the ROI, middle row and cyan box in Figure 4.11, and well outside the ROI, bottom row and green box in Figure 4.11.

Figures 4.12 and 4.13 show the reference image, from unfiltered data in the left column, the uncorrected IWROI data in the middle column and the corrected IWROI data in the right column. We see that the uncorrected image is badly corrupted by the transition between the filtered and unfiltered regions. The area outside the ROI is significantly darker due to the higher average energy of the filtered beam. After the correction process we find the image is substantially improved. The region inside the ROI is very well recovered, both in image intensity as well as the detail shown in the bones of the sphenoid sinuses shown in the enlarged section in the middle row. The region outside the the ROI is also relatively well recovered, though with greater noise and slightly higher intensity indicating an over correction in the data preprocessing. The smoother reconstruction kernel provides better control of the noise in the outer region but also sacrifices detail in the finer bone structures see in the enlarged images. These images achieve the goal of the IWROI imaging - significant dose reduction outside the ROI while providing ample detail for registration in an IGRT application - as discussed in chapter 6, Conclusion.

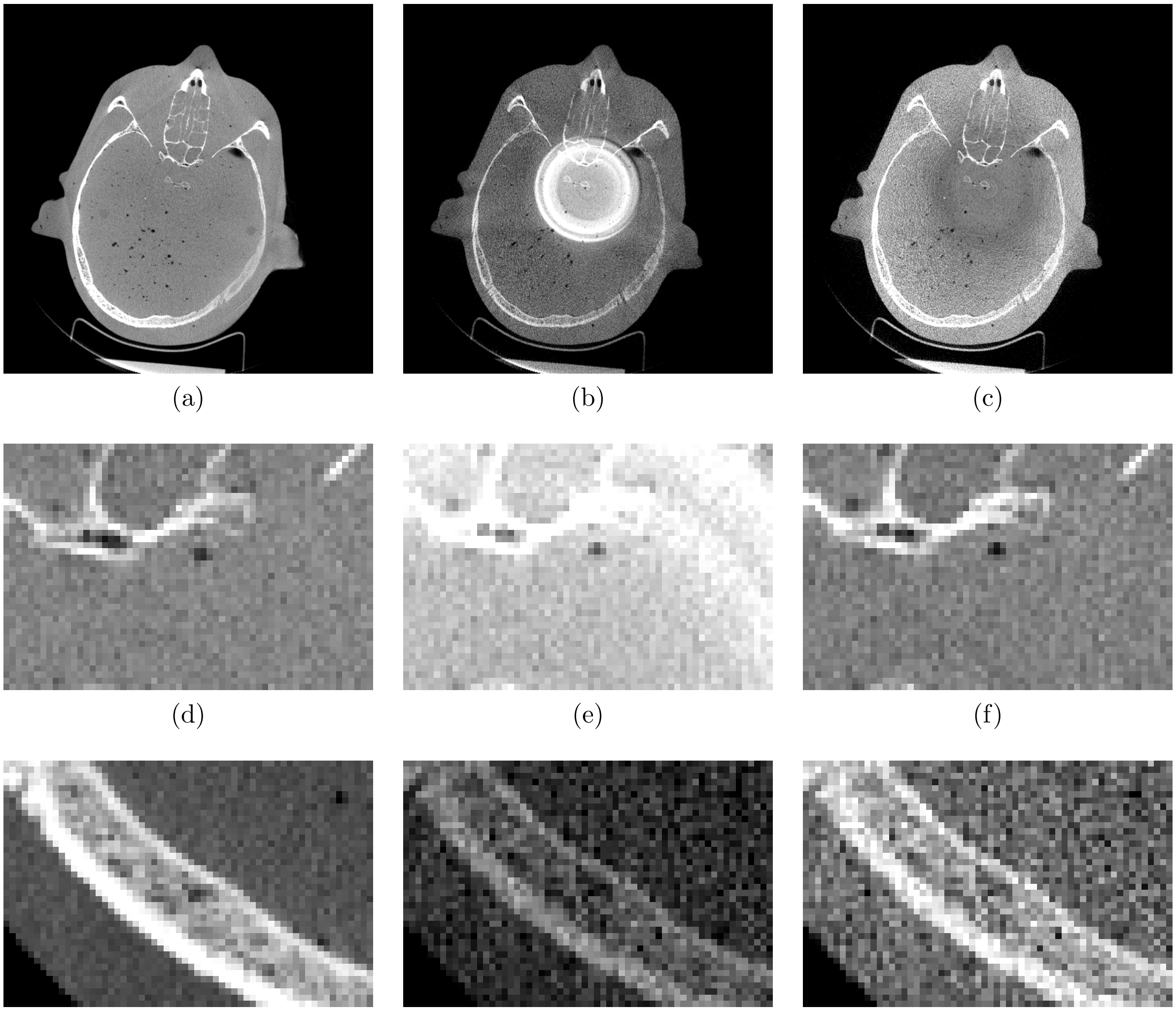

(a) (b) (c)

(d) (e) (f)

(g) (h) (i)

Figure 4.12: The top row, from left to right is a reference image with a standard acquisition, an IWROI acquisition without any corrections applied and the IWROI result with the data corrections applied. The lower row contains a sub-region from with in the ROI from the images above. Display window in top two rows is [0.05,0.3] and [0.1,0.4] in bottom row.

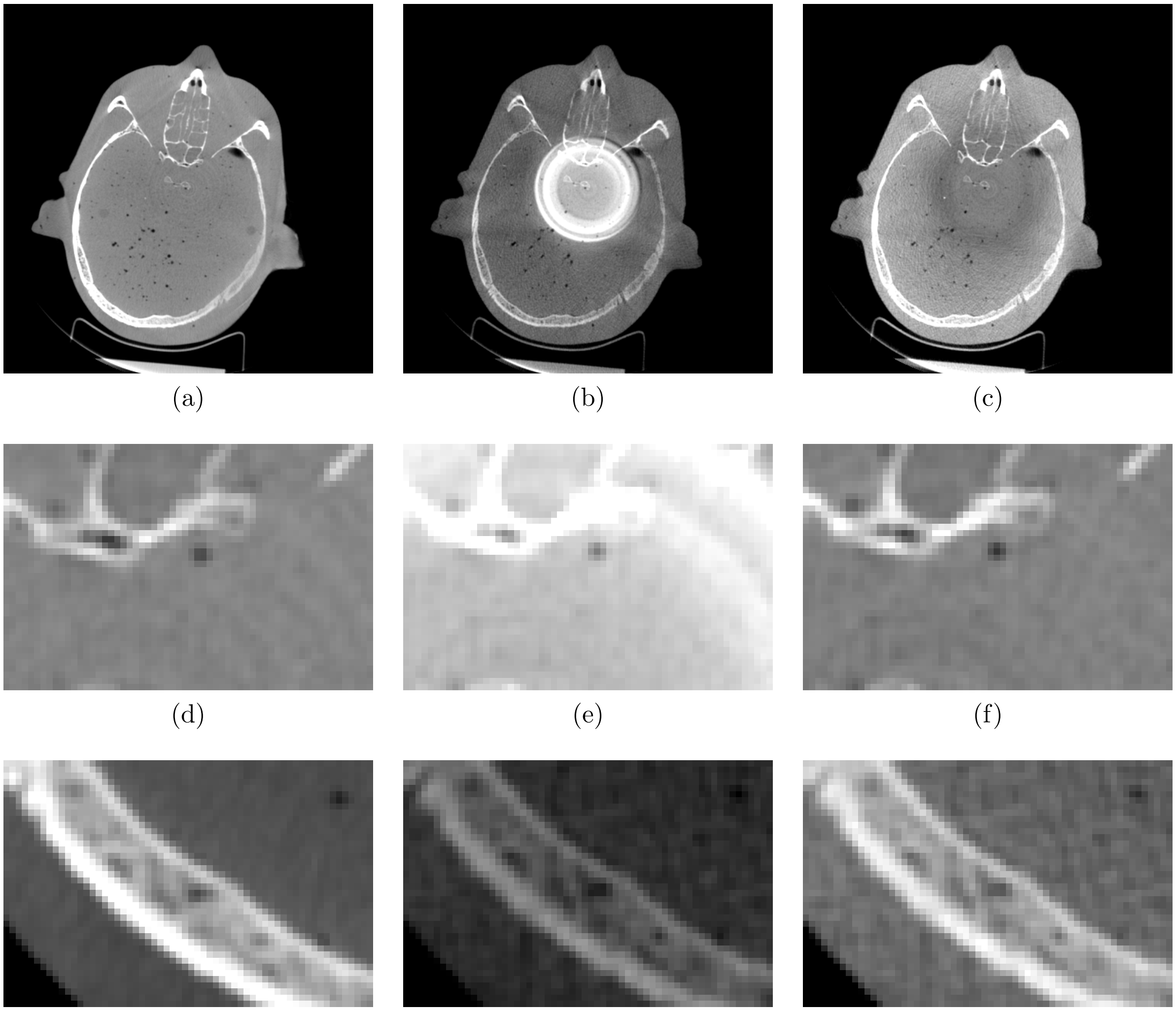

(a) (b) (c)

(d) (e) (f)

(g) (h) (i)

Figure 4.13: Same as Figure 4.12 but with smoother filter kernel, resulting in lower noise in the outer region but loss of detail in the inner. Display window in top two rows is [0.05,0.3] and [0.1,0.4] in bottom row.

4.3.4 Monte Carlo Dose Study

Direct measurement of the dose can be very accurate however it is limited to point (e.g. TLD) or 2D area (e.g. film) measurements at specific places in compatible phantoms. A model based dose calculation method can give full 3D, patient specific dose distributions. Most radiation therapy treatment planning systems use convolution / superposition based algorithms[122–126] which are fast and can be quite accurate for the megavoltage treatment beam where the Compton interaction dominates. However these methods are much less accurate for lower energy photons where the photoelectric interactions become significant[127–129]. The two different beam qualities also increases the complexity and would need to be considered separately in an analytic calculation. Monte Carlo modeling can include detailed interaction and transport models providing accurate results for all x ray energies and can readily accommodate the intensity weighting filters in the beam model. We used the EGSnrc[130] package from the National Research Council of Canada. The kV xray tube was modeled in BEAMnrc[131] from engineering drawings provided by Varian (On-Board Imager and PortalVision Monte Carlo Data Package, Dwg #100040466-03, Rev1, Varian Oncology Systems).

The DOSXYZnrc package can use the BEAMnrc model to calculate the dose in a voxelized phantom definition[132]. The voxelized model is created from the simulation CT dataset using the CTcreate tool distributed with the DOSXYZnrc package. The beam model with a sample photon shower and a surface rendering of the head phantom is shown in Figure 4.15. Greater detail of the Monte Carlo modeling can be found Appendix B, the relevant results will be presented here.

The Monte Carlo model was validated for fixed gantry positions against Gafchromic XR-QA2 film in a homogeneous solid water phantom. To test the CT calculations in heterogeneous media a piece of Gafchromic film was placed between slabs of the RANDO head phantom and cut to shape. The film was analyzed using a multi-channel method based on the work of Micke et al.[133] as described in Appendix B. The results for the IWROI case are shown in Figure 4.14, the film measures dose to water and does not show the increased

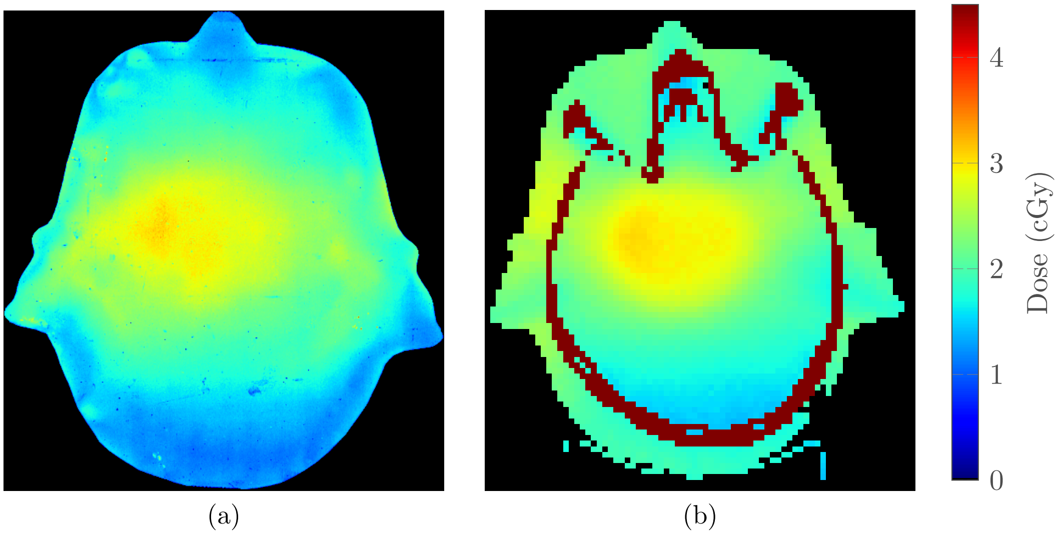

(a) (b)

Figure 4.14: Dose to RANDO head for IWROI scan film measurement (left) and Monte Carlo calculation (right)

absorption in bone but otherwise is in good agreement with the Monte Carlo results. Near the surface the film doses appear a few mGy lower, which may be due to the difficulty of completely eliminating air gaps between the film and the RANDO slabs.

As mentioned above, the Monte Carlo calculations give a full 3D dose distribution specific to the patient. This can be seen in Figure 4.16. The dose distribution is alpha blended with a volume rendering of the CT dataset. The right anterior superior quadrant has been cut away to show the dose concentration in the central ROI.

The absolute dose distribution for the unfiltered, reference scan and the IWROI are shown on the transverse and sagittal planes in Figure 4.17 and the histogram of the full volumes in Figure 4.18. These data show that overall the dose is down substantially. The difference images are shown in Figure 4.19. This shows that the dose, in general, outside the ROI is down around 2.5 cGy but even more importantly the surface dose is down as much as 7 cGy. In Figure 4.20 there are ratio images. The middle row is the ratio of the IWROI to the unfiltered scan. Most of the volume outside the ROI is down to about 35 % of the unfiltered dose. The inner region is also reduced to about 75 % of the unfiltered dose due to the reduced scatter fluence coming from the outer region. The bottom row shows the ratio

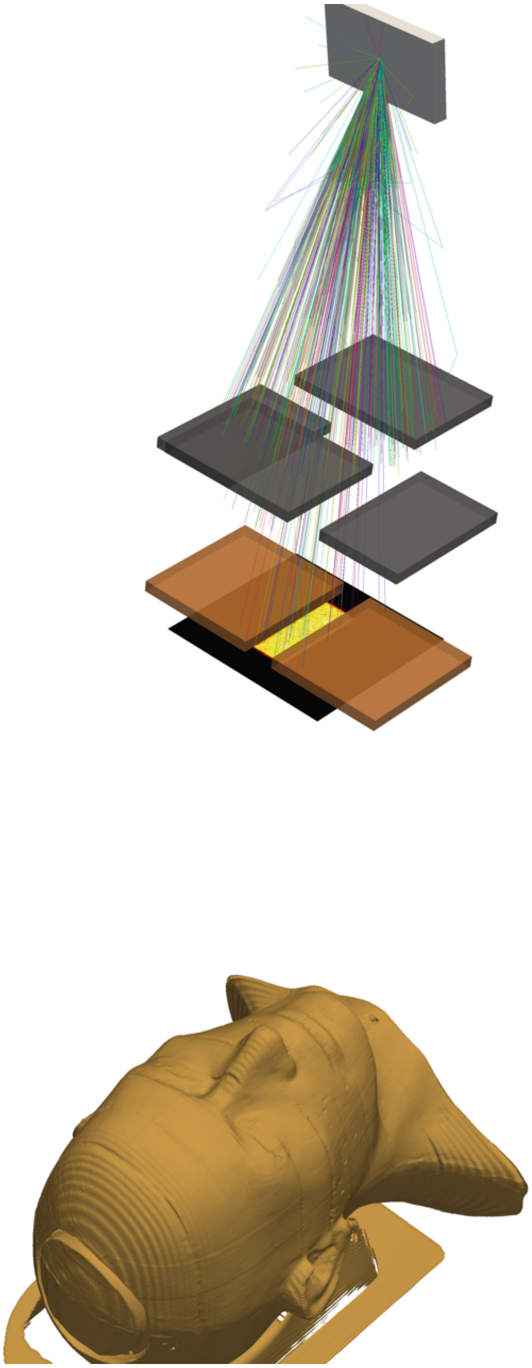

Figure 4.15: The major components of the x ray tube model are shown, the anode (light gray), primary collimators (dark gray) and intensity weighting filters (copper). A simulated photon shower is shown as the multicolored rays. The fluence is scored as phasespace file immediately below the filters, the intensity is shown as the heat map image. The phase space file is then rotated about and propagated into the head phantom model.

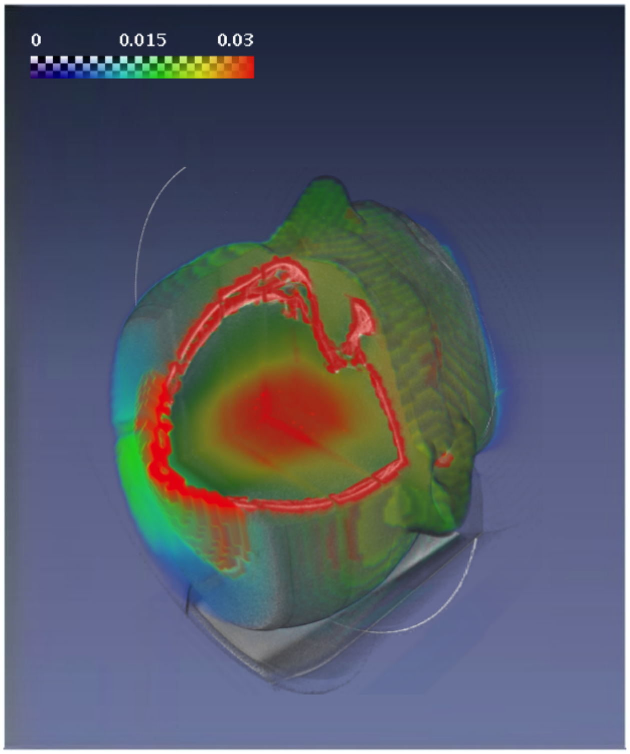

Figure 4.16: 3D dose Monte Carlo dose distribution for RANDO IWROI in Gy

of the dose from the same scan with radiopaque blades to the IWROI dose. The opaque blades represent the limit in the dose savings from intensity weighting and we find that the Cu1 level procides nearly as much dose sparing.

In radiation therapy the dose to nearby healthy organs is a major concern. The 3D dose distribution can be hard to visualize and understand so the information is often presented as a dose-volume histogram[134] (DVH). A cumulative DVH plots the volume of a structure receiving at least a given dose. This a convenient method for comparing dose distributions with regard to their biological impact. For the RANDO phantom we created a “target” structure inside the ROI as well as simulated eyes to represent realistic organs at risk and finally created a structure of the remaining soft tissue volume. The structures and DVH are shown in Figure 4.21. The DVH curves of both filtered results are universally substantially lower than the unfiltered curve.

In the Monte Carlo simulation there are latch variables that can be set to keep track of which photon have undergone scattering events. Then by scoring the fluence at the detector

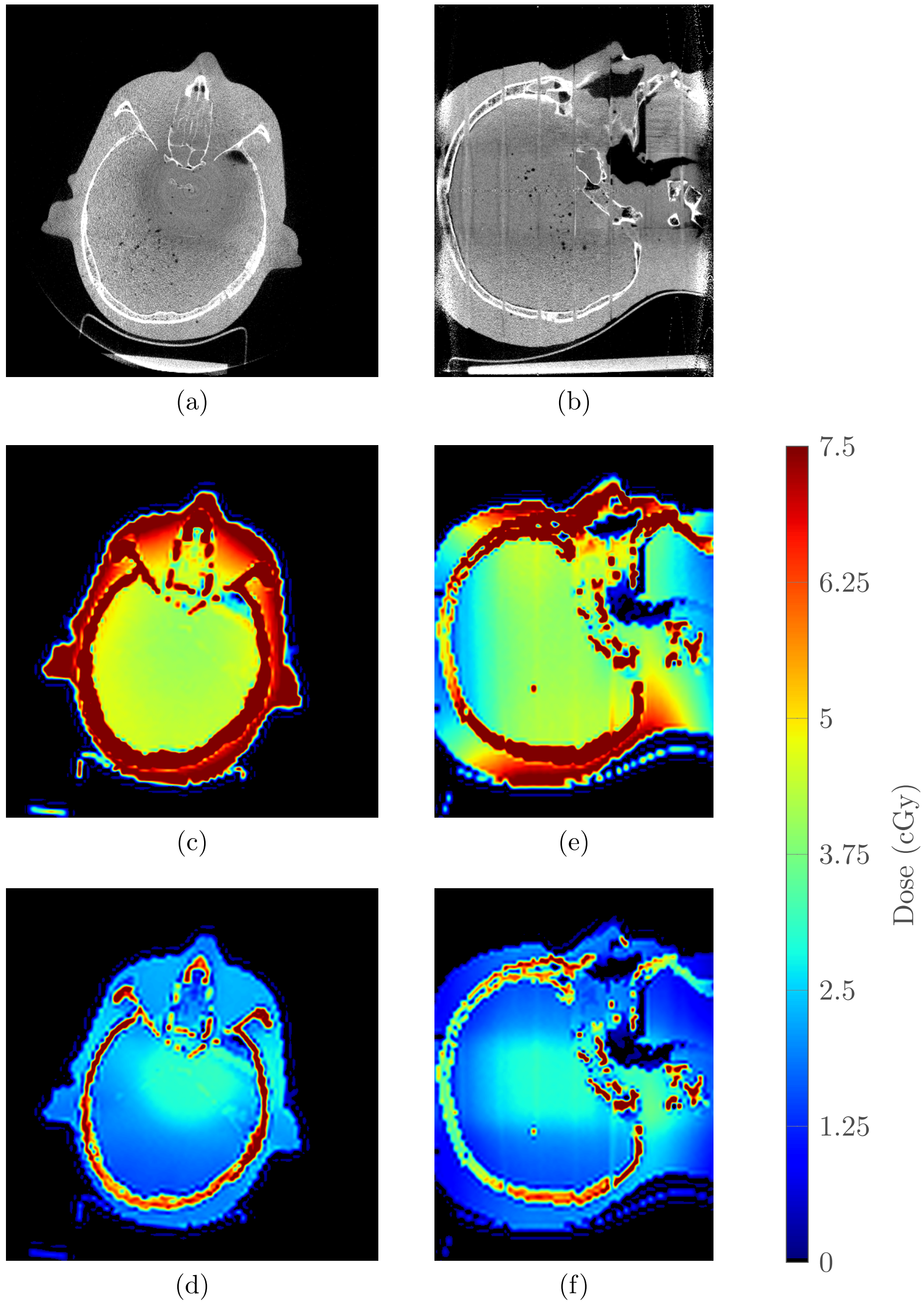

Figure 4.17: The absolute dose from Monte Carlo calculation shown on transverse (left) and sagital (right) planes for unfiltered (middle row) and Cu1 filtered IWROI (bottom row).

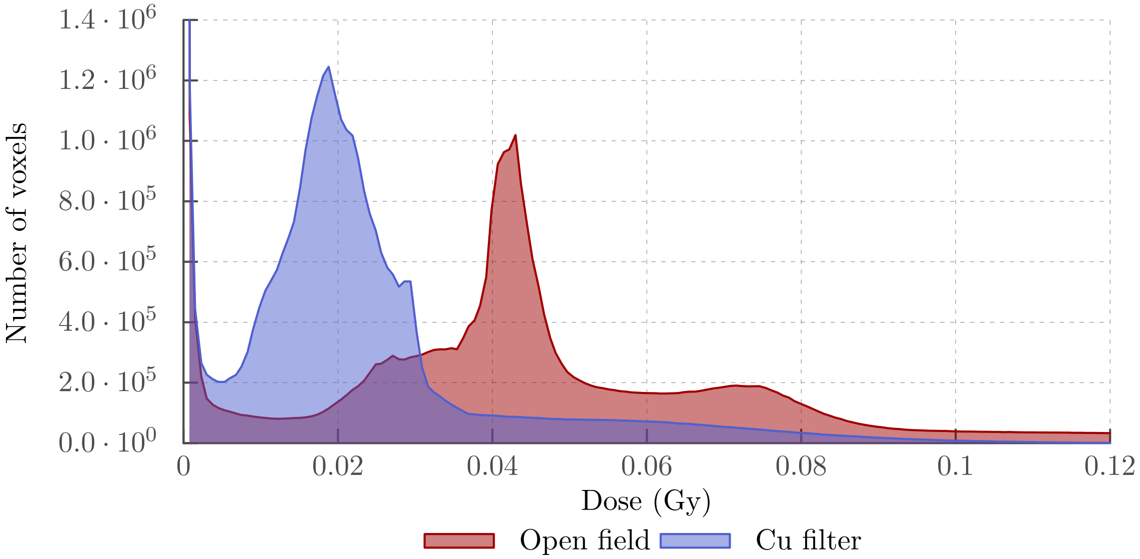

Figure 4.18: Histogram of dose to head phantom from Monte Carlo calculation

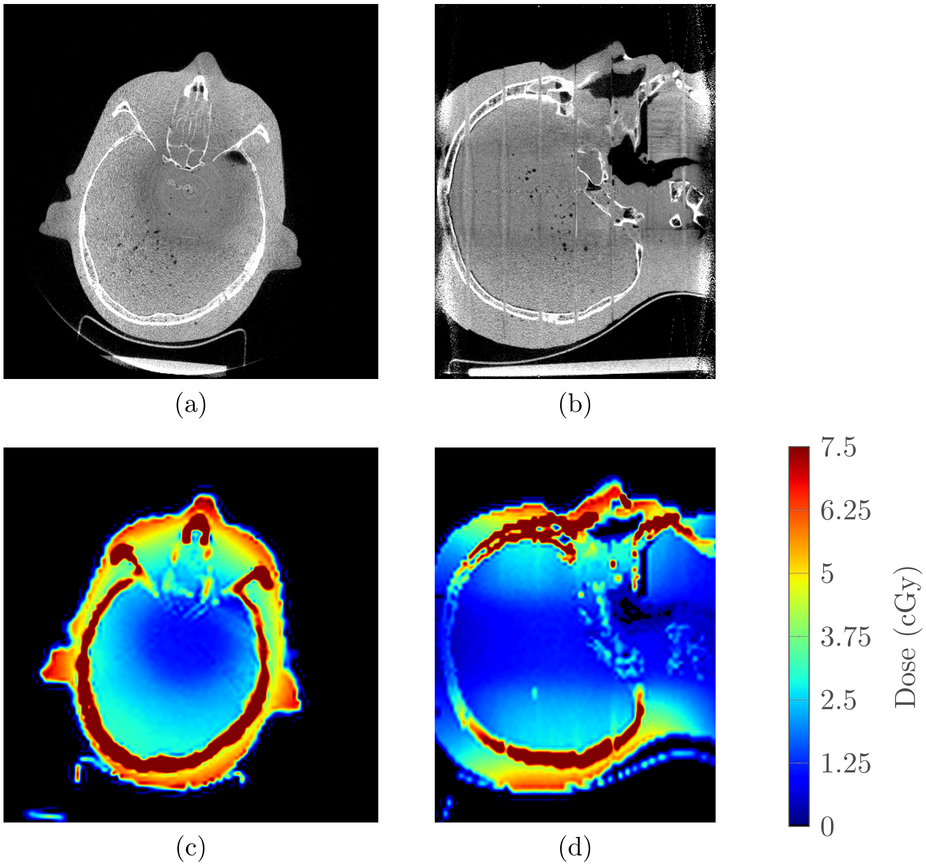

(a) (b) (c) (d)

Figure 4.19: The difference between the reference and IWROI doses shown in Figure 4.17

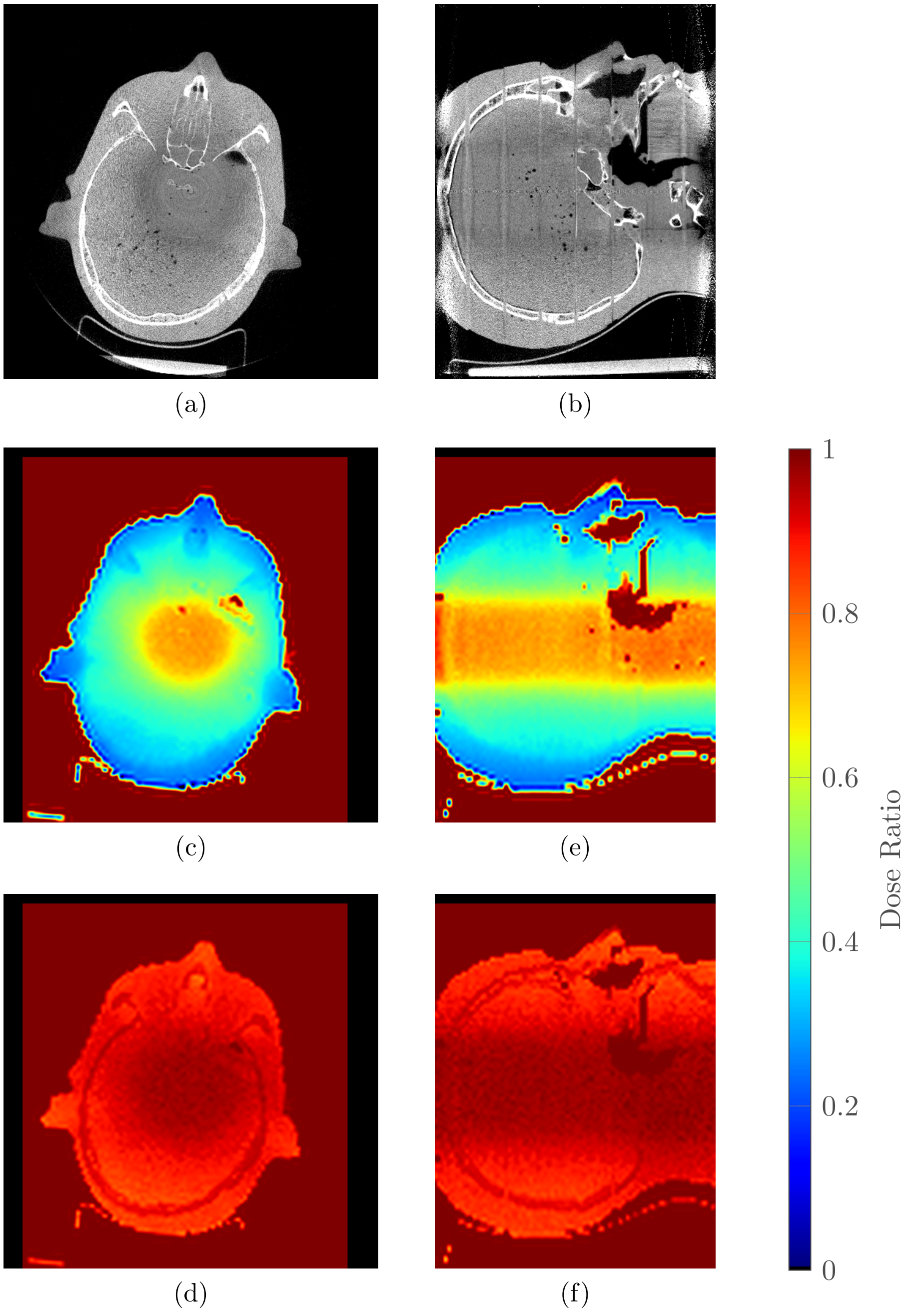

Figure 4.20: In the middle row is the ratio of the IWROI and reference doses shown in Figure 4.17. The bottom row is the ratio of the IWROI dose to a scan with lead blades in place of the copper.

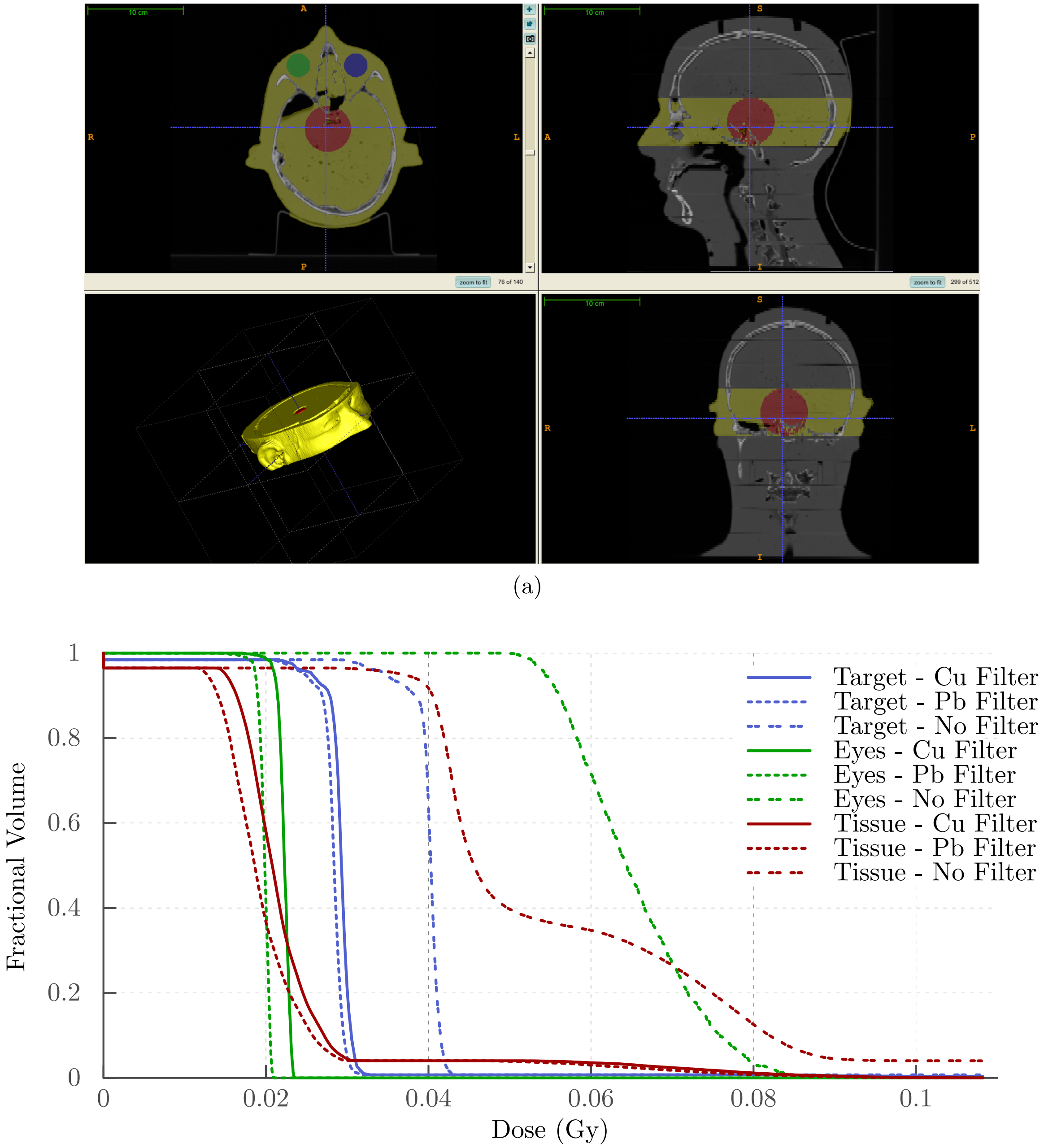

(a)

(b)

Figure 4.21: Top images shows the structures used for the DVH plot, below. The “target” is the red sphere, the “eyes” are the blue and green spheres and the “tissue” is the yellow structure.

Imaging Condition	Scatter to Primary Ratio
Open Field	1.26
5 cm Aperture, Cu blades	0.45
5 cm Aperture, Pb blades	0.33

Table 4.5: The scatter to primary fluence ratio at the detector center for the different filters with a 30 cm × 30 cm × 30 cm solid water cube phantom

plane we can determine which of the photons contributing to a projection image are from scatter and which are primary beam. The scatter to primary ratio (SPR) of the energy fluence is shown in table 4.5 for an open field as well as copper filters and lead blades set at a 5 cm aperture with a 30 cm × 30 cm × 30 cm cube of solid water centered in the field. For the open field the SPR is 126 %, the scattered photons outnumber the primary photons and this is reduced to 45 % for the IWROI and 33 % for the conformal aperture. Siewerdsen and Jaffray provide an analysis of the effects of scatter on image quality in CBCT[23] and show that the inaccuracy in the reconstruction of homogenous, cylindrical phantom where inaccuracy was defined as the deviation in mean reconstruction value from the expected value for 120 % SPR is about −32 % and for 30 % SPR this drops to about 12 %. However, they controlled the scatter magnitude by changing the collimation of the x ray field in the axial direction. Intensity weighting filters change the shape of the scatter field in a different way, the true effect of scatter on image quality for IWROI imaging could be determined by adding a detector model to Monte Carlo simulations above and performing reconstructions with and without the scatter field contribution.

4.4 Summary

To overcome some of the the limitations of the conformal ROI imaging technique presented in the previous chapter the intensity weighted ROI imaging method was developed. Filters were used to spatially vary the intensity of the beam in-place of the opaque blades in the conformal method. In this way, the full data required by standard reconstruction algorithms is acquired.

However, the parts of the projection data measured with the low intensity (filtered) beam have higher noise which propagates back in to the reconstructed image resulting in a high quality image within the ROI and a lower quality, noisy image of the rest of the patient. The lower quality region can still be useful in image guidance, e.g. for alignment to high contrast structures such as bone or the skin surface. In the static approach presented in this chapter the intensity weighting filters were rigidly mounted to the x ray source. This configuration results in a cylindrical ROI aligned on the axis of rotation.

The preliminary studies showed 3 mm of copper filtration to perform the best of the materials and thicknesses considered. This level of filtration was shown to provide nearly all of the dose saving of a conformal technique while still providing sufficient information for reconstruction. In the case of the 5 cm cylindrical ROI in the RANDO head phantom the the dose to most of the volume outside the ROI was down to about 35 % of the unfiltered dose.

CHAPTER 5

DYNAMIC INTENSITY WEIGHTED REGION OF INTEREST IMAGING

5.1 Introduction

As we have seen in chapter 3, some peripheral regions can be reconstructed from the limited data provided by conformal illumination using chord based reconstruction algorithms. These methods can recover the ROI exactly; however they provide no image information outside the ROI. In image-guided radiation therapy, in addition to the often difficult visualization of the target we also need to verify the overall patient setup which usually involves high contrast structures such as skeletal structures and the skin surface away from the target region. In chapter 4 we showed that by using minimally transmitting copper filters instead of opaque lead blades the outer region can also be recovered, albeit with higher noise, with nearly all the dose savings provided by the conformal illumination. However both of these techniques have had limitations in the shape and placements of the ROI. In the conformal case the limitation was defined by the reconstruction algorithm which limited the ROI to peripheral regions that could be filled with untruncated chords. In the static IWROI case in the preceding chapter the ROI was limited to a cylinder coaxial with the imager rotation. In this chapter we combine the dynamic hardware and techniques of chapter 2 and chapter 3 with the IWROI methods of chapter 4 to develop dynamic IWROI (dIWROI) imaging to extend the benefits of IWROI to more flexible regions of interest.

This chapter will first revisit the setup of the collimator for dynamic imaging followed by a validation of the collimator performance in delivery a dynamic trajectory. We then present modifications to the data correction strategies from the IWROI chapter to handle the dynamic imaging case. Finally, image reconstruction and dose reduction results are presented for both peripheral and interior ROIs.

5.1.1 Collimator Setup

The dynamic collimator was setup in the same manner as section 3.4.2. The collimator was mounted in place of the bow-tie filter and the electronics board was stuck to the front face of the gantry with plastic velcro type mounts. The clear plastic covering of the LINAC display is the only area large enough and flat enough for the electronics board. The power supply was placed off to the side. A long power cable was run onto the gantry, the vertical run was mostly in the space beside the EPID with a plastic cable mount on the bottom surface with a loop in the cable to take the strain during rotation here. A cerrobend weight was hung from an IV stand and used with the block and tackle system as a cable retractor. The lead covers were removed from the blades for the IWROI imaging application The inclinometer was zeroed with the gantry in the 0° position, the photograph in Figure 5.1 shows that the angle readout of the LINAC and the collimator continue to agree well when rotated away from 0°.

Static Calibration Validation

The blades were calibrated with the method described in subsection 2.2.4. After the new calibration table was uploaded to the collimator 4 images were taken with both blades commanded to specific positions. The edge positions were identified in the images with the same method as used in the automated calibration. The results are shown in Table 5.1. The average error was 2.75 pixels, which is 0.7 mm at the isocenter, recall that 1 pixel is 0.26 mm at the iso. It appears the error observed in the Blade 2 position in the first trial is an outlier, it is possible that the time delay left between setting the new position and acquiring the radiograph was insufficient for the blade to reach a static position.

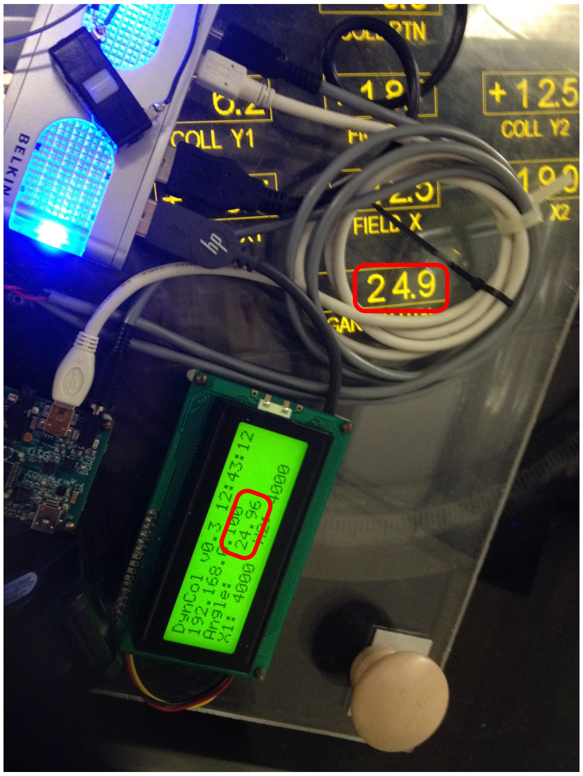

Figure 5.1: The collimator LCD showing the angle measure matches the onboard gantry display. Note values in red boxes, the upper box with the orange lettering is the Gantry readout and shows 24.9 and the green LCD display contains the collimator readout and shows 24.96

Command		Measured		Error	
B1	B2	B1	B2	B1	B2
800	200	802	190	2	10
600	300	599	299	1	1
550	500	553	500	3	0
900	700	905	700	5	0

Error Summary	
Mean	2.75
StdDev	3.37

Table 5.1: Results of the static validation test where B1 and B2 represent the two opposed blades. Values are in pixels in the image.

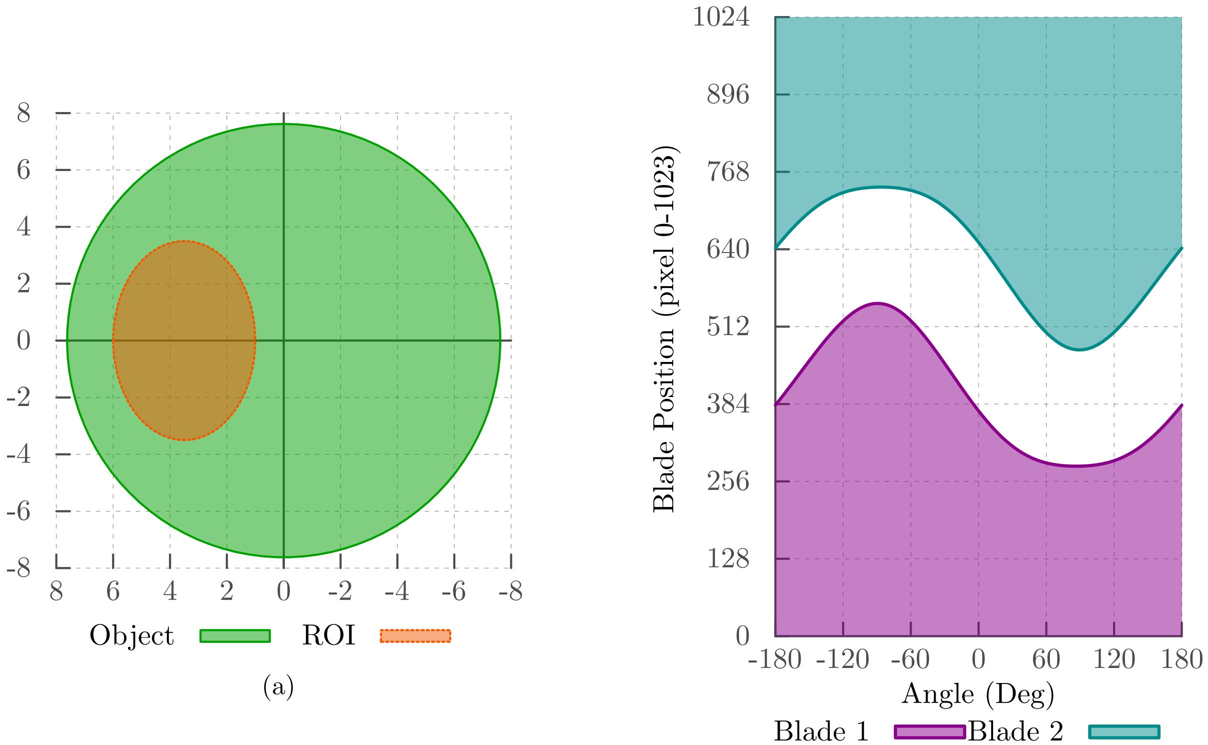

(a)

(b)

Figure 5.2: A 5 cm × 7 cm elliptical ROI located 3.5 cm off the axis of rotation (left) and the corresponding collimator blade trajectory (right)

Dynamic Calibration Validation

The blade position accuracy was also tested in a dynamic setting. The trajectory for a 5 cm × 7 cm elliptical ROI located 3.5 cm off the axis of rotation was generated and uploaded to the collimator. The ROI can be seen in Figure 5.2a and the blade trajectory for that ROI in Figure 5.2b. Three consecutive air scans were taken for this trajectory and the blade edge positions automatically extracted as described previously, this data is plotted in Figure 5.3 and the error data summarized in Table 5.2. The errors in the dynamic case are larger, ranging from -10 to 20 pixels, however in the plots of the errors we see that while the blade position may deviate from the blade trajectory there is remarkable repeatability between scans. If we look at the deviation from the mean observed position, rather than the planned position, as shown in Figure 5.4 we find that the scan to scan variation is less than ± 1.75

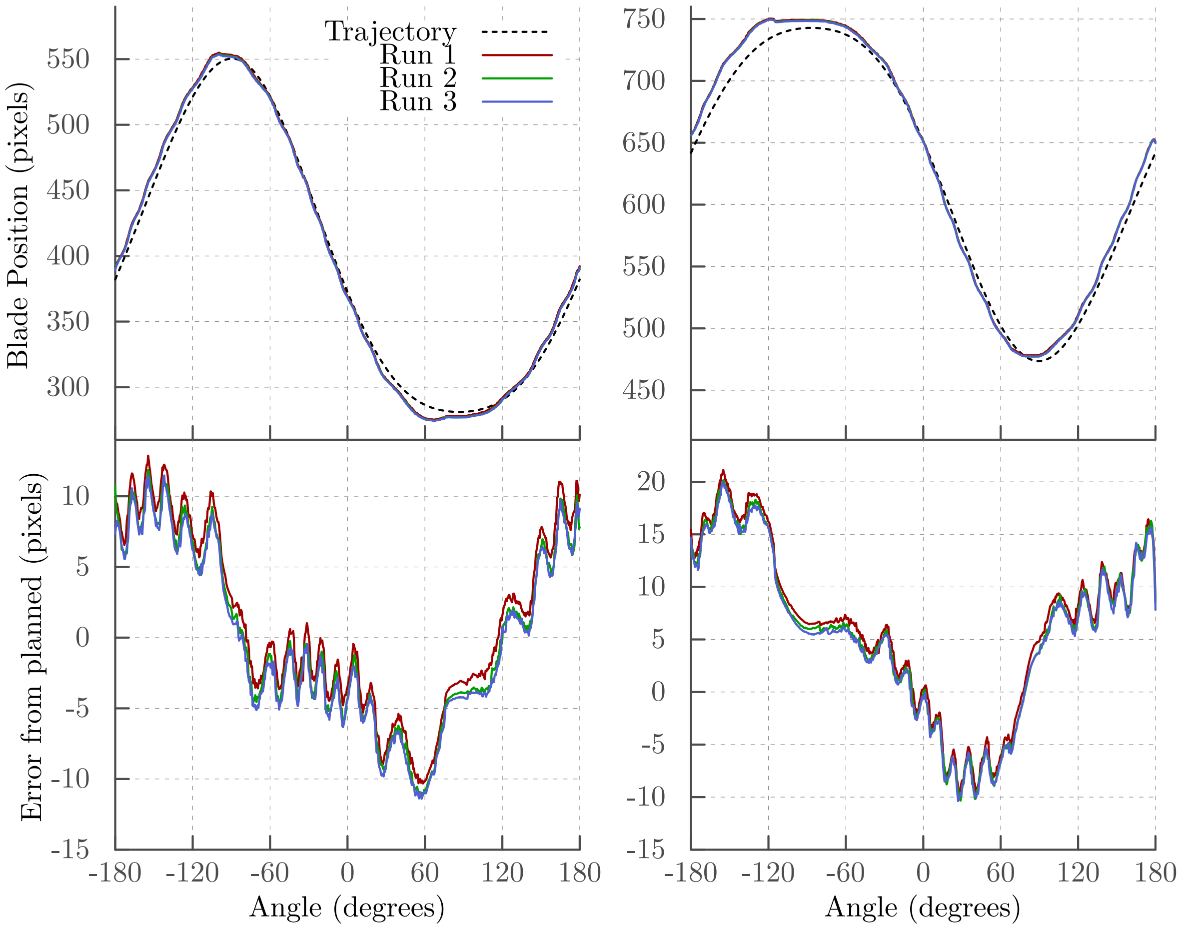

Figure 5.3: Blade trajectory for the above ROI

pixels.

The system is more precise than accurate. Accurate dynamic motion control is difficult and depends on many factors, such as the motor capabilities, the electronics and PID tuning parameters. Additionally, for the study here the changing system geometry complicates things further. The blade calibration is performed at a single, stationary gantry angle, however as the gantry rotates the position and orientation of the collimator mounted to the kV source housing changes relative to the detector, mostly due to gravitational sag. Even the position of physically fixed filters project to different pixel positions over the course of a scan, this is why we do the registration step in the log-normalization for the static intensity

	Blade1		Blade2	
Scan	Mean(Abs(error))	Std(Error)	Mean(Abs(error))	Std(Error)
1	5.342	6.240	8.586	7.762
2	5.326	6.130	8.220	7.749
3	5.367	6.126	8.062	7.710

Table 5.2: The error in blade position for the dynamic trajectory given in pixels on the image

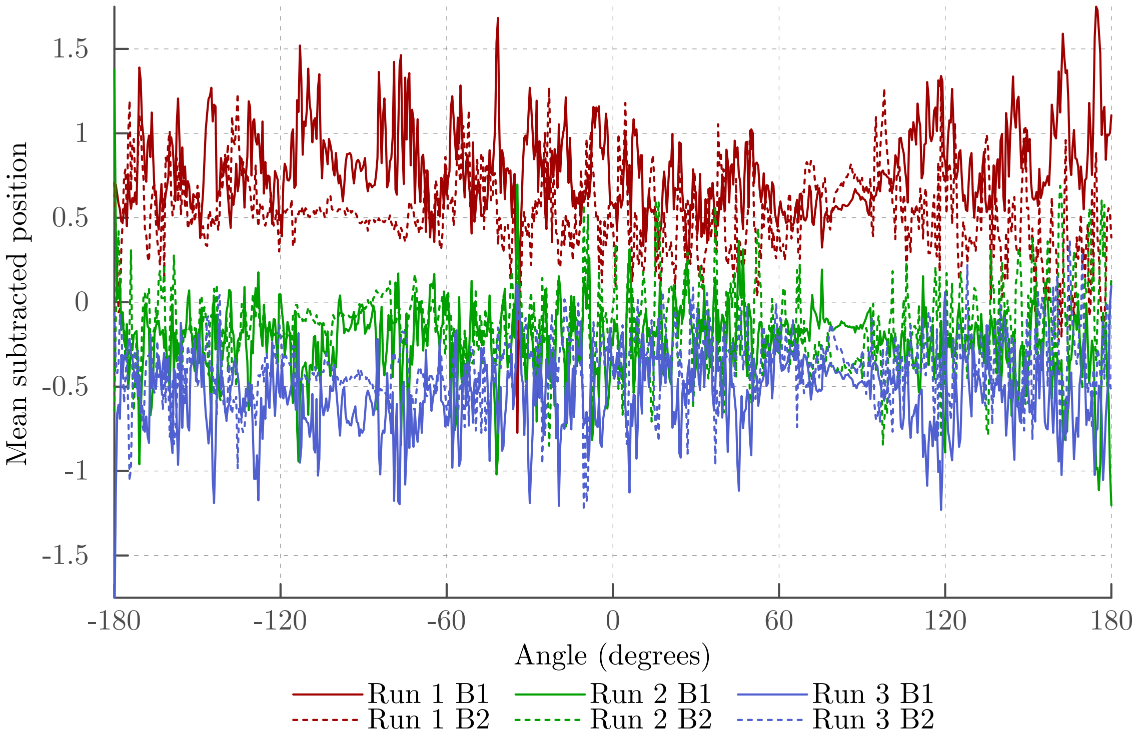

Figure 5.4: The mean subtracted blade positions demonstrating good scan to scan repeatability

weighting. The precision comes from the fact that most of the issues are repeatable. The gantry components sag in nearly the same way in every rotation. The inaccuracies from the motor dynamics and control system are also repeatable, given the same input (gantry angle vs time) the collimator system produces the same output (blade position vs time). In this situation precision is more important than accuracy, since the reconstruction requires data from two scans and deviations between those scans lead to artifacts. Also, in principle, with some care, the inaccuracies can be calibrated out with steps like an angular dependent blade calibration. The scan to scan variabilities arise from random elements, such as vibrations in the machine, that are very difficult to control or correct for but are thankfully relatively small in magnitude.

5.1.2 Data corrections

The data corrections that were developed for static IWROI imaging were further developed and modified to handle the new challenges of the dynamically changing intensity weighting.

Log-Normalization

In subsection 4.3.2 a method for co-registering and averaging the I_0 scan data to reduce transition region artifacts and provide noise control was introduced. That method cannot be used for the dynamic IWROI data as the filter positions vary frame by frame in the dynamic case. Alignment of the I and I_0 data begins by selecting the closest angular match. From the scan to scan variability we saw in the previous section we can expect this to get the filter edges aligned to within a few pixels. To take care of the remaining misalignment the I_0 frame is split in the middle of the aperture and each half is independently registered to the I frame using the method described in subsection 4.3.2. Without the benefits of averaging over an entire scan, noise control in I_0 is provided by optionally performing an anisotropic diffusion denoising on each I_0 frame prior to the log normalization. Anisotropic diffusion is a non-linear denoising method that typically provides better edge preservation than traditional smoothing filters.

Beam Quality and Scatter Training

In section 4.2.2 an analytic correction for the differing beam energies in the filtered and unfiltered part of the projections was described. The value of that correction was based on a measurement in solid water slabs however we found in that in some cases manually tweaking this value resulted in better image quality so a method for automatically learning an ideal value from an experimental data set of a simple object was developed as described below. Additionally the scatter field was approximated as a convolution of the I projection data with a Gaussian kernel, the magnitude and width of which were also fit in the training process.

A homogeneous solid plastic cylinder was scanned with the off center, elliptical ROI of Figure 5.2a for which the ideal projections could be modeled analytically. The parameters for the beam quality and scatter corrections were optimized to minimize the difference between the IWROI measured projection data and the modeled data. These values were then used for correcting the dIWROI data presented in this chapter.

Edge Smoothing

An optional correction for removing rings in the transition region using an averaging filter to smooth the area of the projection image in the vicinity of the edge was described in subsection 4.3.2. For the dynamic data this step has been replaced with a different method for smoothing out sharp edges in the sinogram after the log-normalization step which can be caused by misalignment of the blade edges between the I and I_0 data sets as described in section 4.2.2. The region in the sinogram ±10 pixels from the identified edge position was replaced with a spline fit spanning the gap. This reduced sharp artifacts in the transition from inside to outside the ROI in the reconstructed image and it typically results in a less pronounced blurring effect than the averaging filter used in the static IWROI reconstruction.

However the spline fit can occasionally become unstable and exacerbate artifacts. The results in this chapter will be shown both with and without the spline smoothing applied.

5.2 Results

The results are divided into two sections. The first explores dynamic IWROI imaging as an alternative to the conformal ROI imaging presented in chapter 3 using the same phantoms and ROIs but with copper filtration instead of opaque lead blades. The second section addresses the fully-encapsulated, interior ROI. All reconstructions were performed with the FDK algorithm and results shown use a smooth kernel with the cut-off frequency set to 60 % of the Nyquist frequency with a Hann window apodization.

5.2.1 Peripheral ROI

The experiments of section 3.4 were repeated with the same phantoms, in the same position with the same ROI and blade trajectories only here the lead covers were removed from the blades leaving just 3 mm of copper.

Image Reconstruction

The results from the RANDO phantom are shown in Figure 5.5. The conformal imaging result is shown again in (b) for comparison. The ROI is generally well recovered but with artifacts at the edges. The dIWROI results are shown in the bottom row, with the spline edge smoothing applied in (d) and not in (c). In this case the spline smoothing reduces the severity of the dark streak at the long edge interface. The intensity is a bit higher in the dIWROI images due to the additional scatter correction which subtracts the estimated scatter fluence from the projection data, effectively increasing the estimate of the attenuation. Qualitatively the ROI is just as well recovered in the dIWROI as the conformal image with the additional benefit of a reasonably good image of the rest of the head. In the outer region

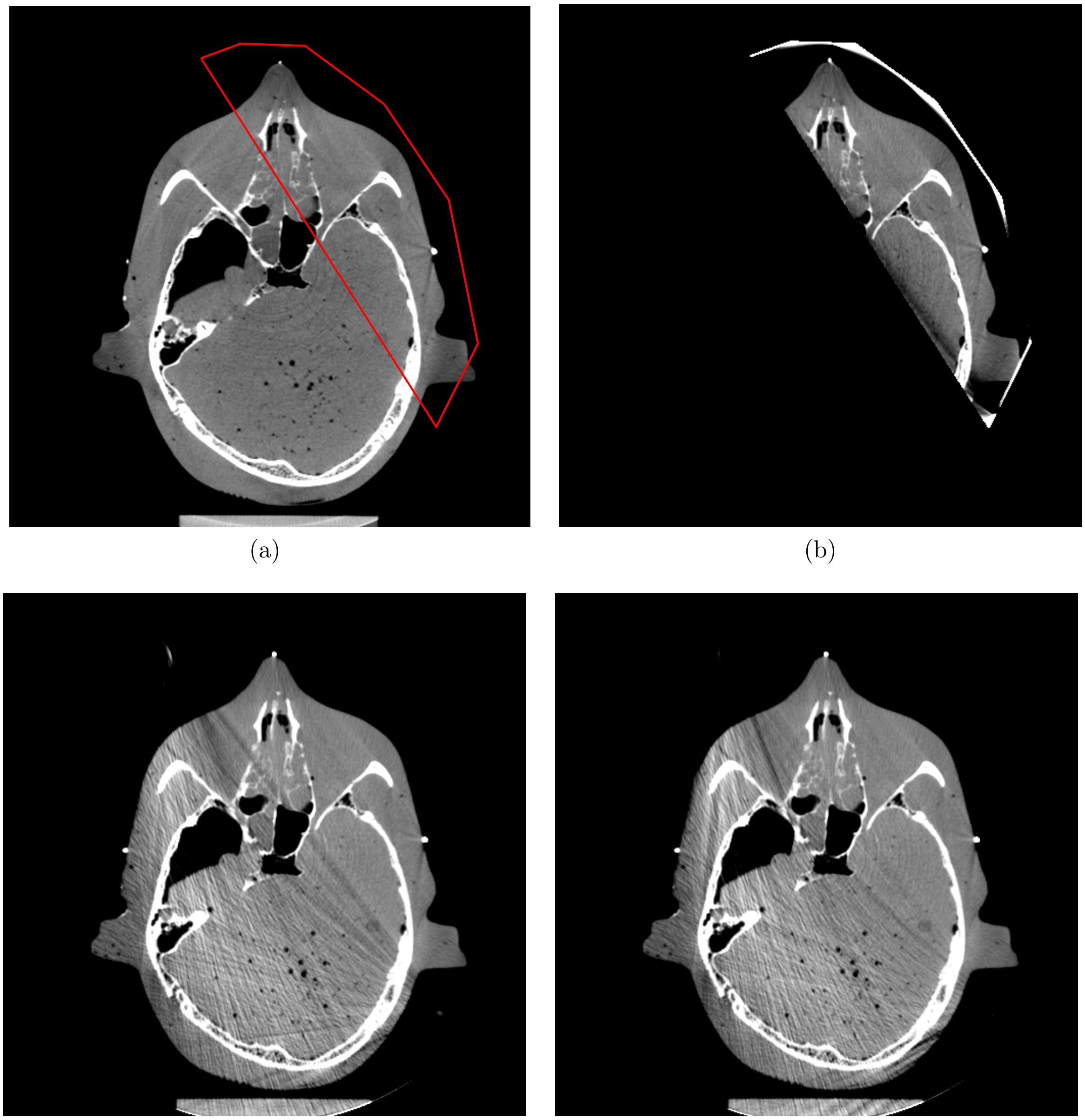
(a) (b) (c) (d)

Figure 5.5: Top left, the unfiltered, reference reconstruction with the ROI contour overlaid in red. Top right, the BPF reconstruction of the conformal dataset (Pb blades). Bottom row, the FDK reconstruction of the dynamic IWROI (Cu Blades) with (right) and without (left) the spline smoothing applied. Display window [0.1,0.3]

the noise is higher and there are some pronounced streak artifacts but it contains sufficient information for patient alignment.

Figure 5.6 contains the results for the chicken phantom, organized in the same way. The results are also very similar. The ROI again is just as well recovered in the dIWROI image. Enlargements of regions containing soft tissue boundaries are shown in Figure 5.7. Again the dIWROI images are brighter than the top images due to the scatter correction. In this data set there is more of an intensity mismatch between the ROI and the outer region suggesting that the correction parameters derived from the cylindrical phantom are less suitable for the chicken than they were for RANDO. Again the spline smoothing provides some benefit, most noticeable in the reduction of the star artifact at the center of the anterior surface. This phantom, unlike RANDO, also has low contrast, soft tissue structures and we see that the muscle interfaces in the thigh within the ROI are well preserved but nearly obscured in the contralateral side. However the high contrast structures would still provide useful information for alignment.

Dose Reduction

The dose reduction of the dIWROI imaging was quantified using the Monte Carlo framework described in subsection 4.3.4 and Appendix B. This method provides accurate, patient and ROI specific 3D dose distributions. The dose distribution is shown in Figure 5.8 and as a ratio of the unfiltered scan in Figure 5.9. Most of the imaging dose is now deposited in the target and from the histogram we see that the dose in the rest of the head has dropped into the range of 55 % to 80 % of the openfield dose. While this is a substantial dose sparing it is much less than that seen in the static case in Figure 4.20, due to the relative size of the ROI. The dose from the IWROI is almost entirely from the unfiltered portion of the beam so the shape, size and position of the ROI strongly influence the dose sparing potential. This is a factor that should be considered during the acquisition planning step.

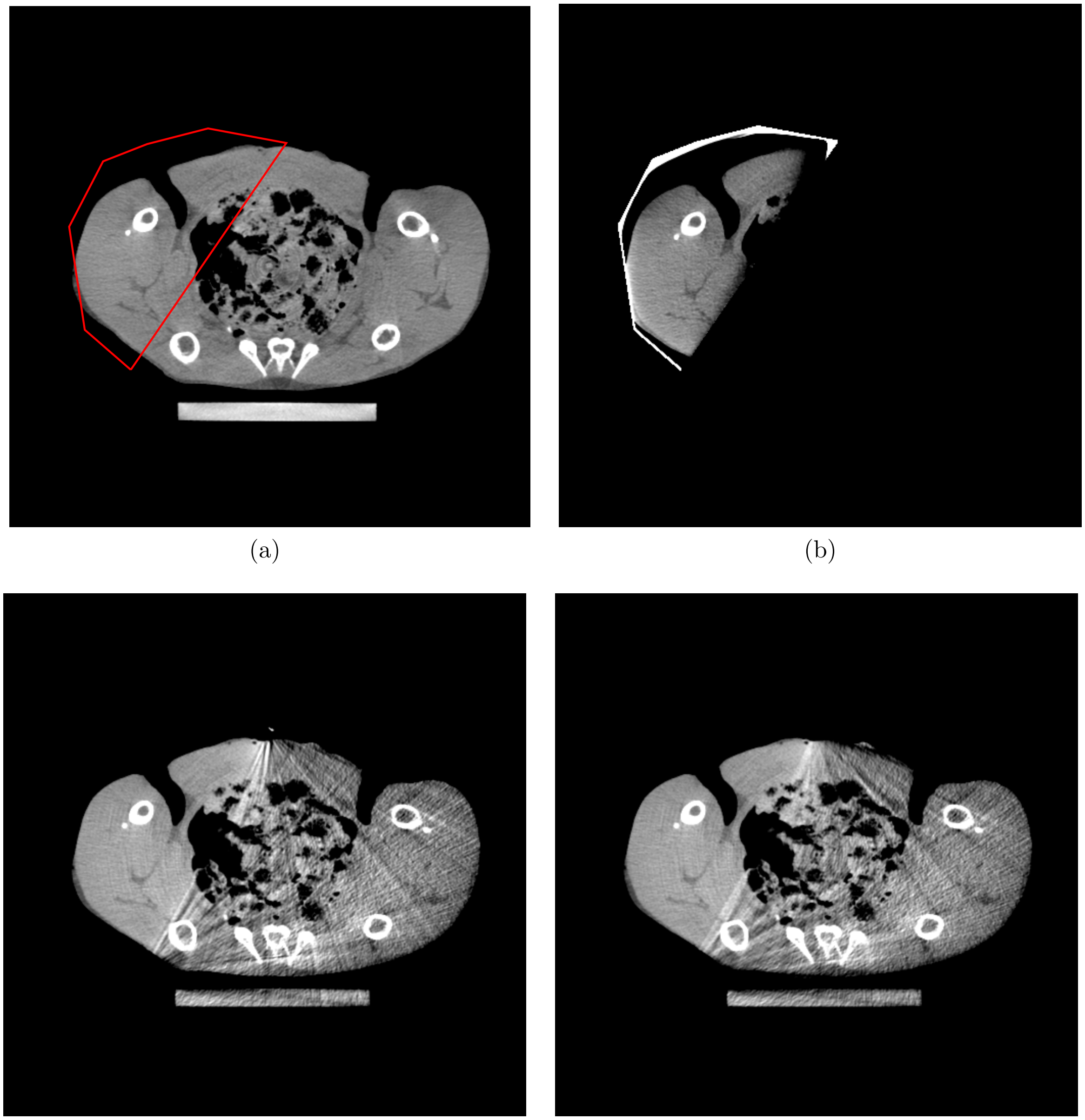

(a) (b)

(c) (d)

Figure 5.6: Top left, the unfiltered, refrence reconstruction with the ROI contour overlaid in red. Top right, the BPF reconstruction of the conformal dataset (Pb blades). Bottom row, the FDK reconstruction of the dynamic IWROI (Cu Blades) with (right) and without (left) the spline smoothing applied. Display window [0.15,0.25]

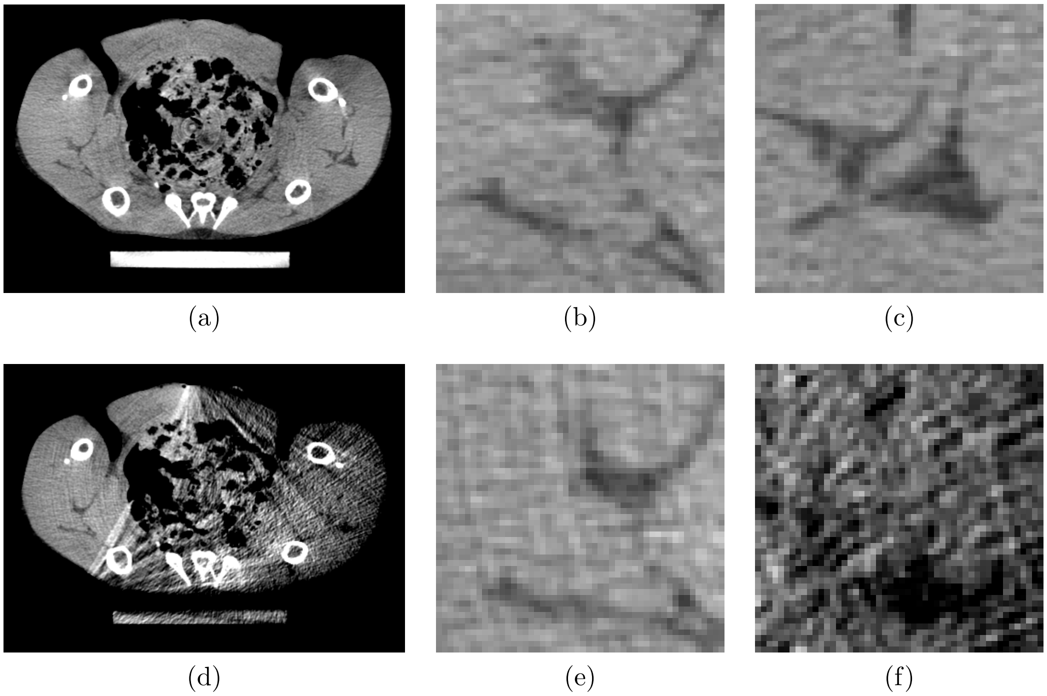
(a) (b) (c)

(d) (e) (f)

Figure 5.7: The chicken phantom, peripheral ROI, reference reconstruction in the top row and dIWROI reconstruction on the bottom. The right two columns are enlargements of 24.4 mm × 24.4 mm regions from within the ROI (middle) and outside (far right). The regions were chosen to show the low contrast muscle boundaries in the thighs. Display window [0.17, 0.23] left and [0.18, 0.24] right.

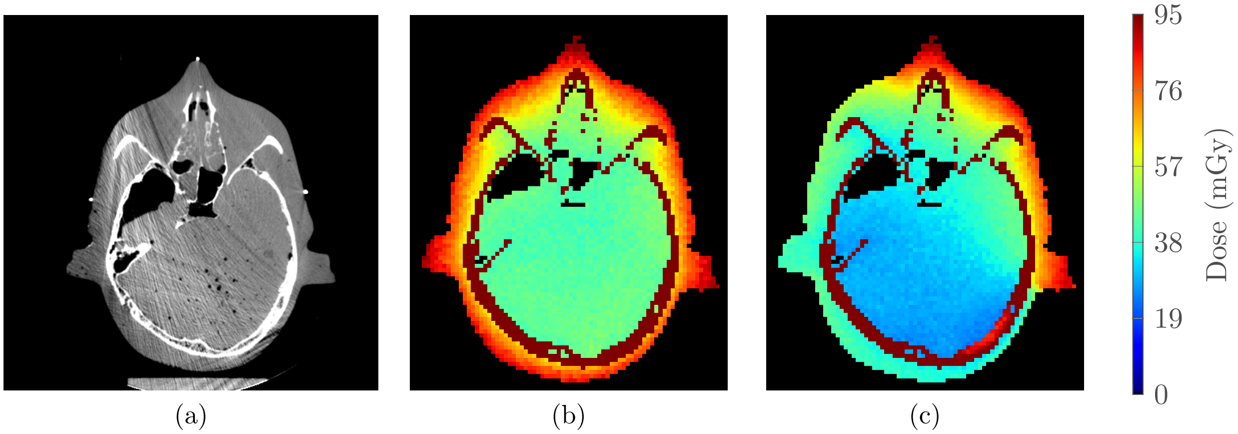

(a) (b) (c)

Figure 5.8: The absolute dose to the RANDO head phantom for the reference scan (middle) and cheek dIWROI scan (right). The surface dose is down dramatically for dIWROI outside the ROI.

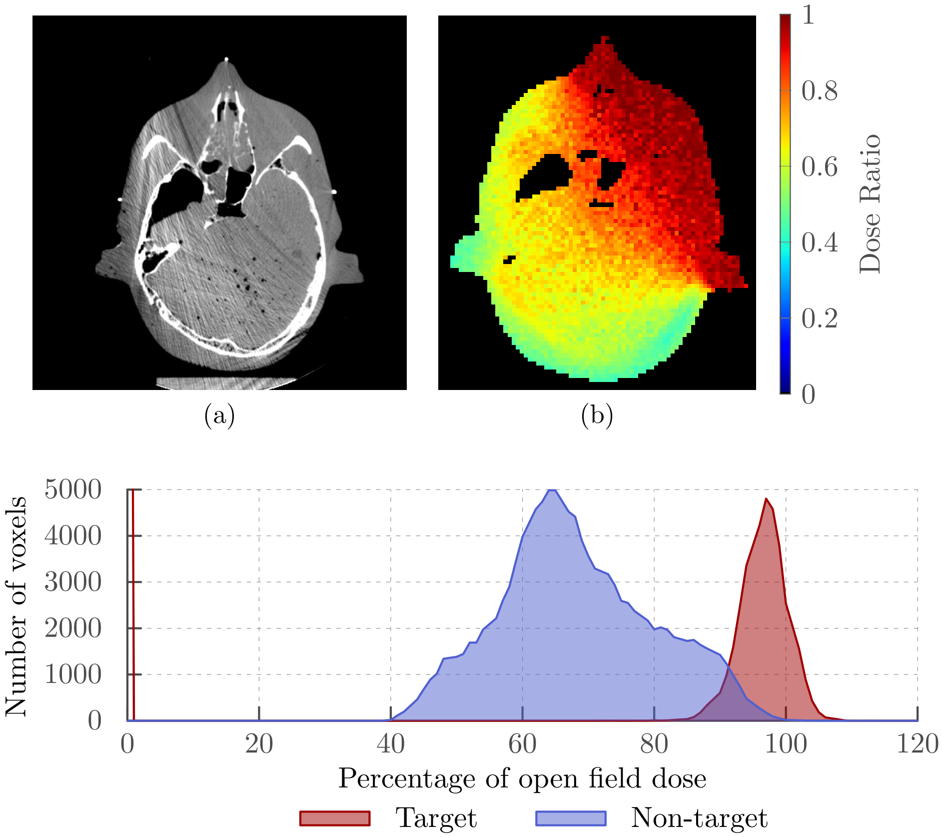

(a) (b)

(c)

Figure 5.9: The Monte Carlo calculated dose for the dIWROI scan is shown as a ratio to the unfiltered reference scan dose. Below is the histogram of the dose ratio for the full volume. Most of the dose is deposited in the target region with the rest of the head receiving significantly less.

5.2.2 Interior ROI

The fully encapsulated, or interior ROI is a problem for traditional ROI imaging techniques, however we have seen in chapter 4 that intensity weighting can provide a compromise that enables reconstruction of these interior regions while providing nearly all of the dose benefits of conformal illumination. Three different interior ROI and phantom combinations were considered. First, the RANDO head phantom with a 5 cm × 7 cm elliptical ROI located 3.5 cm off center, same as the one used with the homogeneous water cylinder for the correction training process as shown in Figure 5.2. Then an arbitrary contour drawn in the inner cavity of the chicken phantom and finally a small 2.5 cm × 3.5 cm elliptical ROI. The small size of the final ROI was chosen chosen to challenge the correction strategies.

Image Reconstruction

The results for the larger elliptical ROI are shown in Figure 5.10. The reference, unfiltered result is in (a), the other 3 images are dIWROI results with different correction strategies. It should be noted that the reference image was taken with a different physical setup so the phantom alignment does not match the dIWROI results, notably it is shifted downward and skewed out of plane slightly so while the structures match well on the left side the ear canal is missing on the right. The image in (b) uses all of the data corrections described at the start of this chapter except the anisotropic diffusion denoising of the I_0 projection images. The bottom left includes the denoising step but does not use the spline interpolation over the blade edges and (d) uses all of the corrections. The noise in the outer region appears slightly greater in (b) however the transition artifacts are less pronounced suggesting that in this case the denoising step may exacerbate the blade edge misalignment effects.

The result without the denoising, 5.10b, is shown again beside the reference image in Figure 5.11 with enlargements of 28.8 mm × 40 mm regions from inside the ROI shown below. The enlargements show that the dIWROI image recovers the details of the fine bone structure near the ear well. The image intensity is again higher in the dIWROI image due to the addition of the scatter correction.

The reconstructed images for the interior ROI of the chicken phantom are shown in Figure 5.12. The reference, unfiltered image is shown with the contour in red in (a). The dIWROI results are shown below, with the spline correction (c) and without (b). The choice of ROI for this dataset turned out to be a major limitation. The intention for using the chicken phantom was to provide an indication of low contrast, soft tissue discrimination performance however, even in the reference image no discernible soft tissue structures appear in the ROI. Additionally, most of the contour edge was placed near high contrast transition in the image, air-tissue or tissue-bone. These high contrast transitions make the blade edge

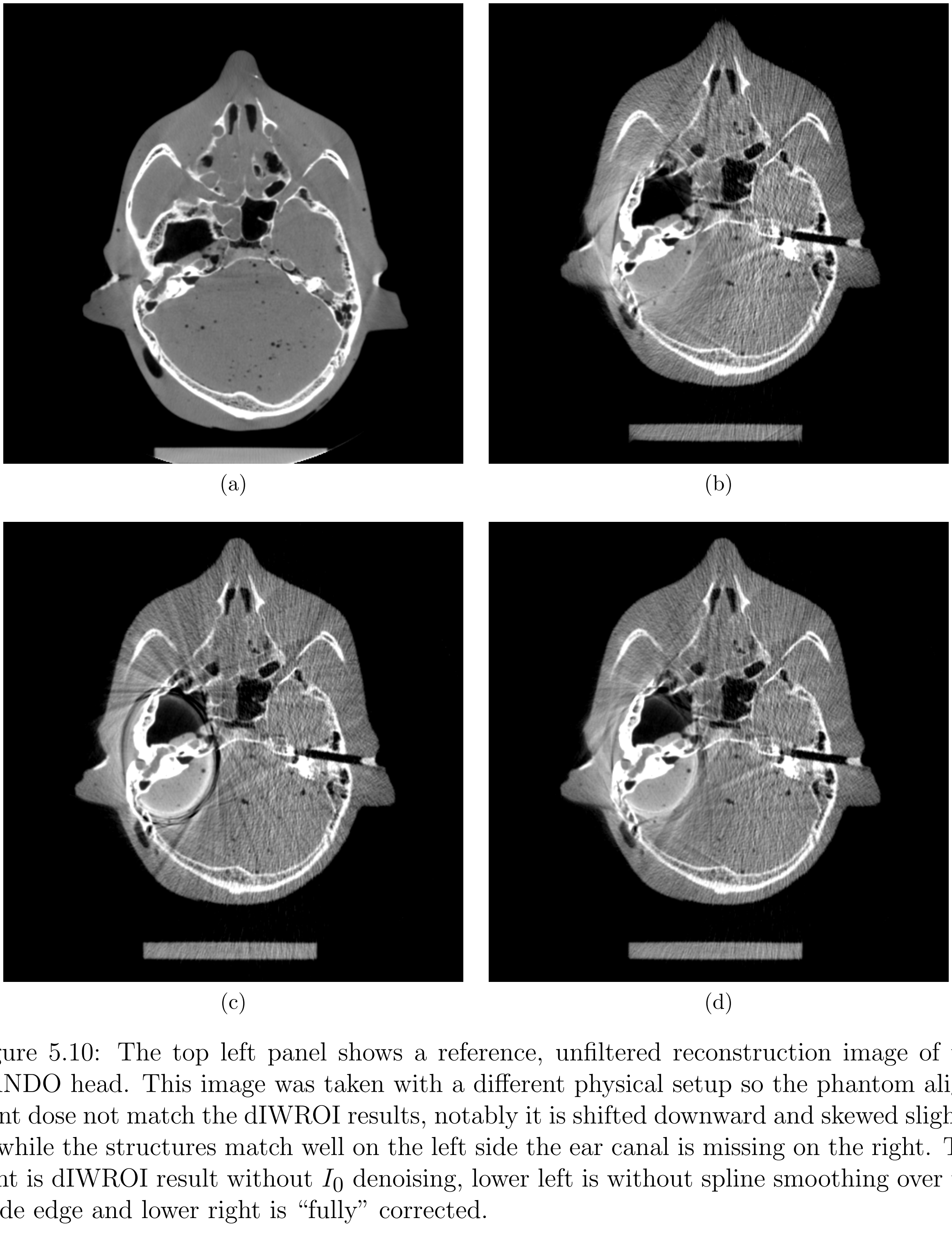
(a) (b) (c) (d)

Figure 5.10: The top left panel shows a reference, unfiltered reconstruction image of the RANDO head. This image was taken with a different physical setup so the phantom alignment dose not match the dIWROI results, notably it is shifted downward and skewed slightly so while the structures match well on the left side the ear canal is missing on the right. Top right is dIWROI result without I_0 denoising, lower left is without spline smoothing over the blade edge and lower right is “fully” corrected.

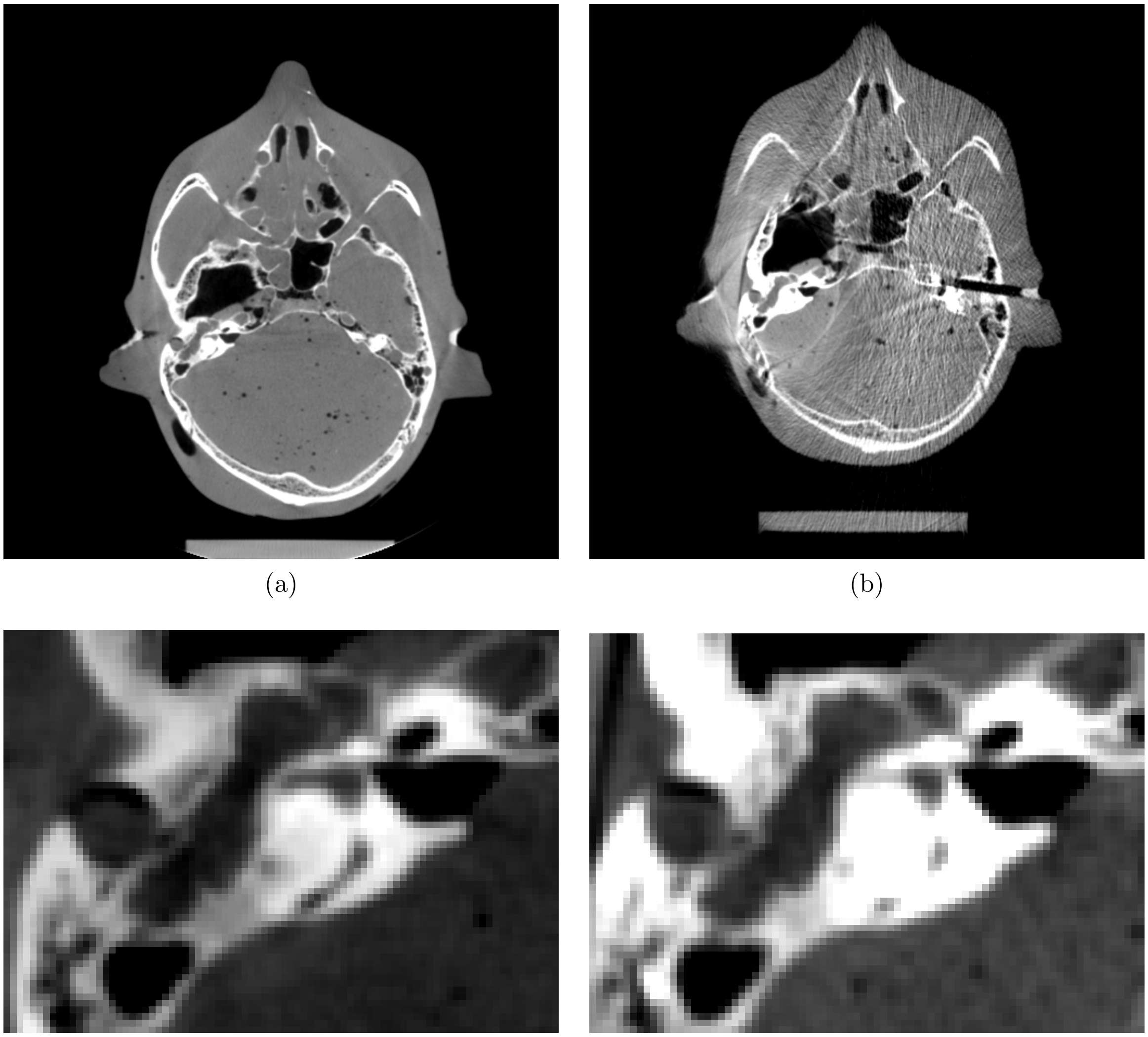

(a)

(b)

(c)

(d)

Figure 5.11: Results for a 5 cm × 7 cm elliptical ROI. On the left is a reference image, taken with an unfiltered beam and on right is dIWROI image from 5.10b. Bottom row contains enlargements of regions with in the ROI. Note that reference data and IWROI were taken with different setups and are not an exact position match. Display window for large images [0.05,0.35] and elarged regions [0.15,0.45] and [0.15,0.6] for the reference and IWROI images respectively, indicating a bias in the bone values for the corrected data.

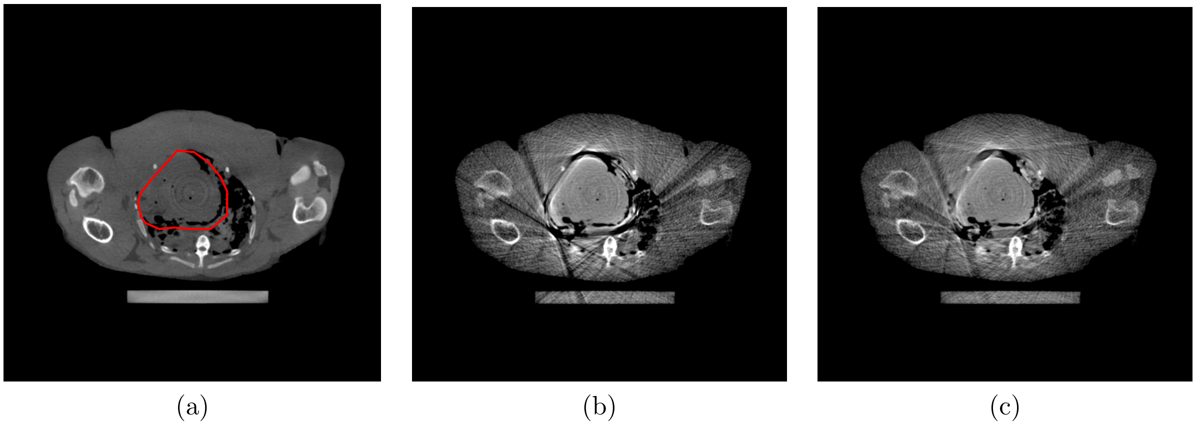
(a) (b) (c)

Figure 5.12: Left image is the reference, unfiltered reconstruction of the chicken phantom with the ROI contour shown in red. Bottom row contains the dIWROI reults with (c) and without (b) the spline smoothing over boundary. Display window [0.15,0.3]

detection used in the log-normalization correction much more challenging. This combined with the fact that beam quality and scatter underperform for the chicken phantom as seen in subsection 5.2.1 result in a poor quality image in the outer region and the nearly homogeneous material inside the ROI provides little indication of image qualtiy with in the reconstruction.

Unlike the previous result, the small elliptical ROI was intentionally chosen to show limitations of the data corrections. The physical factor correction parameters, beam-quality and scatter, are phantom and aperture specific. Using the parameters learned from a significantly larger aperture and a homogeneous data set is likely to underperform. Additionally, the transition artifacts described in section 4.2.2 are intensified in areas of high curvature of the ROI contour. The tangent of the contour points to the view from which the blade edge is projected in to the image. In straight regions of the contour edge there are very few views containing the problematic blade edges contributing to the image in this region so the magnitude of the effect is reduced. In the highly curved sections there are many view from which the errors are contributed, intensifying the artifact. The results for the small ellipse are shown in Figure 5.13 with the same organization as above. The values inside the ROI are showing the failure of the physics factor corrections and the transition region artifcats are very strong. The current limitations of the method along with approaches to improve

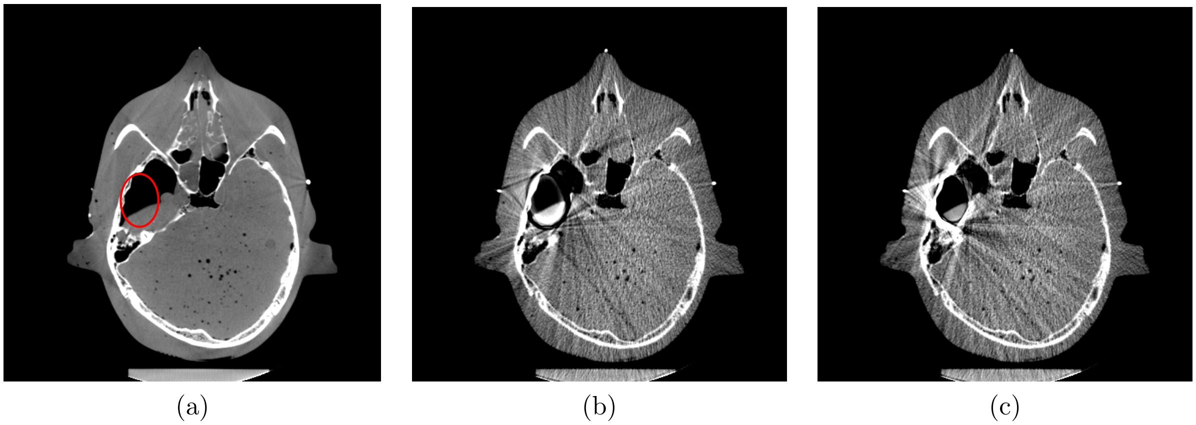
(a) (b) (c)

Figure 5.13: A small, 2.5 cm × 3.5 cm elliptical ROI, chosen intentionally to strain the data correction methods. (b) is without spline smooth, (c) includes the smoothing. Display window [0.1, 0.3].

them will be discussed in chapter 6.

Dose Reduction

The dose sparing provided by this method was again analyzed using the Monte Carlo framework previously introduced. The ratio of the dIWROI to the open field dose and the histogram of the ratio are shown in Figure 5.14. From this histogram we see that the dose to the target region is reduced despite being fully illuminated, this is due to the reduction in scatter fluence coming from the surrounding tissue. Most of the rest of the volume falls in the range of 20 % to 60 % of the open field dose.

A DVH with simulated structures is provided in Figure 5.15 for comparison of the dose distribution of the dIWROI scan and standard, unfiltered scan. The PTV is a 4x6x6 cm ellipsoid wtihin the ROI, the eyes are 1.8 cm spheres placed with in the sockets of the skull and the tissue is all remaining structures. The openfield curves are shown as dashed lines and the dIWROI as solids and for all the dIWROI falls significantly below the openfield.

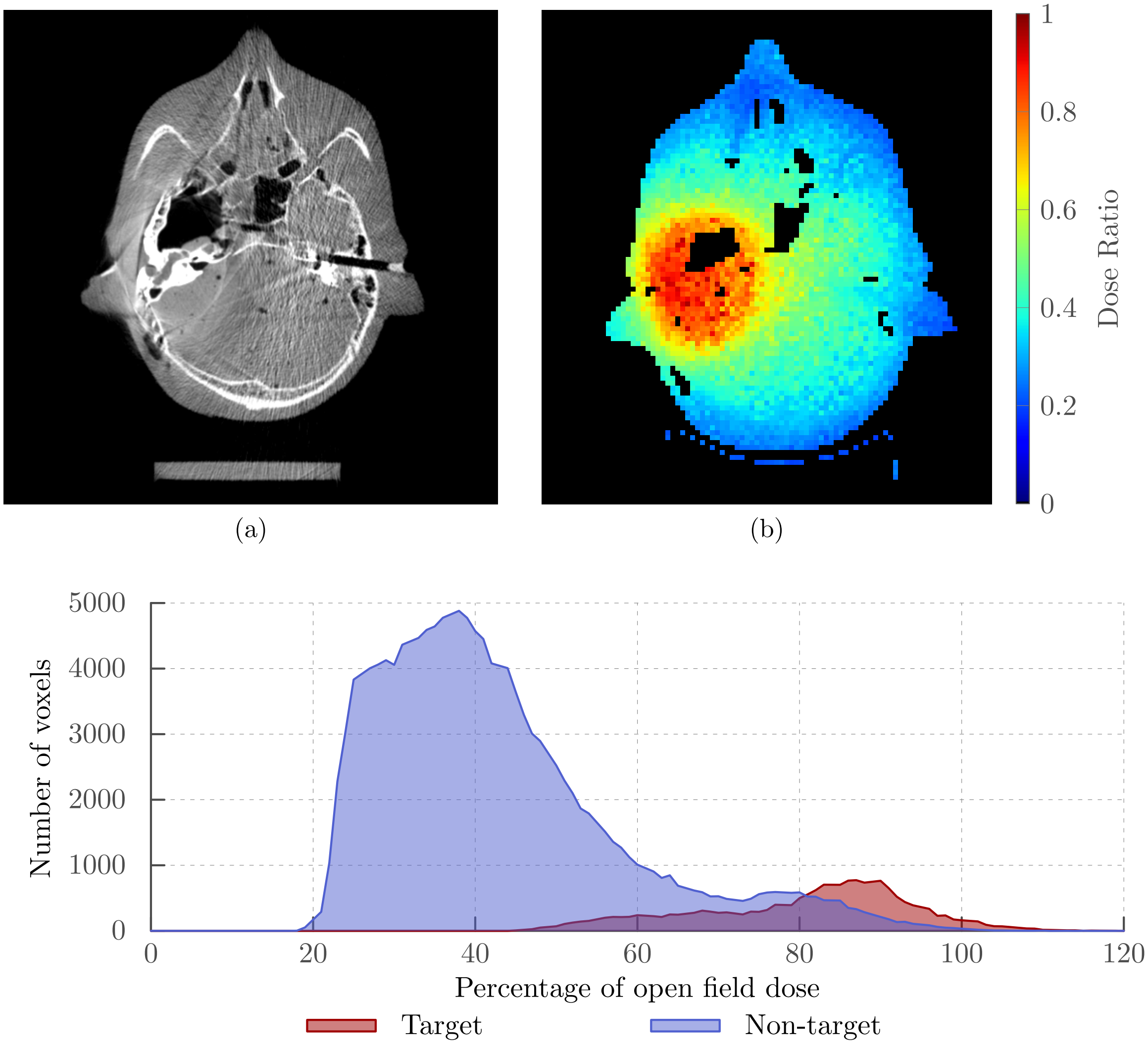

(a) (b)

(c)

Figure 5.14: The large ellipse dIWROI image (a) with the ratio of the dIWROI to the open field dose shown in (b). The histogram of a 10 cm volume is shown in (c)

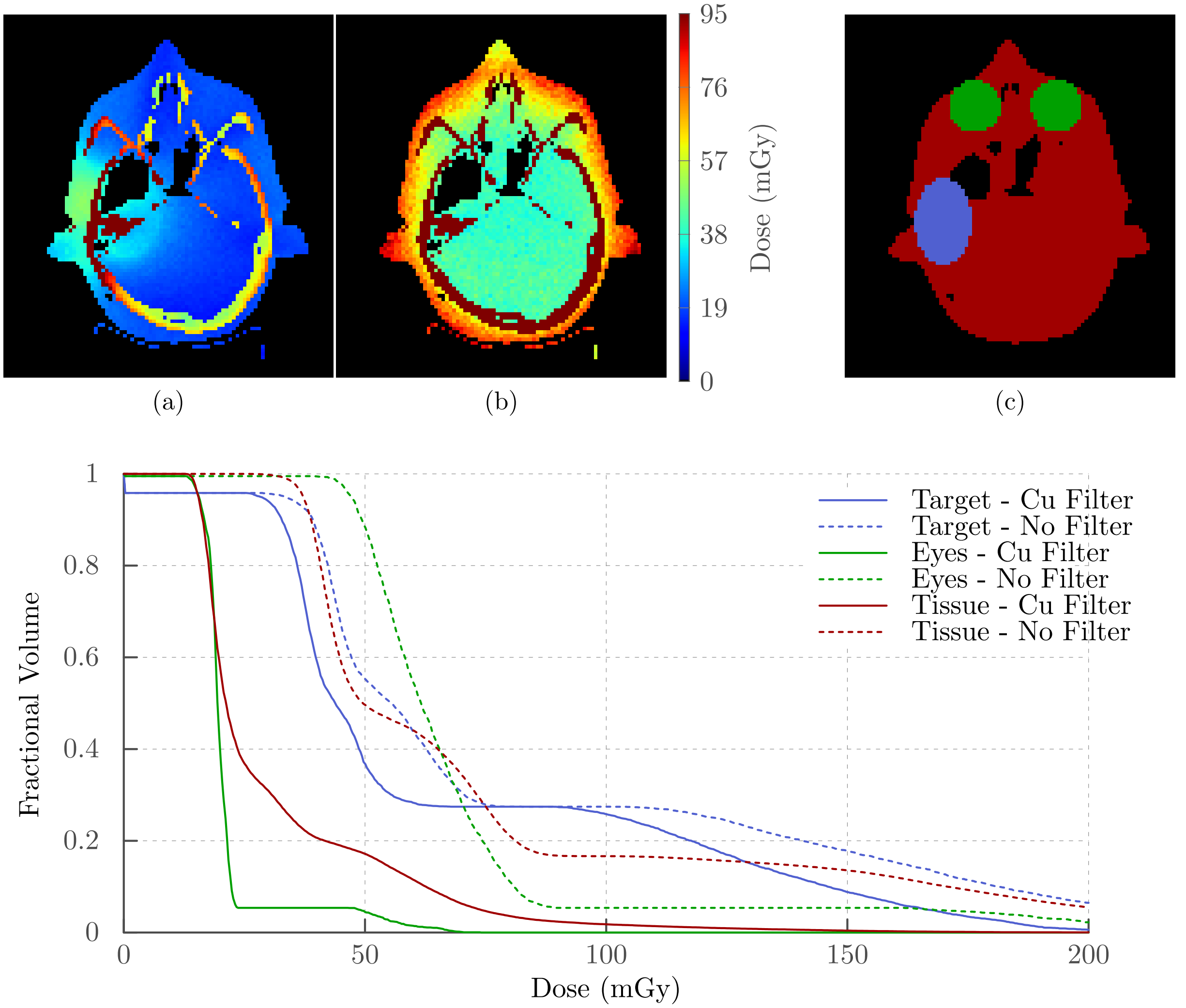

(a) (b) (c)

(d)

Figure 5.15: The absolute dose distributions for the reference and elliptical dIWROI scans in the top left and top center respectively. Below, a DVH for comparison of the dose distribution of the dIWROI scan and standard, unfiltered scan. The PTV is a 4x6x6 cm ellipsoid wtihin the ROI. The eyes are 1.8 cm spheres placed with respect to the appropriate skeletal structure. Tissue represents all remaining unclassified tissues, Structures shown on central slice in top right.

5.3 Summary

This chapter presented the general case of IWROI imaging with dynamic filtration. The dynamic collimator devloped in chapter 2 was used with copper blades allowing the ROI to be arbitrarily shaped and positioned within the field of view. The performance of the collimator was validated under both static and dynamic conditions and demonstrated blade edge position repeatability of better than ±1.75 pixels on the detector.

Several data correction strategies were devleoped to correct for the presence of the filters in the projection images prior to reconstruction. The resultant images showed good image recovery inside the ROI and sufficient information in the outer region for clinical alignment tasks. Monte Carlo modeling was used to quantify the patient specific dose reduction provided by the ROI and IWROI techniques for the sample cases studied. For a reasonably sized internal ROI ($5\,\mathrm{cm} \times 7\,\mathrm{cm}$ ellipse) in the head the dose to the tissues outside the ROI was reduced to 20 % to 60 % of the unfiltered scan dose.

CHAPTER 6

CONCLUSION

6.1 Summary of the work

This work began with a dynamic collimation device that could be mounted directly onto existing clinical imaging hardware. The hardware design and construction as well as the control electronics and logic were described. The performance of the device was measured with respect to specific applications, fluoroscopic imaging in section 2.3 and for tomographic ROI imaging applications in subsection 5.1.1. These studies showed that the prototype collimator had sufficient dynamic capabilities for the tasks proposed.

The first application of the dynamic collimator was for tracking implanted lung fiducials during fluoroscopic imaging. The fluoroscopic imaging provides real time information on the tumor location which can be used for gating the treatment beam or, potentially, for dynamic MLC tracking during external beam radiation therapy. This can improve the accuracy of the radiation delivery and allow for reducing the treatment margins, thereby reducing the therapeutic dose to the surrounding tissues. However, the fluoroscopic imaging is typically done with a large, static x ray field size which results in considerable imaging dose to the patient. We presented an approach for using the dynamic collimator to restrict the illumination to a much smaller aperture which dynamically tracks the fiducial providing the same target location information as the full field fluoroscopy but with substantially reduced patient exposure, for the experimental aperture the dose-area-product was reduced to 3.3 % of a full field acquisition. The complete fiducial tracking system depends on further development of the software algorithms and the software integration with the image acquisition system however the collimator system demonstrated sufficient performance for accurate tracking.

The second imaging application was conformal ROI imaging. This technique used the chord based BPF algorithm to reconstruct an ROI from a restricted illumination cone-beam CT scan. This approach can accurately recover the ROI from data acquired with the x ray field collimated to the bounds of the ROI using the dynamic collimator with radiopaque blades. Limiting the x ray field in this way can reduce the radiation exposure to the tissues outside the ROI. However this technique is limited to peripheral regions which can be completely filled with untruncated chords which requires careful planning of the ROI and the CT acquisition. Additionally this approach provides no image information about the parts of the patient outside the ROI.

In the course of the work on conformal imaging a methodology was developed for predicting potential collisions between the patient and the linac. A patient model was developed from the planning CT volume and stereoscopic optical imaging for parts of the patient that weren't scanned during simulation. The patient model could then be virtually setup with an engineering model of the accelerator surfaces and potential collision could be determined. This was developed to determine the potential of setting up post mastectomy patients off center for ROI imaging with a limited arc. However it has broader application in radiation therapy for non-coplanar fields in IMRT or arc in VMAT or and for non-standard imaging trajectories[105].

In response to the limitations of the conformal ROI imaging technique we developed the intensity weighted ROI imaging method. This approach uses filters to spatially vary the intensity of the beam instead of opaque blades to collimate the beam. In this way we are able to acquire full data of the patient which allows for reconstruction of the whole volume with standard reconstruction algorithms and is not limited to peripheral regions. However, the parts of the projection data measured with the low intensity (filtered) beam have higher noise which propagates back in to the reconstructed image during reconstruct resulting in a high quality image within the ROI and a lower quality, noisy image of the rest of the patient. The lower quality region can still be useful in image guidance, e.g. for alignment to high contrast structures such as bone or the skin surface.

This technique was first demonstrated for the simplified case where the intensity weighting filters were rigidly mounted to the x ray source. This configuration results in a cylindrical

ROI aligned on the axis of rotation. Later we present the general case of dynamic IWROI imaging, in which the filtration is provided by the dynamic collimator, allowing the ROI to be arbitrarily shaped and positioned within the field of view. In both cases the presence of the filters in the projection images in the IWROI technique cause several problems in the data that need to be addressed prior to reconstruction to obtain a useful image. Correction strategies and results were shown for both. Finally, Monte Carlo modeling was used to quantify the patient specific dose reduction provided by the ROI and IWROI techniques for the sample cases studied. For a reasonably sized internal ROI in the head the dose to the tissues outside the ROI was reduced to 20 % to 60 % of the unfiltered scan dose.

6.2 Path forward

The techniques we have developed show promise for targeted imaging with reduced radiation exposure to the patient while still providing sufficient information in the image for clinical tasks. However, the correction strategies could be further improved and made more robust. Several directions for investigation in this regard are introduced with considerations for translation towards clinical implementation. The other component that requires development for implementation is the acquisition planning which involves determining the patient specific ROI and collimator trajectories, which is also discussed below.

6.2.1 Improving the data corrections

Several correction methods were presented to account for the effects of the intensity weighting filters. Under some conditions they performed quite well but for some ROI selections the performance deteriorated. The following are some directions which may make the methods more robust or otherwise generally improve their performance

Beam quality correction

The beam quality correction generally performed well but occasionally introduced some bias in the value of the region outside the ROI. The limitation of the method currently used is that for the correction to be accurate it requires knowledge of the materials along the measurement path. The correction factor for most soft tissues is very similar so the correction originally assumed the composition of the object was all water equivalent. Later the values were modified to represent a mixture of soft tissue and bone but this relative composition remained constant for every ray, for every view. For a more accurate correction the actual distribution water-like and bone-like materials should be accounted for. This could come either from a priori information, in the form of the planning scan in IGRT, or from an initial reconstruction of the data with a global correction factor. Then with a volume representation of the structure the voxels could be classified as air-like, water-like or bone-like. This could likely be done with a simple thresholding of the image, if that is not sufficiently robust a k-means type classifier could be used. From this classified volume data an object specific beam quality correction could be calculated.

Scatter correction

Two different approaches for the scatter correction were used in this work. The estimation method[118] using the tails of the projection data under a partially closed collimator was found to work well when that data was available. When that data was unavailable an alternate approach, estimating the scatter fluence from the projection data itself, as a convolution with a Gaussian kernel, worked well when the scanning conditions closely matched the data set used to determine the size of the Gaussian, however when the size of the imaged object changed or the size of the ROI changed the correction performance was reduced. The scatter fluence is dependent on the imaging conditions as well as the underlying object, so an ideal correction requires knowledge of the underlying object. As in the beam quality correction section above this could be obtained either from the planning scan or from a preliminary reconstruction of the data. Then the scatter field could be estimated for the imaging configuration with analytic scatter models or Monte Carlo simulation, like the approach in Appendix B.

Log Normalization and Edge Correction

As previously described, the log normalization step in the reconstruction process is complicated by the intensity weighting filters. If their positions are mismatched between the air scan (I_0) and the object scan (I) in the division operation then errors are created in the sinogram that tend to present as strong, bright or dark boundaries at the edge of the ROI. These artifacts could be reduced in some cases by applying a smoothing operation over this boundary.

The current process for performing this log normalization requires two scans be acquired for each planned ROI, one of the patient and one air scan. These are currently acquired back to back; however this would not fit well into the clinical work flow. If the collimator hardware were fully integrated into the linac, and not an add on module as it currently exists, and demonstrated sufficient reproducibility then the I_0 scan could be acquired prior to the first treatment, perhaps along with the IMRT QA process. However this increases the burden on clinical staff and requires a high degree of repeatability from the hardware, which could result in a failed reconstruction if a deviation occurs.

Alternatively the I_0 dataset could be generated for a specific scan. This could be done with mathematical model described as a function of the blade positions. Alternatively it could be composited from a library of measured radiographs with the blades in many positions. Both methods require an accurate determination of the blade position in the projections of the object scan. However, due to the large intensity change this can be accomplished pretty robustly with common image processing techniques. The model based method has the benefit of being inherently noise free and requiring little disk space. The library based approach may better capture the details of the beam shape, detector response, etc.

The necessity and form of the edge correction strategy depends on the performance of the log normalization step. In the best case scenario, if the log normalization is well enough matched, there would be no need for further edge correction.

6.2.2 Acquisition Planning

The other important component for further development is the planning step of the acquisition. The current strategy used for planning the scan acquisition is to divide the image into two regions, the area inside the ROI which is in the unfiltered beam for every view to provide the highest quality, and the region outside the ROI which is in the filtered beam for every view for maximum dose spacing. This is achieved by drawing a contour representing the ROI on the planning scan and developing a trajectory for the collimator to follow this contour.

The limitation of this technique is that, as we saw in chapter 5, the quality of the reconstruction can be affected by the shape and placement of the ROI. We found the regions of high curvature in the contour edge inside the object caused worse artifacts and the contour boundaries parallel to and near high contrast edges in the structure of the object also resulted in greater artifacts in the reconstruction. The best results can be achieved by avoiding these situations. These issues need to be considered in 3D for the ROI surface which could be time consuming to do manually. Instead an automatic, or semi-automatic, approach would be preferred in which the physicist or physician planning the treatment would specify the region that should be visualized with the highest quality and the contours that specify the most sensitive organs. The imaging ROI could be determined with an optimization approach by penalizing boundary curvature inside the patient, proximity to high gradient regions and views containing the OARs in the unfiltered beam, with the condition that the high quality region remain unfiltered.

Graham[62,63] and Bartolac[64,65] have reported on “Intensity-Modulated” cone-beam CT which is a similar concept to the IWROI methods present here. Their approach has been a theoretical study of the relationship of incident fluence and image SNR and to generate continuous fluence modulation patterns to achieve a specified SNR distribution. This approach provides a continuous trade off between the local imaging dose and image quality; however the fluence patterns they generate would be difficult to generate. Combining their theoretical planning methods with the dynamic collimator and real data reconstructions presented here could produce a general framework for patient specific, task prescribed, variable image quality with reduced and targeted imaging dose.

6.3 Significance

The dose to the patient from image guidance in IGRT is small compared to the therapeutic dose that is delivered. However, unlike the therapy beam, the imaging beam is untargeted and deposited equally in healthy tissues. Additionally the cumulative imaging doses may be rising due to the increased frequency of imaging. The AAPM task group 75 states that the dose from imaging procedures can not be considered negligible[36] and the official guideline of the United States Nuclear Regulatory Commission is to follow the ALARA principle[135]:

> ALARA (acronym for "as low as is reasonably achievable") means making every reasonable effort to maintain exposures to radiation as far below the dose limits in this part as is practical consistent with the purpose for which the licensed activity is undertaken, taking into account the state of technology, the economics of improvements in relation to state of technology, the economics of improvements in relation to benefits to the public health and safety, and other societal and socioeconomic considerations, and in relation to utilization of nuclear energy and licensed materials in the public interest.

With this in mind we have developed imaging techniques that contain sufficient information to have clinical utility with substantially lower dose away from the target region than conventional methods.

Appendices

APPENDIX A

COLLIMATOR FABRICATION

This appendix contains the detailed design, fabrication and assembly information of the dynamic collimator presented in the chapter 2. With the exceptions of the DryLin N series low profile, low friction linear guide rails (Igus Inc, Providence, RI) and the L16 linear actuators (Firgelli Technologies, Victoria, British Columbia) every piece of the collimator was custom designed and hand fabricated by the author in the Department of Radiation and Cellular Oncology machine shop. The tools available in the shop and used for this project include:

- Bridgeport 2J vertical mill, manual
- Nardini MS-1440E manual lathe
- DoALL 16" ML bandsaw
- Rockwell 70-400 drill press
- Pexto PS-66 6 in Notcher

This appendix is broken into three sections. First the fabrication of the parts is described, followed by details of the assembly and finally the engineering drawings. The drawings included exploded assembly views for the major configurations shown in Figure A.1 and major sub-assemblies as well as dimensioned part drawings for every piece that was made.

A.1 Fabrication

The fabrication began with the structural base of the collimator blades which are made from copper and serve as the filters in the IWROI studies. The 1/8 in copper was rough cut to size and then all edges were finished in the mill with particular care taken with the leading edges, those that will be in the imaging field. As show in Figure A.4 the blades have four pairs of holes sized for a close fit on the mounting studs of the carriages provided with the Igus slide

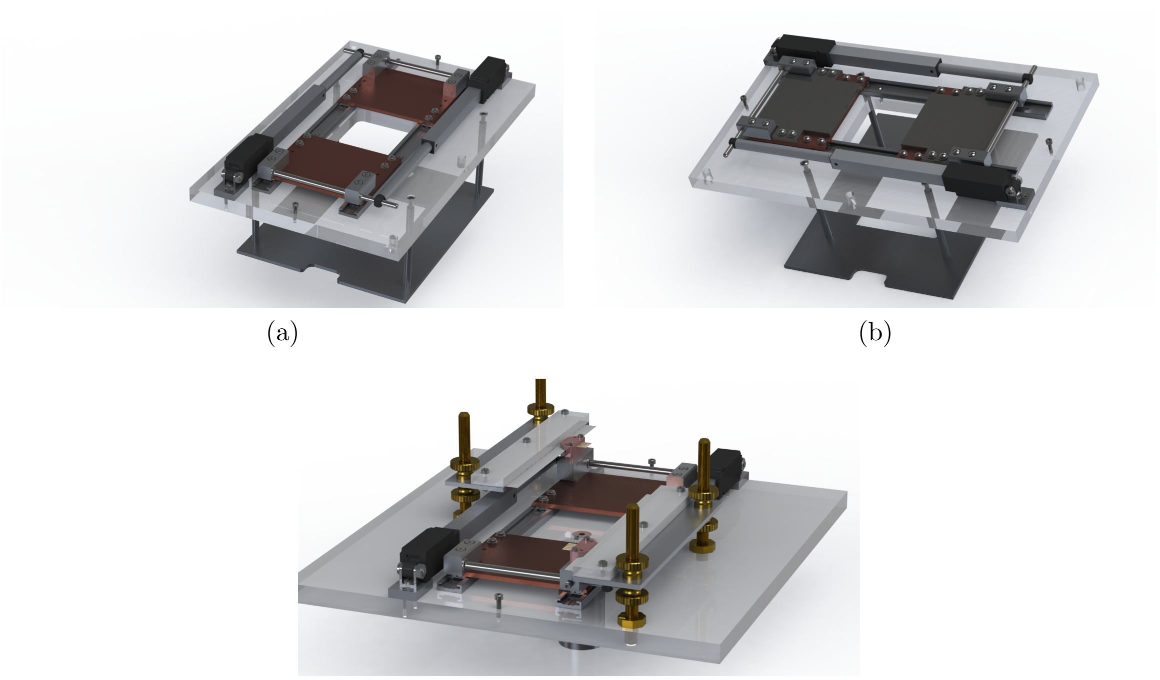

(a) (b)

(c)

Figure A.1: Three configurations of the hardware

rails. They also have two pairs of M3x0.5 mm tapped holes for mounting the optional lead covers. With the copper blades cut and drilled the Igus carriages could be mounted which would allow testing of the rail alignments. The next step was the plastic base plate to which the rails would be mounted.

The plastic base in Figure A.20 was rough cut to shape and mounted in the mill table vice. Index marks were made for setup reference and the two parallel sets of 4 2.5 mm holes for the slide rail mounting were drilled and tapped. With the rails attached to the base plate but the mounting screws left slightly lose the blades ran smoothly, however with the screws tightened down the blades began to bind. To remedy this the mill head was carefully retrammed, that is the mill head spindle was squared to the mill table surface, and the center section of the plastic base plate was resurfaced in the mill with a fly cutter set wide enough to cover both tracks in a single pass. Afterwards the surface was sufficiently flat and the cars ran in the tracks without binding when fully tightened down to the plastic base plate.

With the blade bodies running in the tracks, the next step was to attach the linear actuators for the blades. A rigid, stainless steel rod (Figure A.6) spanning the width of the blade was used to transfer the actuator motion to the blade. Two aluminum blocks (Figure A.5) were milled to mount over the rear Igus carriages and hang off the back to keep the steel rod out of the imaging field. The mounting screws were counter bored and the hole for the rod was sized for a tight clearance fit to prevent any slop in the motion transfer. The drive rod was turned down at one end to fight tightly in the actuator clevis end and two notches were made for retaining rings. The other end of the motor was mounted with the included U brackets, however a spacer block Figure A.12 was machined to raise this bracket to the proper height to keep the actuator parallel with the plastic base surface. It was milled to shape and 3 holes were drilled. The outer two are countersunk clearance holes for M3x0.5mm flat head screws to attach the spacer block to the plastic base plate. The center hole was drilled and tapped with 8-32 standard threads for mounting the included U bracket from Firgelli.

The plastic base plate was remounted and indexed in the mill. Four M3x0.5 thread holes were added outside the guide rails to receive the motor spacer blocks. Two more were added near the edges along the motion centerline for stop screws to prevent the blades running of the ends of the tracks. The center point of the base plate was drilled and counter sunk for a 1/4”-20 screw with a 1/8 in offset hole for an alignment pin. Finally, four 5/16”-40 holes were added for the vertical supports of the encoder clamping mechanism. These vertical supports were custom made 5/16-40 threaded brass studs. They were custom made as threaded rod in this diameter with a suitably fine pitch could not readily sourced however a 5/16-40 die was already available in the shop. To facilitate the amount of threading that needed to be done a custom, extending die holder was designed and fabricated to fit the tailstock of the Nardini lathe allowing for the threads to be cut under power. Custom nuts had to be created to match this thread, four were made from standard hex stock and 8 were made by drilling out and retapping 1/4-20 knurled nuts.

The clamping mechanism for the transmissive strip of the linear encoder was made from an aluminum plate lower and acrylic plate upper. The upper piece was cut to shape, with the sharp edges broken to prevent marring the encoder strip, and three clearance holes for 6-32 standard screws were drilled. The lower piece was similarly cut to shape, also with edges broken, got three holes drilled and tapped to receive the screws from the upper piece. It got two clearance holes as well to go over brass support studs which were slightly over sized to allow for some tilt if needed. The final piece of the encoder assembly base was the cylinder (Figure A.24) that was mounted to the center of the back plastic base plate which enabled the whole assembly to be mounted in a rotary chuck for testing.

The lead covers for the blades included a 1/8 in thick layer of lead (Figure A.8) and a 1/32 in thick layer of steel (Figure A.7). The lead was sandwiched between the copper base and the steel layer. The sole purpose of the steel layer was to provided structural integrity to the soft lead piece. The lead and steel pieces were cut to shape in the Pexto notcher. The corners were removed to accommodate the drive rod attachment block in the rear and the carriage mounting hardware in the front. Four clearance holes for M3x0.5 screws were dilled in each piece for attachment to the copper blade.

To attach the optical encoder readout module to the blade assembly an aluminum mounting bracket was fabricated (Figure A.18). This was cut from aluminum bar stock and milled to the same width as and slightly longer length than the drive rod mounting block. The center section was then milled out so it fit snugly over the drive rod block. An M3x0.5 thread hole was drilled and tapped in one end for a set screw to secure the bracket in place. Two 3-56 standard thread holes were put in the top for attaching the US Digital encoder module.

At this point all pieces required for the encoder feedback assembly were complete. Once those measurements were finished several modifications were made to the hardware. The center of the plastic base plate was milled out to provide an obstructed bath for the imaging beam. Additionally four clearance holes for 6-32 standard screws were drilled in a square pattern for attachment to the bowtie filter mounting plate assembly. The filter attachment plate (Figure A.14) was modeled from careful measurement of the flat portion of the bowtie filter carrier from Varian. It was cut from 1/8 in aluminum plate. The center section was milled out to provided a window for the imaging beam. Additionally the oval at the top and the cut-out at the bottom were cut in the mill to mimic the attachment points of the original. Four clearance holes were drilled and countersunk for 6-32 flathead screws matching the pattern on the plastic baseplate. The countersinks were cut sufficiently deep to ensure that the screw heads were completely recessed as the plate is flush mount to the kV source housing. Stand-off for raising the plastic base plate to the appropriate height off the filter mounting were made from aluminum rod stock with the ends center drilled and tapped in the lathe with a 6-32 thread.

A.2 Assembly

A.2.1 Blade assembly

The two blade assemblies, as shown in Figure A.3 are the principal moving components of the device. The main structural component of this assembly is the copper blade ①. The holes in the corners are sized such that the mounting studs from the Igus carriages ③ snap in to place. The forward screws and washers can then be tightened into place. The drive rod mounting blocks ④ are aligned over the rear carriages and the mounting screws and washers are inserted through the mounting block and tightened into place. The head of the screw should be completely recessed in the counterbore and the screws should not protrude through the Igus carriages. The drive rod ⑤ is then inserted through the aluminum mounting blocks and the grooves in the rod should align closely with the inside surfaces of the block. The retaining rings are installed in these grooves to prevent the rod from moving. This is the basic blade assembly for the IWROI tasks. Optionally the lead blade and steel cover ⑩ can be fastened into place using the four threaded holes in the copper blade.

A.2.2 Encoder feedback base

The encoder feedback measurement assembly is shown in Figure A.16. This assembly begins with the fixed components shown in Figure A.19. The rails ⑤ can be installed in the resurfaced center region of the plastic base plate ① with 4 M3x0.5mm screws each. The alignment pin is press fit into the mounting cylinder ② and fixed tightly into place with the 1/4-20 flat head screw. The motor spacer block ⑥ are fastened in place with 2 M3x0.5mm flat heads each and the vendor supplied U bracked ⑨ is then mounted to the spacer plate with an 8-32 round head screw.

The brass hex nuts ⑬ are turned partway onto the brass thread studs ⑫ which are then screwed into the plastic base plate. They are fixed in place by tightening the hex nut down against the plastic base plate. The lower knurled nut is turned onto to each of the vertical studs, knurled side down. The lower piece of the encoder clamp assembly ⑯ is then installed on the the vertical studs and the top knurled nut ⑭ is tightened down to hold it in place. The encoder strip and and top plate of the clamp are added later after the height is properly adjusted for the blades.

The dynamic components can then be added to the assembly as shown in Figure A.16. The assembled blades ① can be slide on to the rails and the retaining screws tightened in place to keep them from running back off the rails. The actuator ㉜ can be inserted on to the drive rod of the blade assembly and then rotated down in to the U bracket and fastened into place with the screw and nylon lock nut. The encoder module assembly ㉘ is placed over the rod mounting block of the blade assembly on the side with the encoder strip clamp. The height and alignment of which are manually adjusted with the knurled nuts to achieve the manufacturer supplied alignment tolerances and the strip is clamped in place.

A.2.3 Dynamic collimator

The assembly of the dynamic collimator is in many ways similar to the encoder assembly above. Again we can first consider the fixed components shown in Figure A.9 or Figure A.10

where the difference is simply the orientation of the mounting plate, transversely aligned for CT imaging and axially aligned for fluoroscopic tracking, respectively. The rails ② and motor mounting hardware ③, ⑥ are attached to the plastic base plate ① as above. The standoffs are mounted first to the aluminum filter plate with 4 6-32 flat head screws. The heads of the screws must be fully recesed for proper mounting. The filter mounting plate assembly can then be attached to the plastic based plate, in either orientation, with 4 6-32 round head screws. To this the blades, motors and retaining screws can be added as shown in Figure A.2 and as described above.

A.3 Drawings

A complete set of engineering drawings for all custom components follows. The drawings are presented in a hierarchical order by assembly as indicated by the following index:

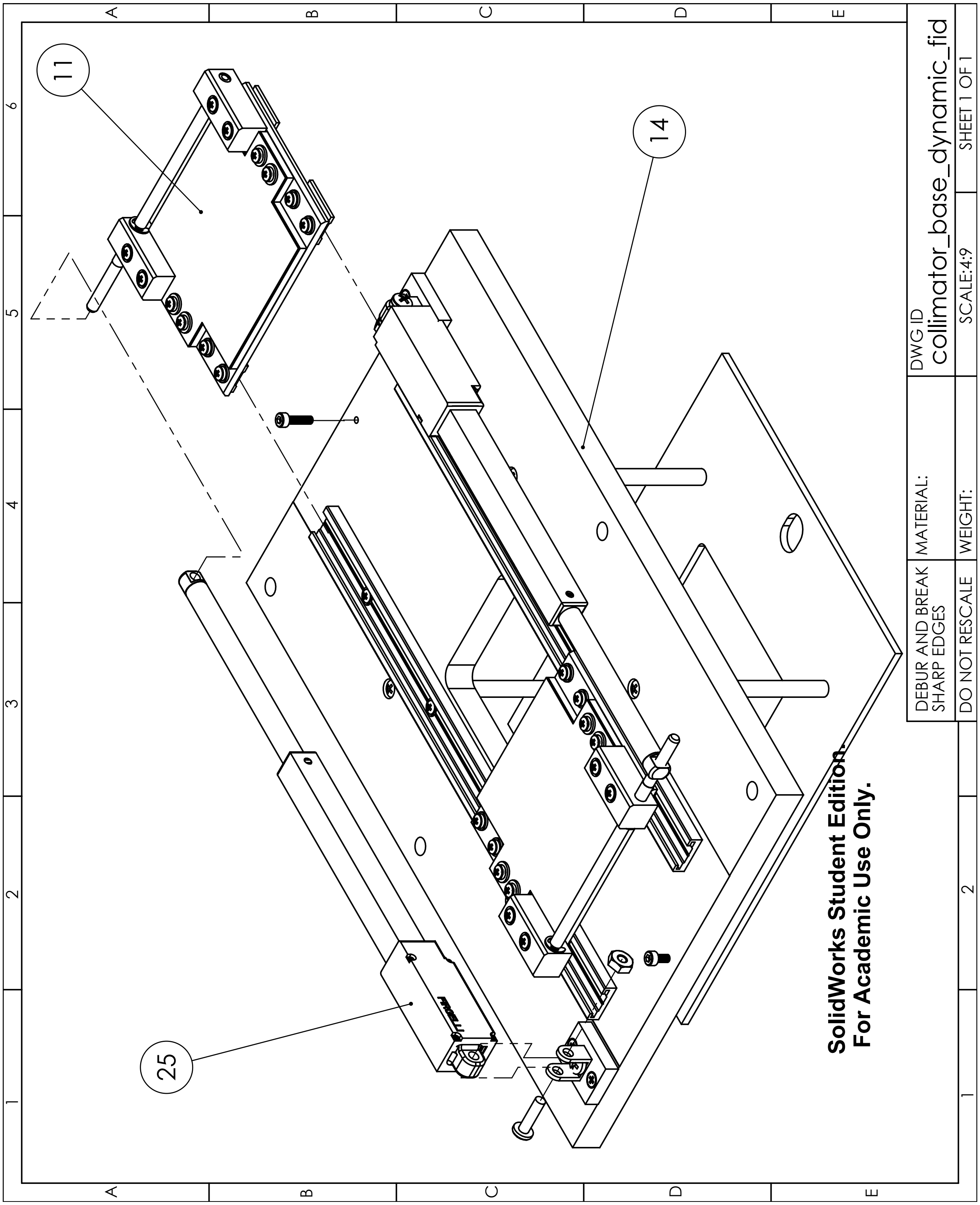

Figure A.2: Assembly of the collimator in the fiducial tracking configuraton. ㉕ is the firgelli actuator, ⑪ the blade assembly (Figure A.3) and ⑭ the plastic base plate (Figure A.11)

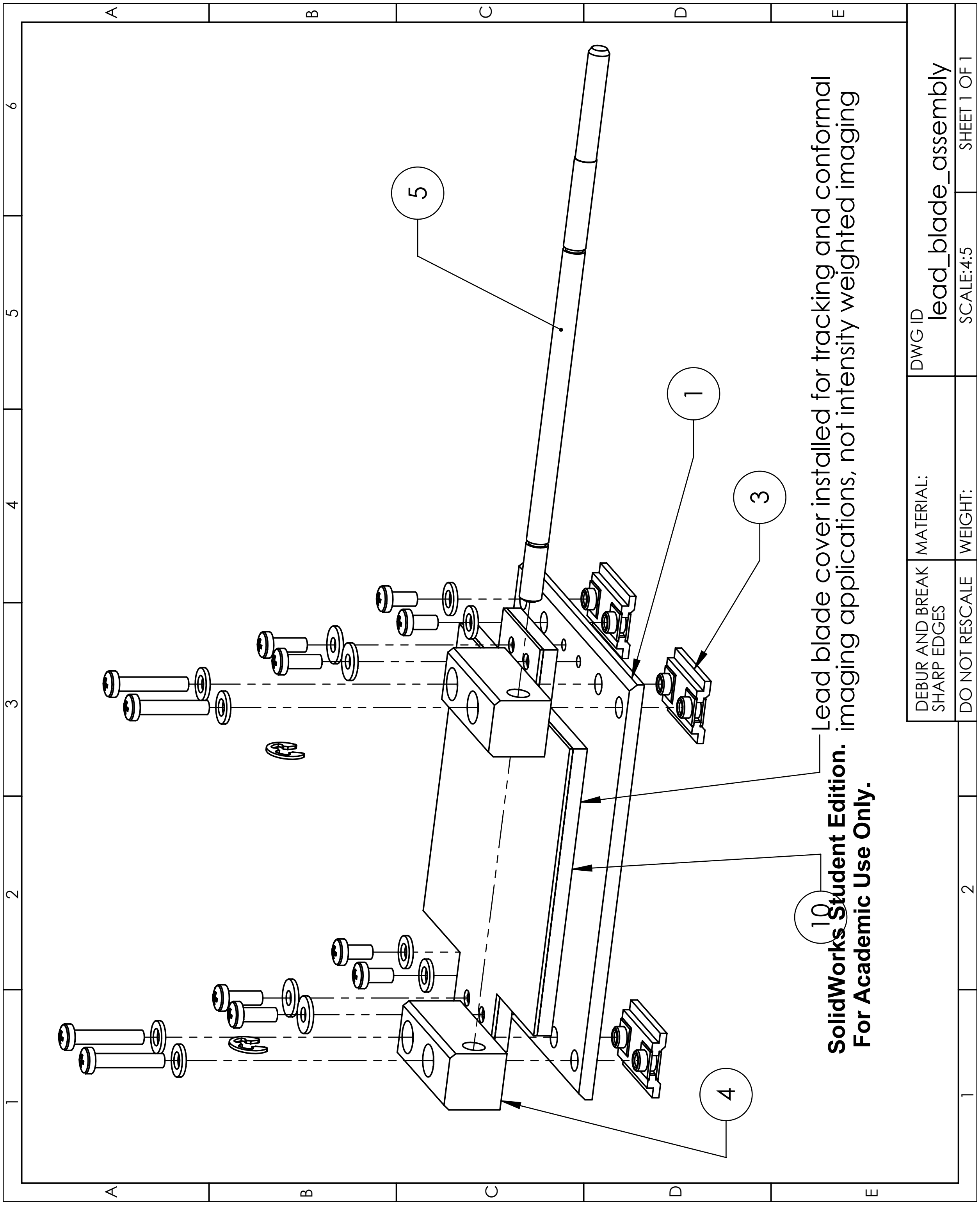

Figure A.3: Assembly of the blade car with lead cover. ① is the copper blade (Figure A.4), ③ is the Igus Drylin carraige, ④ (Figure A.5) connects the drive rod ⑤ (Figure A.6) to the blade. ⑩ is the optional lead blade cover (Figure A.8).

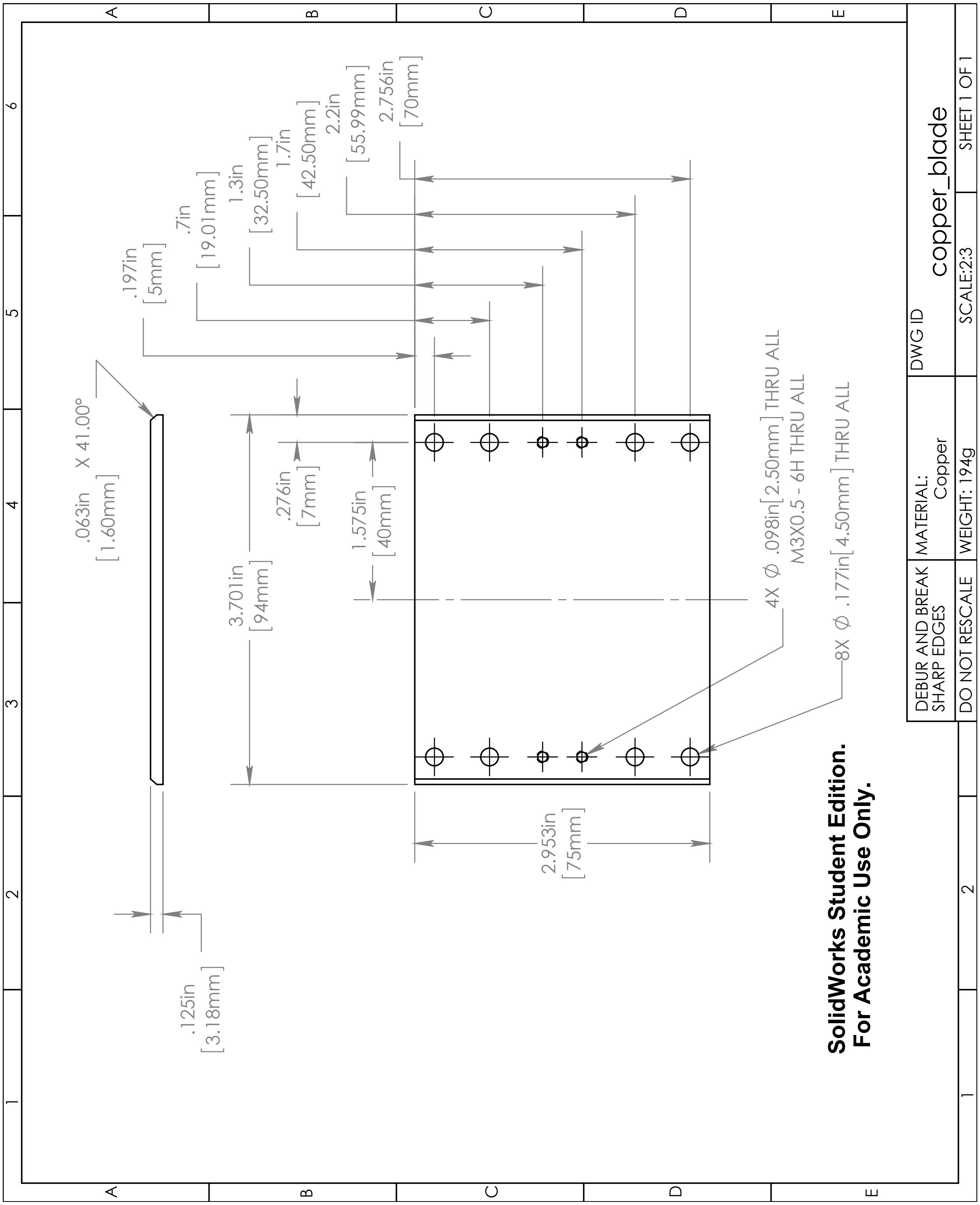

Figure A.4: The copper filter and structural base of the collimator blade car

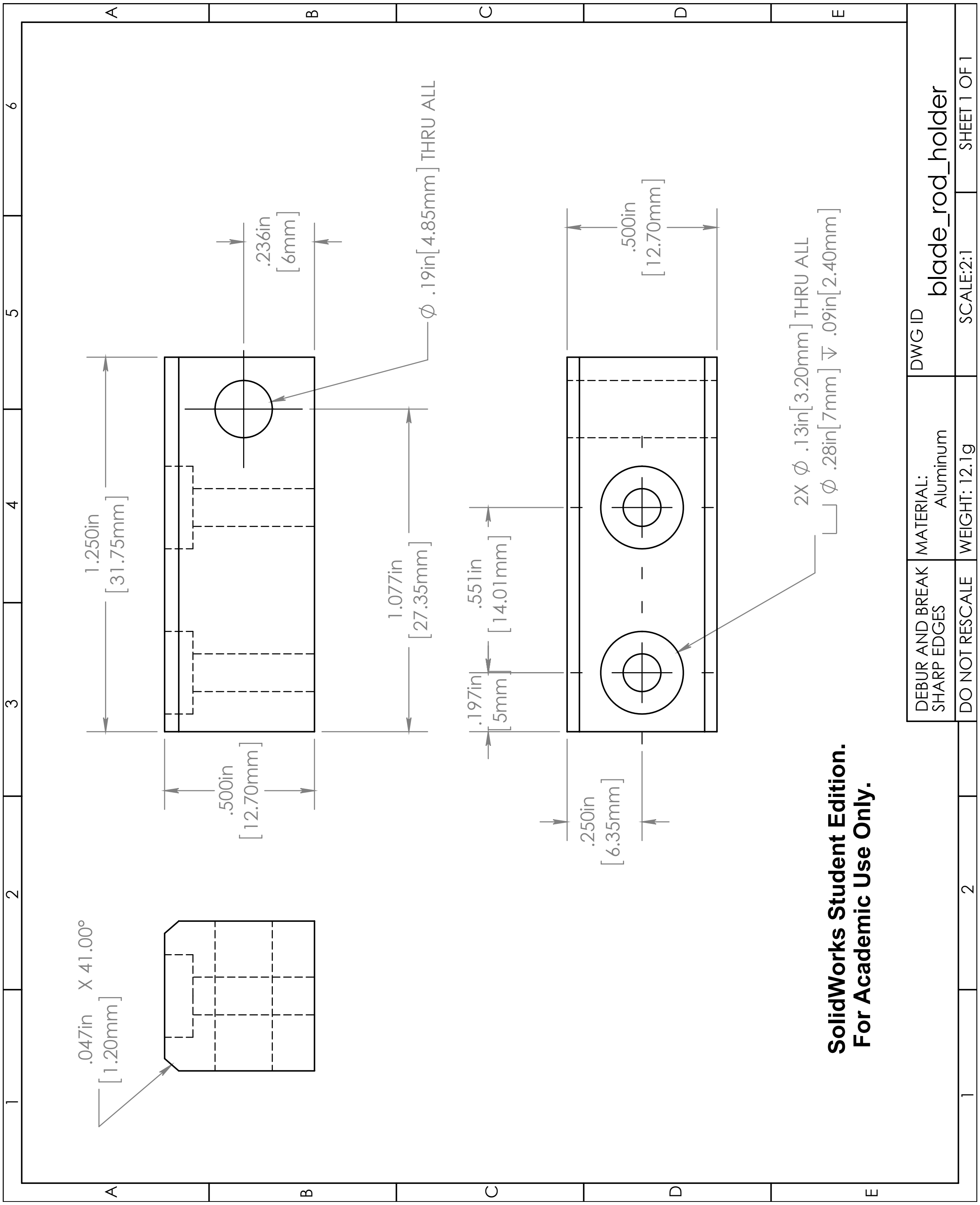

Figure A.5: A mounting block to attach the drive rod (Figure A.6) to the copper blade

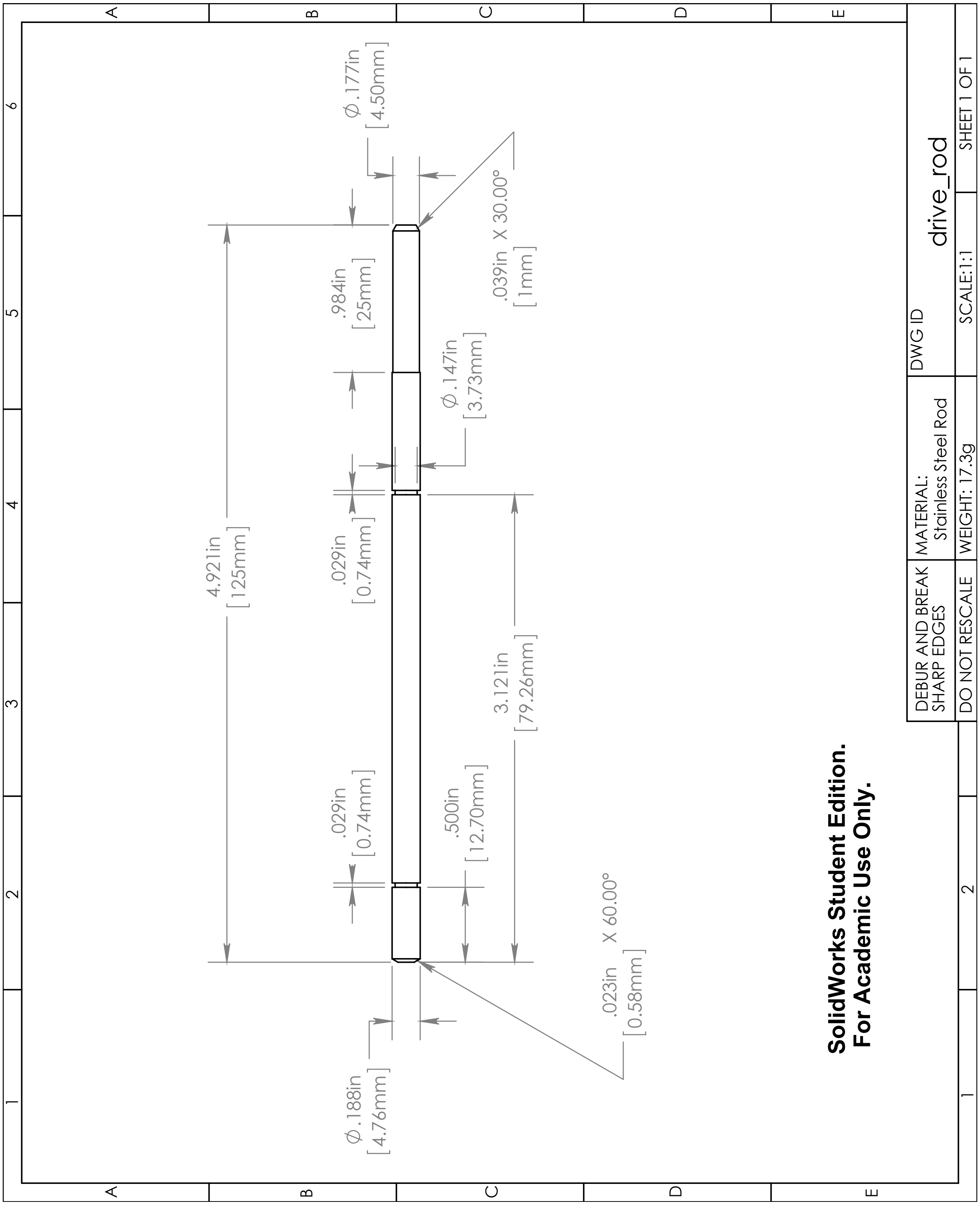

Figure A.6: Stainless rod that connectors the firgelli linear actuator to the blade car.

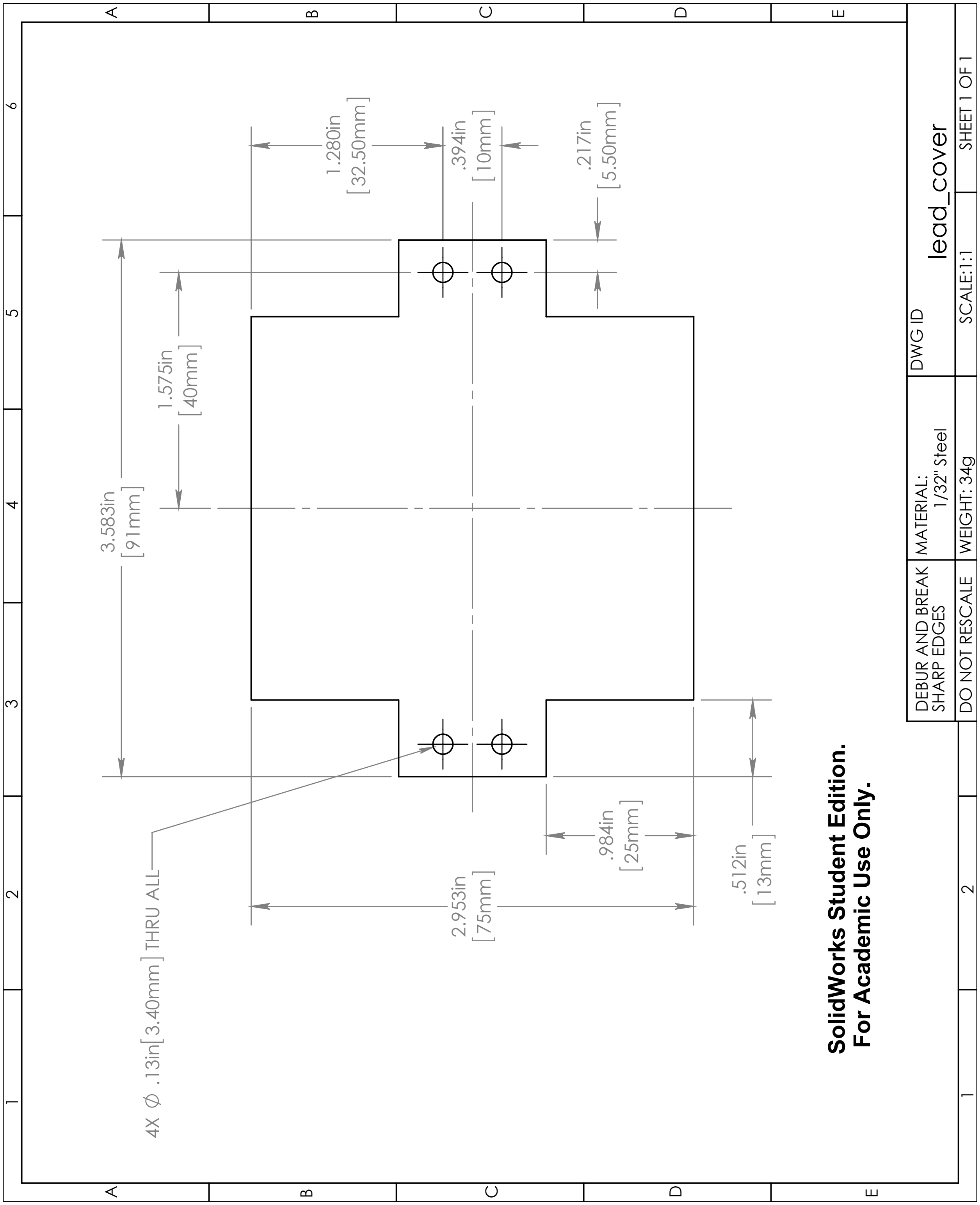

Figure A.7: A thin steal cover to match the lead blade (Figure A.8) to give structural ridgity

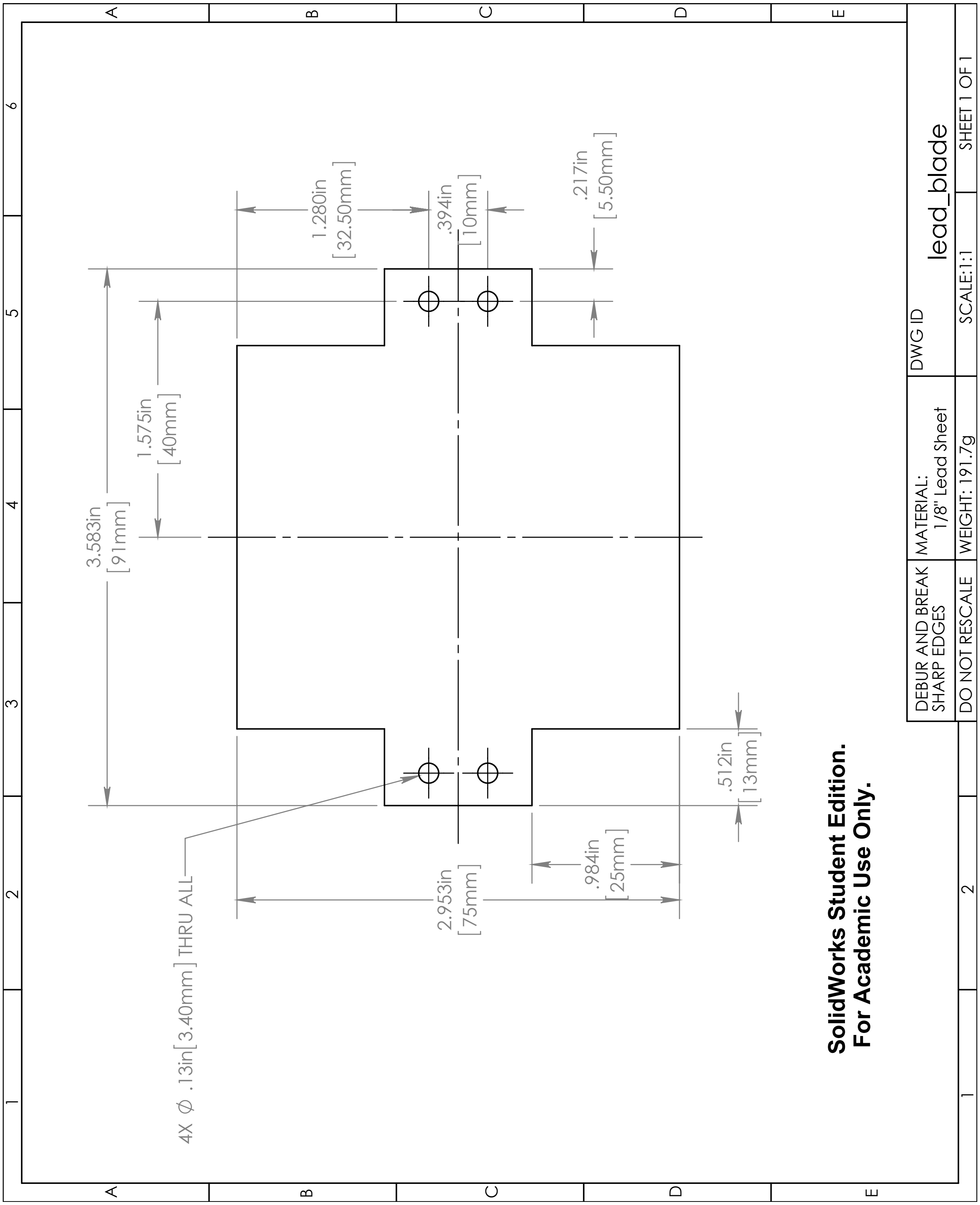

Figure A.8: The lead blade that can be mounted on top of the copper blade for radio-opaque applications.

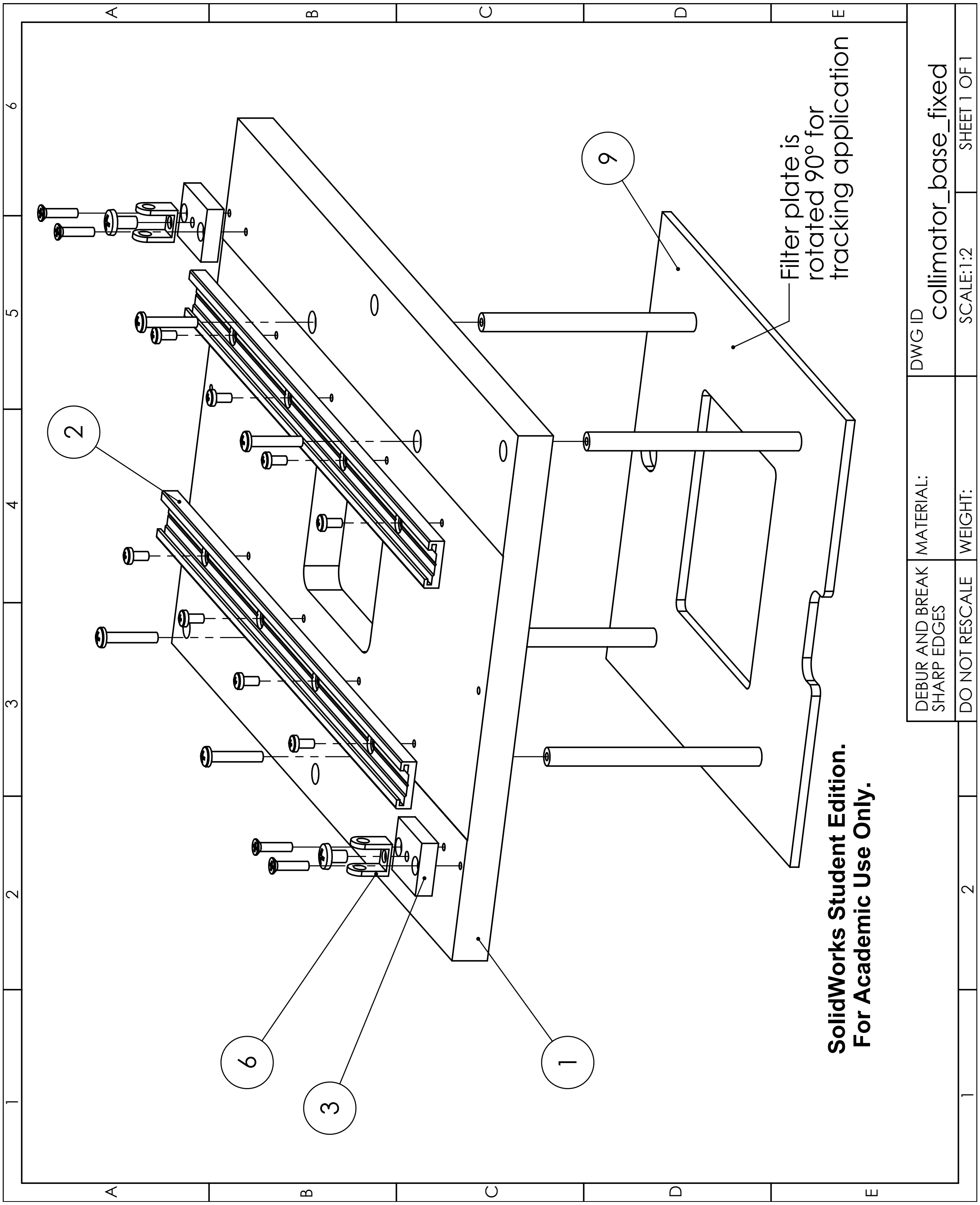

Figure A.9: Exploded assembly of the static parts of the collimator. The plastic base plate ① (Figure A.11) is attached to the filter plate ⑨. The firgelli motor mounts ⑥ are raised off the base plate with spacers ③ and the igus rails ② are attached.

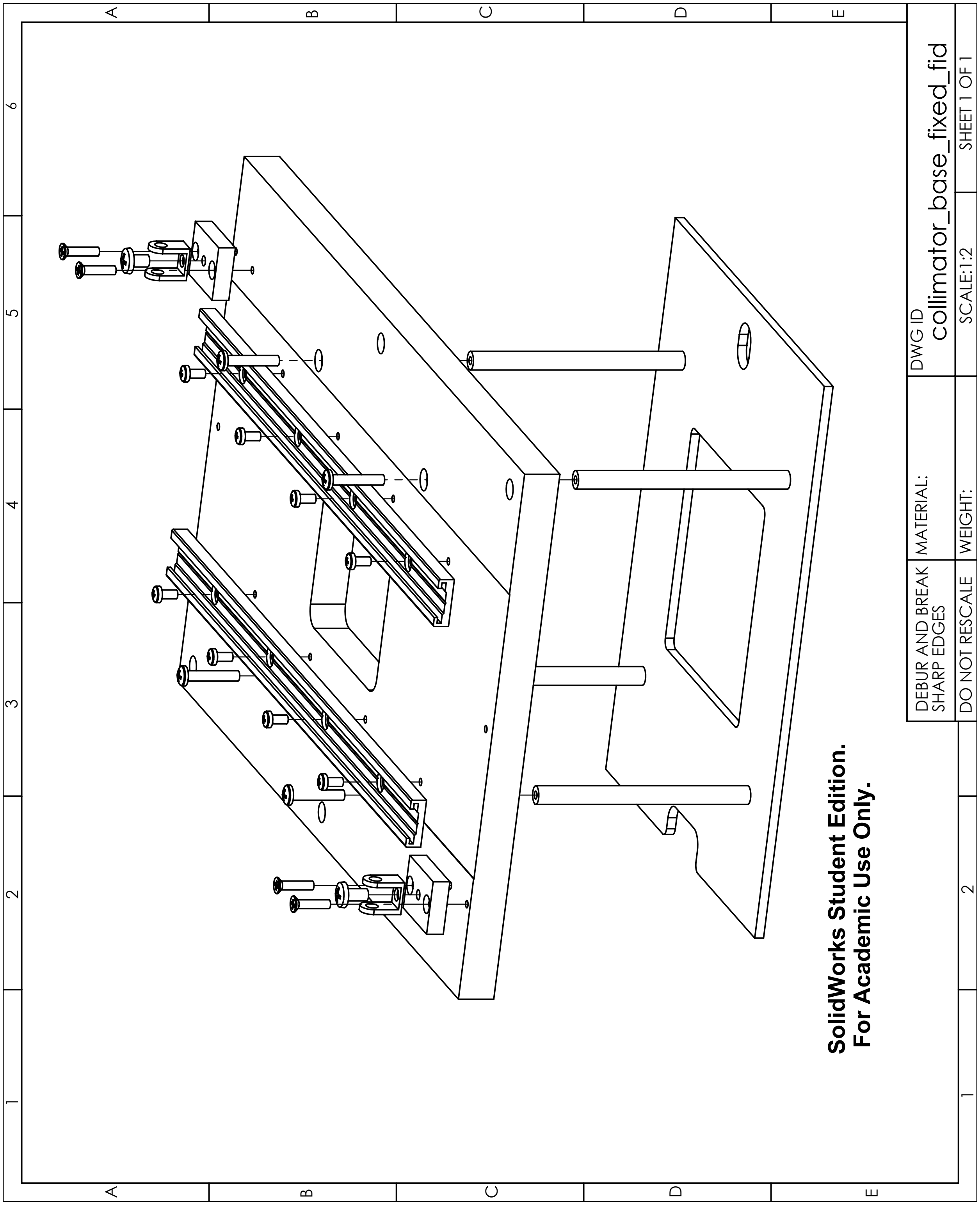

Figure A.10: Same as Figure A.9 however the mounting plate has been rotated 90° relative to the collimator base plate.

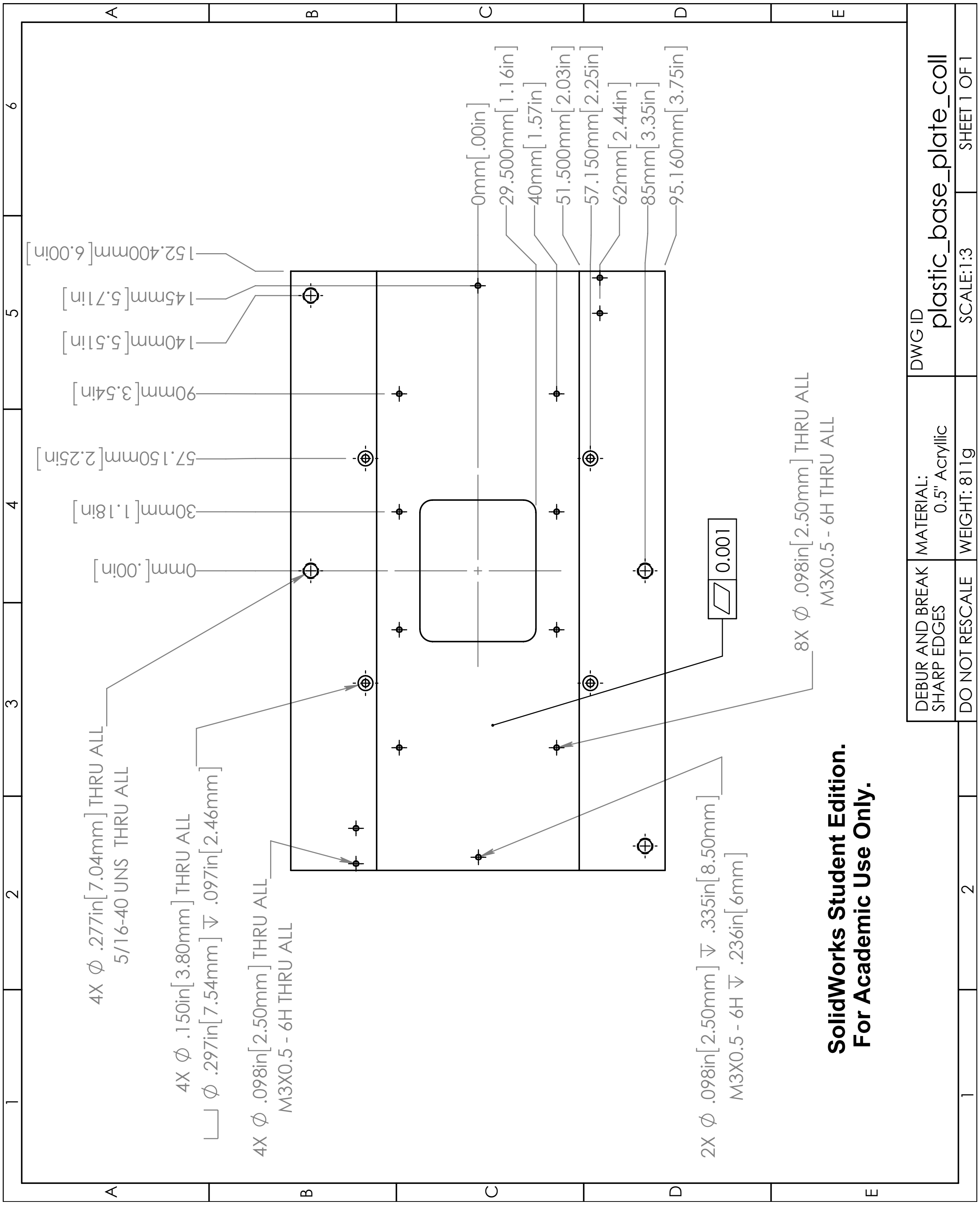

Figure A.11: Plastic base plate for the collimator.

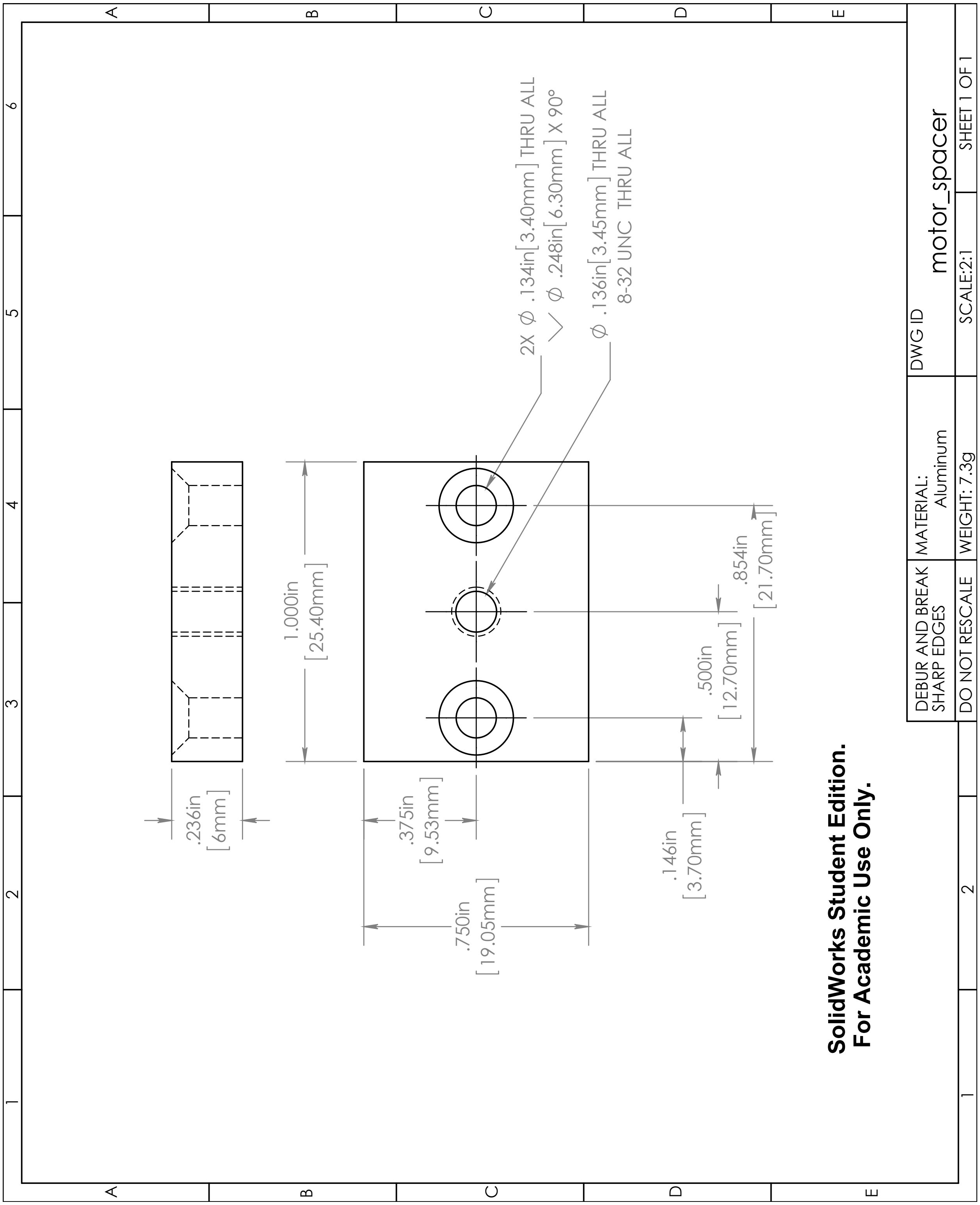

Figure A.12: A simple aluminum spacer to raise the mouter mounting bracket to the right high above the plastic base plate.

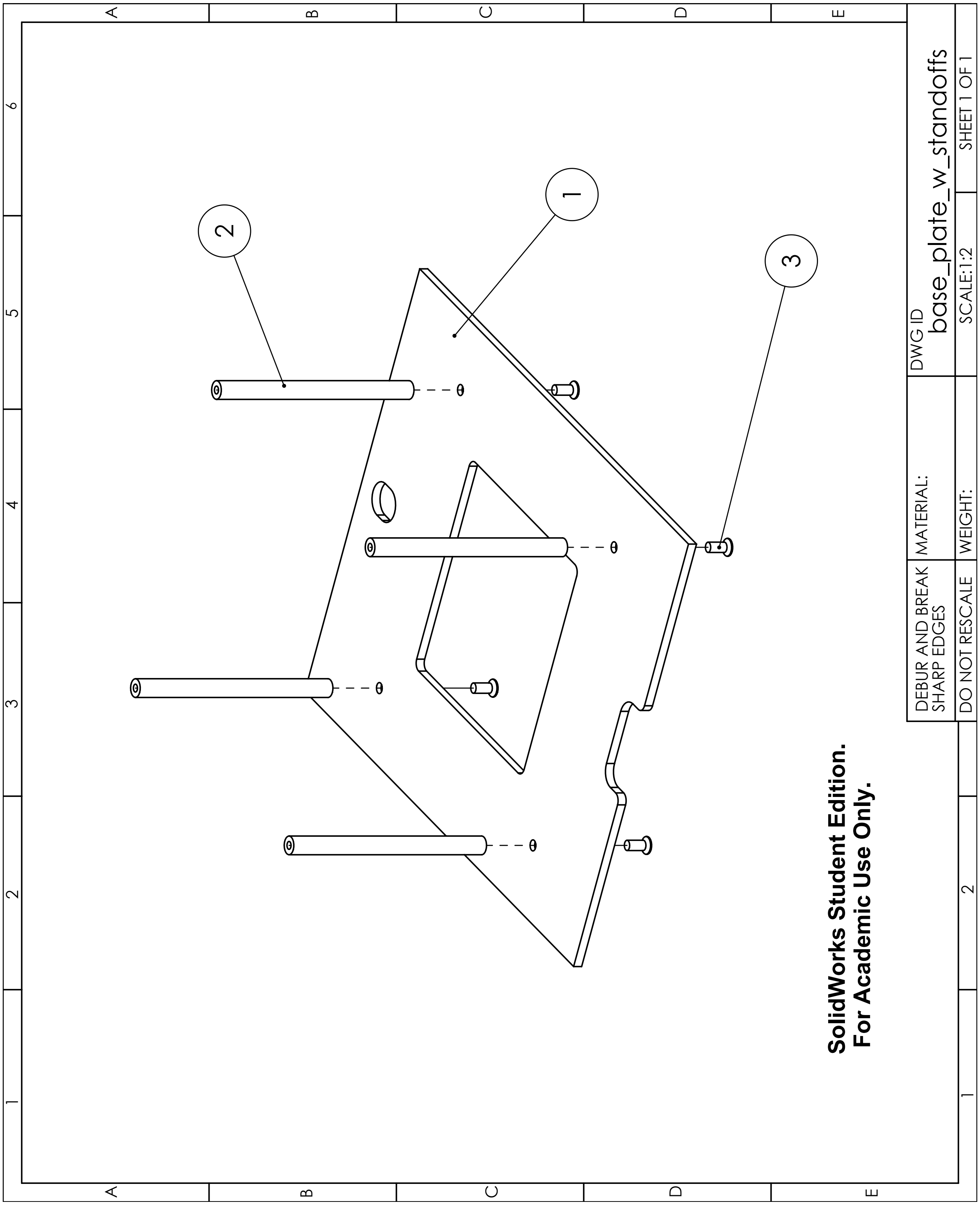

Figure A.13: An exploded assembly view of ① filter plate (Figure A.14) and ② stand offs (Figure A.15)

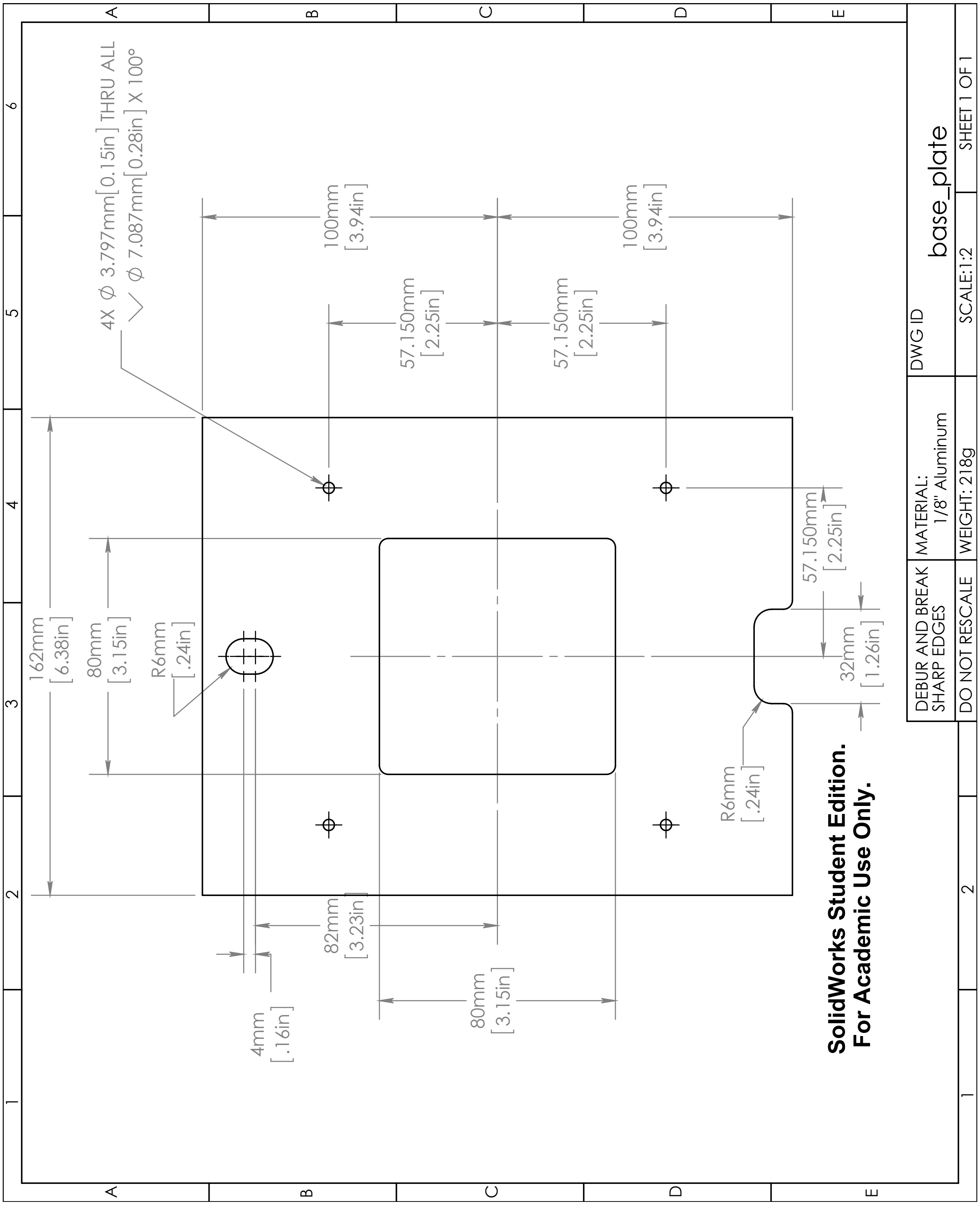

Figure A.14: Filter plate to match bowtie filter carrier

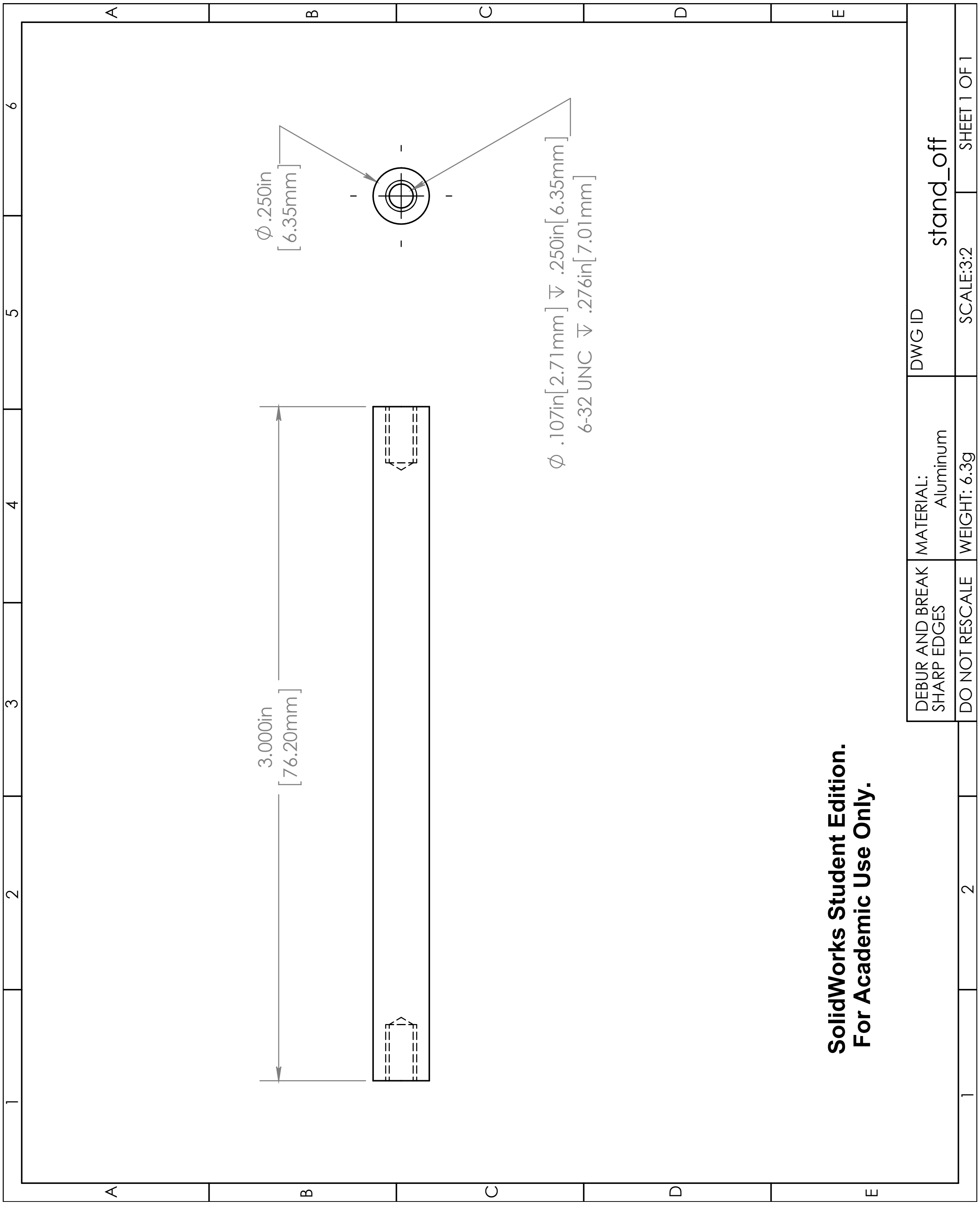

Figure A.15: Aluminum standoff to raise collimator off source housing

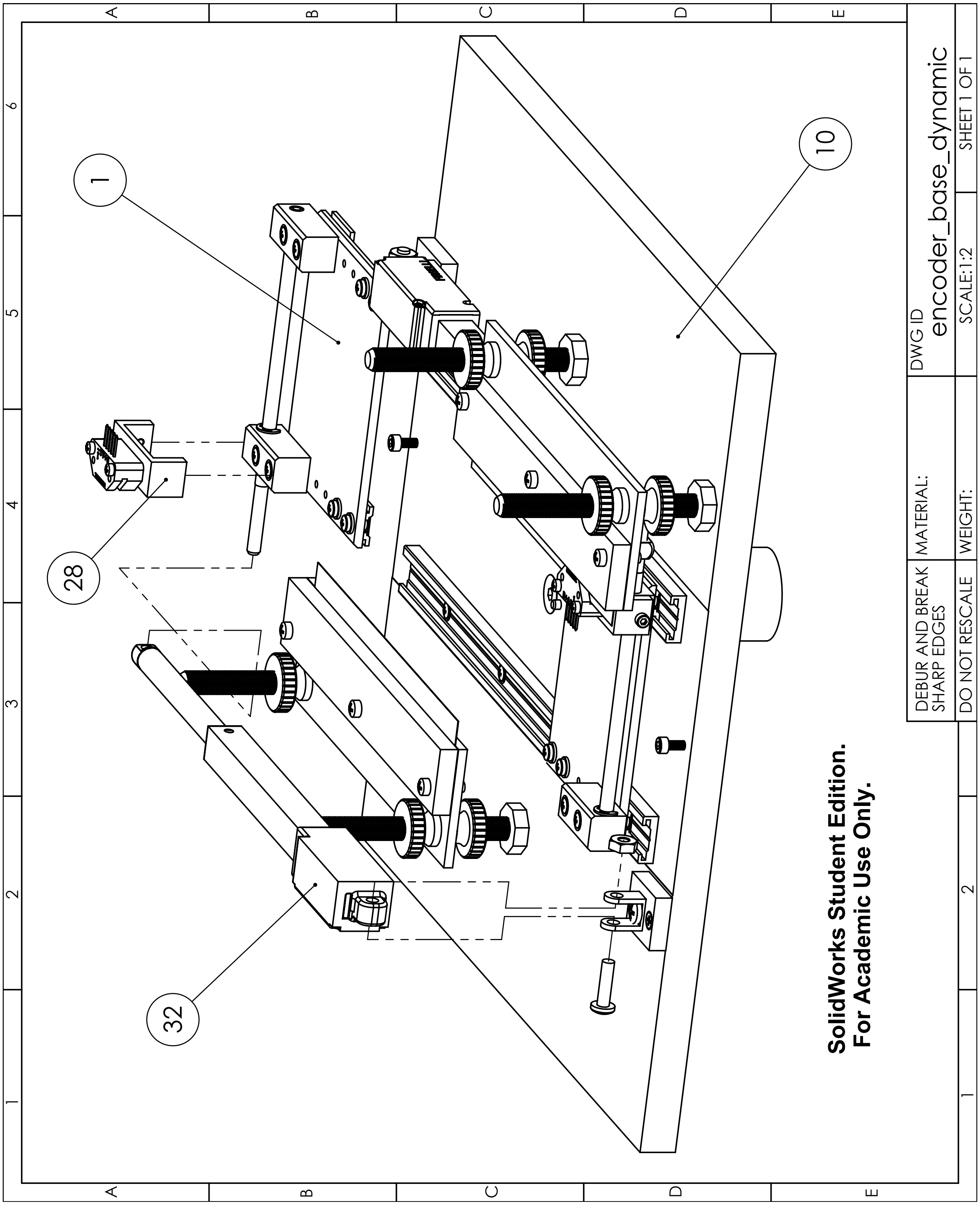

Figure A.16: Assembly used for the encoder feedback measurements. ㉘ holds the encoder readout and clamps to blade rod hold (Figure A.5). ㉜ is the firgelli actuator, ① the blade assembly (Figure A.3) and ⑩ the plastic base plate (Figure A.11).

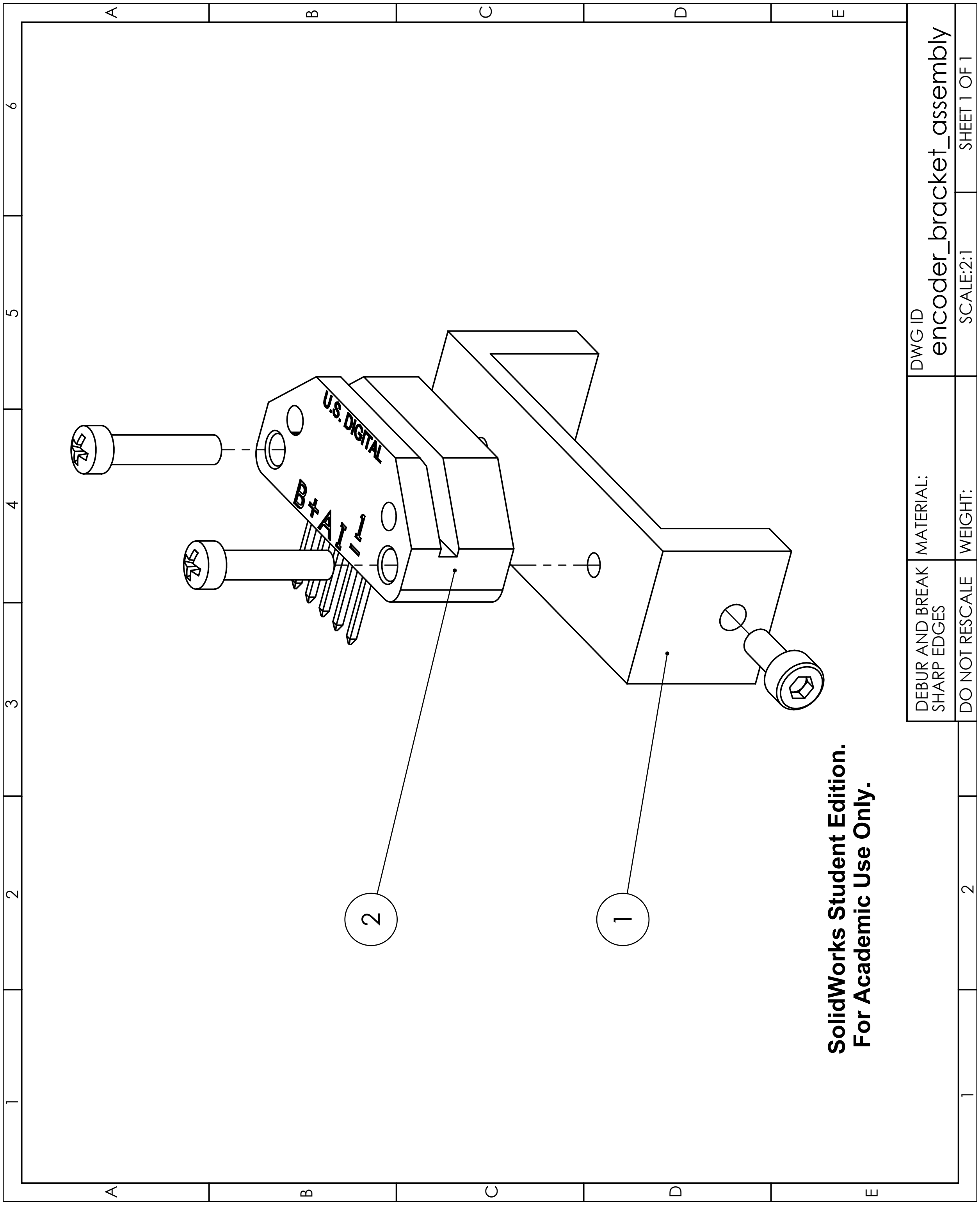

Figure A.17: The US digital encoder module ② is mounted to the encoder bracket ① (Figure A.18) which is attached to the blade rod holder (Figure A.5) and held in place with the set screw.

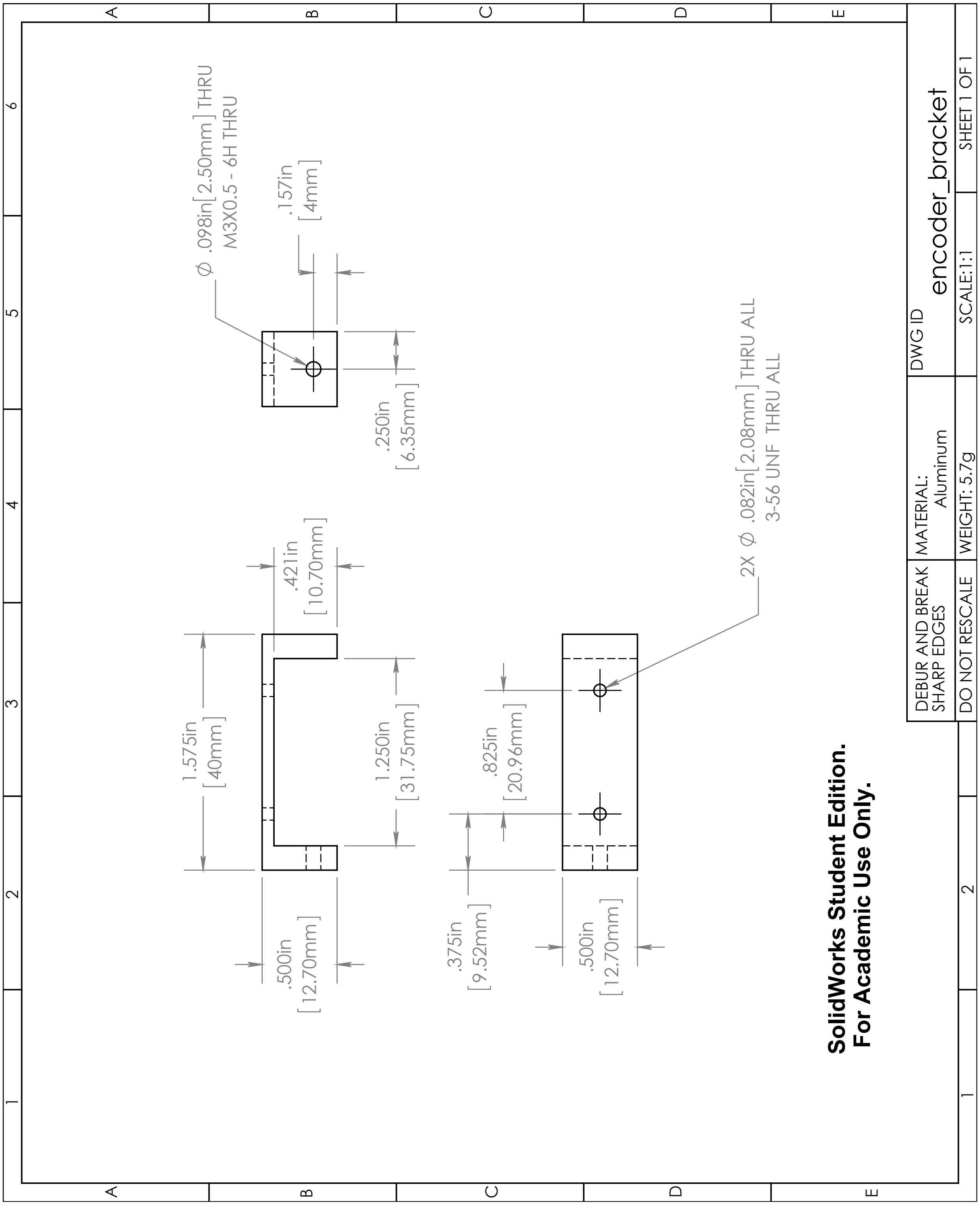

Figure A.18: A bracket to carry the encoder module and clamp onto the blade assembly

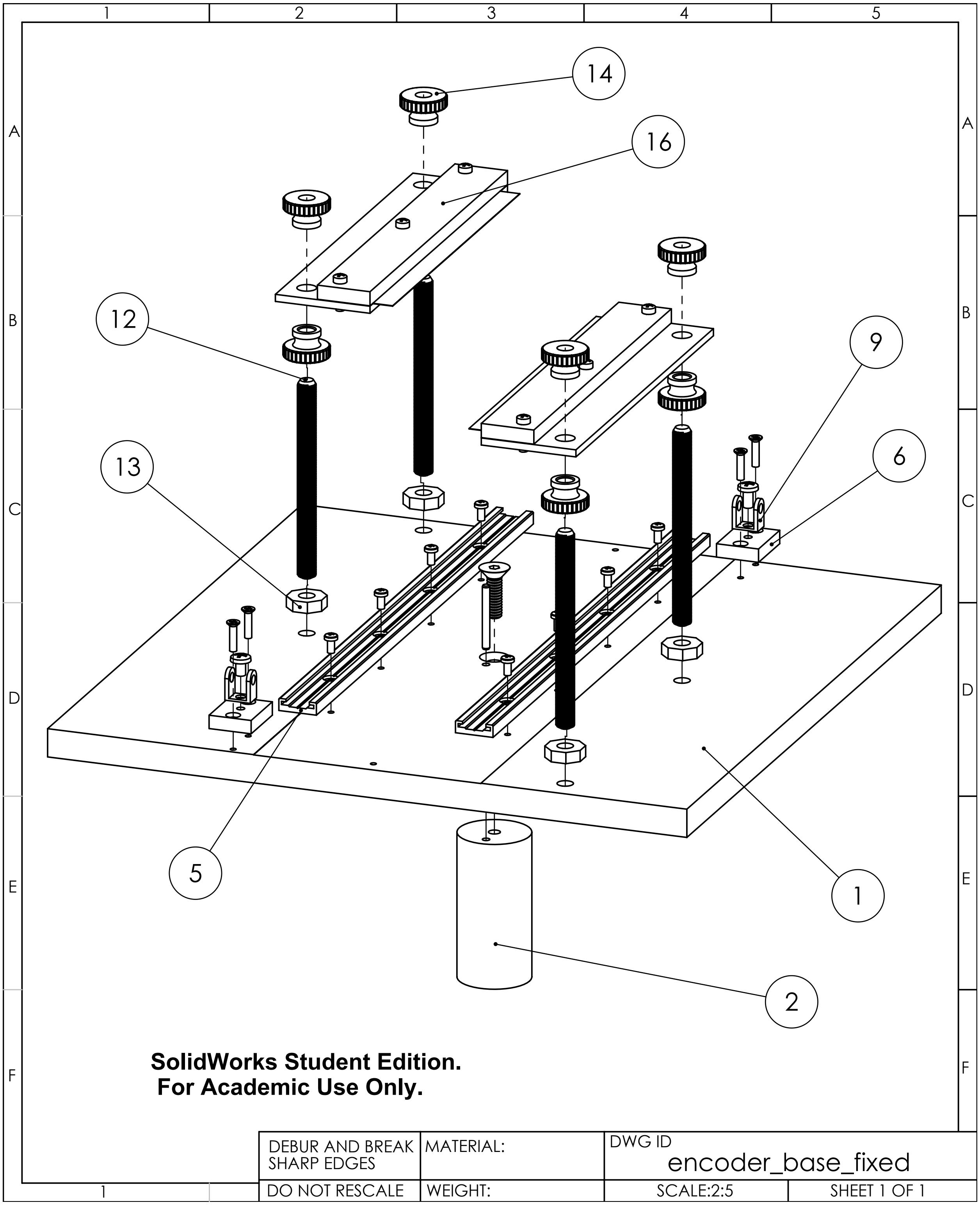

Figure A.19: Assembly of the stationary components of the encoder base assembly (Figure A.16). Part identification and assembly instructions given in section A.2.

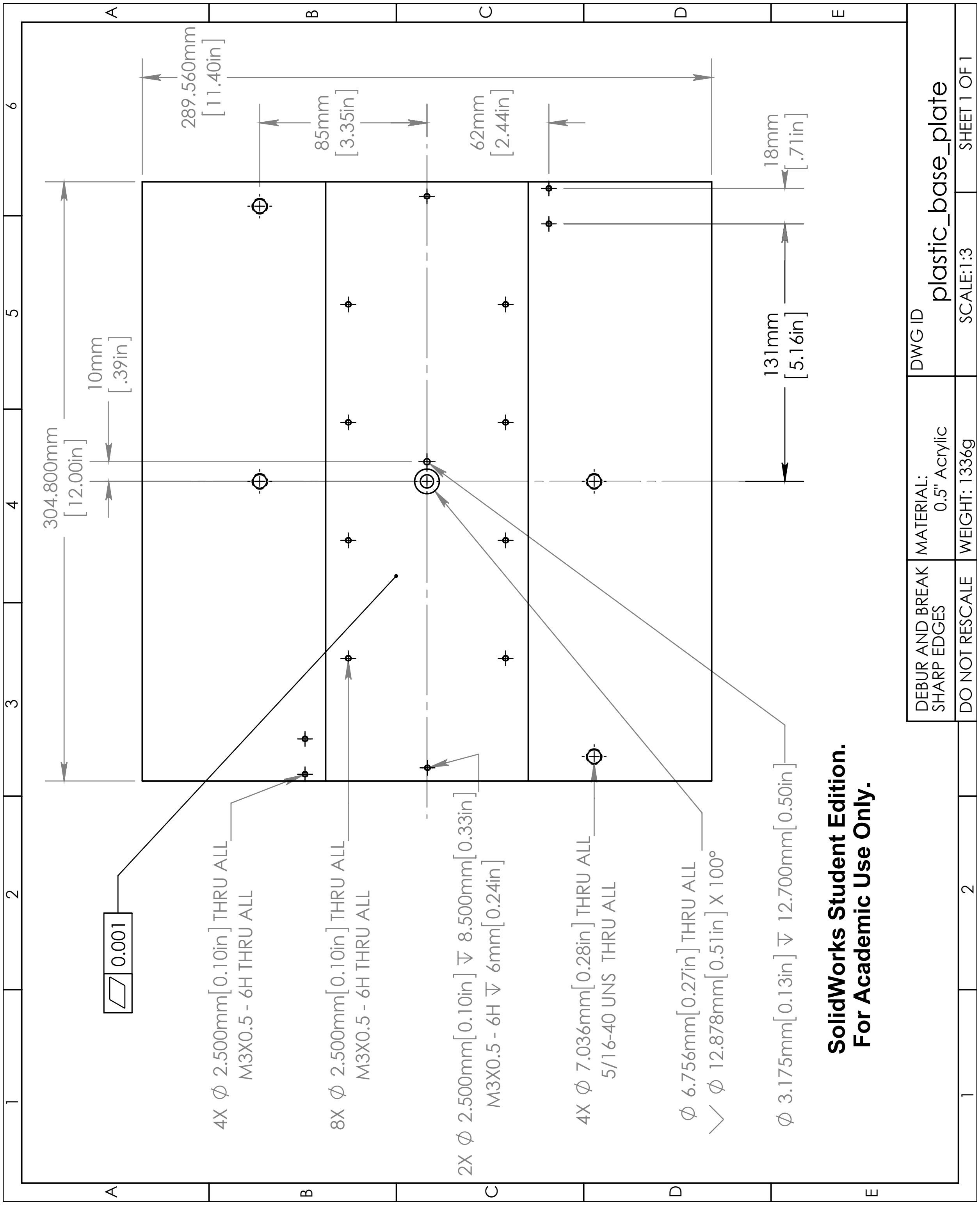

Figure A.20: The plastic base plate for the encoder assembly, is then further cut down into Figure A.11 for the collimator assembly.

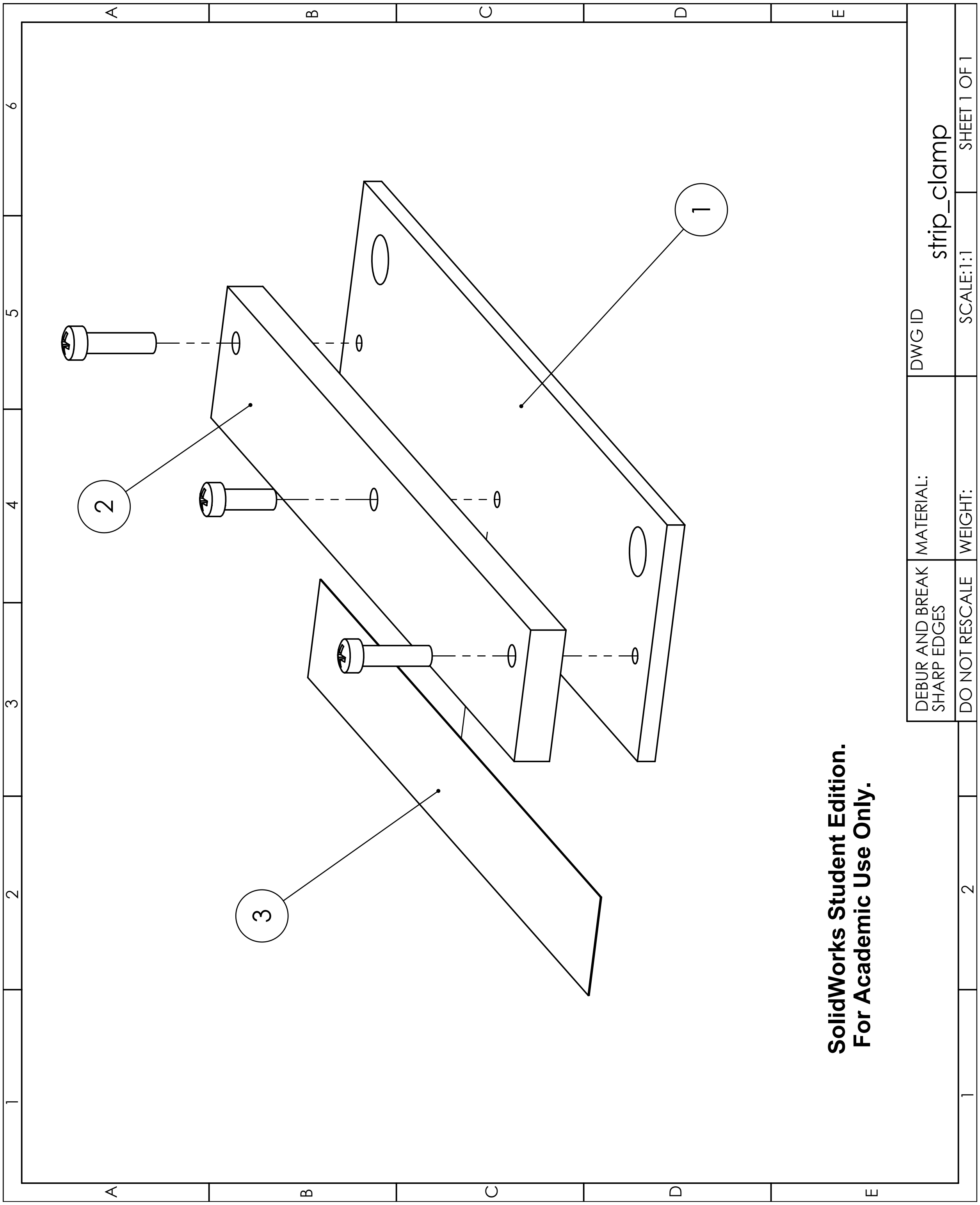

Figure A.21: Assembly of the clamp mechanism used to align and hold the transmissive strip ③ of the linear encoder mechanism. ① the lower piece (Figure A.22) and ② the upper (Figure A.23)

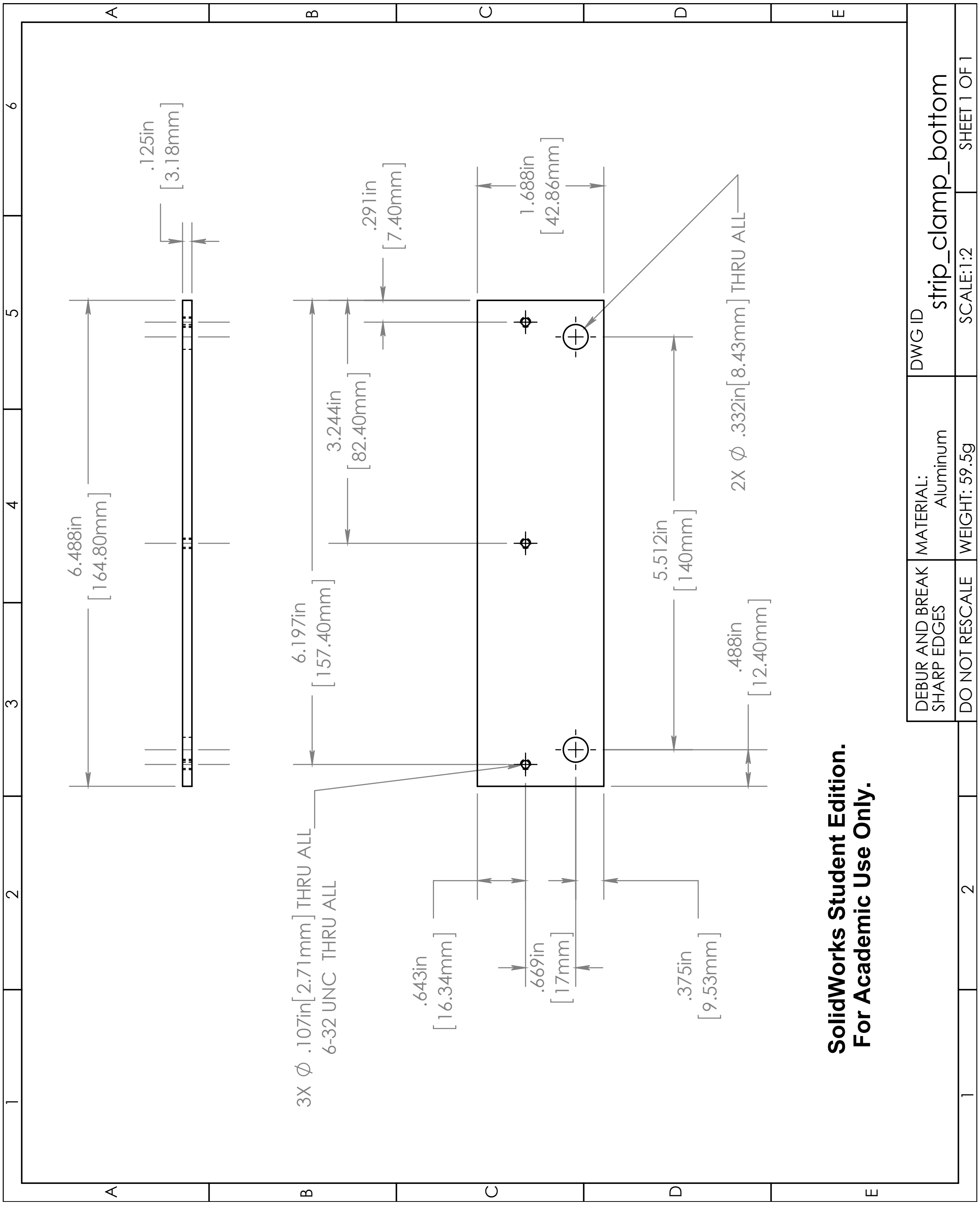

Figure A.22: The lower plate of the clamp mechanism for the transmissive strip of the linear encoder.

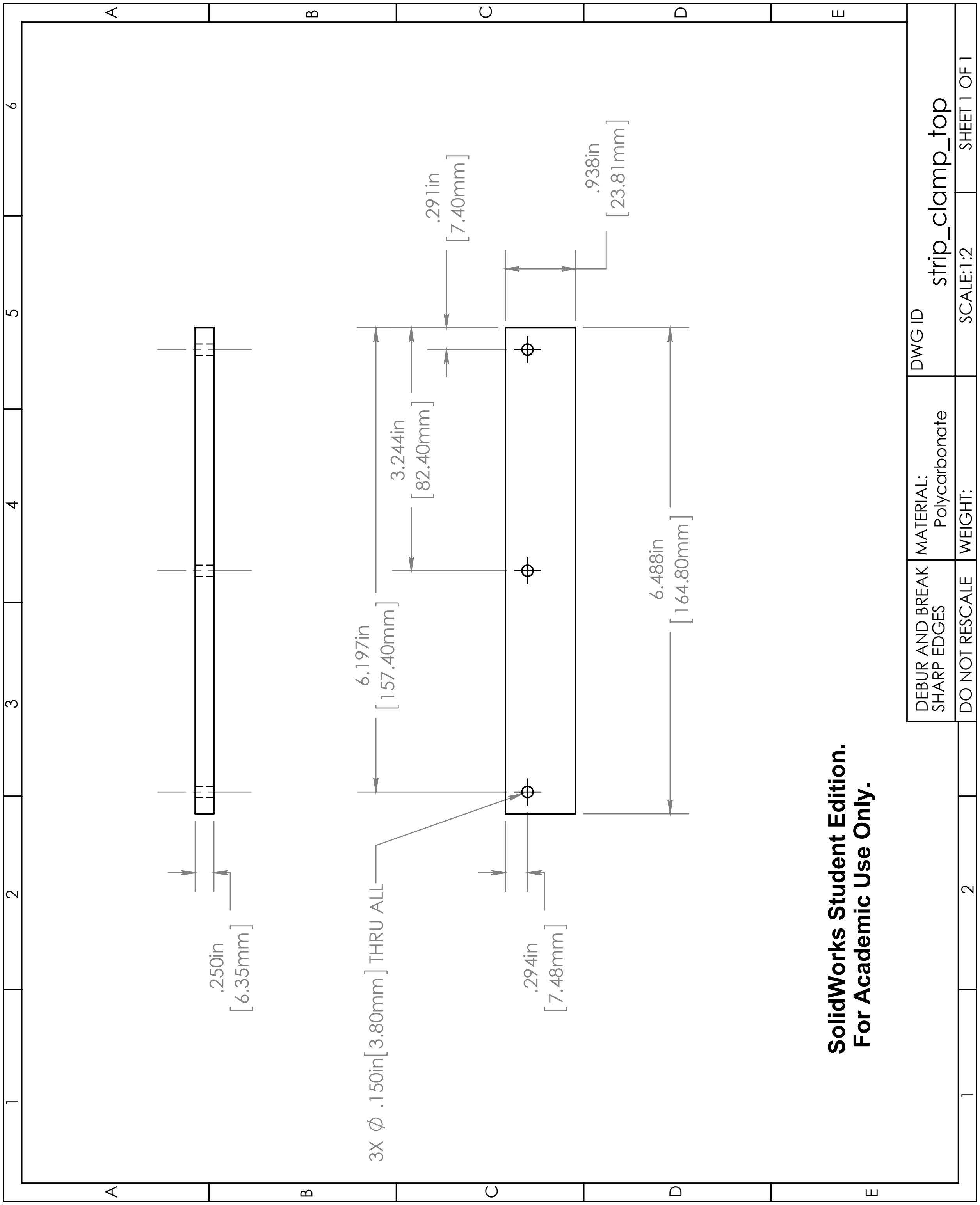

Figure A.23: The upper plate of the clamp mechanism for the transmissive strip of the linear encoder.

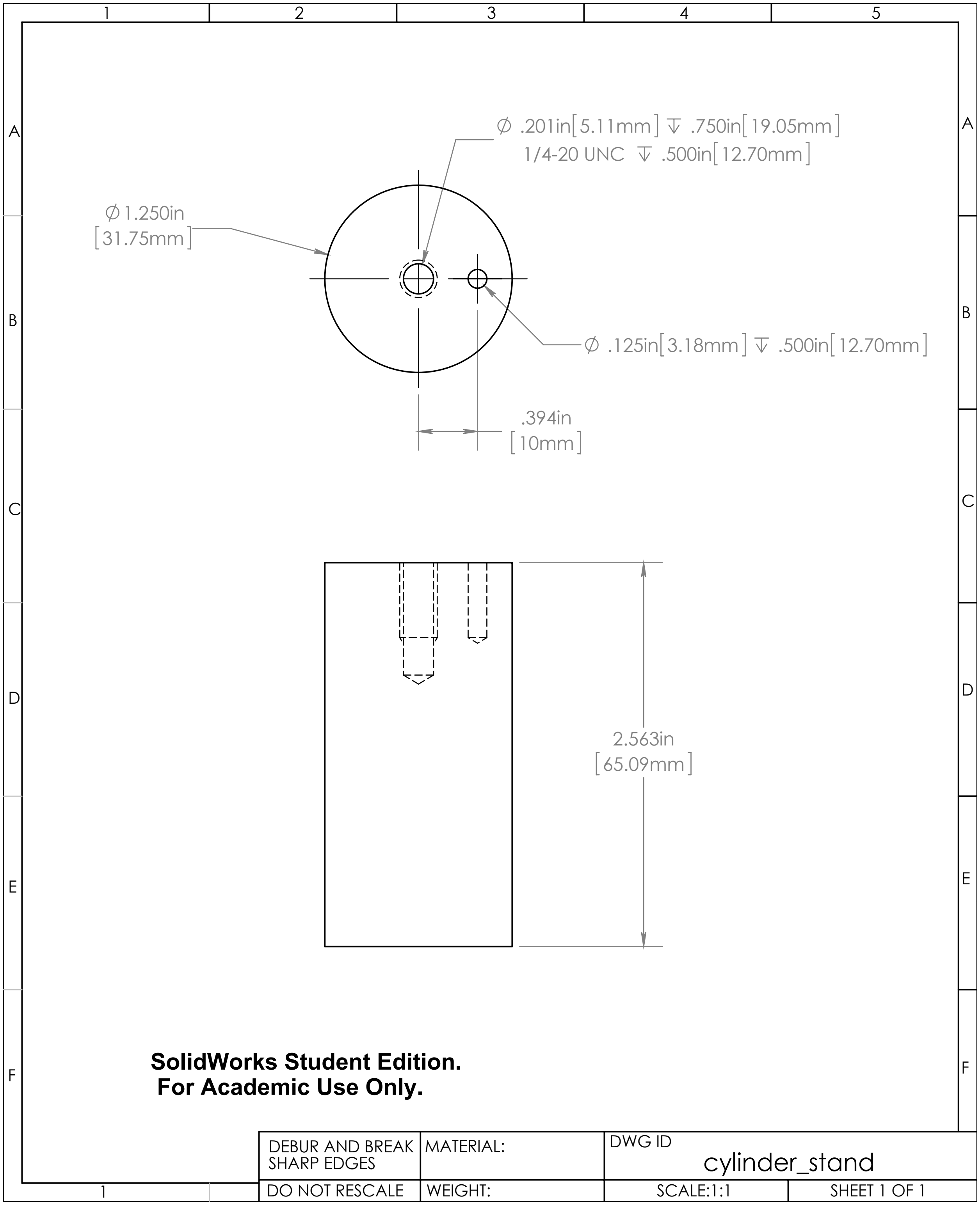

Figure A.24: A cylinder mounted to the back side of the plastic base plate in the encoder feedback assembly (Figure A.19). Used to hold assembly in rotary chuck. Cylinder is held in place with a center drilled screw and an alignment pin to prevent rotation relative to base plate.

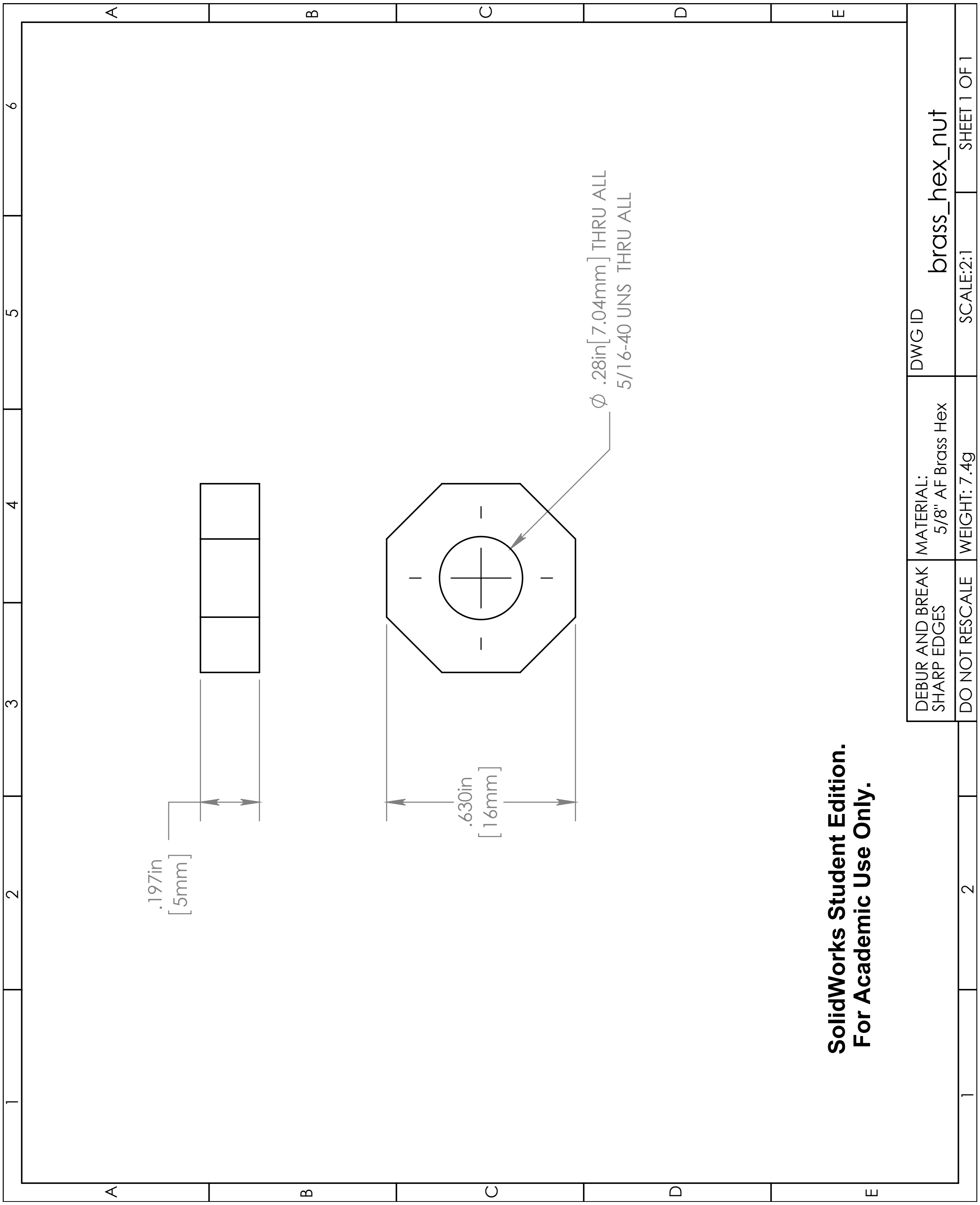

Figure A.25: Custom 5/16-40 hex nuts for securing the encoder clamp adjustment rods to the plastic base

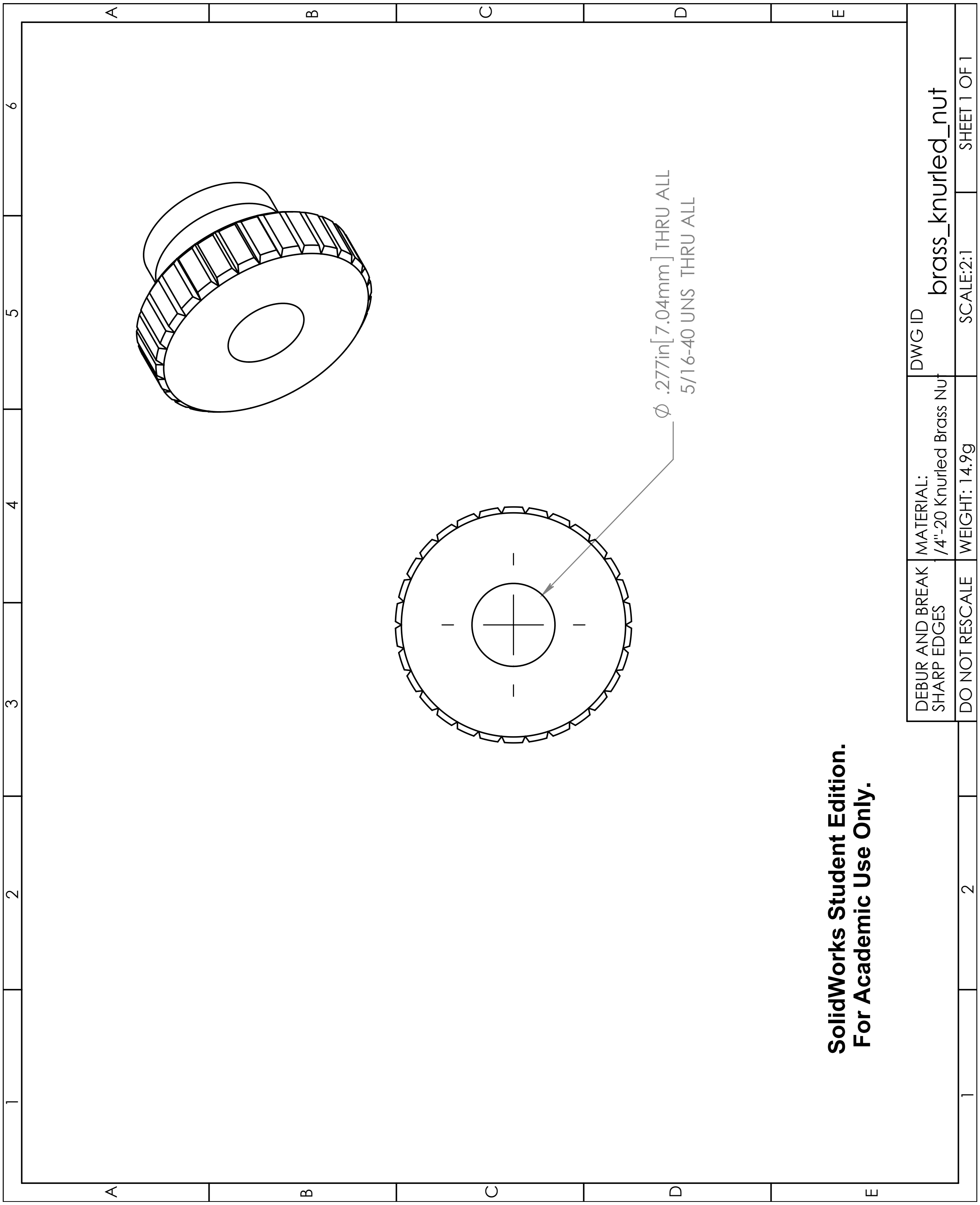

Figure A.26: Custom 5/16-40 knurled nuts for adjusting the encoder clamp height

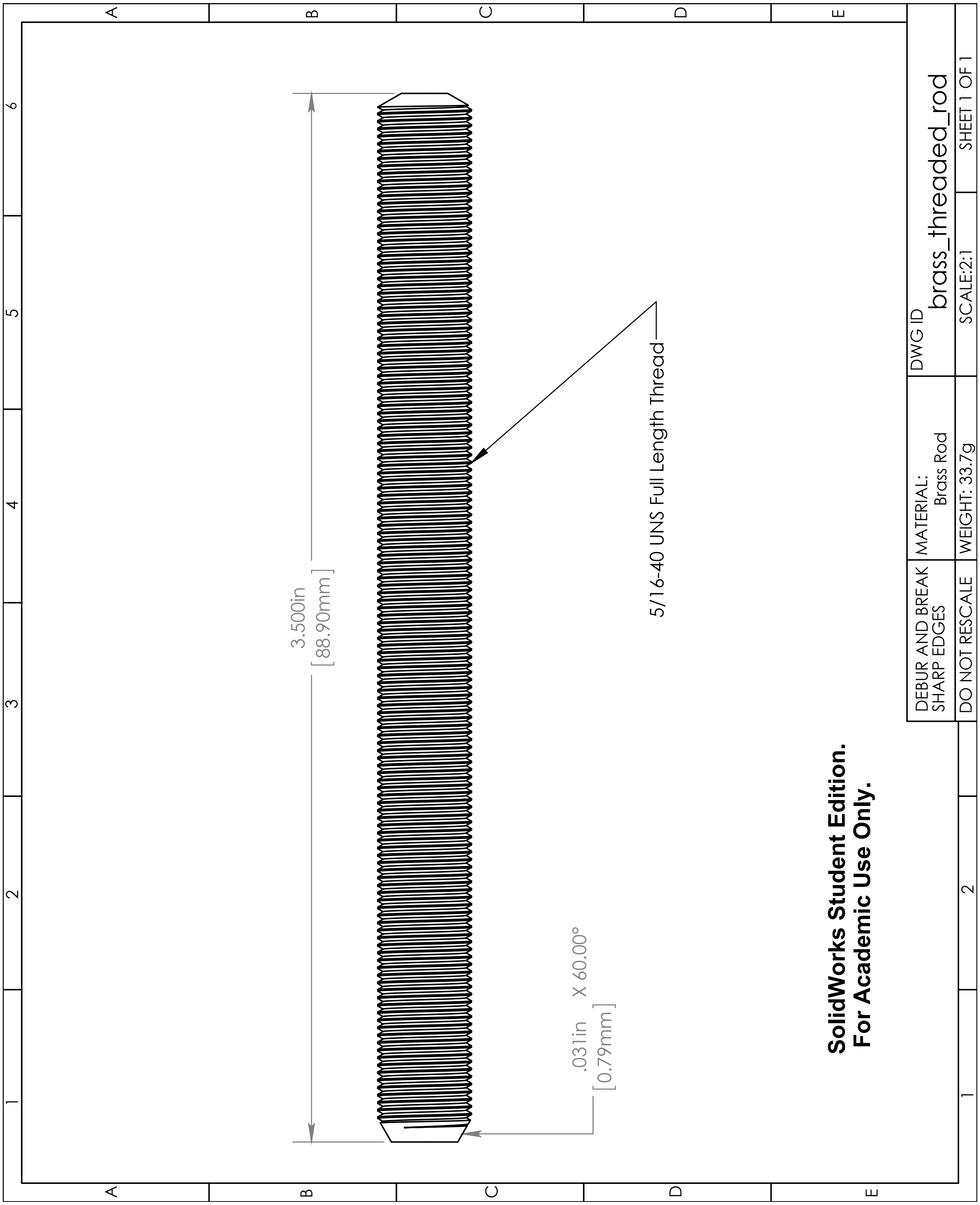

Figure A.27: 5/16-40 threaded brass rod for support and adjustment of encoder clamps

APPENDIX B

MONTE CARLO METHODS

Charles Pelizzari, Erik Pearson, Meredith Sadinski

To obtain quantitative estimates of dose and scatter reduction with conformal and IWROI imaging, we performed extensive simulations using the EGSnrc Monte Carlo system. A model of the OBI source was created with the BEAMnrc user code, using geometry from Varian (On-Board Imager and PortalVision Monte Carlo Data Package, Dwg #100040466-03, Rev1, Varian Oncology Systems). The BEAMnrc component modules XTUBE, SLABS and JAWS were used to model the X-ray tube's W95-Rh5 rotating anode, glass / oil / polycarbonate composite exit window, Al prefilter, upper and lower lead OBI blades, Cu or Pb ROI filter blades, and intervening air gaps. Static filter blades were positioned 15 cm from the anode on the bowtie carrier, dynamic blades 10 cm farther from the anode on the dynamic collimator. Different filter blade materials and IWROI aperture sizes could then be modelled by changing the material and geometry parameters in the relevant component module. The origin of the BEAMnrc coordinate system was located 1 cm above the center of the anode with the Z-axis along the output beam direction. A 0.5 mm diameter electron beam at energy 125 keV impinged on the center of the anode at an angle of 12° above the XY plane and in the XZ plane. The bowtie filter was not included since in our experiments it was replaced with either static filter blades or the dynamic collimator mount. The OBI model is shown in Figure B.1. Selected properties of the simulations are given in the table below.

Three-dimensional dose distributions were computed using the DOSXYZnrc user code. For static IWROI imaging, the beam size and position do not vary with angle. For this case it was possible to compute a single phase space plane just downstream of the ROI blades, which was then sampled for multiple angles of incidence to simulate the CBCT irradiation (DOSXYZnrc "source 8"). The phase space was created from a simulation of

Parameter	Value(s)
Incident electron energy	125 keV
Beam geometry	0.5 mm circular parallel beam with -12° angle of incidence
Global electron cutoff ECUT	512 keV
Global photon cutoff PCUT	1 keV
Physical processes and variance reduction techniques	Directional bremsstrahlung splitting Bremsstrahlung cross-section enhancement (anode) Electron impact ionization Atomic relaxation Bound Compton scattering Rayleigh scattering

Table B.1: Monte Carlo simulation parameters

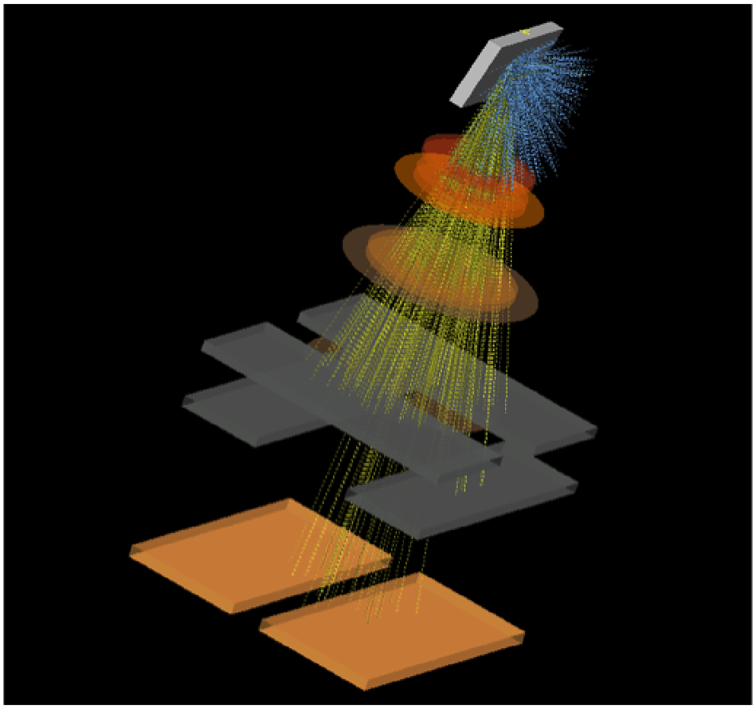

Figure B.1: BEAMnrc model of the OBI source showing anode (light gray), X and Y blades (gray) and static Cu filters. For size scale, note distance from anode to copper blades is 15 cm. Disk structures represent the composite exit window and Al filter.

5×10^9 incident electrons, resulting in 5×10^7 photons downstream of the Cu IWROI filters set for a 5 cm × 20 cm aperture at isocenter. This took approximately 150 total computation hours, but was run in parallel on the SIRAF cluster allowing the results to be obtained overnight. These photons were used to simulate 360 equally-spaced beams propagating through a 3D model of the Rando head created from a simulation CT scan. Approximately 10 million incident photons were simulated at each angle. The CTCREATE program was used to generate the model with 3 tissue classes (air, ICRU soft tissue, ICRU bone) on a grid of 2.5 mm × 2.5 mm × 2.5 mm, and dose was accumulated on this same grid. Standard error in scored dose was $< 1\,\%$ at all points. The dose calculation process took 10 hours.

For dynamic ROI imaging the incident beam size and position vary with gantry angle, so a single phase space source could not be used to simulate this technique. In this case we used DOSXYZnrc "source 9", a full BEAMnrc simulation for each projection angle, each with its own asymmetric jaw settings conforming to the ROI. It was found that simulating 1 million incident photons at each of 180 equally spaced angles gave satisfactory results, with 1 % to 2 % dose uncertainty within the ROI and 2 % to 3 % elsewhere.

Conveniently DOSZYZnrc scores dose in Gray per incident particle in the original simulation, i.e. per electron incident on the anode. Thus the results were readily scaled to dose per milliamp-second and thence to integrated mAs for the CBCT scans:

$$\begin{aligned} D_{CBCT}(mGy) =& D(Gy/electron) \div 1.602 \cdot 10^{-19} \times I(mA) \\ & \times t(sec/projection) \times N(projections/scan) \end{aligned} \tag{B.1}$$

For the central static ROI, simulations were done for a 20 cm × 20 cm open field (normal CBCT scan), lead ROI blades (conformal ROI scan) and 3 mm thick copper blades (IWROI scan). For interior ROIs the conformal scan cannot be reconstructed using analytic methods, but this simulation was done to assess the degree to which the IWROI technique approaches the dose sparing of an "ideal" conformal scan. For the asymmetric ROI scans requiring the

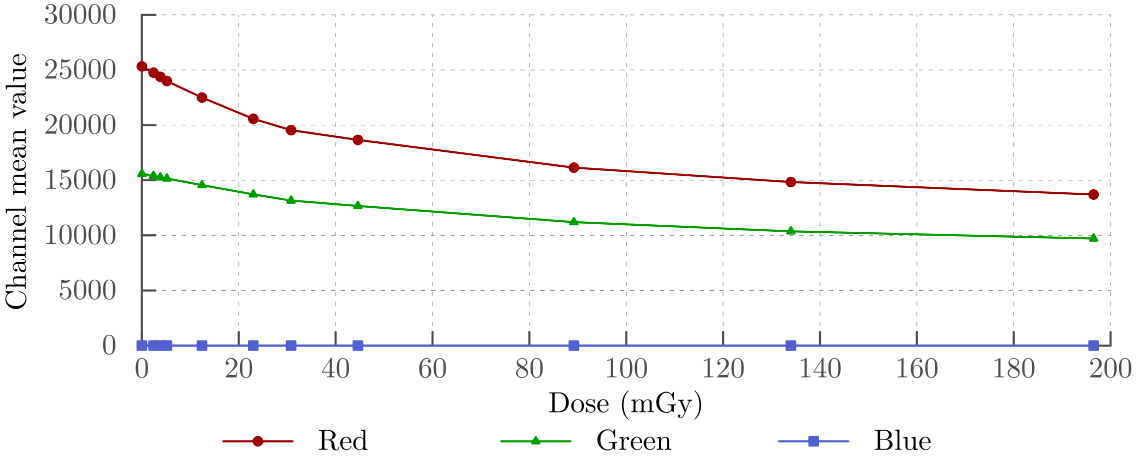

Figure B.2: Calibration curves for red, green and blue channels of XR-QA2 film for 125 kVp, W anode, 2 mm Al filtration.

dynamic collimator, open-field and IWROI scans were simulated.

Monte Carlo doses were compared to film measurements in a transverse plane of the RANDO phantom for several irradiation conditions. The measurement utilized Gafchromic XR-QA2 film which was calibrated using a 125kVp beam from a small animal irradiator (X-Rad225Cx, Precision X-ray, Inc) at 12 known doses from 0 mGy to 200 mGy. The resulting calibration curve is shown in Figure B.2. The calibration and RANDO experimental films were scanned (5 scans per film, averaged) on an Epson Perfection 10000XL color scanner and saved in TIFF files with 16 bits per color channel. Scanned images were converted to dose using a multichannel method based on the ratio of signals in the red and green channels (with XR-QA2 film the blue channel has no dose response). From the 2.5 mm × 2.5 mm × 2.5 mm DOSXYZnrc grid, a transverse plane was chosen reasonably close to the film plane, although small errors in both in plane and out of plane rotations due to setup differences remain. An example comparison is shown in Figure 4.14 for the static IWROI scan of a central 5 cm diameter region. The agreement between film and Monte Carlo doses in the interior is excellent, while near the surface the film doses appear a few mGy lower, which may be due to the difficulty of completely eliminating air gaps between the film and the RANDO slabs.

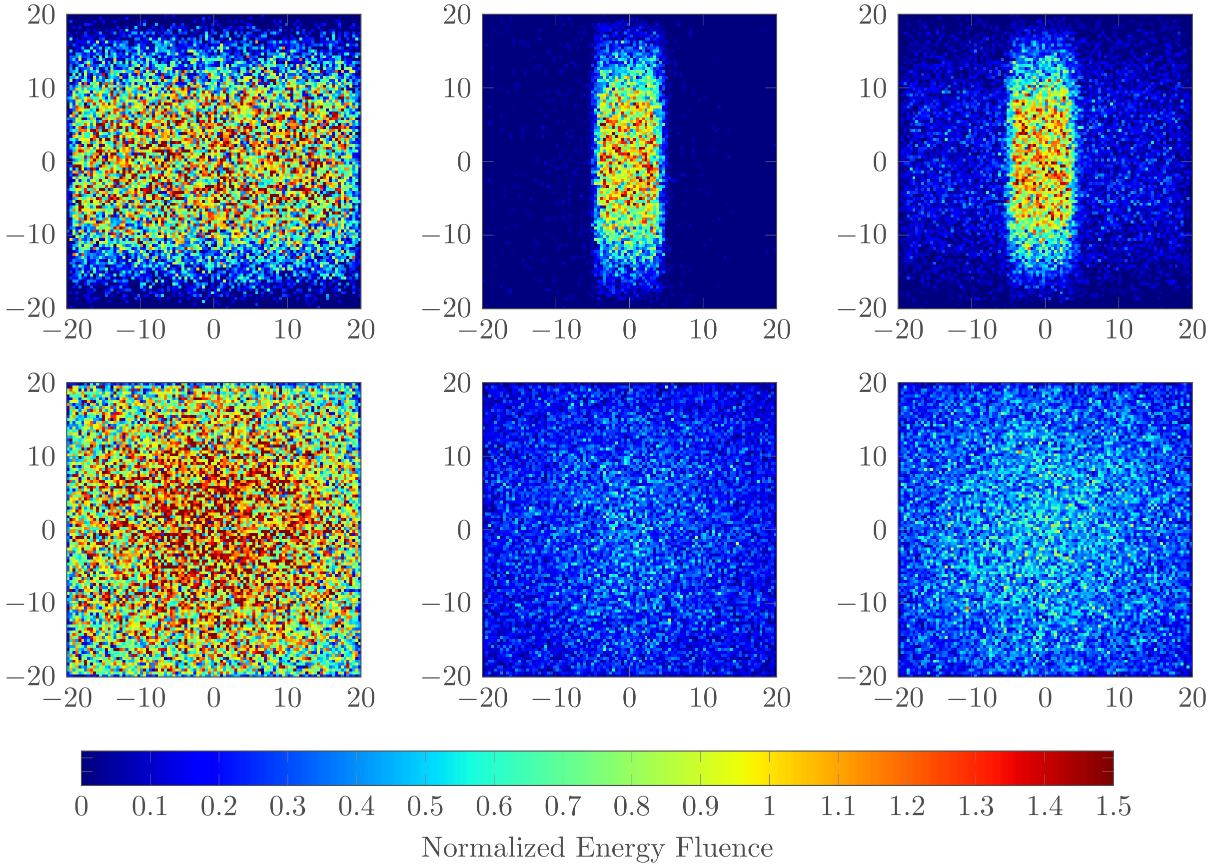

Figure B.3: Primary (top) and scattered (bottom) photon energy fluence at the detector plane for open (left), Pb collimated (center) and Cu filtered (right) beams.

We also investigated reduction of scatter contamination in projection images using Monte Carlo simulations. For this purpose we computed the phase space of photons on a plane 150 cm from the source (the nominal SDD of the OBI) with the beam passing through a 30x30x30 cm stack of water-equivalent plastic at SSD=90 cm between the source and detector. Simulations were performed for a 20 cm × 20 cm "open" beam and 5 cm × 20 cm beams formed by both lead blades and copper filters. The simulations were run with latching on, so bits were set in a status word for each photon indicating where it had intereacted. Photons whose status words indicated no interactions in the solid water stack were further analyzed to verify that their direction at the phase space plane indeed pointed directly away from the source, to eliminate false positive primary photons. Photons passing this test were classified as primary, all others as scattered. Scatter / primary ratios were then calculated for areas on the scoring plane both inside and outside the collimated beam. Results are shown in Figure B.3 and summarized in Table 4.5. As expected, the conformal field collimated by lead blades has a much lower scatter/primary ratio compared to the open field, while the intensity-weighted field shaped by copper filter blades achieves somewhat less, though still very significant reduction in scatter contamination. This means that the IWROI reconstructed images will have less scatter contamination, and thus potentially higher image quality inside the ROI, in addition to the dose saving outside the ROI due to severely reduced photon fluence.

The energy spectrum of primary and scattered photons was also assessed for the open and IWROI beams. Spectra are shown in Figure B.4 for incident (upstream of the solid water phantom), and Figure B.5 for primary and scattered photons inside and outside the 5×20 field. The hardening of the incident spectrum by the Cu filters is very significant, leading to approximately double the transmission of Cu-filtered compared to unfiltered photons through the 30 cm phantom. The spectrum of the primary unfiltered photons is also significantly hardened by transmission through the phantom, though their spectrum is still softer than that of the Cu filtered beam, which by comparison is only slightly affected by transmission through the phantom. The spectrum of scattered photons is essentially independent of position. This is because most of them originate from the intense unfiltered center of the incident beam, in addition to which the wide spatial spread of scatter (as reflected in Figure B.3, center column) ensures there is little correlation between the position of a scattered photon on the detector plane and its original location in the incident beam.

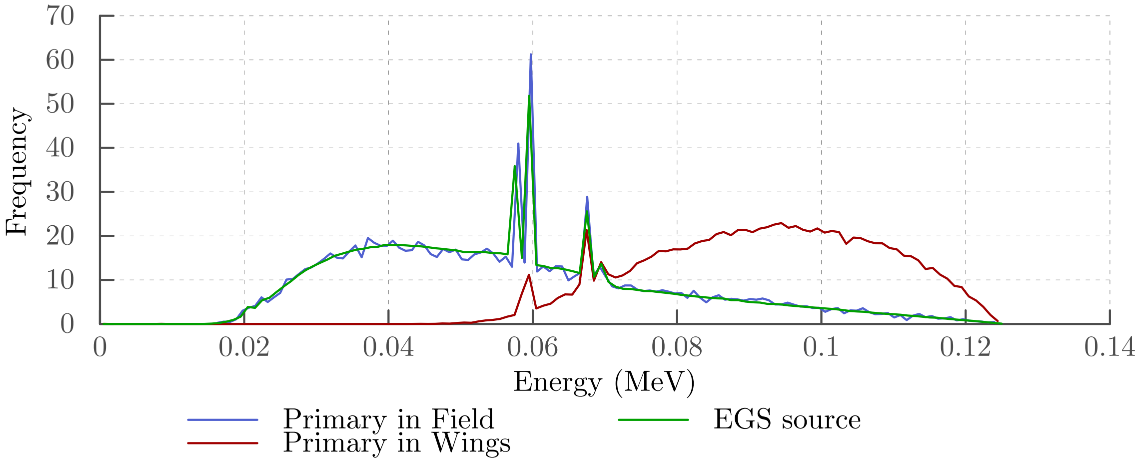

Figure B.4: Energy spectra of incident photons: green, source spectrum; blue, primary photons inside collimated field, red, primary photons under Cu filters.

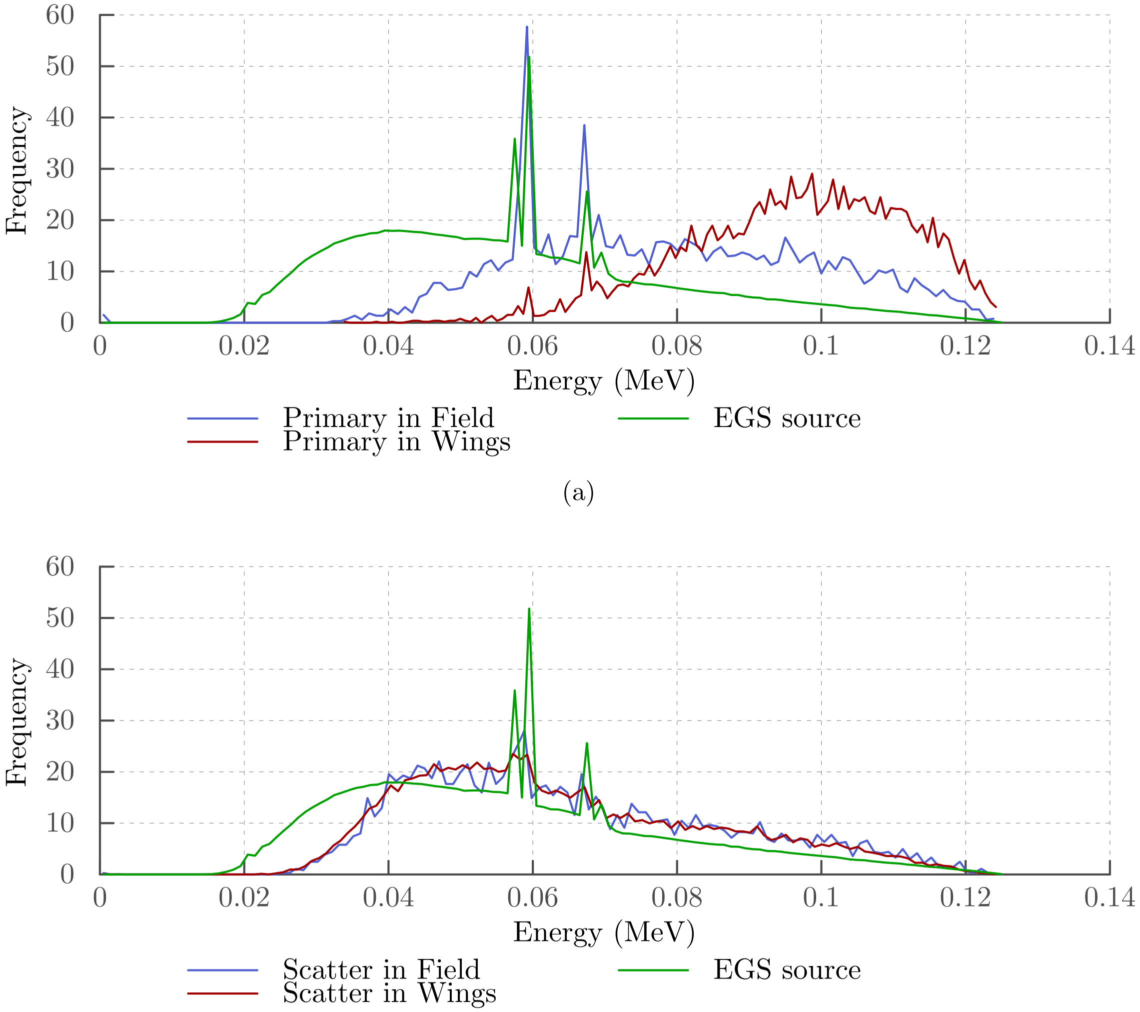

(a)

(b)

Figure B.5: Energy spectra of primary (top) and scattered (bottom) photons after transmission through 30 cm of solid water. Green: source spectrum; blue: photons in central unfiltered region; red: photons away from central region under Cu filters.

REFERENCES

[1]W. C. Röntgen, “On a new kind of rays”, Science **3**, 227–231 (1896).

[2]G. Meggitt, *Taming the rays* (Lulu, May 2010).

[3]Vocus/PRWEB, *Imv reports general x-ray procedures growing at 5.5% per year, as number of installed x-ray units declines*, (Feb. 2011) `http://www.prweb.com/releases/prweb2011/2/prweb8127064.htm` (visited on 02/13/2012).

[4]E. C. Beckmann, “CT scanning the early days”, British Journal of Radiology **79**, 5–8 (2006).

[5]A. M. Cormack, “Representation of a function by its line integrals, with some radiological applications. ii”, Journal of Applied Physics **35**, 2908–2913 (1964).

[6]A. M. Cormack, “Representation of a function by its line integrals, with some radiological applications”, Journal of Applied Physics **34**, 2722–2727 (1963).

[7]G. N. Hounsfield, “Computerized transverse axial scanning (tomography): part 1. description of system”, British Journal of Radiology **46**, 1016–1022 (1973).

[8]Vocus/PRWEB, *Latest imv ct survey shows hospitals gain ct procedures at imaging centers' expense*, (June 2011) `http://www.prweb.com/releases/2011/6/prweb8559972.htm` (visited on 02/13/2012).

[9]A. Kak and M. Slaney, *Principles of computerized tomographic imaging* (IEEE Press, 1988).

[10]B. D. Smith, “Cone-beam tomography: recent advances and a tutorial review”, Optical Engineering **29**, 524–534 (1990).

[11]D. A. Jaffray, J. H. Siewerdsen, and D. G. Drake, “Performance of a volumetric ct scanner based upon a flat-panel imager”, 204–214 (1999).

[12]R. Ning, X. Tang, R. Yu, D. L. Conover, and D. Zhang, “Flat-panel-detector-based cone beam volume ct imaging: detector evaluation”, 192–203 (1999).

[13]N. Jung, P. L. Alving, F. Busse, N. Conrads, H. J. Meulenbrugge, W. Ruetten, U. W. Schiebel, M. Weibrecht, and H. K. Wieczorek, “Dynamic x-ray imaging system based on an amorphous silicon thin-film array”, 396–407 (1998).

[14]D. A. Jaffray, D. G. Drake, M. Moreau, A. A. Martinez, and J. W. Wong, “A radiographic and tomographic imaging system integrated into a medical linear accelerator for local-

ization of bone and soft-tissue targets", International Journal of Radiation Oncology* Biology* Physics **45**, 773–789 (1999).

[15] D. A. Jaffray and J. Siewerdsen, "Cone-beam computed tomography with a flat-panel imager: initial performance characterization", Medical physics **27**, 1311 (2000).

[16] D. A. Jaffray, J. H. Siewerdsen, J. W. Wong, A. A. Martinez, et al., "Flat-panel cone-beam computed tomography for image-guided radiation therapy", International journal of radiation oncology, biology, physics **53**, 1337–1349 (2002).

[17] L. Feldkamp, L. Davis, and J. Kress, "Practical cone-beam algorithm", J. Opt. Soc. Am. **1**, 612–619 (1984).

[18] J Siewerdsen, "Mo-a-301-01: essentials of ct image reconstruction: 3d filtered backprojection", Medical Physics **38**, 3706 (2011).

[19] D. L. Parker, "Optimal short scan convolution reconstruction for fan beam ct", Medical Physics **9**, 254 (1982).

[20] P. M. Joseph and R. D. Spital, "A method for correcting bone induced artifacts in computed tomography scanners", Journal of Computer Assisted Tomography **2** (1978).

[21] P Rüegsegger, T. Hangartner, H. Keller, and T. Hinderling, "Standardization of computed tomography images by means of a material-selective beam hardening correction", Journal of computer assisted tomography **2**, 184–188 (1978).

[22] J. Hsieh, R. C. Molthen, C. A. Dawson, and R. H. Johnson, "An iterative approach to the beam hardening correction in cone beam ct", Medical Physics **27**, 23–29 (2000).

[23] J. H. Siewerdsen and D. A. Jaffray, "Cone-beam computed tomography with a flat-panel imager: magnitude and effects of x-ray scatter", eng, Medical physics **28**, 220–31 (2001).

[24] J. Hsieh, *Computed tomography: principles, design, artifacts, and recent advances*, Vol. 114 (Society of Photo Optical, 2003).

[25] H. Coutard, "Roentgen therapy of epitheliomas of the tonsillar region, hypopharynx and larynx from 1920 to 1926", Am J Roentgenol **28**, 313–31 (1932).

[26] N. Smith, I. Meir, G. Hale, R. Howe, L. Johnson, P. Edwards, D. Hawkes, M. Bidmead, and D. Landau, "Real-time 3d surface imaging for patient positioning in radiotherapy", in International journal of radiation oncology biology physics, Vol. 57 (Oct. 2003).

[27] J. Lattanzi, S. McNeeley, A. Hanlon, T. Schultheiss, and G. Hanks, "Ultrasound-based stereotactic guidance of precision conformal external beam radiation therapy in clinically localized prostate cancer", Urology **55**, 73–78 (2000).

[28]D Letourneau, J. Wong, M Oldham, M Gulam, L Watt, D. Jaffray, J. Siewerdsen, and A. Martinez, “Cone-beam-ct guided radiation therapy: technical implementation”, English, Radiother Oncol **75**, 279–286 (2005).

[29]U. Oelfke, T. Tcking, S. Nill, A. Seeber, B. Hesse, P. Huber, and C. Thilmann, “Linac-integrated kv-cone beam ct: technical features and first applications”, Medical Dosimetry **31**, Image-Guided Radiation Therapy, Part 1: Target Delineation and Localization, 62 –70 (2006).

[30]P. S. Cho, R. H. Johnson, and T. W. Griffin, “Cone-beam ct for radiotherapy applications”, Physics in Medicine and Biology **40**, 1863 (1995).

[31]S. Yoo and F.-F. Yin, “Dosimetric feasibility of cone-beam ct-based treatment planning compared to ct-based treatment planning”, English, Int J Radiat Oncol **66**, 1553–1561 (2006).

[32]M. Oldham, D. Létourneau, L. Watt, G. Hugo, D. Yan, D. Lockman, L. H. Kim, P. Y. Chen, A. Martinez, and J. W. Wong, “Cone-beam-ct guided radiation therapy: a model for on-line application”, Radiotherapy and Oncology **75**, 271.E1 –271.E8 (2005).

[33]J. M. Balter and M. L. Kessler, “Imaging and alignment for image-guided radiation therapy”, eng, J Clin Oncol **25**, 931–7 (2007).

[34]L. Xing, B. Thorndyke, E. Schreibmann, Y. Yang, T.-F. Li, G.-Y. Kim, G. Luxton, and A. Koong, “Overview of image-guided radiation therapy”, eng, Med Dosim **31**, 91–112 (2006).

[35]D Jaffray, “Emergent technologies for 3-dimensional image-guided radiation delivery”, Seminars in radiation oncology (2005).

[36]M. J. Murphy, J. Balter, S. Balter, J. A. BenComo, I. J. Das, S. B. Jiang, C. M. Ma, G. H. Olivera, R. F. Rodebaugh, K. J. Ruchala, H. Shirato, and F.-F. Yin, “The management of imaging dose during image-guided radiotherapy: report of the aapm task group 75”, eng, Medical physics **34**, 4041–63 (2007).

[37]M. W. Kan, L. H. Leung, W. Wong, and N. Lam, “Radiation dose from cone beam computed tomography for image-guided radiation therapy”, International Journal of Radiation Oncology*Biology*Physics **70**, 272 –279 (2008).

[38]M. K. Islam, T. G. Purdie, B. D. Norrlinger, H. Alasti, D. J. Moseley, M. B. Sharpe, J. H. Siewerdsen, and D. A. Jaffray, “Patient dose from kilovoltage cone beam computed tomography imaging in radiation therapy”, Medical Physics **33**, 1573–1582 (2006).

[39] H Greess, H Wolf, U Baum, M Lell, M Pirkl, W Kalender, and W. A. Bautz, "Dose reduction in computed tomography by attenuation-based on-line modulation of tube current: evaluation of six anatomical regions", Eur Radiol **10**, 391–4 (2000).

[40] W. A. Kalender, H Wolf, C Suess, M Gies, H Greess, and W. A. Bautz, "Dose reduction in ct by on-line tube current control: principles and validation on phantoms and cadavers", Eur Radiol **9**, 323–28 (1999).

[41] P. J. La Rivière, "Penalized-likelihood sinogram smoothing for low-dose ct", Med Phys **32**, 1676–83 (2005).

[42] J. Wang, H. Lu, J. Wen, and Z. Liang, "Multiscale penalized weighted least-squares sinogram restoration for low-dose x-ray computed tomography", IEEE Trans Biomed Eng **55**, 1022–31 (2008).

[43] J. Wang, T. Li, H. Lu, and Z. Liang, "Noise reduction for low-dose single-slice helical ct sinograms", IEEE Trans Nucl Sci **53**, 1230–1237 (2006).

[44] S. H. Manglos, G. M. Gagne, A Krol, F. D. Thomas, and R Narayanaswamy, "Transmission maximum-likelihood reconstruction with ordered subsets for cone beam ct", Phys Med Biol **40**, 1225–41 (1995).

[45] F. J. Beekma and C Kamphuis, "Ordered subset reconstruction for x-ray ct", Phys Med Biol **46**, 1835–44 (2001).

[46] J. Nuyts, B. De Man, P. Dupont, M. Defrise, P. Suetens, and L. Mortelmans, "Iterative reconstruction for helical CT: a simulation study", Physics in Medicine and Biology **43**, 729–738 (1998).

[47] S. LaRoque, E. Sidky, and X. Pan, "Accurate image reconstruction from few-view and limited-angle data in diffraction tomography", Journal of the Optical Society of America A **25**, 1772–1782 (2008).

[48] E. Sidky, C. Kao, and X. Pan, "Accurate image reconstruction from few-views and limited-angle data in divergent-beam CT", Journal of X-Ray Science and Technology **14**, 119–139 (2006).

[49] E. Sidky, C. Kao, and X. Pan, *Effect of the data constraint on few-view, fan-beam ct image reconstruction by tv minimization*, Presented at IEEE Nuclear Science Symposium Conference, 2006.

[50] F. Natterer, *The mathematics of computerized tomography* (Society for Industrial and Applied Mathematics, Jan. 2001), p. 222.

[51] A Faridani, D. Finch, E. Ritman, and K. Smith, “Local tomography .2”, English, Siam J Appl Math **57**, 1095–1127 (1997).

[52] M. A. Anastasio, D. Shi, X. Pan, C. Pelizzari, and P. Munro, “A preliminary investigation of local tomography for megavoltage ct imaging”, Medical Physics **30**, 2969–2980 (2003).

[53] M. A. Anastasio, Y. Zou, E. Y. Sidky, and X. Pan, “Local cone-beam tomography image reconstruction on chords”, JOSA A **24**, 1569–1579 (2007).

[54] A. Katsevich, “An improved exact filtered backprojection algorithm for spiral computed tomography”, Advances in Applied Mathematics **32**, 681 –697 (2004).

[55] J. Pack, F. Noo, and R. Clackdoyle, “Cone-beam reconstruction using the backprojection of locally filtered projections”, Medical Imaging, IEEE Transactions on **24**, 70–85 (2005).

[56] F. Noo, R. Clackdoyle, and J. D. Pack, “A two-step hilbert transform method for 2d image reconstruction”, Physics in Medicine and Biology **49**, 3903 (2004).

[57] M. Defrise, F. Noo, R. Clackdoyle, and H. Kudo, “Truncated hilbert transform and image reconstruction from limited tomographic data”, Inverse Problems **22**, 1037 (2006).

[58] X. Pan, Y. Zou, and D. Xia, “Peripheral and central ROI-image reconstruction from and data-redundancy exploitation in truncated fan-beam data”, Med. Phys **32**, 673–684 (2005).

[59] L. Yu, Y Zou, E. Sidky, C. Pelizzari, P Munro, and X. Pan, “Region of interest reconstruction from truncated data in circular cone-beam CT”, English, Ieee T Med Imaging **25**, 869–881 (2006).

[60] Y. Zou, X. Pan, and E. Y. Sidky, “Theory and algorithms for image reconstruction on chords and within regions of interest”, eng, J Opt Soc Am A Opt Image Sci Vis **22**, 2372–84 (2005).

[61] Y. Zou and X. Pan, “Exact image reconstruction on pi-lines from minimum data in helical cone-beam CT”, Physics in Medicine and Biology **49**, 941 (2004).

[62] S. Graham, J. Siewerdsen, H. Keller, D. Moseley, and D. Jaffray, *Intensity-modulated cone-beam CT for patient-specific distribution of SNR*, Presented at AAPM, 2005.

[63] S. Graham, J. Siewerdsen, and D. Jaffray, *Intensity-modulated fluence patterns for task-specific imaging in cone-beam CT*, Presented at SPIE Medical Imaging, 2007.

[64] S. Bartolac, S. Graham, J. Siewerdsen, and D. Jaffray, “Fluence field optimization for noise and dose objectives in ct”, Medical Physics **38**, S2–S17 (2011).

[65]S. Bartolac, S. Graham, J. Siewerdsen, and D. Jaffray, *An inverse planning method for intensity modulated computed tomography*, Presented at AAPM, 2010.

[66]T. P. Szczykutowicz and C. A. Mistretta, “Design of a digital beam attenuation system for computed tomography: part i. system design and simulation framework”, Medical Physics **40**, 021905, 021905 (2013).

[67]T. P. Szczykutowicz and C. Mistretta, “Practical considerations for intensity modulated ct”, 83134E–83134E–11 (2012).

[68]G. F. Franklin, J. D. Powell, and A. E. Naeini, *Feedback control of dynamic systems*, 4th ed. (Prentice Hall, 2002).

[69]Y. Censor, M. Jiang, and G. Wang, *Biomedical mathematics: promising directions in imaging, therapy planning, and inverse problems* (Medical Physics Publising, 2010).

[70]K. Ohara, T. Okumura, M. Akisada, T. Inada, T. Mori, H. Yokota, and M. J. Calaguas, “Irradiation synchronized with respiration gate”, International Journal of Radiation Oncology*Biology*Physics **17**, 853 –857 (1989).

[71]H. D. Kubo, P. M. Len, S. ichi Minohara, and H. Mostafavi, “Breathing-synchronized radiotherapy program at the university of california davis cancer center”, Medical Physics **27**, 346–353 (2000).

[72]A. Schweikard, G. Glosser, M. Bodduluri, M. J. Murphy, and J. R. Adler, “Robotic motion compensation for respiratory movement during radiosurgery”, Computer Aided Surgery **5**, 263–277 (2000).

[73]S. B. Jiang, “Technical aspects of image-guided respiration-gated radiation therapy”, Medical Dosimetry **31**, ¡ce:title¿Image-Guided Radiation Therapy, Part 2: Cone-Beam Imaging and Respiratory Motion¡/ce:title¿, 141 –151 (2006).

[74]H. Shirato, S. Shimizu, T. Kunieda, K. Kitamura, M. van Herk, K. Kagei, T. Nishioka, S. Hashimoto, K. Fujita, H. Aoyama, K. Tsuchiya, K. Kudo, and K. Miyasaka, “Physical aspects of a real-time tumor-tracking system for gated radiotherapy”, International Journal of Radiation Oncology*Biology*Physics **48**, 1187 –1195 (2000).

[75]P. J. Keall, V. R. Kini, S. S. Vedam, and R Mohan, “Motion adaptive x-ray therapy: a feasibility study”, Physics in Medicine and Biology **46**, 1 (2001).

[76]C. Ozhasoglu and M. J. Murphy, “Issues in respiratory motion compensation during external-beam radiotherapy”, International Journal of Radiation Oncology*Biology*Physics **52**, 1389 –1399 (2002).

[77] J. W. Wong, M. B. Sharpe, D. A. Jaffray, V. R. Kini, J. M. Robertson, J. S. Stromberg, and A. A. Martinez, “The use of active breathing control (ABC) to reduce margin for breathing motion”, International Journal of Radiation Oncology*Biology*Physics **44**, 911 –919 (1999).

[78] S. S. Vedam, V. R. Kini, P. J. Keall, V. Ramakrishnan, H. Mostafavi, and R. Mohan, “Quantifying the predictability of diaphragm motion during respiration with a noninvasive external marker”, Medical Physics **30**, 505–513 (2003).

[79] J. D. Hoisak, K. E. Sixel, R. Tirona, P. C. Cheung, and J.-P. Pignol, “Correlation of lung tumor motion with external surrogate indicators of respiration”, International Journal of Radiation Oncology*Biology*Physics **60**, 1298 –1306 (2004).

[80] M. S. Hoogeman, J. J. Nuyttens, P. C. Levendag, and B. J. Heijmen, “Time dependence of intrafraction patient motion assessed by repeat stereoscopic imaging”, International Journal of Radiation Oncology*Biology*Physics **70**, 609 –618 (2008).

[81] R. I. Berbeco, S. B. Jiang, G. C. Sharp, G. T. Y. Chen, H. Mostafavi, and H. Shirato, “Integrated radiotherapy imaging system (IRIS): design considerations of tumour tracking with linac gantry-mounted diagnostic x-ray systems with flat-panel detectors”, Physics in Medicine and Biology **49**, 243 (2004).

[82] H. Shirato, S. Shimizu, T. Shimizu, T. Nishioka, and K. Miyasaka, “Real-time tumour-tracking radiotherapy”, The Lancet **353**, 1331–1332 (1999).

[83] R. Wiersma, W. Mao, and L. Xing, “Combined kV and MV imaging for real-time tracking of implanted fiducial markers”, Medical physics **35**, 1191 (2008).

[84] R. D. Wiersma, N Riaz, S. Dieterich, Y. Suh, and L Xing, “Use of mv and kv imager correlation for maintaining continuous real-time 3d internal marker tracking during beam interruptions”, Physics in Medicine and Biology **54**, 89 (2009).

[85] P. Kupelian, T. Willoughby, A. Mahadevan, T. Djemil, G. Weinstein, S. Jani, C. Enke, T. Solberg, N. Flores, D. Liu, D. Beyer, and L. Levine, “Multi-institutional clinical experience with the calypso system in localization and continuous, real-time monitoring of the prostate gland during external radiotherapy”, International Journal of Radiation Oncology*Biology*Physics **67**, 1088 –1098 (2007).

[86] H. Shirato, M. Oita, K. Fujita, Y. Watanabe, and K. Miyasaka, “Feasibility of synchronization of real-time tumor-tracking radiotherapy and intensity-modulated radiotherapy from viewpoint of excessive dose from fluoroscopy”, International Journal of Radiation Oncology*Biology*Physics **60**, 335 –341 (2004).

[87] W. Mao, R. Wiersma, and L. Xing, “Fast internal marker tracking algorithm for onboard MV and kV imaging systems”, Medical physics **35**, 1942 (2008).

[88] W. Mao, N. Riaz, L. Lee, R. Wiersma, and L. Xing, "A fiducial detection algorithm for real-time image guided IMRT based on simultaneous mv and kv imaging", Medical Physics **35**, 3554–3564 (2008).

[89] E. Rietzel, S. J. Rosenthal, D. P. Gierga, C. G. Willett, and G. T. Chen, "Moving targets: detection and tracking of internal organ motion for treatment planning and patient set-up", Radiotherapy and Oncology **73**, S68–S72 (2004).

[90] U Johnson, D Landau, J Lindgren-Turner, N Smith, I Meir, R Howe, H Rodgers, S Davit, and C Deehan, "Real time 3d surface imaging for the analysis of respiratory motion during radiotherapy", International Journal of Radiation Oncology* Biology* Physics **60**, S603–S604 (2004).

[91] N Smith, I Meir, G Hale, R Howe, L Johnson, P Edwards, D Hawkes, M Bidmead, and D Landau, "Real-time 3d surface imaging for patient positioning in radiotherapy", International Journal of Radiation Oncology* Biology* Physics **57**, S187–S187 (2003).

[92] T. R. Willoughby, P. A. Kupelian, J. Pouliot, K. Shinohara, M. Aubin, M. Roach III, L. L. Skrumeda, J. M. Balter, D. W. Litzenberg, S. W. Hadley, et al., "Target localization and real-time tracking using the calypso 4d localization system in patients with localized prostate cancer", International Journal of Radiation Oncology* Biology* Physics **65**, 528–534 (2006).

[93] "Novel breathing motion model for radiotherapy", International Journal of Radiation Oncology*Biology*Physics **63**, 921 –929 (2005).

[94] T. Zhao, W. Lu, D. Yang, S. Mutic, C. E. Noel, P. J. Parikh, J. D. Bradley, and D. A. Low, "Characterization of free breathing patterns with 5d lung motion model", Medical physics **36**, 5183 (2009).

[95] A. Katsevich, "Analysis of an exact inversion algorithm for spiral cone-beam CT", Physics in medicine and biology **47**, 2583 (2002).

[96] Y. Zou and X. Pan, "Image reconstruction on pi-lines by use of filtered backprojection in helical cone-beam ct", eng, Physics in Medicine and Biology **49**, 2717–31 (2004).

[97] J. Pack and F Noo, "Cone-beam reconstruction using 1d filtering along the projection of m-lines", English, Inverse Problems **21**, 1105–1120 (2005).

[98] F. Noo, R. Clackdoyle, and J. D. Pack, "A two-step hilbert transform method for 2d image reconstruction", eng, Physics in Medicine and Biology **49**, 3903–23 (2004).

[99] X. Pan, D. Xia, Y. Zou, and L. Yu, "A unified analysis of FBP-based algorithms in helical cone-beam and circular cone-and fan-beam scans", Physics in Medicine and Biology **49**, 4349 (2004).

[100] Y. Zou, X. Pan, and E. Sidky, “Image reconstruction in regions-of-interest from truncated projections in a reduced fan-beam scan”, Physics in Medicine and Biology **50**, 13 (2005).

[101] X. Pan, Y. Zou, and D. Xia, “Image reconstruction in peripheral and central regions-of-interest and data redundancy”, Medical physics **32**, 673 (2005).

[102] E. Huang, S. Tucker, E. Strom, M. McNeese, H. Kuerer, A. Buzdar, V. Valero, G. Perkins, N. Schechter, K. Hunt, et al., “Postmastectomy radiation improves local-regional control and survival for selected patients with locally advanced breast cancer treated with neoadjuvant chemotherapy and mastectomy”, Journal of Clinical Oncology **22**, 4691 (2004).

[103] V. Gebski, M. Lagleva, A. Keech, J. Simes, and A. Langlands, “Survival effects of postmastectomy adjuvant radiation therapy using biologically equivalent doses: a clinical perspective”, JNCI Journal of the National Cancer Institute **98**, 26 (2006).

[104] X. Pan, D Xia, Y Zou, and L. Yu, “A unified analysis of FBP-based algorithms in helical cone-beam and circular cone- and fan-beam scans”, English, Physics in Medicine and Biology **49**, 4349–4369 (2004).

[105] E. Pearson, S. Cho, C. Pelizzari, and X. Pan, “Non-circular cone beam ct trajectories: a preliminary investigation on a clinical scanner”, in Nuclear science symposium conference record (nss/mic), 2010 ieee (IEEE, 2010), pp. 3172–3175.

[106] D. Xia, L. Yu, E. Y. Sidky, Y. Zou, N. Zuo, and X. Pan, “Noise properties of chord-image reconstruction”, English, Ieee T Med Imaging **26**, 1328–1344 (2007).

[107] X. Han, D. Xia, E. Y. Sidky, and X. Pan, *Noise properties of the discrete finite hilbert transform*, Presented at IEEE Nuclear Science Symposium and Medical Imaging Conference, Oct. 2008.

[108] S. Cho, E. Pearson, D. Xia, X. Han, C. Pelizzari, and X. Pan, “A preliminary study of intensity-weighted roi imaging in cone-beam ct”, in Proceedings of the spie, Vol. 6913 (2008), p. 255.

[109] S. Cho, “Advanced reconstruction techniques in cone-beam computed tomography for image-guided radiation therapy”, PhD thesis (University of Chicago, 2009).

[110] A. R. Pineda, D. J. Tward, A. Gonzalez, and J. H. Siewerdsen, “Beyond noise power in 3d computed tomography: the local nps and off-diagonal elements of the fourier domain covariance matrix”, Medical Physics **39**, 3240–3252 (2012).

[111] E. Pearson, S. Cho, X. Pan, and C. Pelizzari, *Region-of-interest imaging for cone-beam CT in radiation therapy*, Presented at Varian Research Partners Symposium, Apr. 2008.

[112] E. Pearson, S. Cho, X. Pan, and C. Pelizzari, *Dose reduction in CBCT via intensity-weighted region-of-interest imaging*, Presented at AAPM, July 2008.

[113] E. Pearson, S. Cho, X. Pan, and C. Pelizzari, *Comparison of achievable dose reduction in CBCT for the prostate using intensity-weighted and conformal region of interest imaging techniques*, Presented at ASTRO, Nov. 2009.

[114] S. Cho, E. Pearson, C. Pelizzari, and X. Pan, "Noise analysis in intensity-weighted region-of-interest imaging for cone-beam ct", in Proceedings of the spie, Vol. 7258 (2009), p. 706.

[115] S. Cho, E. Pearson, C. Pelizzari, and X. Pan, "Region-of-interest imaging with intensity-weighting in circular cone-beam ct for image-guided radiation therapy", Medical Physics **36**, 1184–1192 (2009).

[116] X. Tang, R. Ning, R. Yu, and D. L. Conover, "Investigation into the influence of x-ray scatter on the imaging performance of an x-ray flat-panel imager-based cone-beam volume ct", 851–860 (2001).

[117] A. Malusek, M. P. Sandborg, and G. A. Carlsson, "Simulation of scatter in cone beam ct: effects on projection image quality", 740–751 (2003).

[118] J. Siewerdsen, M. Daly, B Bakhtiar, D. Moseley, S Richard, H Keller, and D. Jaffray, "A simple, direct method for x-ray scatter estimation and correction in digital radiography and cone-beam ct", English, Medical physics **33**, 187–197 (2006).

[119] N. L. Childress, L. Dong, and I. I. Rosen, "Rapid radiographic film calibration for imrt verification using automated mlc fields", Medical Physics **29**, 2384–2390 (2002).

[120] M. Sadinski, E. Pearson, and C. Pelizzari, "Dose reduction intensity weighted region of interest and true region of interest conebeam CT imaging: a monte carlo and phantom stud", in RSNA annual meeting (2012).

[121] W. Giles, J. Bowsher, H. Li, and F.-F. Yin, "Crescent artifacts in cone-beam ct", Medical physics **38**, 2116 (2011).

[122] T. R. Mackie, J. W. Scrimger, and J. J. Battista, "A convolution method of calculating dose for 15-mv x rays", Medical Physics **12**, 188–196 (1985).

[123] T. R. Mackie, A. F. Bielajew, D. W. O. Rogers, and J. J. Battista, "Generation of photon energy deposition kernels using the egs monte carlo code", Physics in Medicine and Biology **33**, 1 (1988).

[124] R. Mohan, C. Chui, and L. Lidofsky, "Differential pencil beam dose computation model for photons", Medical Physics **13**, 64–73 (1986).

[125]A. Ahnesjo, “Collapsed cone convolution of radiant energy for photon dose calculation in heterogeneous media”, Medical Physics **16**, 577–592 (1989).

[126]A. Ahnesjö, P. Andreo, and A. Brahme, “Calculation and application of point spread functions for treatment planning with high energy photon beams”, Acta Oncologica **26**, 49–56 (1987).

[127]P. Alaei, B. J. Gerbi, and R. A. Geise, “Lung dose calculations at kilovoltage x-ray energies using a model-based treatment planning system”, Medical Physics **28**, 194–198 (2001).

[128]P. Alaei, B. J. Gerbi, and R. A. Geise, “Generation and use of photon energy deposition kernels for diagnostic quality x rays”, Medical Physics **26**, 1687–1697 (1999).

[129]P. Alaei, B. J. Gerbi, and R. A. Geise, “Evaluation of a model-based treatment planning system for dose computations in the kilovoltage energy range”, Medical Physics **27**, 2821–2826 (2000).

[130]I Kawrakow and D Rogers, “The EGSnrc code system: monte carlo simulation of electron and photon transport”, (2000).

[131]D. Rogers, B Walters, I. Kawrakow, et al., “BEAMnrc users manual”, NRC Report PIRS **509** (2001).

[132]I Kawrakow and B. Walters, “Efficient photon beam dose calculations using DOSXYZnrc with BEAMnrc”, Medical physics **33**, 3046 (2006).

[133]A. Micke, D. F. Lewis, and X. Yu, “Multichannel film dosimetry with nonuniformity correction”, Medical Physics **38**, 2523–2534 (2011).

[134]R. Drzymala, R Mohan, L Brewster, J Chu, M Goitein, W Harms, and M Urie, “Dose-volume histograms”, International Journal of Radiation Oncology* Biology* Physics **21**, 71–78 (1991).

[135]U. N. R. Commission et al., “Standards for protection against radiation”, Washington, DC: US Government Printing Office **10**, 20–1001 (2006).